UPC

DOCTORAL THESIS

Experimental Evidence for the Quantum Condensation of Ultracold Dipolar Excitons

Thesis advisor:
Maciej Lewenstein
Thesis co-advisor:
François Dubin

Author:
Mathieu Alloing

A thesis submitted in fulfilment of the requirements
for the degree of Doctor of Philosophy

April 2014

"S'il n'y a pas de solutions c'est qu'il n'y a pas de problème."

Jacques Rouxel

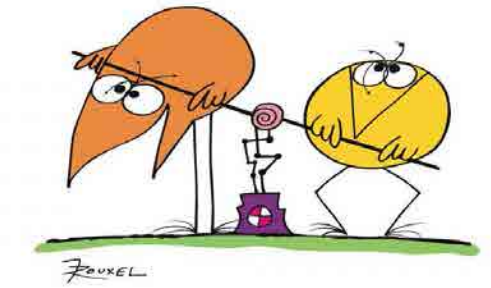

ABSTRACT

In this thesis, we report experimental evidence of a "gray" condensate of excitons, as predicted theoretically by M. Combescot et al. Most importantly, the condensate is characterized by the macroscopic population of dark excitons coherently coupled to a weak population of bright excitons through fermion exchanges. Such quantum condensation results from the excitons internal structure, with a dark i.e. optically inactive ground state. It is actually very similar to what occurs in the phases of superfluid ^{3}He or in the more recent spinor condensates of ultracold atomic Bose gases. While it is our belief that such a "gray" condensate will eventually be observed in other excitonic systems, our study focus on its appearance together with the macroscopic auto-organization of dipolar excitons. Precisely we emphasize fragmented exciton rings in an electrically biased GaAs single quantum well. This very striking pattern was first observed independently by the groups of L. Butov and D. Snoke. It was interpreted as the result of an ambipolar diffusion of carriers in the quantum wells. The fragmentation of the macrosopic ring observed at low temperature by Butov and coworkers, and the subsequent evidence for long-range spatial coherence together with complex pattern of polarization, led Butov et al. to interpret the fragmentation as an evidence for the transition to a quantum regime where coherent exciton transport dominates.

Our experiments led us to a very different interpretation. Indeed, we show that for our sample the formation of the fragmented ring is dominated by the diffusion of dipolar excitons in an optically induced electrostatic landscape. This potential landscape arises from the modulation of the internal electric field by excess charges injected in the QW by the same excitation beam which induces the ring. Dipolar excitons then explore a potential landscape characterized by a wide anti-trap inside the ring and more strikingly by microscopic traps distributed along the circumference of the ring. There, i.e. in the outside vicinity of the ring, a confining potential is responsible for the formation of "islands" where the population of dark excitons is dominant. Due to the low energy splitting between the bright and dark excitonic states in our sample, the observation of a dominant population of dark excitons signals that excitons condense in the low-lying dark states.

To confirm this interpretation we show that the weak photoluminescence emitted in the outer vicinity of the ring exhibits macroscopic spatial coherence, up to 10 times larger than the de Broglie wavelength. Islands of extended coherence are in fact identified and quickly disappear upon increase of the bath temperature. This leads to an evolution of the coherence length strongly dependent on the temperature. Finally, we show that the photoluminescence emitted in the vicinity of the fragmented ring is dominantly linearly polarized and also organized in islands outside the ring. All these observations confirm the predicted signatures of a "gray" condensate, as formulated by M. and R. Combescot.

Keywords : dipolar exciton, excitonic BEC, fragmented ring, electrically biased semiconductor heterostructure

RESUM

En aquesta tesis, mostrem evidència experimental d'un condensat “gris” d'excitons, tal com prediu la teoria de M. Combescot et al. En particular, el condensat està caracteritzat per la població macroscòpica d'excitons foscos acoblats coherentment a una població baixa d'excitons brillants a través d'intercanvis fermiònics. Aquesta condensació quàntica es dóna com a resultat de l'estructura interna dels excitons, amb un estat fonamental fosc i.e. òpticament inactiu. És de fet molt similar al que passa en les fases de ^{3}He superfluid o en els més recents condensats d'espinors de gasos atòmics ultrafreds de Bose. Encara que nosaltres creiem que un condensat “gris” serà eventualment observat en altres sistemes excitònics, el nostre estudi es focalitza en la seva manifestació juntament amb l'auto-organització macroscòpica d'excitons dipolars. Precisament, ens centrem en els anells excitònics fragmentats en un GaAs sol pou quàntic elèctricament polaritzat. Aquest sorprenent patró va ser observat independentment per primer cop pels grups de L. Butov i D. Snoke. Va ser interpretat com el resultat d'una difusió ambipolar de portadors en pous quàntics. La fragmentació de l'anell macroscòpic observada a baixes temperatures per Butov i els seus col•laboradors, i la posterior evidència de coherència espacial de llarg abast juntament amb un patró de polarització complex, va portar a Butov et al. a interpretar la fragmentació com una evidència de la transició cap al règim quàntic en el que domina el transport coherent d'excitons.

El nostre experiment ens va portar cap una interpretació molt diferent. En efecte, mostrem que per la nostra mostra la formació d'anells fragmentats és dominada per la difusió d'excitons dipolars en un perfil electrostàtic òpticament induït. Aquest perfil de potencial sorgeix de la modulació del camp elèctric intern per un excés de càrregues injectades en el PQ pel mateix feix d'excitació que indueix l'anell. Les excitons dipolars exploren per tant un perfil de potencial caracteritzat per una anti-trampa ampla dins de l'anell i més sorprenentment per trampes microscòpiques distribuïdes al llarg de la circumferència de l'anell. Allà, i.e. en la proximitat exterior de l'anell, un potencial de confinament és el responsable de la formació d'“illes” on la població d'excitons foscos és dominant. Degut a la baixa separació energètica entre els estats excitònics brillant i fosc en la nostra mostra, l'observació d'una població dominant d'excitons foscos senyala que els excitons es condensen en els estats foscos de més baixa energia.

Per tal de confirmar aquesta interpretació, mostrem que la dèbil fotoluminescència emesa en la proximitat exterior exhibeix coherència espacial macroscòpica, fins a 10 vegades major que la longitud d'ona de de Broglie. Illes de coherència ampliada són de fet identificades i desapareixen ràpidament en incrementar la temperatura del focus. Això porta cap a una evolució de la longitud de coherència que depèn fortament de la temperatura. Finalment, mostrem que la fotoluminescència emesa en la proximitat de l'anell fragmentat està dominantment polaritzada linealment i organitzada també en illes fora de l'anell. Totes les observacions confirmen les senyals característiques previstes per un condensat "gris", tal com està formulat en la teoria desenvolupada per M. i R. Combescot.

Paraula clau : excitons dipolars, condensat de Bose-Einstein excitònic, anells fragmentats, sol pou quàntic elèctricament polaritzat

Acknowledgments

First of all I would like to express my gratitude to Pr. Maciej Lewenstein for having given to me the opportunity of doing this PhD and for its support to our experimental group even though he is in in principle more dedicated to theoretical works.

Our experiment was born thanks to the support of Pr. Juergen Eschner and I wish to express my gratitude to him and his group. In particular I would like to thank Jan Huwer, Felix Rhode for their help and finally to Hannes Gothe for sharing a flat and (many) jars of Nutella with me.

My PhD would never have been possible without the dedication and the trust of Francois Dubin who is much more than my thesis co-advisor. I consider myself very lucky to have had the opportunity to work with him and to have benefited from his experience. I wish you, Sylvia, Nicola and Emma a great new start in Paris.

During my PhD our small group almost doubled its size (from 2 to 3 !) with the arrival of Mussie Beian. He and his concentration of good mood have been a great contribution to the rest of my PhD and I am very grateful to him. Mussie, I wish you all the best for your continuation !

The beginning of my PhD was mostly dedicated to install the experimental setup and I would like to thank the members of the mechanical and electronic workshops of ICFO for their help. Mounting a new experiment and developing it have shown to me how important it is to have at your disposal such dedicated and competent persons.

I am very grateful to the group of Hugues de Riedmatten and espacially to Matteo Cristiani (Matlab master !) who was always available to answer my questions and to provide very interesting insights to my work. I deeply wish you all the best for your future projects.

A thesis on semiconductors can not be done without samples and in this regards I had the chance to collaborate with Luisa Gonzalez, Yolanda Gonzalez, David Fuster and Aristide Lemaître whose expertise in epitaxy was invaluable to provide high quality samples. I would particularly like to thank our colleagues of the IMM who were always enthusiastic and motivated to try new heterostructures and who produced the fantastic sample used in this manuscript. Obtaining a working sample is a long and delicate process and I am very grateful to Luis Enrique, Johann Osmond and Carme Gomez for their patience and dedication in teaching and helping me through the various techniques of sample processing.

Finally I wish to express my gratitude to Monique and Roland Combescot for their invaluable inputs and comments of my work. It was a great privilege to collaborate with such highly knowledgeable theoreticians.

Last but not least I would like to thank my entire family and my friends. I am

in particular very grateful to my parents and my sister for supporting and inspiring me during my studies and all these years.

PUBLICATIONS

M. Combescot, R. Combescot, M. Alloing and F. Dubin. Optical signatures of a fully dark exciton condensate, *Europhysics Letters*, **105** 47011 (2014).

M. Alloing, M. Beian, D. Fuster, Y. Gonzalez, L. Gonzalez, R. Combescot, M. Combescot and F. Dubin. Evidence for a Bose-Einstein condensate of excitons, arXiv:1304.4101 (2013).

M. Alloing, A. Lemaître, E. Galopin, and F. Dubin. Optically programmable excitonic traps, *Scientific Reports*, **3** 1578 (2013).

M. Alloing, A. Lemaître, E. Galopin, and F. Dubin. Nonlinear dynamics and inner-ring photoluminescence pattern of indirect excitons, *Phys. Rev. B*, **85**(24) 245106 (2012).

M. Alloing, A. Lemaître and F. Dubin. Quantum signature blurred by disorder in indirect exciton gases, *Europhysics Letters*, **93** 17007 (2011).

C. Trefzger, M. Alloing, C. Menotti, F. Dubin and M. Lewenstein. Quantum magnetism and counterflow supersolidity of up-down bosonic dipoles, *New Journal of Physics*, **12**(9) 093008 (2010).

Contents

To my family and my friends...

Introduction

In 1924-25, Albert Einstein and Satyendra Nath Bose [1, 2] established that below a threshold temperature a large fraction of a dilute gas of bosons should experience a stimulation towards the ground state of the system. This stimulation results in a fifth state of matter, a Bose-Einstein condensate (BEC), characterized by the macroscopic occupation of the ground state. The transition to a Bose-Einstein condensate occurs below a critical temperature which for a uniform three-dimensional gas of non-interacting bosons can be expressed as $T_c \propto n^{2/3}/m$, where n and m are respectively the density and the mass of the bosons. Despite strong experimental challenges to cool atomic gases in the microkelvin regime, the first irrefutable observation of a Bose-Einstein condensation was obtained in 1995 by Cornell, Wieman and later by Ketterle with Rubidium and Sodium vapors [3, 4]. Since then, the demonstration of BEC for several atomic species has unfold a whole new area of many-body physics (see [5] for a review).

This observation came somewhat as a surprise since following the proposal of Blatt and Moskalenko [6, 7] and the calculations of Keldysh [8] in the 1960s, physicists were expecting the condensation of semiconductor excitons to be easier. Indeed, due to their low effective mass, excitons are supposed to condense at temperatures directly achievable in cryogenic environments. Over the last decades, various claims have been made for the observation of an exciton BEC but the lack of convincing results led to a global skepticism of the scientific community over the possibility of realizing at all a Bose-Einstein condensate of excitons.

One of the drawback of semiconductor is that contrarily to atomic gases, excitons do not evolve in vacuum but in an extremely dense crystal matrix which strongly influences the exciton physical properties. Nevertheless, the long search for an excitonic BEC have benefited from the improvement of epitaxial growth techniques for semiconductor to reduce the number of impurities and the development of quantum wells to confine the exciton motion [9, 10]. Following the proposal of Lozovik and Yudson [11], the last 20 years have seen the development of electrically biased semiconductor heterostructures

[12, 13] thus increasing the level of control over excitonic gases and allowing the realization of various landscapes and devices for excitons [14–22]. In such heterostructures, the group of L. Butov managed to observe long-range spatial coherence in an electrostatic trap created by electrodes deposited at the surface of the heterostructures [23]. Let us mention that remarkable results have also been obtained by V. Timofeev et al. in a ring trap [24–28].

An alternative approach to tackle the condensation of excitons involves lowering even further the effective mass. To this aim, semiconductor microcavities have been studied, as these allow to enter the strong coupling regime between excitons and photons. This results in exciton-polaritons [29], i.e. composite bosons with have an effective mass four order of magnitude lighter than of excitons. Studying exciton-polaritons caused a renewed interest in condensation in solid-state systems and very rapidly experiments produced results consistent with the observation of a BEC of excitons-polaritons [30–33]. However, a few years were necessary for the community to reach a consensus and to agree on the interpretation of the results as condensation of exciton-polaritons. Nowadays, studies of exciton-polaritons lie in a very active field which provided remarkable experiments [34–44].

In 2007, M. Combescot et al. [45, 46] proposed an explanation for the difficulty to obtain condensation in a pure excitonic system. For a long time it was known that due to their composite nature, excitons in quantum wells can be found in four different states : two bright ones optically coupled to the light and two dark states which do not recombine by emitting photons and lie at lower energy [47–49]. The energy splitting between the bright and dark excitonic states is due to interband Coulomb scattering. Therefore, if Bose-Einstein condensation of excitons can occur, then it must take place within the dark states which energy is the lowest. Thus, the condensate of excitons can not be observed by conventional experimental techniques relying on measurements of the photoluminescence emitted by bright excitons. While this behavior holds in the very dilute regime, Combescot et al. [50] showed that at higher densities, exciton interactions coherently introduce a bright part to the condensate. The condensate thus becomes "gray" and can, fortunately, be studied through the very weak photoluminescence of its bright part.

In this manuscript, we report experimental evidence of such a "gray" condensate, through the experimental observations of all its characteristics. Our experiments are based on the analysis of macroscopic patterns of dipolar excitons, first observed in 2002 in biased GaAs double quantum wells heterostructures simultaneously by the groups of L. Butov and D. Snoke [51, 52]. This observation of a photoluminescence ring several hundreds of micrometers from the excited region raised a large interest in the exciton community. More striking was the observation by Butov at al. of a self-organization of the photoluminescence ring in fragments below a bath temperature of 2K. Numerous theoretical models were then developed to interpret the formation mechanism of ring, notably relying on the charge separation (electrons and holes) in the quantum wells [53–56]. However, to date, no consensual model describing the fragmentation has been proposed.

In the past years, the group of L. Butov has extensively studied fragmented rings [57–60] and most importantly published in 2012 experimental results showing that the photoluminescence of the ring locally exhibits long-range spatial coherence and complex polarization patterns [61]. The authors interpreted these results as the signature for a transition towards a quantum regime dominated by coherent exciton transport and spin-orbit coupling.

Our study of fragmented rings formed in an electrically biased GaAs single quantum well has led us to a very different interpretation which will be progressively developed according to the following outline :

- Chapter I presents basic properties of excitons in biased quantum well and rapidly describe Bose-Einstein condensation. We then introduce the composite nature of excitons and show how it led Monique and Roland Combescot to predict the appearance of a "gray" condensate.
- In chapter II we present the basic characteristics of our sample and our experimental setup with a particular emphasis on Mach-Zehnder interferometry.
- Chapter III enters in the core of the manuscript where we study the response of our fragmented ring to the modification of the experimental parameters by studying both the direct photoluminescence and its spectrum. We also measure the dynamics of the ring both spatially and spectrally. While many of our results are consistent with previous observations and theoretical models, our sample exhibits important differences which lead us to conclude that a quasi-stationary potential landscape for excitons exists and actually appears together with the fragmented ring.
- In chapter IV, using pump-probe techniques, we demonstrate that, in the regime where the fragmented ring is formed, excitons explore an electrostatic landscape controlled by free charges injected by the laser excitation. These effectively screen the internal electric field. The accurate measurement of this potential reveals local traps distributed along the circumference of the ring, *a priori* responsible for the fragmentation. Thus, we precisely retrieve the distribution of the exciton density at

the position of the ring and demonstrate “islands” in the outside vicinity of the ring where the population of dark excitons is dominant. Due to the low energy splitting between the bright and dark excitonic states in our sample, this observation of a dominant population of dark excitons proves the existence of a “gray” condensate.

- In order to confirm the formation of a “gray” condensate, we measure in chapter V the spatial coherence of the photoluminescence using shift-interferometry. This method shows that in the outer vicinity of the ring, excitons exhibit a spatial coherence up to 10 times larger than the de Broglie wavelength. These islands of extended coherence quickly disappear upon increase of the bath temperature. From these measurements we obtain the evolution of the coherence length with the bath temperature, which is consistent with a first-order transition. We finally measure the polarization and found it to be dominantly linear and also organized in “islands” outside the ring.
- Finally we conclude this manuscript by recapitulating the main results and by presenting some “exotic” fragmented patterns.

We would like to mention that the experiments presented in this manuscript only cover the last two years of the PhD. While previous works (in particular the results reported in [62]) helped us to interpret some of the results presented here, we chose not to include them in order to keep a unity of meaning for the manuscript. Let us finally note that during the writing of this manuscript the group of R. Rapaport reported experiments consistent with the condensation of dipolar excitons in dark states [63].

Chapter I

General properties of excitons

Here, we give some key characteristics of excitonic systems. The description is kept general since the subject is extensively covered in numerous books and articles (see e.g. [64–66]). We progressively introduce our system by describing successively the formation and properties of excitons in bulk semiconductors, in quantum wells and finally in biased quantum wells. In a second part we will briefly present some concepts on Bose-Einstein condensation of excitons with a particular emphasis on the recent theoretical prediction of a "gray" condensate of excitons.

I.A General Properties

I.A.1 Exciton in bulk semiconductor

In the simplest case, the ground state of a semiconductor is constituted by a fully occupied valence band and completely empty conduction band separated by a bandgap energy E_g. The elementary excitation of such a system occurs when, upon for instance the absorption of a photon, an electron from the valence band is promoted into the conduction band, thus leaving a single empty state called a *hole* in the valence band (see fig. I.1). Electron and hole are characterized by effective masses m_e and m_h and equal but opposite elementary charges $\mp e$. The two particles experience a mutual Coulomb attraction thus creating an hydrogen-like bound metastable state called an *exciton.*

In the case of Wannier excitons, i.e. when the Bohr radius of the particles is much larger than the lattice constant, and assuming isotropic and parabolic energy bands, the total energy of the exciton E_X can be calculated and reads :

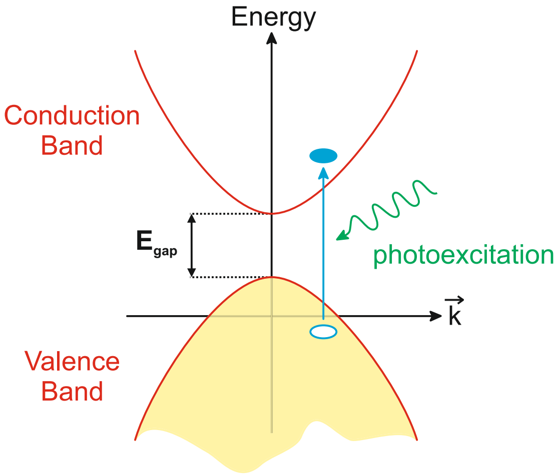

FIGURE I.1: Photo-absorption promoting an electron from the valence band to the conduction band. Electron and hole are represented respectively by filled and open circles.

$$E_X = E_g + \frac{\hbar^2 \mathbf{k}^2}{2M_X} - \frac{Ry^*}{n^2}, \quad n = 1, 2, 3, \ldots \quad \text{with} \tag{I.1}$$

$$Ry^* = \frac{\hbar^2}{2\mu a_0^2} \quad \text{and} \tag{I.2}$$

$$a_0 = \frac{\hbar^2 \epsilon_b}{e^2 \mu} \tag{I.3}$$

where $M_X = m_e + m_h$ is the total mass of an exciton, Ry^* the effective Rydberg energy, n the principal quantum number, $\mu = \frac{m_e m h}{m_e + m_h}$ the reduced mass of an exciton, ϵ_b the dielectric constant of the hosting medium and a_0 the excitonic Bohr radius. Note that here we neglect the electron-hole exchange interaction which leads to extra shifts and splittings of the exciton states. In this thesis we study excitons in GaAs for which $\epsilon_b \sim 13$ and $\mu \sim 0.2 m_0$, where m_0 is the free electron mass. Thus we obtain an exciton Bohr radius of $a_0 \sim 12$nm while the exciton binding energy is given by the effective Rydberg energy $Ry^* = E_b \sim 8$meV.

I.A.2 Band Structure of bulk GaAs

To understand the properties of an exciton, we need to study the band structure of the semiconductor. GaAs crystallizes in a zinc-blende structure such that the fundamental absorption edge of GaAs corresponds to direct transitions from the highest valence band to the lowest conduction band at the Γ point ($\mathbf{k} = 0$) in the first Brillouin zone. There, the valence band electrons exhibit p-like symmetry while the conduction band electrons possess s-like symmetry. With the inclusion of spin, there are two s-like conduction bands and six p-like valence bands degenerate at the Γ point. These bands are $|S_{1/2}\rangle$ with total angular momentum $J = 1/2$, $|P_{3/2}\rangle$ with $J = 3/2$, and $|P_{1/2}\rangle$ with $J = 1/2$. When spin-orbit effects are included, the two split-off hole states ($|P_{1/2}\rangle = |J = 1/2, m_J = \pm 1/2\rangle$) drop in energy (see fig. I.2), opening a gap between them and the light ($|J = 3/2, m_J = \pm 1/2\rangle$) and heavy-hole $|J = 3/2, m_J = \pm 3/2\rangle$) bands without affecting the s-like states. These bands have, in general, different curvature so that they split away from the Γ-point ($\mathbf{k} \neq 0$). Therefore the effective masses of the heavy-hole, light-hole and electron are respectively $0.5m_0$, $0.08m_0$ and $0.067m_0$.

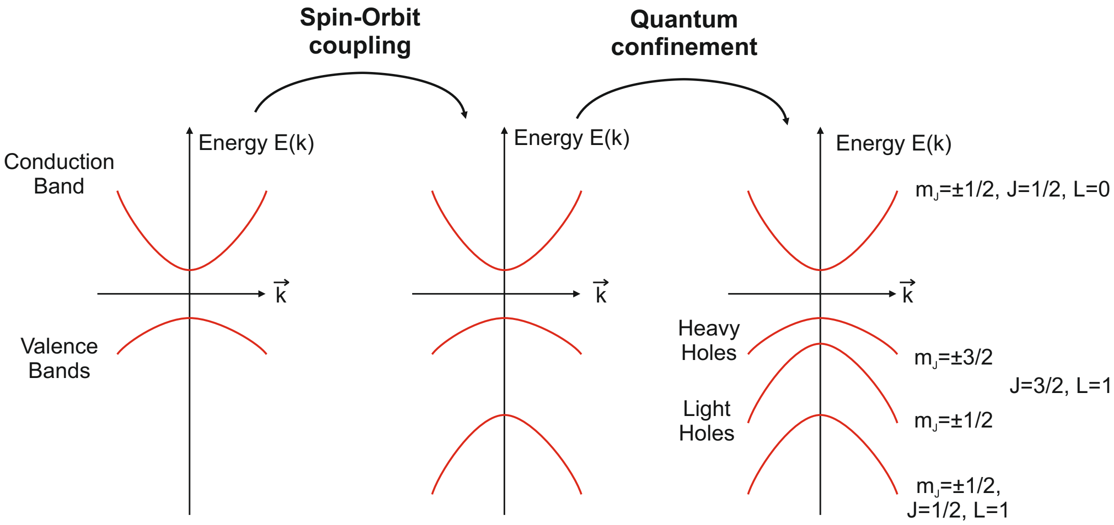

FIGURE I.2: Modification of energy bands due to spin-orbit coupling and quantum confinement.

I.A.3 Exciton is SQW

In this thesis, we study a single 25nm-wide GaAs quantum well embedded in AlGaAs (see structure of the sample in fig. II.1). This leads to a quantization of the motions of the electrons and holes along the growth direction which has an important impact on the energy states.

First of all the effective masses of the heavy and light holes are modified leading to an anisotropy along the quantum well plane and the perpendicular (growth) direction. The dispersion equation can be described by the Luttinger Hamiltonian which allows the calculation of the effective masses near the Γ point. One can find that the masses of the holes along the growth direction remains quite similar to the bulk GaAs case, however the masses in the quantum well plane changes and we obtain an average of $0.11m_0$ and $0.20m_0$ for the heavy and light holes. Let us note that the electron mass remains unchanged.

The second effect is to lift the degeneracy of the light and heavy hole bands at the Γ point (see fig. I.2). This can be understood if we consider the confinement energy E_{cf} for the n-th confined state in quantum well with infinite barriers and thickness L which reads

$$E_{cf} = \frac{n^2\hbar^2\pi^2}{2mL^2} \tag{I.4}$$

Therefore, since heavy and light holes have different effective masses in the confinement direction, their energy bands become separated (see fig. I.2). For our sample and experimental conditions, the light hole band is lower in energy and therefore we will only consider excitons formed by heavy holes and electrons.

Finally, the presence of a quantum well also modifies the binding energy and the Bohr radius of the exciton. In the ideal two-dimensional limit of vanishing well width and infinite barrier height the last term in the expression of E_X described by eq. I.1 is modified to $-\frac{Ry^*}{n^2} \rightarrow -\frac{Ry^*}{(n-1/2)^2}$. Thus the binding energy of the ground state exciton in a quantum well is $4Ry^*$ while the Bohr radius is $2a_0$, i.e. excitons are more tightly bound.

I.A.4 Life cycle of excitons

Through optical excitation, electron/hole pairs can be created at very high energies. These free carriers then relax to their respective sub-bands via emission of longitudinal acoustic phonons or through two-body scatterings. Eventually, the mutual Coulomb attraction dominates allowing the formation of excitons. These initial excitons have high kinetic energy and can relax through exciton-exciton, exciton-free carrier and exciton-acoustic phonon scattering to reach the lowest excitonic energy band and a quasi-thermal equilibrium. Cold excitons (i.e. at the bath temperature) with $\mathbf{k}_\parallel \sim 0$ can then recombine by emitting detectable photons. The overall process is depicted in fig. I.3. Let us note that the QW being by construction a two-dimensional structure, the momentum conservation along the QW growth direction (z-direction) is relaxed, therefore cooling to the lattice temperature, via emission of bulk longitudinal acoustic phonons, is about three orders of magnitude faster for excitons in QW than that in the bulk [67, 68].

The coupling of excitons with the photon field necessary for the radiative recombination depends on the conservation of both energy and in-plane-momentum (momentum conservation perpendicular to the plane is relaxed) such that only excitons in a small fraction of the phase space, the so-called radiative zone, can decay radiatively. Given that in quantum wells, excitons are confined to move in a plane, the exciton energy reads

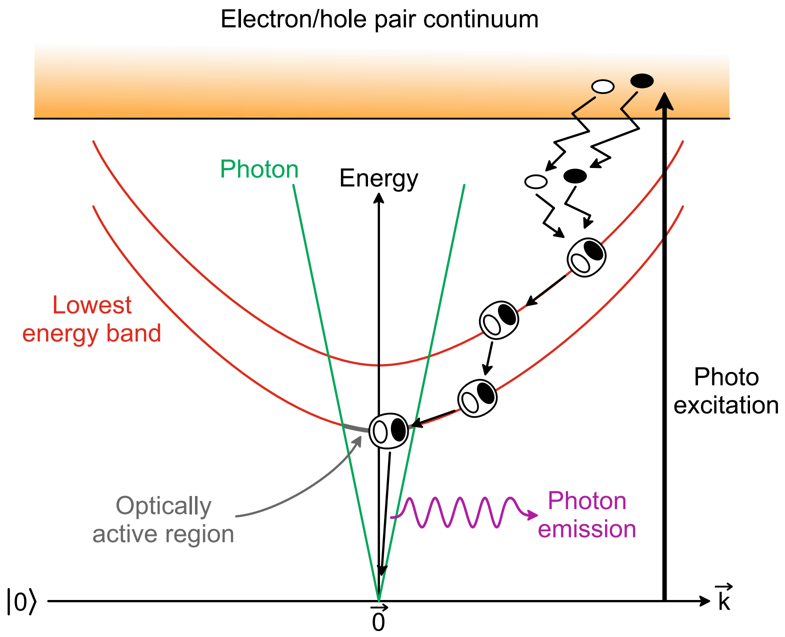

FIGURE I.3: Life cycle of an exciton. Electrons and holes are respectively represented by filled and open circles, while bound excitons are portrayed by circled electron/hole pairs. The various arrows display the photoexcitation, the cooling and the recombination of exciton.

$$E_X = E_g + E_{cf} - E_b + \frac{\hbar^2 \mathbf{k}_\parallel^2}{2M_X} \tag{I.5}$$

where $\hbar \mathbf{k}_\parallel$ is the in-plane momentum, and E_b is the binding energy. The energy of the photon E_γ in the crystal is

$$E_\gamma = \hbar \frac{c}{n} k = \hbar \frac{c}{n} \sqrt{k_\perp^2 + \mathbf{k}_\parallel^2} \tag{I.6}$$

where $\hbar k_\perp$ is the momentum along the z-axis (i.e. the growth direction) and n the refractive index of the crystal. There are many values of $k_\perp$ satisfying this condition, since denoting $E_0 = E_g + E_{cf} - E_b$ and solving $E_X = E_\gamma$ for $k_\perp$ yields

$$k_\perp = \sqrt{\frac{n^2}{\hbar^2 c^2} \left(E_0 + \frac{\hbar^2 \mathbf{k}_\parallel^2}{2M_X} \right)^2 - \mathbf{k}_\parallel^2} \tag{I.7}$$

which has a real root if

$$\frac{n}{\hbar c} \left(E_0 + \frac{\hbar^2 \mathbf{k}_\parallel^2}{2M_X} \right) > k_\parallel \tag{I.8}$$

where $k_\parallel = |\mathbf{k}_\parallel|$. This inequality possess two solutions such that :

$$k_\parallel < k_\parallel^* = \frac{cM_X}{n\hbar}\left(1 - \sqrt{1 - \frac{2n^2E_0}{c^2M_X}}\right) \quad \text{or} \tag{I.9}$$

$$k_\parallel > k_\parallel^* = \frac{cM_X}{n\hbar}\left(1 + \sqrt{1 - \frac{2n^2E_0}{c^2M_X}}\right) \tag{I.10}$$

It can be shown that the second inequality would lead to values of $k_\parallel$ beyond the first Brillouin zone. Thus only excitons with energy lower than $\delta E = \hbar^2 {k_\parallel^*}^2/2M_X$ can participate in photon emission which defines the light cone (see fig I.3). If we consider $E_0 \sim 1519$meV (i.e. $E_0 \sim E_g^{\mathrm{GaAs}}(T_b = 0.34\mathrm{K})$), $M_X \sim 0.2m_0$ and $n_{\mathrm{GaAs}} \sim 3.6$, we obtain $k_\parallel^* \sim 2.8 \times 10^7\mathrm{m}^{-1}$ and $\delta E \sim 150\mu$eV. At $T_b = 0.34$K, the thermal energy is $k_BT_b \sim 30\mu$eV. Therefore if we assume a Maxwell-Boltzmann distribution, all thermalized excitons are inside the light cone at the lowest bath temperature. Let us note that in reality only a fraction of the radiative photons are collected due to the numerical aperture of the experimental setup and refraction of the light at the interface between the surface of the sample and the exterior.

As a final remark for this section it is interesting to see that while we can create a large range of energy for the electron/holes pairs, our insight on the system through the photoluminescence is limited by the observation of a very small portion of the exciton gas.

I.A.5 Exciton in electrically biased QW

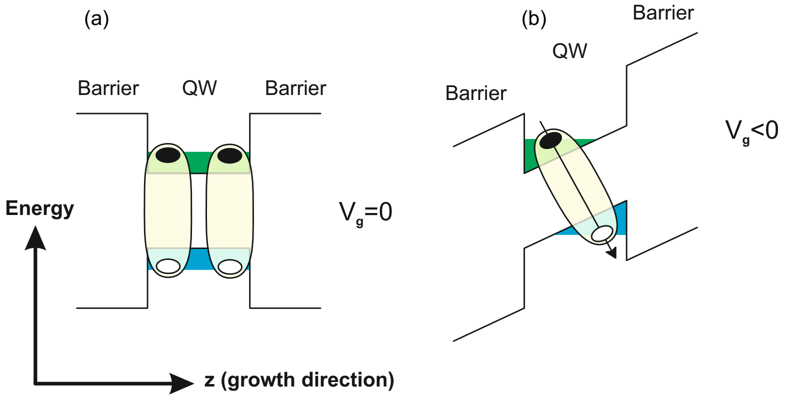

FIGURE I.4: (a) Energy bands of an unbiased QW, the excitons are direct. (b) Biased QW, the electrons and holes are pushed apart on opposite side of the QW creating spatially indirect excitons with a strong electric dipole momentum aligned perpendicularly to the QW plane.

When voltage is applied perpendicularly to the QW, the energy bands tilt and electrons and holes are pulled apart towards the opposite sides of the QW (see fig. I.4), thus leading to *spatially indirect excitons* (as opposed to *direct excitons* when no voltage is applied). This separation yields important effects. First of all, the overlap between the electron and hole wavefuntions in the QW is greatly reduced which leads to a significant increase of the radiative lifetime of the excitons. This ensures lifetimes of ~ 100ns, i.e. at least an order of magnitude longer than the typical thermalization timescale thus allowing the formation of excitons cooled down at the bath temperature. Then since the electrons and holes are now localized in the opposite edge of the QW, the excitons they form exhibit a strong electric dipolar momentum $\mathbf{d}$. Such excitons are then also referred to as *dipolar excitons*. The appearance of the dipolar momentum has various important consequences :

- Excitons now directly interact with the electric field $\mathbf{E}$ inside the sample through the dipolar potential $V_X = -\mathbf{d} \cdot \mathbf{E}$.
- Excitons experience a dipolar interaction U_X between them which depends on the length of the dipolar momentum and the density of excitons, among other parameters.

Dipole-electric field interaction If we apply a voltage V_g to a large enough electrode at the top of the sample, the resulting internal electric field is uniform in the QW and oriented along the growth axis. Thus, in order to minimize the interaction energy, the electric dipole of the excitons will always be aligned with the internal electric field resulting in $V_X < 0$, which also means that the exciton dipole is aligned perpendicularly to the QW plane. One can immediately see the advantage of such interaction. Indeed by a combination of various electrodes on top of the sample and by applying different voltages on these, it is possible to modulate the value of the internal electric field in the QW plane. Since dipolar excitons are high-field seekers this allows one to engineer any desired potential landscape to trap dipolar excitons. This technique has been extensively used to create trapping potentials, excitonic circuits, artificial quantum dots,... [14–16, 20–22, 27, 69]. Let us note that the modulation of the internal electric field leads to components both perpendicular and parallel to the QW plane. The creation of such potential landscape usually relies on tailoring the perpendicular electric field while the intensity of the in-plane electric field is designed to be minimum. Indeed a too strong in-plane electric field would rapidly yield a ionization of excitons since electrons and holes would be pulled in opposite directions [70, 71].

As mentioned previously the tailoring of the potential landscape is usually accomplished by depositing different electrodes on top of the sample. However one also has to take into account the presence of free charges in the sample which will modify the internal electric field and thus the potential for the excitons. This effect has been demonstrated in various works [62, 72, 73] and will be crucial for the interpretation of some of the results presented in this manuscript.

The interaction between dipolar excitons and the electric field yields a direct modification of the energy of the photoluminescence emitted when excitons recombine. In particular if we consider the simplified case of a voltage V_g applied between large enough electrodes in a sample of thickness l, the internal electric field $\mathbf{E}$ is uniform in the QW plane and oriented only along the growth direction (z-axis) such that $\mathbf{E} = E_z = V_g/l$ (if we neglect other contributions to the internal electric field). The interaction thus becomes $V_X = -edV_g/l$ (d being the dipole length) such that above a critical value of V_g (i.e. when the regime of dipolar excitons is well established), the peak energy of the exciton spectral line will shift linearly with the applied voltage. Such behavior allows clear measurements of the dipole length and is an evidence for the existence of excitonic compounds with electric dipole momentum.

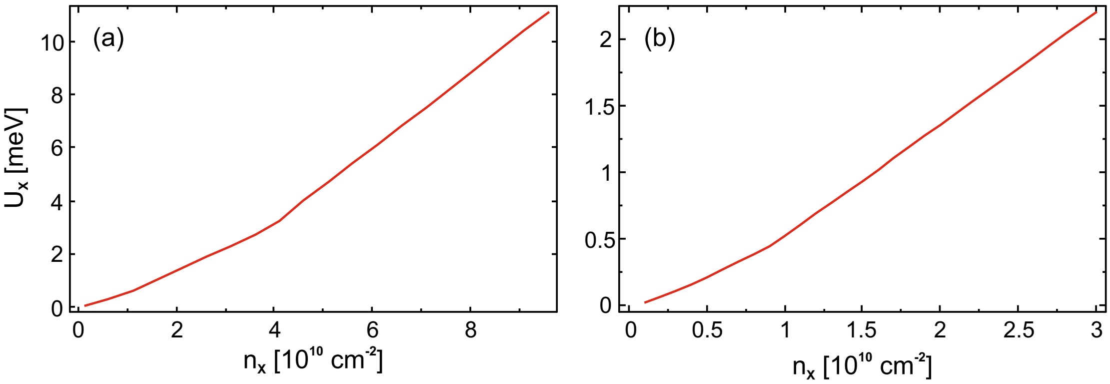

Figure I.5: (a) Variation of the dipole-dipole interaction U_X with the density of excitons n_X for a dipole length of 15nm and at a bath temperature of 340mK using the formula from [74]. (b) Same as (a) with a focus on lower values of the density.

Dipole-dipole interaction In most systems (including ours) the internal electric field is dominantly oriented parallel to the growth axis such that the dipole momentum of excitons is aligned perpendicularly to the quantum well. Thus excitons experience strong dipolar repulsions. This repulsion stabilizes the exciton gas against the formation of an electron/hole plasma allowing the study of a neutral gas of excitons at densities larger than normally possible for a unbiased QW. It will also result in a blueshift of the energy of the exciton photoluminescence as the density of excitons increases. The most basic approximation of the relation between the exciton density n_X and the energy blueshift U_X resulting from dipolar repulsions is called the plate capacitor formula and reads $U_X = \frac{4\pi e^2 d}{\epsilon_b} n_X$. However this formula does not take in account neither correlations between the excitons nor the bath temperature. Theoretical studies have been performed to include these effect and are detailed in [75–77]. In this manuscript, we will use the formula described in [74] to link the blueshift of the photoluminescence to the density of excitons. The corresponding calibration curves are presented in fig. I.5. Let us note that the exact theoretical relation between the exciton density and the photoluminescence blueshift is still under strong debates in the community such that the calibration we use should be considered as an estimation of the density.

We have seen that biasing a QW leads additional terms V_X and U_X to the total energy of the exciton gas. In most experiments, the variation of the energy of the photoluminescence due for instance to modifications of the applied voltage, excitation power and bath temperature only comes from these two terms. Being able to measure accurately U_X in various places of a quantum well plane or for variations of the experimental parameters is of fundamental interest since it allows an estimation of the density of excitons. However V_X and U_X both affect simultaneously the energy of the photoluminescence and are susceptible to vary, such that a measurement of the density based on the energy of the photoluminescence may not be trusted without a precise knowledge of the potential landscape for the excitons. This is particularly the case for samples where free carriers modify the internal electric field.

As a last remark, let us stress that the energy of the photoluminescence gives us indications on the interactions occurring to the exciton gas. The linewidth and overall shape of the exciton spectral line also give an insight on the physical properties within the exciton gas. Indeed various scattering processes for instance between excitons, excitons and carriers and excitons and longitudinal optical phonons will lead to an homogeneous broadening of the spectral line while disorder at the QW interfaces (caused for example by interface roughness, impurities, alloy fluctuations) will induce an inhomogeneous broadening. It has recently been shown that correlated behavior mediated by the dipolar interaction could cause an asymmetry of the exciton line [78].

I.B Bose-Einstein Condensation of excitons

I.B.1 General BEC

In this section we are not going to present detailed calculations on Bose-Einstein condensation which can be found in textbooks [79, 80] but we will only give its main characteristics.

First of all Bose-Einstein condensation is characterized by a macroscopic occupation of the ground state of the system. This means that the bosons will condense in the state at the lowest energy regardless of the activation energy $E = k_B T$ due to the temperature and the energy splitting δE between the ground state and the first excited state. On the contrary, to be sure that condensation is occurring, it is preferable that to have $\delta E < E$ in order to observe an occupation of the ground state superior to the normal occupation given by a Maxwell-Boltzmann distribution. For instance, for atomic condensates [4], the atomic cloud is trapped in an harmonic potential of typical frequencies in the 10-100Hz regime. This leads to a level spacing in the range of $\delta E = h\nu \sim 10^{-13}$eV. The typical critical temperature for achieving condensation with cold atoms is $\sim \mu$K which gives an activation energy of $E \sim 10^{-10}$eV. Thus the ratio $E/\delta E$ is of the order of magnitude of 10^3.

Upon condensation, the bosons in the ground state exhibit a unique macroscopic wavefunction. This effect can be observed through interferometric measurements and and the gas exhibits long-range spatial coherence with coherence length several times larger than the de Broglie wavelength. The transition between a thermal gas of bosons and a condensate is marked by a contraction in phase space with a shrinking of both the spatial extension and momentum distribution of the cloud.

Let us finally note that textbook Bose-Einstein condensation can not occur in a purely two-dimensional geometry due to a constant density of states. Nevertheless condensation can arise in a finite two-dimensional system, which is for instance the case in a trapping potential. For example, for a gas of ideal bosons in a two-dimensional box of area $S \sim 10\mu\text{m}^2$ with density $n \sim 5.10^{10}\text{cm}^{-2}$, mass $M \sim 0.22 m_0$ and degeneracy $g = 4$ (i.e. typical values which can be found in systems of dipolar excitons), the critical temperature T_c reads

$$T_c = \frac{4\pi\hbar^2 n}{2Mk_B g} . \frac{1}{\log nS/g} \sim 1\text{K} \tag{I.11}$$

which is easily reachable in a cryostat.

As explained in the introduction to this manuscript, excitons, as composite-bosons, have been suggested as promising candidates to observe Bose-Einstein condensation in solid state. The interest in the community was recently renewed due to the strong development of systems with dipolar excitons. Indeed these excitons present multiple advantages favoring the appearance of a condensate : they have a very long lifetime which allows them to cool down to the lattice temperature, the presence of dipolar repulsion authorizes much larger densities while keeping a neutral exciton gas and a screening of the disorder, and finally the presence of the electric dipole momentum allows a very accurate engineering of the potential landscape and in particular of trapping potential compulsory to achieve condensation in two-dimensional systems. However systems with dipolar excitons are not without inconvenience, in particular due to the composite nature of the excitons as composed of two fermions. This yields additional phenomena which we describe in the following section.

I.B.2 Internal structure of excitons and BEC

In the previous sections we have ignored the composite nature of excitons. Indeed in GaAs QW, excitons are formed by two fermions : an electron from the valence band with angular momentum $m_J^e = \pm 1/2$ and a heavy hole from the highest valence band for which $m_J^h = \pm 3/2$. Thus excitons can be found in four distinct states : two bright ones with total spin $S = \pm 1$, i.e. $|S = +1\rangle = |m_J^e = -1/2, m_J^h = +3/2\rangle$ and $|S = -1\rangle = |m_J^e = +1/2, m_J^h = -3/2\rangle$ and two dark ones with total spin $S = \pm 2$, i.e. $|S = +2\rangle = |m_J^e = +1/2, m_J^h = +3/2\rangle$ and $|S = -2\rangle = |m_J^e = -1/2, m_J^h = -3/2\rangle$ [47–49]. Only the bright excitonic states are coupled to the photon field with polarization σ^+ and σ^- and can decay radiatively. This also means that only bright excitons are directly created upon photoexcitation. The formation of dark excitons can result from the spin flip of one of the charges prior to the formation of excitons or from carrier exchange between excitons. Inversely, two dark excitons can exchange their fermionic constituents to yield bright excitons, as depicted in fig. I.6(a). Dark excitons not being coupled to the light, they can only decay through non-radiative processes. The exciton gas is therefore in general always composed of the four different kind of excitons which constantly exchange charges.

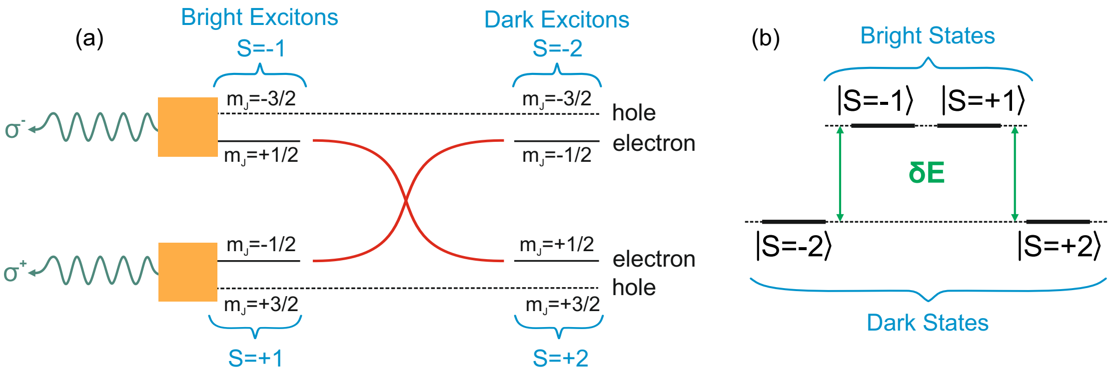

FIGURE I.6: (a) Exchange of carriers leading to bright and dark excitons and the recombination of bright excitons leading to the emission of σ^+ and σ^- polarized photons. (b) Energy splitting between bright and dark excitonic states.

In most of the literature the ground state of the excitonic system is generally considered to be four-fold degenerate between the two bright and two dark states. However M. Combescot et al. have recently demonstrated [45] that it is not the case. Indeed, they showed that due to interband Coulomb scattering (i.e. electron/hole exchange which is equivalent to the absorption/emission of a virtual photon), the two bright states experience a repulsive interaction which increases their energy. Thus the bright and dark states lie at different energies separated by a splitting δ, the dark states being at lower energy (see fig. I.6(b)). A very important consequence of this result is that Bose-Einstein condensation of exciton must occur within the dark states since they constitute the ground state (let us note that in this case the ground state is two-fold degenerate which differs from the textbook situation for Bose-Einstein condensation and seems to be a characteristics of the condensation of composite-bosons).

For a 25nm-wide single quantum well of GaAs, experiments have estimated the energy splitting δE between the bright and dark states to be in the range of 10 to 20μeV [81, 82] (for double quantum wells δE is much smaller, i.e. a few μeV). For comparison the activation energy at our lowest bath temperature is $E = k_B.340\text{mK} \sim 30\mu\text{eV}$. This means than for a thermal exciton gas the bright and dark states are equivalently populated.

Thus a condensate of excitons must be dark, i.e. it does not emit photons. This result renders its observation very complicated through usual experiments which rely on the study of the photoluminescence and could explain the difficulty to directly observe an excitonic condensate. On the other hand it means that if we manage to observe an imbalance of population between the dark and bright states with a larger population of dark excitons, this directly implies a Bose stimulation towards the dark states and that the exciton gas (or at least part of it) is condensed. Let us note that recent experimental proposals have been made in order to probe a fully dark condensate [83, 84].

Finally let us note that in a subsequent theoretical work, Monique and Roland Combescot have demonstrated that for a sufficiently high exciton density ($\sim 10^9\text{cm}^{-2}$), exciton interactions can open of coherent coupling channels between dark and bright states. Therefore the dark condensate will exhibit a bright coherent part and the condensate will then become “gray”. The underlying process for this coherent coupling is the exchange of two fermions (electron or hole) between two dark excitons, as shown in fig. I.6(a). The resulting bright excitons will eventually recombine radiatively and the analysis of their photoluminescence can be used to probe the characteristics of the condensate. In particular the lowest energy for degenerate dark states is achieved for a linear superposition of the two dark states by excitons, again due to fermion exchanges. Since this superposition is then coherently transferred to the degenerate bright states, the resulting photoluminescence is linearly polarized (as a coherent superposition of σ^+ and σ^- polarized photons).

I.B.3 What do we expect to observe ?

To conclude this first chapter let us summarize the experimental evidences for the observations of a “gray” condensate. Firstly, below a critical temperature, we should observe a loss of intensity corresponding to the Bose stimulation towards the dark states. It would be then necessary to obtain a precise measurement of the density of exciton and the intensity of the photoluminescence to confirm a higher population ratio of dark excitons. Let us recall that the observation of a dominant population of dark excitons compared to bright ones is a direct sign of an exciton condensate due to the very small energy splitting between the bright and dark states. If we can vary the density of excitons or if the density is already high enough we should observe a low photoluminescence intensity at the position of the dark condensate. This photoluminescence should exhibit long-range spatial coherence as it reflects the extended wavefunction of the condensate and a dominantly linear polarization due to the coherent coupling between bright and dark excitons. Let us also consider that, as we have already mentioned, Bose-Einstein condensation can only occur in a two-dimensional system in the presence of a confining potential. Such observation in the same region of the condensed gas of excitons would then constitute a “comforting” evidence.

Chapter II

Sample and experimental techniques

In the first part of this chapter, we introduce the structure of our sample and its basic characteristics. In particular we study the response of the photoluminescence for values of the applied voltage similar to the ones at which most experiments on dipolar excitons are usually performed [19, 27, 69, 85]. Thus we compare our device to equivalent structures which have been reported in the literature. This allow us to quantify the quality of our sample. It is important to note that in order to create the fragmented ring studied throughout this thesis, we will have to bias our sample with much higher voltages (in absolute value). This means that our device is then operated in a very different regime where photo-injected charges play a dominant role. In a second part of the chapter we describe the experimental set-up with a particular emphasis on the Mach-Zehnder interferometer. Indeed interferometric measurements will be extensively used to obtain key results on both the long-range spatial coherence (for which we will vary the lateral shift between the two arms of the interferometer) and the spectral components of the photoluminescence (we will then vary the path length difference between the two arms).

II.A Sample

The sample described in this thesis was grown by molecular beam epitaxy by David Fuster, Luisa González and Yolanda González through a collaboration with the IMM-Instituto de Microelectrónica de Madrid (CNM-CSIC), Spain. It consists of a 1 μm-thick metal-i-n^{+} field-effect device where a 25 nm wide GaAs quantum well is embedded (see fig. II.1). The quantum well is surrounded by $Al_{0.33}Ga_{0.67}As$ barriers incorporating 2

(2/2nm) GaAs/$\mathrm{Al}_{0.33}\mathrm{Ga}_{0.67}$As superlattices placed above (15-periods) and below (10-periods) the QW. The quantum well is placed 900 nm below wide semi-transparent gate electrodes (6nm Ti/4nm Au) deposited on the surface of the sample (we deposited many independent electrodes such that if the region of the sample corresponding to an electrode happened to deteriorate we could still bias and study another part of the sample). Each gate is connected to Au pads on ceramics using wire-bonding which allows us to apply a voltage bias V_g. A thick n^+-GaAs layer (Si-doped 10^{18} cm^{-3}) substrate serves as back electrode. The sample is glued with silver paste on the oxygen-free copper sample holder. The sample holder is also connected electrically to provide the ground. The energy bands structure is depicted in fig. II.2.

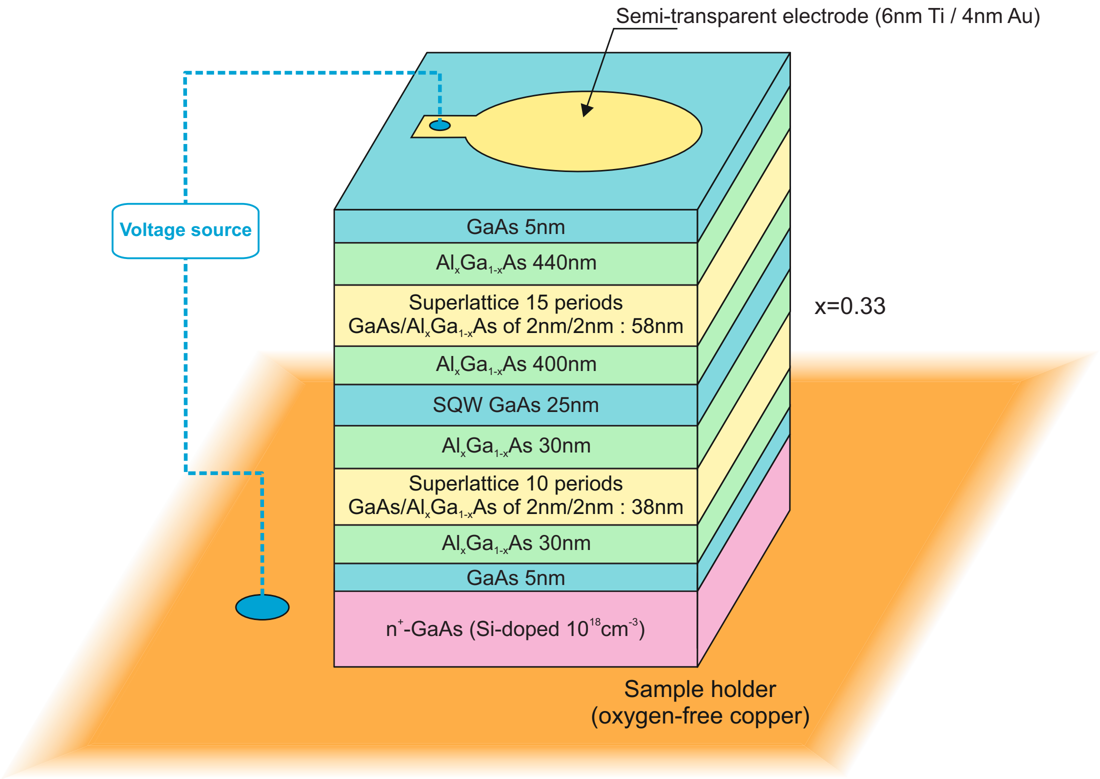

FIGURE II.1: Structure of the sample.

The sample is equivalent to a photodiode and presents two Schottky contacts (metal-i and i-n^+ interfaces). Its characteristic current/voltage behavior is shown in fig II.3(k)). Increasing the photoexcitation power or the bath temperature induces an increase (in absolute value) of the current due to the photocreation of carriers in the first case and an increase of the carrier kinetic energy in the second case.

To assess the quality of the sample we performed a characterization of the electrical behavior and the photoluminescence using a pulsed laser excitation at a wavelength of 641.5nm and a bias V_g much lower ($|V_g| < 2\mathrm{V}$) than for the rest of the experiments ($P_{ex}(641.5) = 20\mu\mathrm{W}$ for a 10μm-wide (FWHM) beam with a pulse length of 500ns

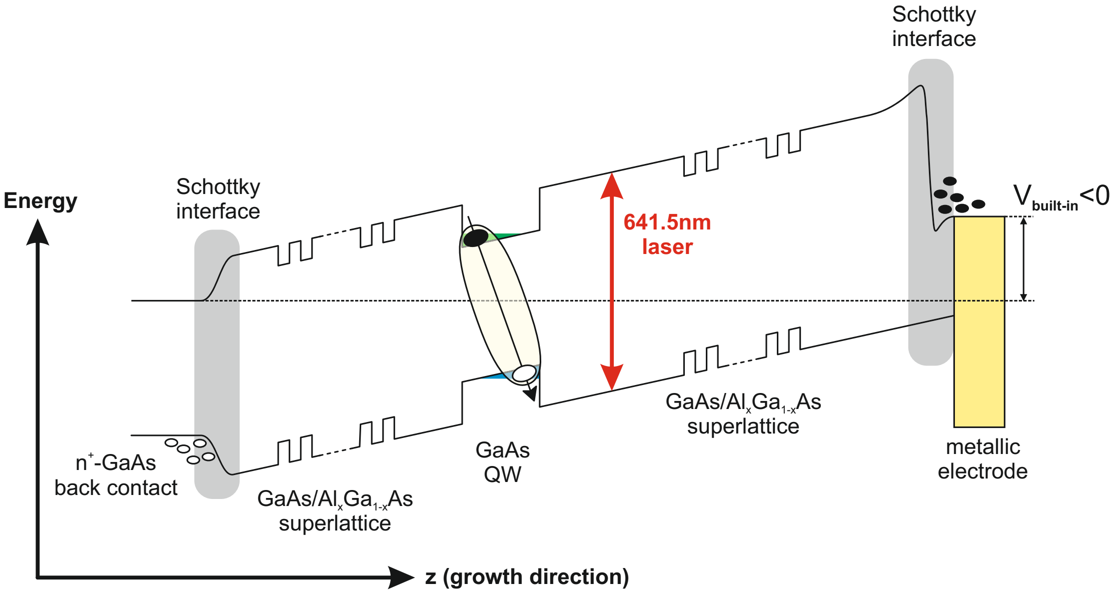

FIGURE II.2: Energy bands structure of the sample when the electrical circuit is closed but no voltage is applied. Photocreated electrons (resp. holes) represented by filled circles (resp. empty circles) accumulate at the barrier created by the Schottky interface between the $\mathrm{Al}_x\mathrm{Ga}_{1-x}\mathrm{As}$ barrier and the metallic electrode at the top of the sample (resp. between the n^+-GaAs back contact and the $\mathrm{Al}_x\mathrm{Ga}_{1-x}\mathrm{As}$ barrier at the bottom of the sample) effectively creating a negative built-in voltage $V_{\text{built}-\text{in}}$. Due to the built-in electric field, electrons and holes are being pushed apart to opposite side of the GaAs QW resulting in excitons with an electric dipole aligned along the growth direction. The wide red arrow represents the laser excitation at 641.5 nm i.e. at the energy bandgap of the $\mathrm{Al}_x\mathrm{Ga}_{1-x}\mathrm{As}$ barrier.

with a repetition rate of 2μs). The data are recorded during the laser pulse due to the extremely short decay time of the photoluminescence in this range of applied voltage. Figs. II.3(a-b) present the spatially resolved spectrum at low excitation power and open-circuit (flat energy band situation). One can see a very sharp ($\sim$ 400μeV FWHM) emission line centered at 1521.5meV which we attribute to the direct exciton transition. The presence of the smaller line at lower energy is not uncommon and can be related to the interactions between excitons and free charges. We will meet again this additional line throughout the thesis and discuss it further in a later section.

When the electrical circuit is closed but no voltage is applied (see fig. II.3(c-d)) the main line dramatically shifts towards the lower energy as if the exciton dipole was interacting with an electric field ($-e.d.E_z$). This phenomena is the direct consequence of the presence Schottky contacts (gray region in fig. II.2) in our sample. Indeed at these interfaces the exact alignment of the energy bands is controlled by the existing gap states (which are equivalent to local potential traps) [62, 65, 72, 86, 87]. Free charges photocreated by the excitation beam can then be captured at these interfaces. In particular, electrons are mostly trapped at the top interface (metal-i) while holes are mostly trapped at the bottom interface (i-n$^+$) creating an effective electric field in the sample. This resulting negative “built-in” voltage can be compensated by applying a positive voltage to return to the flat band situation (fig. II.3(e-f)). From a more general point of view, we observe that the injection of free charges can strongly affect the internal electric field and as we will see later when discussing the formation mechanism of the fragmented ring, the influence of free charges is indeed of great importance. As mentioned previously the spectrum in the flat band situation is composed of 2 lines : the direct exciton line and a line at lower energy. When the applied voltage is changed around the value of the “built-in” compensation voltage, the relative intensity of the 2 lines gets inverted as shown in figs. II.3(g-h) and (i-j), and by scanning the gate voltage V_g one obtain the set of spectra shown on fig. II.4(a). As on can see for $V_g < -V_{\text{built-in}} \sim 0.9\text{V}$, the dominant line is the low energy line which starts shifting towards the lower energy as $|V_g|$ is increased. Then for $V_g < -1$ the redshift is even more pronounced. The black line in fig. II.4(b) shows the variation of the energy position of the main spectral line with V_g, which exhibits two distinct linear behaviors (green lines) corresponding to dipole lengths of ∼2.2nm for $-1 < V_g < -V_{\text{built-in}}$, and ∼12.2nm for $V_g < -1$. We then see that in the first domain ($-1 < V_g < -V_{\text{built-in}}$) the QW is not fully polarized, while for $V_g < -1$ the electrons and holes are being pushed apart further to the opposite sides of the QW resulting in a much larger electric dipole, which is in the order of magnitude of the theoretical value we expect for our QW size. This measurement thus confirms that for $V_g < -1$ the photoluminescence comes from dipolar excitons (or from a gas of dipolar excitons in interactions with free charges). This general behavior for excitons in SQW (or DQW) is very common and was also described in [69, 88–90].

Let us now consider the red line in II.4(b) which shows the spectral Half-Width-Half-Maximum (HWHM) of the main line. As one can see when V_g is lowered below -1V the spectral width increases dramatically. This indicates that we might go from a regime where dipolar exciton are dominant to a regime where charge neutrality is not as well-preserved and dipolar excitons strongly interact with free charges (we could even imagine the appearance of an electron-hole plasma). This is not a situation where experiments on dipolar excitons are usually performed in the literature, and considering the fact that the experiments described in the following chapters are being performed at even lower V_g it is legitimate to think that the system will probably be quite far from a simple neutral dipolar exciton gas. However, we will see that when the experimental conditions allow the formation of a fragmented ring we observe again a narrow spectral line which shifts linearly in energy when varying the applied voltage, thus signing the presence of dipolar exciton which exhibit a dipolar length similar to the one measured for lower gate voltage. Finally the spectral linewidth of direct excitons at the flat band condition is a good indication of the quality of the QW interfaces. Indeed we expect interfaces roughness to yield an inhomogeneous broadening of the spectral line. This effect can be understood by considering that spatial fluctuations of the interfaces, discordance in the crystal lattice agreement and trapped impurities vary the electrostatic and structural confinement for excitons, effectively broadening the emission spectrum [91, 92]. We measured a linewidth (Full-Width-Half-Maximum) as low as 400μeV at the lowest bath temperature which we attribute to a signature of very high quality QW interfaces.

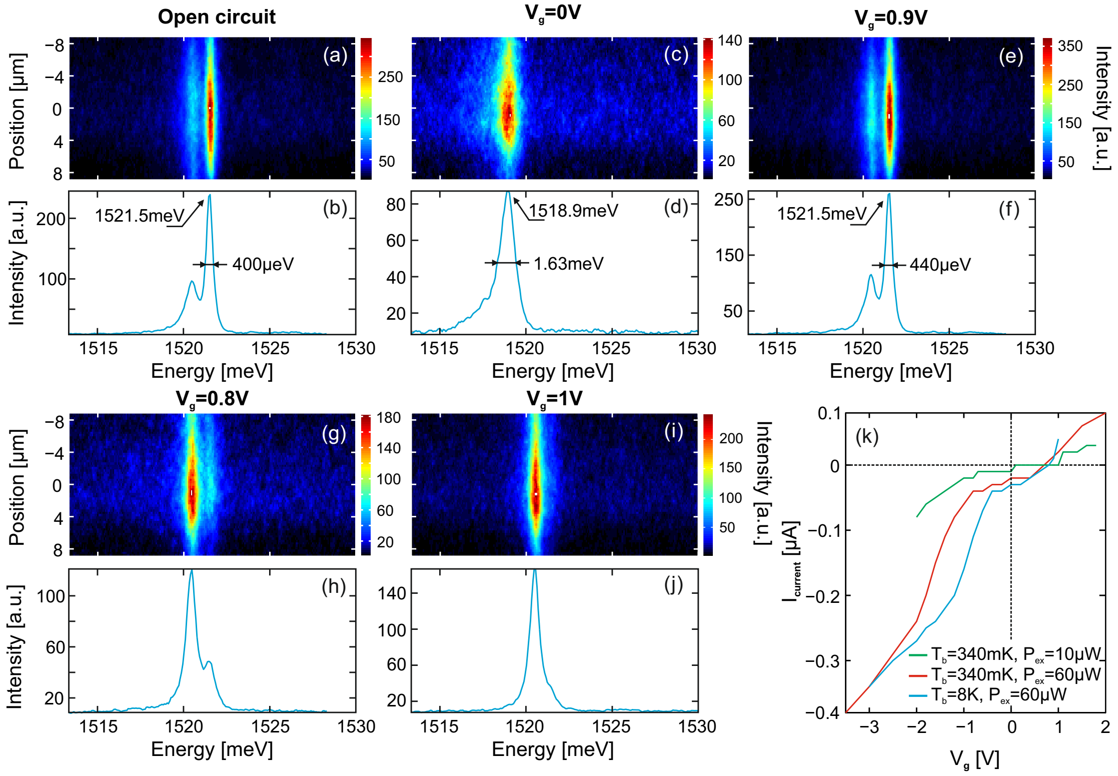

FIGURE II.3: (a,c,e,g,i) Spatially resolved spectra for various applied gate voltage V_g and the corresponding profiles (b,d,f,h,j averaged along the vertical axis). The spectra were recorded at $T_b = 340$mK. The background signal on the spectra comes from the broadband GaAs bulk emission. (k) I/V characteristics of the sample for various bath temperature and excitation power.

Fig. II.5(a) shows the spectral profiles of the photoluminescence at the flat band situation for various bath temperatures. First of all, we note that as plotted in fig. II.5(b), the value of the gate voltage necessary to compensate the built-in is highly dependent on the temperature. This is expected since when increasing the bath temperature, the activation energy of the free charges can become sufficient to overcome the trapping potential created at the Schottky interfaces, effectively decreasing their density at these interfaces and the built-in voltage. The second effect is the energy redshift of both spectral components when increasing the temperature (black line in fig. II.5(c)). This can be partially explained by considering the temperature dependency of the GaAs QW bandgap. It scales in first approximation like the GaAs bulk bandgap $E_g(T_b) = E_g(0) - \frac{\alpha T_b^2}{T_b+\beta}$ (where $E_g(0)$ is the QW bandgap at 0K and α, β are coefficients characteristics of the GaAs [93, 94]) and therefore decreases when the temperature increases. However

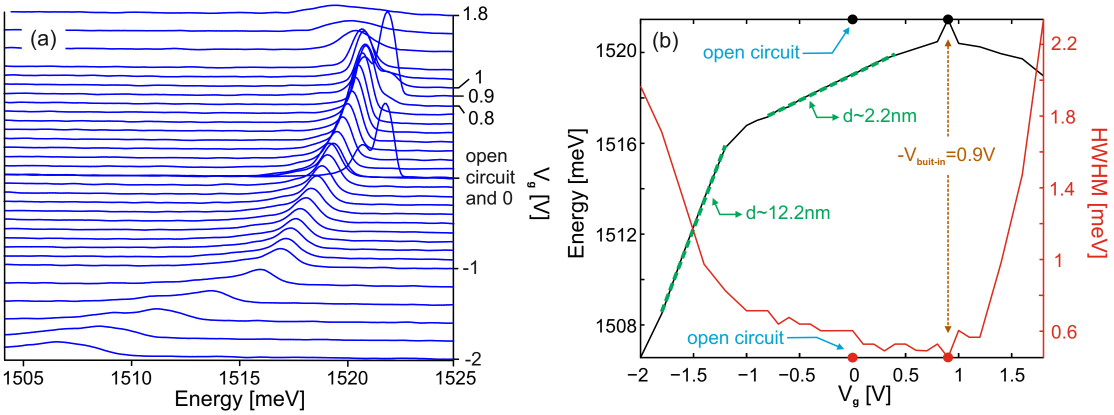

FIGURE II.4: (a) Spectrum profiles for various gate voltage V_g at $T_b = 340$mK. The profiles have been vertically shifted with respect to each other proportionately to their respective V_g. (b) Peak energy (black line) and spectral Half-Width-Half-Maximum (red line) of the main spectral line of the profiles displayed in (a), the green lines represent local linear regression of the energy position. The filled circles mark the data for the open circuit and $V_g = -V_{\text{built-in}}$

this would only accounts for a redshift of $\sim 500\mu$eV (between 0.34 and 14K) and we then end up with no explanation for the remaining redshift. In any case we see that cooling down the sample leads to an energy blueshift of the spectral line. This blueshift will occur independently of the other experimental conditions since it comes (at least partially) from a renormalization of the bandgap of the QW. In particular this means that when varying the bath temperature one has to be very careful when trying to associate a blueshift of the dipolar exciton line to an eventual modification of the exciton density. Finally one can see in fig. II.5(a) that the direct exciton line broadens with the temperature, eventually confounding itself with the line at lower energy (the spectral width is displayed by the red line in fig. II.5(c)). We attribute this behavior to the increase of the coupling between excitons and acoustic phonons of the crystal lattice [68, 91, 92] which causes a homogeneous broadening of the line.

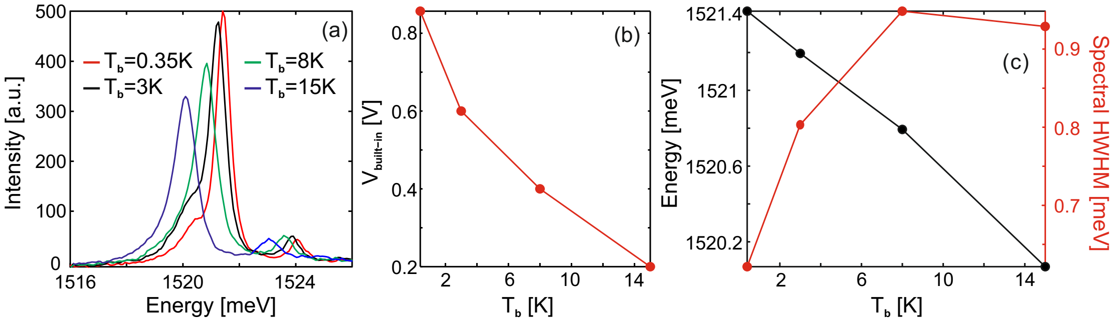

FIGURE II.5: (a) Spectral profiles at flat-band for various bath temperatures. The small lines at higher energy mark the 2s transition. (b) Values of the built-in voltage at each temperature. (c) Energy position (black line) and spectral HWHM (red line) of the main spectral line of (a).

To conclude this part, let us note that the behavior of our sample with the applied voltage is consistent to previous samples described in the literature [19, 27, 69, 85]. In particular we have been able to measure the value of the dipole length of excitons in our QW and found it to be adequate to the size of the QW. We would like to stress again that the previous analysis was intended as a general introduction to our sample for experimental conditions allowing comparisons to similar studies which can be found in the literature. However those experimental conditions are not the ones for which we will study the fragmented ring in the rest of this thesis.

As a general remark, our sample proved to be extremely fragile which is not surprising since it is first and foremost a very thin diode which renders it for instance very sensitive to electrostatic discharges. As a result we have often observed parts of the sample becoming useless (i.e. the region of the sample corresponding to a given electrode would for example present a very strong current or not produce interesting photoluminescence patterns) which forced us to regularly study another electrode in order to find again favorable experimental conditions.

II.B Experimental setup

Here, we present the experimental setup (see fig. II.6) and it various components. It can be divided in three parts : first the engineering of the excitation laser beams with diode lasers, pulsing and beam-shaping setups, then the cryostat and finally the photodetection line. This basic setup allows us to simultaneously illuminate our sample with excitation beams of various wavelengths and shapes, to vary the bath temperature and the applied voltage and finally to record time-resolved direct images or spatially resolved spectra of the photoluminescence. In order to obtain a deeper insight on the properties of the photoluminescence emitted by the sample, we added two setups to the detection line : a Mach-Zehnder interferometer and a polarization modification/filtering setup. The former allows us to study the spatial coherence or the spectral structure of the photoluminescence depending on the configuration of the interferometer while the latter quantifies its polarization. The setups for Mach-Zehnder interferometry and polarization measurements are described in details in the next sections.

II.B.1 General setup

Cryostat In our experiment we placed our field-effect device on the Helium 3 insert of a closed cycle Helium 4 optical cryostat (Heliox-ACV from Oxford Instruments). A microscope objective of 8.55mm effective focal length (from Edmund Optics) is embedded

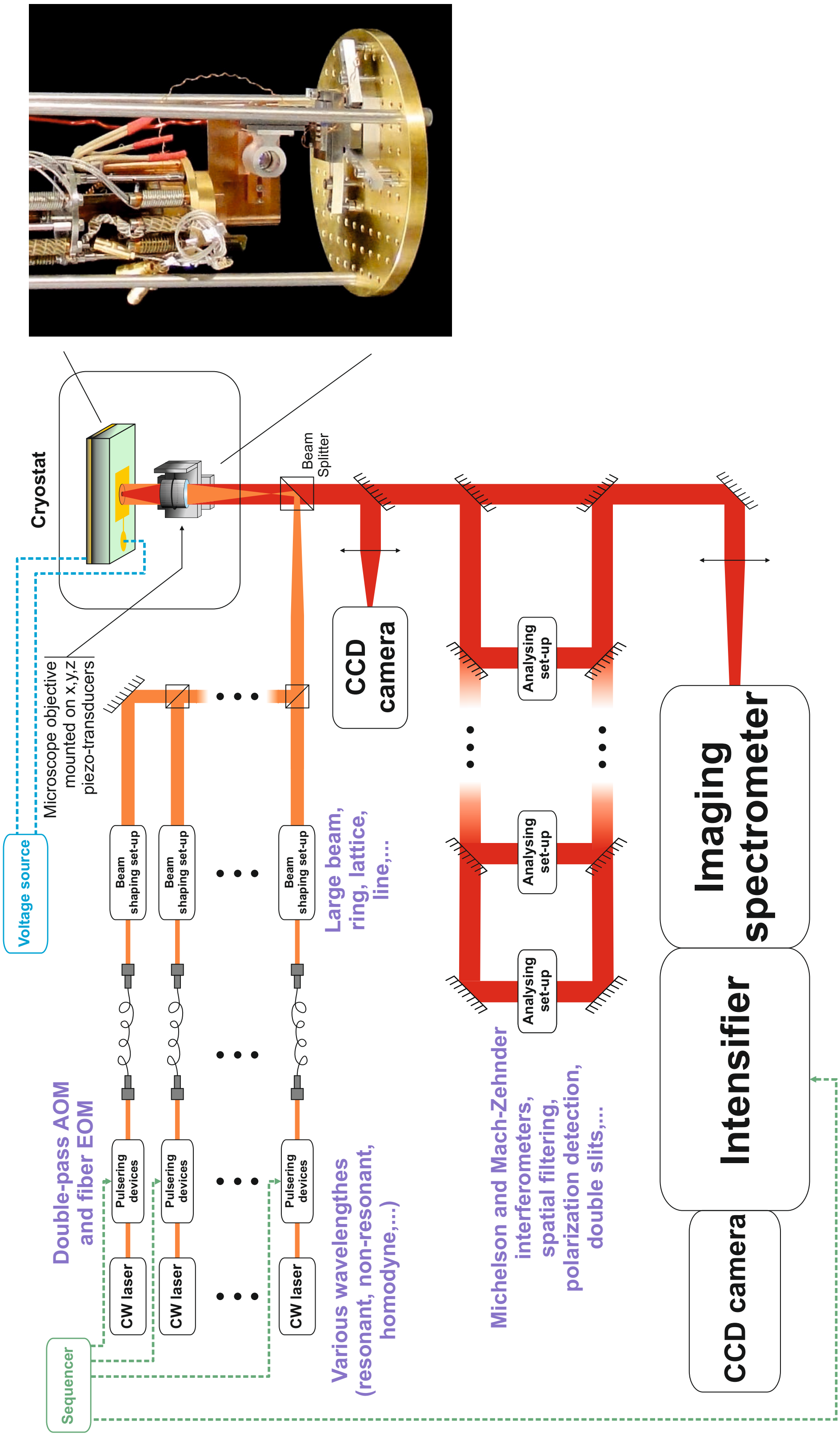

FIGURE II.6: Experimental Setup.

inside the cryostat in front of the sample and positioned by piezo-electric transducers (ML17 from MechOnics-Ag). We optimized the optical resolution of our microscope by introducing a mechanical coupling between the Helium 3 insert and the part holding the microscope objective. Thus we measured that the amplitude of mechanical vibrations does not exceed 2 microns (in a frequency range up to ~1 kHz) while the sample can be cooled to a temperature T_b as low as 340mK. In the experiments, the microscope objective was used to excite the semiconductor sample but also to collect the photoluminescence that was re-emitted. The voltage bias V_g is provided by an external voltage source (from Aim & TTi) connected to the various electrodes on the sample via constantan wires (up to 16 connections) or BNC cables (4 connections) and wire-bonding. The back electrode of the sample is connected to the cryostat mass to ensure a well defined ground. The steady current was measured using a Fluke multimeter with a resolution of 0.01μA. It is important to note that while our cryogenic system has the advantage of not having to be constantly refilled, this system presents two main drawbacks. The first disadvantage has already been mentioned and concerns the mechanical vibrations created by the pulse tube which compresses the ^{4}He and cools down the cryostat to the base temperature of 2.5K. The second inconvenience is that the system which cools down the sample to lower temperatures (namely the ^{3}He insert) only allows us $\sim$ 6 hours at the lowest bath temperature (for temperatures above 2.5K we do not have any time limitation). Therefore all measurements are a compromise between exposure time and available time, i.e. between having enough statistics and being sure to finish a set of data. This often prevented us to perform all wanted measurements on a single run and in particular, in many occasions, we had to split the set of measurements between different days with the risk of not been able to maintain the exact same experimental conditions (indeed re-condensing the ^{3}He to reach the lowest bath temperature often leads to a modification of the sample position with respect to the microscope objective thus affecting the shape of the fragmented ring).

Laser excitation To create excitons in the sample we dispose of 3 CW diode lasers (DL-100 from Toptica) at various wavelengths : 641.5nm to excite slightly above the transition of the $Al_{0.33}Ga_{0.67}As$ barriers, 790nm to excite between the GaAs QW and barrier transitions (or to excite resonantly a typical 8nm GaAs / 4nm $Al_{0.33}Ga_{0.67}As$ / 8nm GaAs DQW), and 840nm (~ photoluminescence energy) to optimize the alignment or to perform homodyne detection. All 3 laser beams are individually pulsed by both electro-optic (integrated-optical modulator from JenOptic) and acousto-optic modulators (Crystal Technologies Inc.). The electrical pulses for the modulators are provided either by a delay generator (DG645 from Stanford Research Systems) or a GHz sequencer (Hydra from Signadyne) which allows us to use up to 6 independent excitation pulses with rising and falling edges of ~2ns and ~5ns for the electro-optic and acousto-optic switches respectively. The laser beams are then mixed and sent through various beam-shaping lines to obtain different excitation beam geometries on the sample via the microscope objective : small (FWHM$\sim$5μm), wide (FWHM$\sim$100μm), line and ring (see section VI.B) and 1D or 2D lattices.

Photodetection The alignment of the excitation beam and the navigation on the sample is done using "white" surface imaging with a broadband LED and a CCD camera. To analyze the photoluminescence we installed various setups including spatial filtering (with a 200/60 magnification), Mach-Zehnder and Michelson interferometers and polarization analyzer. All setups are mounted on the optical table and can be used by adding magnetic-flip mirrors. The photoluminescence is ultimately focused with a 200mm lens on the entrance slit of an imaging spectrometer (Acton SP2500 from Princeton Intrusment with mirror, 600l/mm and 1800l/mm gratings) coupled to an intensified CCD camera (Picostar-UF from La Vision, with pixels of 13.9μm effective size). The intensified camera is triggered by the delay generator for time-resolved measurements. Thus, this setup allows us a time resolution down to 200ps, either in real space or including a spectral resolution down to 200μeV (for the 600l/mm grating, the 1800l/mm grating was not used for the experiments described in this thesis because of lack of signal). Let us note that this spectral resolution refers to the linewidth of a spectral line, indeed the value of the peak energy can be determined with an accuracy of $\sim$ 50μeV. The reflection of the excitation laser beam from the cryostat in the detection line is filtered using a band-pass filter at 840±5nm (centered at the energy of the photoluminescence) and a longpass at 664nm (both from Semrock).

Spatial resolution The optics used in the experimental setup allow us to calculate the magnification which combined with the size of the pixel of the intensified CCD camera should give the spatial resolution of our system. However the situation is not that simple since imaging theory says that a combination of optical elements will always lead to a limited spatial resolution. In our case we also have to take in account additional factors such as the mechanical vibrations of the cryostat for example. Since the effect of these factors is difficult to quantify the easiest way to know the optical resolution is then to measure it. The most direct way is to record an image of an infinitely small pattern on the sample and to measure the corresponding intensity profile. The optical resolution is then the spatial extension of this profile (for example its full-width half-maximum).

We do not have such small patterns on the surface of our sample however we have larger features of known dimensions and we will see that these can equivalently be used to calibrate the optical resolution. Thus we recorded the image of a known pattern on the top surface of the sample (in this case an arrow with a width $w = 10\mu$m, see fig. II.7(a)).

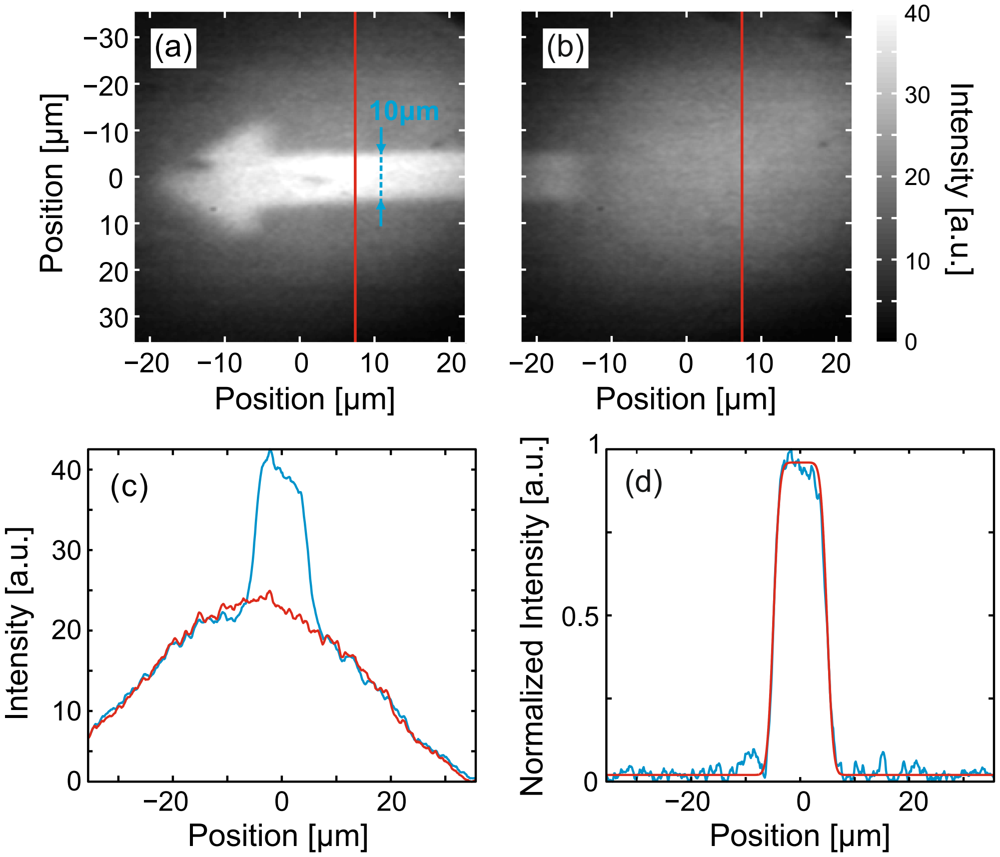

FIGURE II.7: (a) Image of an arrow pattern of 10μm width obtained by illuminating the surface of the sample with the broadband LED. (b) Same data taken away from the arrow. (c) Intensity profiles along the red lines in (a) and (b), the blue line (resp. red line) corresponding to the image (a) (resp. (b)). (d) Blue line : normalized subtraction of the 2 profiles in (c). Red line : best fit to the blue curve using the function $I_{\text{obs}}(z)$ described in the main text.

The arrow is made of the same semi-transparent material as the electrode and more reflecting than the bare surface of the sample. We illuminate the arrow with a wide beam coming from the broadband LED and record the light which is reflected. We also record a background image away from the arrow. The two images are presented in figs. II.7(a) and (b). The intensity profiles of the reflected light for the two images along the vertical z-axis are displayed in fig. II.7(c). In principle for an infinite spatial resolution the normalized subtraction of these two profiles should give an intensity profile $I(z)$ with an almost perfect unit pulse shape (also known as rectangle function) with an extension corresponding to the width of the arrow i.e. $I(z) = \text{rect}(z/w) = H(z+w/2) - H(t-w/2)$ where H is the Heaviside function. However as seen in fig. II.7(d) the profile given by our images presents rising and falling edge of $\sim 2-4\mu$m which indicates that we have a limited optical spatial resolution (the imperfection of the lithography of the arrow and the limited size of the pixels of the recording camera are negligible in comparison). A standard way to incorporate the effect of a limited optical resolution to the expression of the intensity of a signal is to combine the intensity profile with the Point Spread

Function PSF [58, 95, 96] using a convolution product. It is also very common to use a Gaussian function for the expression of the PSF i.e. PSF(z) $= e^{-z^2/2\sigma^2}$ [97]. Thus if we follow the previous ideas the profile we observe $I_{\text{obs}}(z)$ can be expressed as $I_{\text{obs}}(z) = A\, I(z) * \text{PSF}(z)$, where A is a normalization constant. One can note that for an infinitely small arrow $I(z)$ would reduce to a Dirac delta function and the previous convolution product would only give the PSF. Therefore we see that measuring the optical resolution with a large feature is equivalent to the ideal situation of the measurement of a very small pattern. In particular in our case the optical resolution is given by the full-width half-maximum of the point spread function i.e. $\sigma.2\sqrt{2\log 2}$.

The red line in fig. II.7(d) shows the best fit of $I_{\text{obs}}(z)$ to the measured profile by adapting σ. This fit thus allows us to retrieve the optical resolution and we find it to be $\sim 1.8\mu$m. A similar procedure will be used to include the effect of the limited spatial resolution to the expression of the first-order correlation function (see section II.B.2.b) and its application to experimental data will provide a value for the optical resolution in agreement with the one found here (see section V.A.1).

II.B.2 Mach-Zehnder interferometry

The purpose of Mach-Zehnder interferometry is to quantify the first-order coherence degree of the photoluminescence. Indeed the photons (described by the electric field) resulting from the recombination of excitons reflect the wavefunctions of these excitons. The degree of coherence of the exciton gas can then be analyzed using the first-order correlation function. This method has successfully been used for the detection of extended spatial coherence of dipolar excitons [23, 61], excitons-polaritons [98, 99] and atoms [100]. In the most general case the first-order correlation function reads (the description is equivalent for the wavefunctions) :

$$g^{(1)}\left(\mathbf{r}_1, t_1; \mathbf{r}_2, t_2\right) = \frac{\langle E^*\left(\mathbf{r}_1, t_1\right) E\left(\mathbf{r}_2, t_2\right)\rangle_t}{\sqrt{\langle |E\left(\mathbf{r}_1, t_1\right)|^2\rangle_t \langle |E\left(\mathbf{r}_2, t_2\right)|^2\rangle_t}} \tag{II.1}$$

where $E\left(\mathbf{r}_i, t_i\right)$ is the electric field emitted at the position $\mathbf{r}_i$ and at time t_i and $\langle ... \rangle_t$ is time-averaging. If we are only interested in looking at correlations at distance δx along the x-axis and at a time δt, the $g^{(1)}$-function reduces to :

$$g^{(1)}\left(\mathbf{r}; \delta x, \delta t\right) = \frac{\langle E^*\left(\mathbf{r}, t\right) E\left(\mathbf{r} + \delta x, t + \delta t\right)\rangle_t}{\sqrt{\langle |E\left(\mathbf{r}, t\right)|^2\rangle_t \langle |E\left(\mathbf{r} + \delta x, t + \delta t\right)|^2\rangle_t}} \tag{II.2}$$

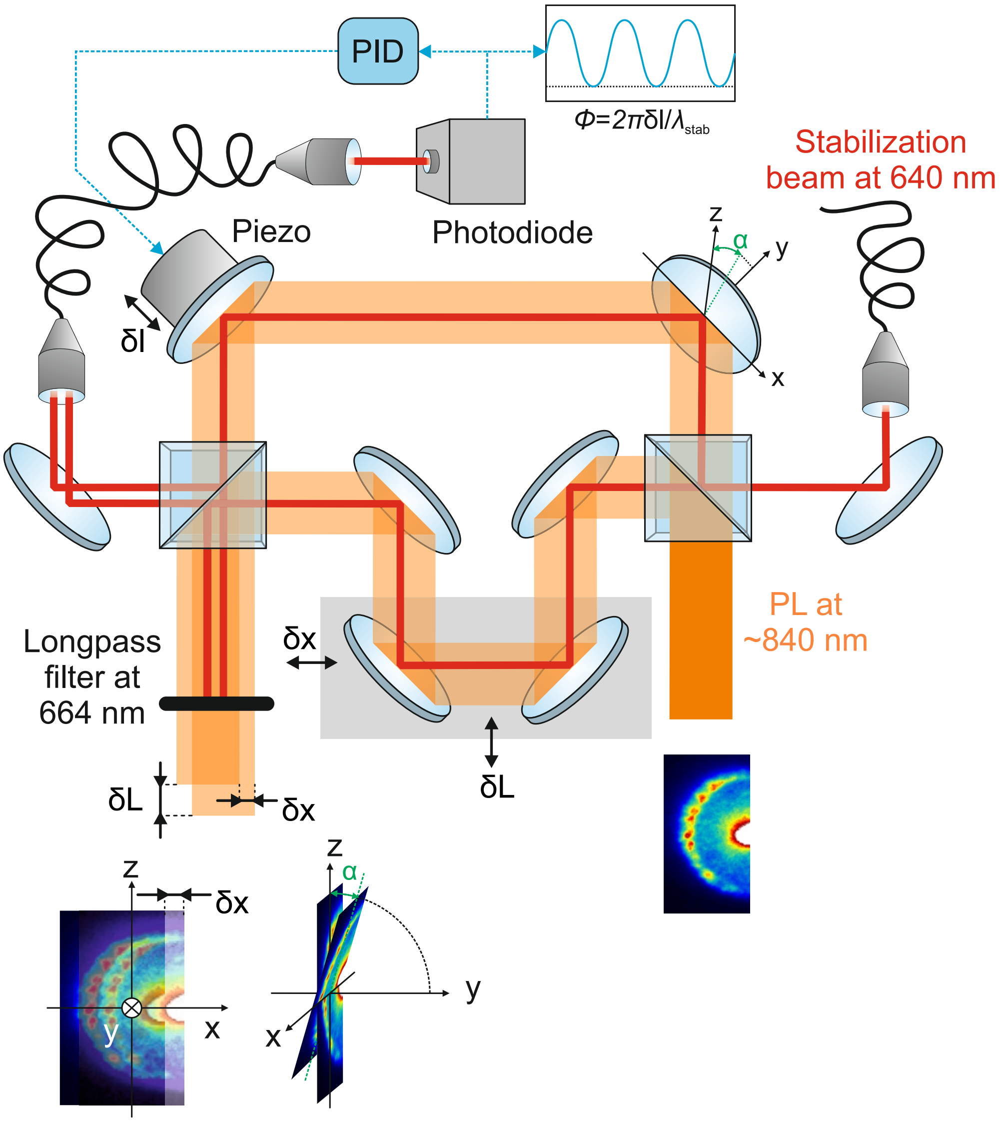

FIGURE II.8: Outline of the Mach-Zehnder interferometer setup. The photoluminescence beam from the sample is depicted by the wide orange strip and the stabilization beam by the smaller red strip. Lateral shift δx and path length difference δL are obtained by using a 2-axis translation stage. The tilt α with respect to the z-axis can be obtained by modifying the orientation of a mirror. The stabilization beam is separated from the photoluminescence at one output of the interferometer by using a longpass filter. The photoluminescence interference is then focused on the entrance slit of the imaging spectrometer. The other output of the interferometer (essentially only the stabilization beam) is coupled to a single-mode fiber and then focused on a photodiode. The signal from the photodiode is then sent to a PID controller to actively stabilize δl by using a piezoelectric transducer.

In our experiment (see fig. II.8), the photoluminescence is split between the two arms of the interferometer which allows us to control the path length difference between the 2 interfering parts as well as their position with respect to each other. We also align the two arms such that the planes of the 2 outputs are tilted by an angle α with respect to the z-axis. Hence, we impose that the interferences fringes are aligned horizontally along the x-axis and α can be tuned to set the fringes period. If we consider a lateral shift δx along the x-axis and a delay time $\delta t = \frac{2\delta L}{c}$ between the 2 arms, the output of the interferometer I_{12} can be modeled as :

$$I_{12}\left(\mathbf{r};\delta x,\delta t\right) = \langle \left| E\left(\mathbf{r},t\right) + e^{i\left(q_\alpha z+\phi+\phi_t\right)} E\left(\mathbf{r}+\delta x, t+\delta t\right)\right|^2 \rangle_t \tag{II.3}$$

where $q_\alpha = \frac{2\pi \sin\alpha}{\lambda}$, λ being the photoluminescence wavelength, $\phi_t = \frac{2\pi.2\delta L}{\lambda}$ is the phase introduced by the length between the 2 arms and ϕ is a random phase. By recording individually the output of the 2 arms $I_1 = \langle \left|E\left(\mathbf{r},t\right)\right|^2\rangle_t$ and $I_2 = \langle \left|E\left(\mathbf{r}+\delta x, t+\delta t\right)\right|^2\rangle_t$, we can compute interferograms or normalized interference patterns $I_{\text{int}} = \frac{I_{12}-I_1-I_2}{\sqrt{I_1 I_2}}$ and we recover the following equation for I_{int} :

$$\begin{aligned} I_{\text{int}}\left(\mathbf{r};\delta x,\delta t\right) &= \left[e^{-i\left(q_\alpha z+\phi+\phi_t\right)} g^{(1)^*}\left(\mathbf{r};\delta x,\delta t\right) + e^{i\left(q_\alpha z+\phi+\phi_t\right)} g^{(1)}\left(\mathbf{r};\delta x,\delta t\right)\right]/2 \\ &= \cos\left(q_\alpha z+\phi+\phi_t+\varphi_{\mathbf{r};\delta x,\delta t}\right)\left|g^{(1)}\left(\mathbf{r};\delta x,\delta t\right)\right| \end{aligned} \tag{II.4}$$

where we have written $g^{(1)}\left(\mathbf{r};\delta x,\delta t\right) = \left|g^{(1)}\left(\mathbf{r};\delta x,\delta t\right)\right| \exp\left(i\varphi_{\mathbf{r};\delta x,\delta t}\right)$. Hence, the contrast of the fringes of the normalized interferences directly gives the degree of coherence of the photoluminescence ($\left|g^{(1)}\left(\mathbf{r};\delta x,\delta t\right)\right|$ is the visibility of the fringes), while the position of the interference fringes reveals the phase $\varphi_{\mathbf{r};\delta x,\delta t}$ of the $g^{(1)}$-function.

In general, interferometers are subject to various disturbances from the environment (temperature gradient, mechanical vibrations,...) resulting mostly in fluctuations of the length difference between the two arms which dramatically alter the quality of the interferograms. These fluctuations are taken in account in the expression of I_{int} by using the phase ϕ, which can be expressed as $\phi = \frac{2\pi\delta l}{\lambda}$. To control this phase we installed a stabilization laser beam at 641.5nm with a narrow band ($\sim$ 10MHz) going through the interferometer. This output of the interferometer is coupled in a single-mode fiber and monitored by a photodiode. The intensity at the photodiode can be expressed by :

$$I_{\text{stab}}(\phi) = 2I_0\cos^2\left(\phi\right) = 2I_0\cos^2\left(\frac{2\pi\delta l}{\lambda_{\text{stab}}}\right) \tag{II.5}$$

where I_0 is the intensity of each of the 2 arms. The output of the photodiode is coupled to a PID controller to control a piezoelectric mounted mirror in the interferometer. Therefore stabilizing the output intensity effectively locks the length difference δl between the 2 arms. Measurements show that we control the phase ϕ of the output interference signals with an accuracy of $\pi/10$ which gives a precision of $\lambda_{\text{stab}}/20 \approx 30$nm of the path-length difference. The phase-lock of the interferometer also provides a very efficient way to obtain spatially resolved mapping of the degree of coherence (see fig.II.9). Indeed, while scanning ϕ, we also scan the intensity value of the interference $I_{\text{int}}\left(\mathbf{r};\delta x,\delta t\right)$ at each point $\mathbf{r}$. Therefore by recording interferograms for various ϕ, one can plot the intensity versus ϕ for each point of the photoluminescence which is an oscillation whose amplitude gives $\left|g^{(1)}\left(\mathbf{r};\delta x,\delta t\right)\right|$. The phase relation between these oscillations is given by $q_\alpha z + \varphi_{\mathbf{r};\delta x,\delta t} + \phi_t$. In principle we should be able to reconstruct the map of the phase of the $g^{(1)}$-function, however we will see that it is not very easy in practice especially because of the dependency in λ of q_α and ϕ_t. Let us note that with this technique the tilt α which allows the visualization of the fringes is not necessary anymore, however it is convenient for alignment purpose and also to provide a direct measurement of the contrast of the interferences in the case of an homogeneous photoluminescence where no spatial fluctuation of the $g^{(1)}$-function is expected (see for instance fig. II.10).

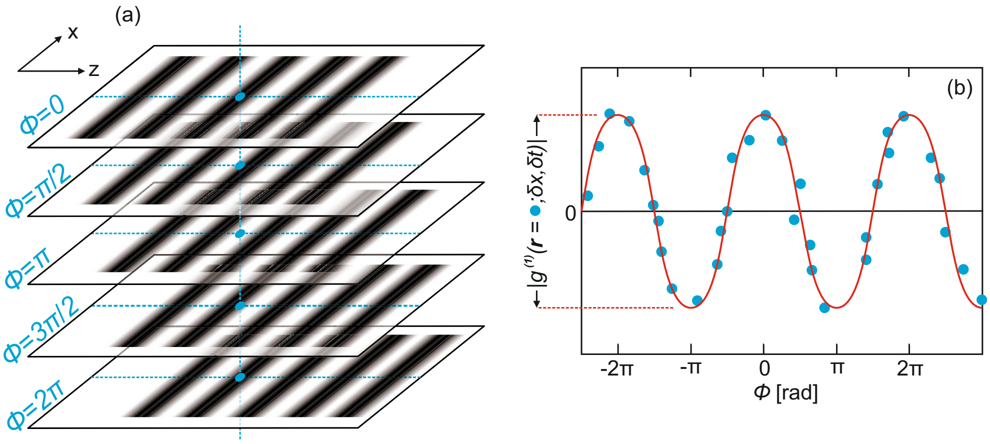

FIGURE II.9: (a) Sketch of the effect of the scan of ϕ (δl) on an interferogram : the fringes “slip” along the z direction. By recording the intensity at a given point in the (x,z)-plane (thick blue dots) for a set of ϕ value, one can reconstruct the variation and fit it with a cosine function : (b). This regression directly gives the value of $\left|g^{(1)}\right|$.

As mention previously, this technique should also allow us to obtain a map of the phase of the $g^{(1)}$-function. The interpretation of the phase of the $g^{(1)}$-function in terms of physical behavior of the exciton gas is far from being trivial. It is however important to note that the first-order correlation function of an exciton gas at the equilibrium is a purely real function (more generally if the system is invariant by time-inversion [101]), and it can be shown [101] that one possibility for the $g^{(1)}$-function to present an imaginary part and thus a phase is for excitons to be in motion. If we consider a collective motion of the exciton gas at velocity $\mathbf{V}$, the wavefunction $\psi(\mathbf{r})$ describing the system has to be multiplied by a phase factor $\exp(i.M_X\mathbf{V}\cdot\mathbf{r}/\hbar).\exp(-i.M_XV^2t/2\hbar)$ where M_X is the mass of exciton and $V=\|\mathbf{V}\|$[79, 101]. In this section we expressed the first-order correlation function in terms of the electric field but an equivalent expression can be found for the wavefunctions such that due to the displacement of excitons, the

$g^{(1)}$-function for a lateral shift δx along the x-axis and a time delay δt will experience the transformation [79, 101]:

$$g^{(1)}(\mathbf{r},\delta x,\delta t) \propto \langle \psi^\dagger(\mathbf{r},t)\psi(\mathbf{r}+\delta x,t+\delta t)\rangle \rightarrow e^{iM_X V_x \delta x/\hbar} e^{-iM_X V_x^2 \delta t/2\hbar} g^{(1)}(\mathbf{r},\delta x,\delta t) \quad \text{(II.6)}$$

where V_x is the velocity of excitons along the x-axis and the normalization of $g^{(1)}(\mathbf{r},\delta x)$ has been omitted (the additional phase factor does not affect $|\psi(\mathbf{r})|^2$). If we only consider a lateral shift then the wavefunctions are taken at the same instant t the factor $\exp(-i.M_X V^2 t/2\hbar)$ disappears. $g^{(1)}(\mathbf{r},\delta x)$ before the transformation is real therefore if we write $g^{(1)}(\mathbf{r},\delta x) = |g^{(1)}(\mathbf{r},\delta x)|\exp(i\varphi_{\mathbf{r},\delta x})$ we obtain that the phase of the $g^{(1)}$-function $\varphi_{\mathbf{r},\delta x}$ is given by $M_X V_x \delta x/\hbar$ where the dependency on $\mathbf{r}$ is transmitted to $V_x(\mathbf{r})$. A similar analysis can be done for a pure time delay and in this case we obtain $\varphi_{\mathbf{r},0,\delta t} = -M_X V^2 \delta t/2\hbar$.

The previous considerations tell us that a direct relation exists between the velocity of excitons and the phase of the $g^{(1)}$-function. In the section dedicated to the shift-interferometry measurements (see section V.A.2) we will see that this relation helps us to interpret the interferograms. Let us note that we only consider alterations of the phase of the $g^{(1)}$-function yielded by “classical” processes, indeed quantum effects such as quantized vortices could also play a role and have for instance been measured in exciton-polariton systems (but we do not observe such phenomena).

In the next two sections we detail the meaning of the $g^{(1)}$-function for 2 particular cases :

- $\delta x = 0$: Only studying the time-correlation is equivalent to perform Fourier transform spectroscopy which gives an insight on the spectral components of the photoluminescence.
- $\delta L = 0$: Setting a path-length difference between the two arms allows us to perform pure shift-interferometry and to extract the coherence length of the photoluminescence.

II.B.2.a Fourier transform spectroscopy

If $\delta x = 0$, the first order correlation function takes the simplified form

$$g^{(1)}(\mathbf{r};\delta t) = \frac{\langle E^*(\mathbf{r},t)\,E(\mathbf{r},t+\delta t)\rangle_t}{\sqrt{\langle|E(\mathbf{r},t)|^2\rangle_t \langle|E(\mathbf{r},t+\delta t)|^2\rangle_t}} \quad \text{(II.7)}$$

To express the electric field one can utilize the power spectral density $f(\mathbf{r},\omega)$ (PSD) as :

$$f(\omega) = \frac{|E_T(\mathbf{r},\omega)|^2}{T} \quad \text{with} \quad E_T(\mathbf{r},\omega) = \frac{1}{\sqrt{2\pi}} \int\limits_T dt E(\mathbf{r},t) e^{i\omega t} \tag{II.8}$$

with T being a time-scale larger than the coherence time of the photoluminescence (it is in fact the same time-scale which is used for the definition of the time-averaging $\langle ... \rangle_t$ in Eq.II.1). The power spectral density can be directly measured using a spectrometer, however one has to take into account the accuracy of the spectral measurement in order to relate the PSD to the spectrum. From the previous definition we can define the *normalized* power spectral density which reads :

$$F(\mathbf{r},\omega) = \frac{f(\mathbf{r},\omega)}{\int\limits_{\mathbb{R}} d\omega f(\mathbf{r},\omega)} \tag{II.9}$$

Using the Wiener-Khintchine theorem [102] it follows that $g^{(1)}(\mathbf{r};\delta t)$ is the Fourier transform of $F(\mathbf{r},\omega)$, i.e. :

$$g^{(1)}(\mathbf{r};\delta t) = \int\limits_{\mathbb{R}} d\omega F(\mathbf{r},\omega) e^{-i\omega\delta t} \tag{II.10}$$

From this equation and the technique described in the previous section, it follows that the visibility of the fringes is equal to the modulus of the Fourier transform of the normalized PSD. However, practically this equation is rather a proportionality relation than a strict equality with the proportionality coefficient which accounts for the characteristics of the the experimental set-up. Indeed the previous equation supposes $\left|g^{(1)}(\mathbf{r};\delta t = 0)\right| = 1$ i.e. a perfect interferometer, while on the other hand of the equation it can be difficult to obtain $F(\mathbf{r},\omega)$ as previously explained. The 2 profiles are therefore usually normalized to 1 for $\delta t = 0$. As an example, we performed the measurements using the photoluminescence of the GaAs bulk excited with a wide 641.5nm laser beam and filtered with a 840±5nm bandpass. The spectral width of the resulting photoluminescence being rather wide ($\Gamma \sim 20.2$meV, see fig. II.10(e)), its coherence time is very low ($\tau_c = h/\Gamma \simeq 200$fs) which also allows us to find the zero path length difference ($\delta L = 0$) with a very good accuracy and to characterize the precision of the Fourier transform spectroscopy.

Figs. II.10(a) and (b) show the normalized interferograms for two values of δL namely 5μm (a) and 65μm (b) away from the zero path difference. The uniformity of

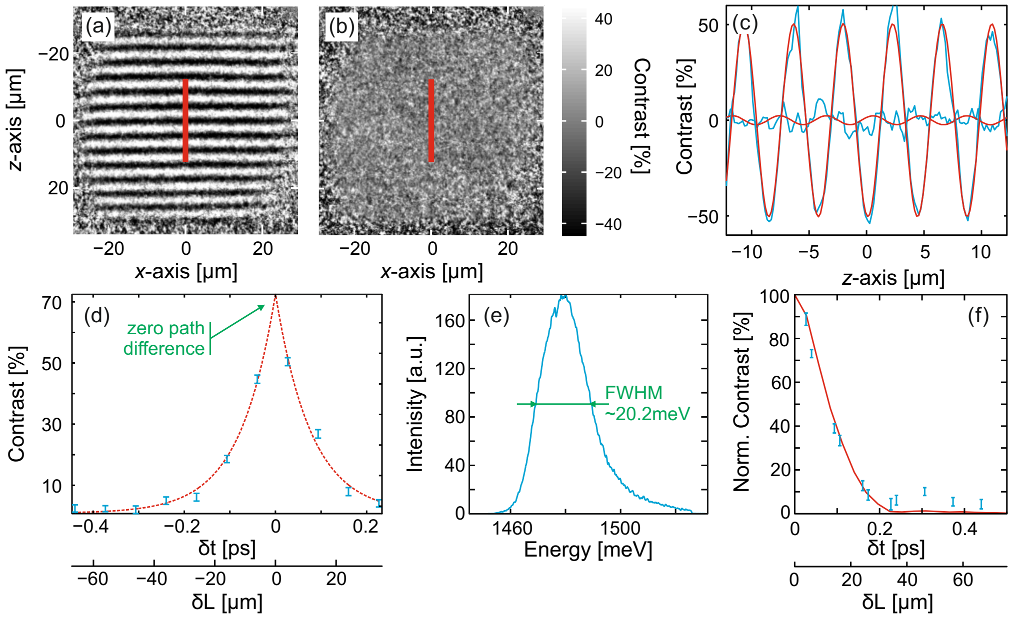

Figure II.10: (a-b) Normalized interferograms of the GaAs bulk emission excited with a wide 641.5nm laser beam. The interferences have been taken for δL values respectively 5μm (a) and 65μm (b) away from the zero path length difference. The red lines represent the positions along which the contrast profiles depicted in blue in (c) are taken. The red lines in (c) are cosine functions fitted to these profiles. (d) Values of the cosine fit amplitude for various $\delta t/\delta L$, the error bars come from the quality of the fits in (c). The dashed red line is a guide for the eyes. (e) Spectrum of the bulk emission filtered with a 840±5nm bandpass. (f) Red line : Normalized profile of the modulus of the Fourier transform of (e) along with the values of the contrast in (d) folded along $\delta L = 0$ (blue error bars).

the fringes allows us to measure the visibility by taking a profile along the z-axis (red line in figs. II.10(a) and (b)) and to fit the obtained profile with a cosine function as shown in fig. II.10(c). The resulting cosine amplitudes (i.e. $|g^{(1)}(x, \delta t)|$) for various δL are plotted in fig. II.10(d). Following the dashed red guide of the eyes lines we are able to infer the value of δL for which the contrast is maximum which corresponds to the zero path difference. In fig. II.10(f) are displayed the normalized Fourier transform (red line) of the GaAs spectrum shown in fig. II.10(e) as well as the data points displayed in fig. II.10(d) folded along the zero-path difference and normalized (blue error bars). Thanks to these measurements we see that we are able to resolved a coherence time as low as $\tau_c \simeq h/\Gamma \simeq 200$fs ($h$ being the Planck constant). Most of the photoluminescence signal studied in this thesis have a spectral linewidth lower than ~3meV which corresponds to a coherence time higher than ~1.4ps, i.e. much higher than the resolution.

For the typical spectral linewidth values encountered in our experiments, Fourier transform spectroscopy would seem to be an overkill. However this method coupled to the reconstruction of the coherence map can provide a useful “at a glance” insight into the spectral structure of the photoluminescence. As a demonstration we use the fictional (but realistic) spectra in fig. II.11(a)). Spectra A (red) and B (blue) are both composed of 2 Gaussian functions shifted by 2meV with 2 different widths (0.5meV and 2meV), the only difference between spectra A and B is the value of the amplitude of the wide part of the spectrum : 100 for B and 200 for A (the amplitude is 400 for the narrow Gaussian). If we now take the normalized modulus of the Fourier transform of these spectra (see fig. II.11(b)), we can see that for δt sufficiently large (e.g. $\delta t_\alpha = 1.5$ps, at the foot of the Fourier transform of the wide line, dashed green line fig. II.11(b)) the value of the Fourier transform is essentially dominated by the Fourier transform of the narrow line (dashed orange line in fig. II.11(b)). This value varies significantly between curves A and B i.e. when the amplitude of the wide Gaussian changes. It can be shown that this value gives an estimation of the ratio between the integrated intensities of the narrow and wide Gaussians if the difference between the 2 Gaussians widths is high enough. According to eq. II.10, this means that if we record a map of the contrast for an appropriate path difference δL, the value of the contrast at a given spatial point of the map would give an indication of the integrated intensities ratio between a wide and a narrow spectrum line. This could prove particularly interesting in the case of the presence of a condensate of excitons which is expected to be associated with the appearance or increase of a narrow spectral line.

The experiments on time-interferometry are described in the appendix A and we will see that while this method provides phenomenological results, its application is not straightforward in the case of a complex system such as the one we study.

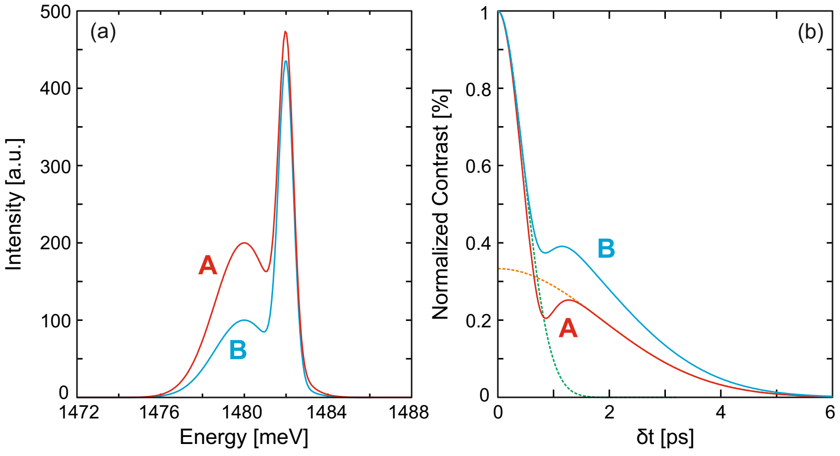

FIGURE II.11: (a) Fictional spectra composed of 2 Gaussian functions. Spectrum (red) A(x) $= C_1 \mathrm{exp}\left[\frac{(x-x_1)^2}{\sigma_1^2}\right] + C_2 \mathrm{exp}\left[\frac{(x-x_2)^2}{\sigma_2^2}\right]$ with $C_1 = 400$, $C_2 = 100$, $x_1 = 1482$ meV, $x_2 = 1480$ meV, $\sigma_1 = 0.5$ meV and $\sigma_2 = 2$ meV and spectrum (blue) B(x) : same parameters but $C_2 = 200$. (b) Normalized modulus of the Fourier transform of A and B (red $\tilde{A}(\delta t)$ and blue $\tilde{B}(\delta t)$ solid lines). Dashed orange (resp. green) line : Fourier transform of $C_1 \mathrm{exp}\left[\frac{(x-x_1)^2}{\sigma_1^2}\right]$ (resp. $C_2 \mathrm{exp}\left[\frac{(x-x_2)^2}{\sigma_2^2}\right]$) for the A parameters. For $\delta t_\alpha \simeq 1.5$ ps, $\frac{C_2\sigma_2}{C_1\sigma_1} \simeq \tilde{A}(\delta t_\alpha)/\left[1 - \tilde{A}(\delta t_\alpha)\right]$.

II.B.2.b Shift-interferometry

After the previous presentation of the utility of time-interferometry measurements we will now discuss the first-order correlation function in the case of a Mach-Zehnder interferometer set at zero path-length difference ($\delta L = 0$) with a lateral shift δx between the outputs of the two arms. We will see that such configuration allows us to quantify the degree of spatial coherence of the exciton gas and to retrieve its coherence length.

General considerations If we set the interferometer at zero-path length difference and follow the previous calculations, we obtain the following expression for $g^{(1)}(\mathbf{r};\delta x)$:

$$g^{(1)}(\mathbf{r};\delta x) \propto \int dk_x n_{k_x}(\mathbf{r}) e^{-ik_x\delta x} \tag{II.11}$$

where $n_{k_x}(\mathbf{r})$ is the momentum distribution of excitons along the x-axis. Before presenting a theoretical expression which can be derived for $g^{(1)}(\mathbf{r};\delta x)$ we would like to give a general idea of the behavior of the g$^{(1)}$-function in a case of interest, namely a partially condensed Bose gas. In this situation [103] the non-normalized first-order correlation function $G^{(1)}(\mathbf{r},\mathbf{r}')$ can be decomposed into a condensed and an uncondensed (thermal) part :

$$G^{(1)}(\mathbf{r},\mathbf{r}') = \psi^*(\mathbf{r})\psi(\mathbf{r}') + G_T^{(1)}(\mathbf{r},\mathbf{r}') \tag{II.12}$$

where $\psi(\mathbf{r})$ is the wavefunction of the condensate while $G_T^{(1)}(\mathbf{r},\mathbf{r}')$ is the first-order correlation function associated to a thermal gas whose normalized expression $g_T^{(1)}(\mathbf{r},\mathbf{r}')$ reads as an exponential decay $\exp(-\pi|\mathbf{r}-\mathbf{r}'|/\lambda_{\mathrm{dB}}^2)$ where $\lambda_{\mathrm{dB}} = h/\sqrt{2\pi M_X k_B T}$ is the thermal de Broglie wavelength. The asymptotic behaviors of the normalized g$^{(1)}$-function then reads :

$$g^{(1)}(\mathbf{r},\mathbf{r}) = 1 \tag{II.13}$$

$$g^{(1)}(\mathbf{r},\mathbf{r}') \simeq g_T^{(1)}(\mathbf{r},\mathbf{r}') \text{ for } |\mathbf{r}-\mathbf{r}'| < \lambda_{\mathrm{dB}} \tag{II.14}$$

$$\lim_{|\mathbf{r}-\mathbf{r}'|\to\infty} g^{(1)}(\mathbf{r},\mathbf{r}') = \frac{\psi^*(\mathbf{r})\psi(\mathbf{r}')}{\sqrt{G^{(1)}(\mathbf{r},\mathbf{r})}\sqrt{G^{(1)}(\mathbf{r}',\mathbf{r}')}} \tag{II.15}$$

Here we recover that a Bose condensate yields a correlation length larger than the de Broglie wavelength. We also recover that for a sufficiently large and uniform system, $g^{(1)}(\mathbf{r},\mathbf{r}')|_{\mathrm{large}\,|\mathbf{r}-\mathbf{r}'|}$ reduces to the local condensate fraction and the correlation length scales as the size of the system. The first-order correlation function would then look like the dark line in fig. II.12(a). Interestingly, if the gas has a limited size, instead of an infinite plateau the first-order correlation function would eventually decrease towards zero with a variation characteristics to the shape and extension of the wavefunction of the condensate (red and blue lines in fig. II.12(a) for example). Experimentally it is usual to estimate the coherence length as the value of $|\mathbf{r} - \mathbf{r}'|$ for which $g^{(1)}(\mathbf{r}, \mathbf{r}')$ reaches a certain value (typically $1/e$). Thus since the rapidity of the decrease of the $g^{(1)}$-function is determined by the extension and shape of the condensate wavefunction we see that the coherence length is directly limited by the size of the condensate. In particular we can not expect to measure a coherence length larger than the size of the condensate. Moreover if the condensate is very small (a few de Broglie wavelengths for example) the $g^{(1)}$-function will not present a plateau even if the condensate fraction is high. Such behaviors have been measured in cold atoms experiment [100].

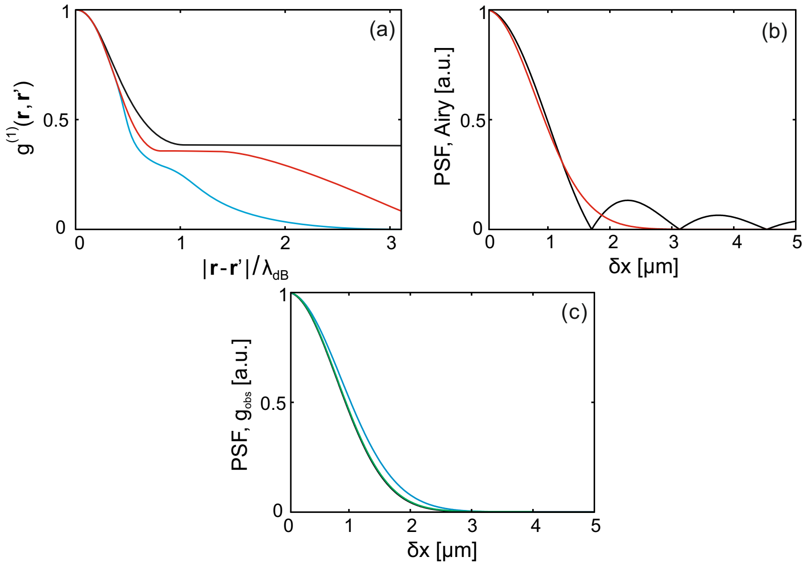

Figure II.12: (a) Evolution of the first order correlation function for a partially condensed infinite and homogeneous boson gas (in black) and for partially condensed boson gas of limited size (in red and blue). The curves does not pretend to describe any real system but aim to give a general idea of the variation. (b) Red line : Point Spread Function $\mathrm{PSF}(\delta x) = e^{-\delta x^2/2\sigma^2}$ with $\sigma = 0.8$ (from measurements in section V.A). Black line : Airy function $\mathrm{Airy}(\delta x) = \frac{Q}{\delta x}.J_1(Q\delta x)$ where $Q = 2\pi\mathrm{NA}/\lambda$ and J_1 is the Bessel function of the first kind. NA is the numerical aperture of the microscope objective and λ the wavelength of the photoluminscence (NA=0.3 and $\lambda \sim 0.84\mu$m for our experiment). (c) Black line : Point Spread Function (same as in (b)). Blue (resp. green) line : normalized $g^{(1)}_{\mathrm{obs}}(\delta x)$ as given by Eq. II.23 with PSF same as (b) and $\xi = \lambda_{\mathrm{dB}}(T_b = 0.34\mathrm{mK})$ (resp. $\xi = \lambda_{\mathrm{dB}}(T_b = 7\mathrm{K})$).

2D Bose gas of excitons The previous considerations give us an idea of the variations of the $g^{(1)}$-function and its behavior depending on the characteristics of the condensate. However those were general observations and we would like to have if possible a more precise theoretical expression of the $\mathrm{g}^{(1)}$-function for a system close to the one we are studying. In particular for a two-dimensional non-interacting Bose gas, $g^{(1)}\left(\mathbf{r};\delta x\right)$ can be calculated and reads (for further details on the calculation see [104]):

$$g^{(1)}\left(\mathbf{r};\delta x\right)=\frac{T}{T_0}\sum_{n=1}^{\infty}\frac{\left(1-e^{-T_0/T}\right)^n}{n}e^{-\pi\delta x^2/n\lambda_{\mathrm{dB}}^2} \tag{II.16}$$

where λ_{dB} is the thermal de Broglie wavelength and $T_0=T_0(\mathbf{r})=\frac{2\pi}{g}\frac{\hbar^2}{k_B M_X}n_X(\mathbf{r})$ is the degeneracy temperature which marks the transition boundary from classical to quantum statistics. If we consider excitons in a GaAs single quantum well then $g=4$ is the spin degeneracy (however we have seen in the first chapter that the bright and dark exciton states are not degenerate so if we consider only the ground state which is dark then $g=2$), $M_X=0.215m_e$ the exciton mass and $n_X(\mathbf{r})$ the density of exciton at the point $\mathbf{r}$ in the quantum well plane. With these notations the occupation number of the ground state is given by $n_{k=0}^{BE}=e^{T_0/T}-1$. From this formula we can see that the degree of coherence will depend on three parameters : the bath temperature, the density of excitons through T_0 and obviously the lateral shift δx. The behavior of the formula is however not straightforward and it is useful to study its asymptotic behaviors for some limits of the physical parameters :

$$\begin{aligned}
g^{(1)}\left(\mathbf{r};0\right) &= 1,\ \forall(T,n_X) && \text{(II.17)}\\
g^{(1)}\left(\mathbf{r};\delta x\right) &= e^{-\pi\delta x^2/\lambda_{\mathrm{dB}}^2},\ \text{for } T\gg T_0 && \text{(II.18)}\\
g^{(1)}\left(\mathbf{r};\delta x\right) &= 1,\ \text{for } T\to 0 && \text{(II.19)}\\
g^{(1)}\left(\mathbf{r};\delta x\right) &\sim 1-\frac{\pi^2\delta x^2}{6\lambda_{\mathrm{dB}}^2},\ \text{for } \delta x\ll\lambda_{\mathrm{dB}} \text{ and } T\lesssim T_0 && \text{(II.20)}\\
g^{(1)}\left(\mathbf{r};\delta x\right) &\simeq 2\frac{T}{T_0}K_0\left(\frac{\delta x}{\delta x_0}\right),\ \text{for } \delta x\gtrsim\delta x'\gg\lambda_{\mathrm{dB}} \text{ and } T\lesssim T_0 && \text{(II.21)}\\
g^{(1)}\left(\mathbf{r};\delta x\right) &\simeq \sqrt{2\pi}\frac{T}{T_0}\sqrt{\frac{\delta x_0}{\delta x}}e^{-\delta x/\delta x_0},\ \text{for } \delta x\gg\delta x_0\gtrsim\delta x' \text{ and } T\lesssim T_0 && \text{(II.22)}
\end{aligned}$$

where $\delta x'=\lambda_{\mathrm{dB}}\sqrt{-(2/\pi)\log(1-e^{-T_0/T})}$, $\delta x_0=\lambda_{\mathrm{dB}}/\sqrt{-4\pi\log(1-e^{-T_0/T})}$ and K_0 is the modified Bessel function of the second kind. The first equation verifies that $g^{(1)}\left(\mathbf{r};\delta x\right)$ is normalized to 1. The second equation shows that at the classical limit the 2D gas obeys the Maxwell-Boltzmann distribution. With the third equation we see that for a purely quantum gas the first-order correlation function is identically equal to 1. Finally the last 3 equalities depicts the behavior of $g^{(1)}\left(\mathbf{r};\delta x\right)$ when the bath temperature is in the order of magnitude of the temperature of quantum degeneracy. Particularly one can see that for large δx, $g^{(1)}\left(\mathbf{r};\delta x\right)$ behaves as an exponential decay (see eq. II.22). It is very usual when analyzing the variations of the $g^{(1)}$-function to define experimentally the coherence length ξ as such $g^{(1)}(\mathbf{r};\xi) = 1/e$. Therefore from the theoretical expression of the $g^{(1)}$-function we obtain that $\xi \sim \delta x_0$ for large δx and in principle we should be able to obtain experimentally the value of the degeneracy temperature and from it the population of excitons in ground-state. For example for an exciton density $n_X = 10^{10}$ cm^{-2} (typical value for dipolar exciton experiments), a bath temperature of $T_b = 0.34$K and spin degeneracy of $g = 2$, we obtain the following theoretical values for the system : $T_0 \sim 1.3$K, $\lambda_{\mathrm{dB}} \sim 280$nm, $\xi \sim \delta x_0 \sim 520$nm and $n^{BE}_{k=0} \sim 44$. Let us recall that the previous model describes a quantum gas of bosons, in the case of a Bose-Einstein condensate the value of the coherence length is expected to be (much) larger.

The previous calculation were done for a non-interacting Bose gas which constitutes a major simplification of the strongly dipolar interacting exciton gas (not mentioning the other possible interactions for instance with the phonons or the composite nature of excitons). Theoretical attempts have been made to include interactions to the Bose gas which show that repulsive interactions tend to increase the critical temperature [105, 106]. Finally Bose-Einstein condensation can not occur in a pure 2D system without a trapping potential. Therefore any application of the above results on experimental data should be taken with precautions.

Effect of the spatial resolution A major influence on measurements of the spatial coherence is the finite optical resolution of the experimental set-up. With simplification it means that a given point of the photoluminescence on the recording camera is in fact the result of an averaging of the photoluminescence over an area around the corresponding point on the sample. This effect is therefore equivalent to the superposition of two laterally shifted images by the interferometer. There are different ways to include the optical resolution on the expression of the $g^{(1)}$-function : through the pupil function, the Airy diffraction pattern or the point spread function (PSF) [23, 58, 95, 96]. A very common assumption for the expression of the PSF is to use a Gaussian function with a full-width half maximum which corresponds to the optical resolution for the electric field of the photoluminescence [95, 97]. These three methods induce modifications of the $g^{(1)}$-function which are fairly similar for small δx and are essentially equivalent to a Gaussian function, the main difference being the presence of a decreasing oscillation pattern for the first two methods at larger δx (see fig. II.12(b)). Since we did not observe such patterns in the experiments reported in this thesis we decided to use a Gaussian-shaped PSF.

To combine the PSF with a theoretical $g^{(1)}$ we used a convolution product meaning that the observable $g^{(1)}_{\mathrm{obs}}$ is equal to $g^{(1)}_{\mathrm{th}}(\mathbf{r};\delta x) * \mathrm{PSF}(\delta x)$. Let us note that the use of a convolution product leads to an under-estimation of the $g^{(1)}$-function [101]. As seen in the previous paragraph the theoretical expression for $g^{(1)}$ is far from being trivial even for a non-interacting Bose gas and is in particular not available for a gas of dipolar excitons. Therefore we will use a practical approach and following the experimental description of the coherence length we model $g^{(1)}_{\mathrm{th}}$ as an exponential decay $e^{-|\delta x|/\xi}$. This expression has the advantages of being simple, in agreement with the $1/e$ empirical definition the coherence length and partially consistent with the non-interacting Bose gas model. Indeed we have seen that at large δx and $T_b \lesssim T_0$, $g^{(1)}_{\mathrm{th}}$ behaves as an exponential decay (see eq.II.22), and since at small δx the observable $g^{(1)}$-function is completely dominated by the optical resolution, the expression of $g^{(1)}_{\mathrm{th}}$ at these points is actually not important. Finally, let us note that for $T \gg T_0$, $g^{(1)}_{\mathrm{th}}$ is a Gaussian function with a width essentially given by the de Broglie wavelength. However since λ_{dB} is very small at high T_b, the Gaussian function is very similar to an exponential decay with characteristics length λ_{dB} and in particular both are equivalent to a Dirac delta-function in the convolution product with the PSF (see fig. II.12(c)). For the fitting of our experimental results we will therefore use the following expression for the $g^{(1)}$-function.

$$g^{(1)}_{\mathrm{obs}}\left(\mathbf{r};\delta x\right) = A\, e^{-|\delta x|/\xi(\mathbf{r})} * e^{-\delta x^2/2\sigma^2} \tag{II.23}$$

where the optical resolution of the experimental setup is given by $\sigma.2\sqrt{2\log 2}$, i.e. the FWHM of the Gaussian function. A is a normalization constant which ensures $g^{(1)}_{\mathrm{obs}}\left(\mathbf{r};0\right) = 1$. In order to fit this function to the experimental curve we also have to take in account that interferometers are never aligned with a 100% contrast at the auto-correlation (namely for $\delta x = 0$ and $\delta t = 0$), thus we will need to multiply A by another constant C_{max} which reflects the maximum reachable value of the contrast at $(\delta x = 0, \delta t = 0)$ for a given set of measurements.

As discussed above, the limited optical resolution of the experimental setup blurs the measurement of the $g^{(1)}$-function at small δx. Another effect of the optical resolution has been recently described in [95] where the authors demonstrate that a sharp enough photoluminescence pattern would produce interferences at given δx even if coming from an incoherent gas. To probe this effect for our experiment, we simulated the ring photoluminescence (which is the sharpest pattern) with the photoluminescence of the GaAs bulk excited with a vertical linear laser beam (details about the linear excitation can be found in section VI.B and appendix B) whose lateral spatial extension was varied. The resulting normalized interferograms are presented in figs. II.13(a-c) where Γ_{line} is the FWHM of the photoluminescence along the x-axis. In these measurements the lateral shift of the interferometer δx was set at 1.5μm which is the value at which we took the maps of the contrast as presented in sections V.A and V.A.2. Figs. II.13(d-f) show the intensity profiles of the 2 arms of the interferometer and the spatially resolved value of the contrast of the fringes along the x-axis (the contrast at a given position along the x-axis was obtained by fitting the interferogram profile along the z-axis at this position with a cosine function). One can see that as predicted [95] for a sharp photoluminescence (see figs. II.13(a) and (d)) we obtain a contrast of $\sim$ 15% on both side of the intensity profiles. The drop of the contrast at 0 comes from the slight asymmetry of the photoluminescence pattern. As the width of the photoluminescence is increased one can see that the fringes become almost indistinguishable while the maximum contrast decreases to be below 10% for $\Gamma_{\text{line}} = 7.6\mu$m. However since there are essentially no discernible fringes the values of the contrast should be interpreted as the limitation of fitting a more-or-less random signal with a cosine function.

Indeed, such a fit will always gives an amplitude up to $\sim$ 8% which should be considered as a lower boundary for the contrast below which it is not possible to distinguish between a random signal with low fluctuation amplitude and fringes with a very low contrast. To conclude, these measurements show that for a signal with a FWHM larger than $\sim 7.6\mu$m we are not able to tell the difference between the effect of the geometry of the photoluminescence and the limitation of the cosine fit which means that in order to interpret contrast value we can only consider values of the contrast above $\sim$ 10% to assess the presence of coherence. Finally the measurements of the width of the ring presented in the next chapter (see fig. III.7 for example) show that the FWHM of the typical ring we study is about 10μm i.e. much larger than 7.6μm. Therefore a lower boundary at 10% for the contrast is probably overestimated in terms of the photoluminescence geometry, nevertheless we will keep this value for the interpretation of the results for clarity. The experimental results of the shift interferometry are presented in sections V.A and V.A.2 and we will see that we can measure contrast value up to 50%. Thus our results can not be explained by this limitation of the optical resolution.

II.B.3 Polarization measurements

As explained in chapter 1, we expect polarization pattern in the photoluminescence of an exciton quantum gas, resulting from the coherent superposition of bright and dark excitonic states.

In our experiments we measured excitonic polarization by transforming a given typical polarization (namely H, V, D, A, σ_+ and σ_-) to a horizontal polarization using $\lambda/2$- and $\lambda/4$-waveplates and filtering the output with a polarized beam splitter. In order to calibrate the angles of the waveplates, we send a perfectly linearly polarized

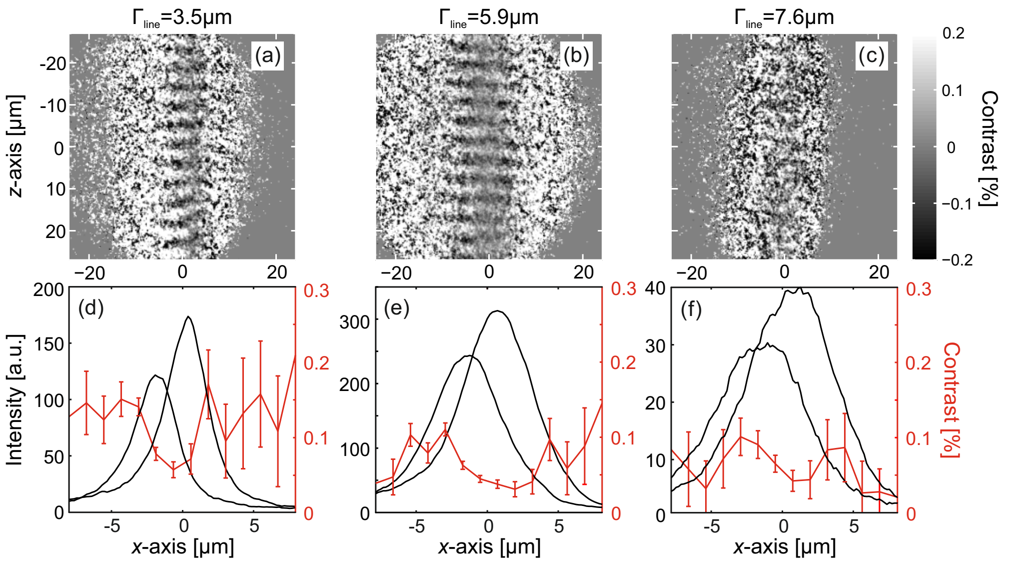

FIGURE II.13: (a-c) Normalized interferograms of the bulk photoluminescence ($V_g = 0$ V) for a vertical linear excitation beam with various FWHM Γ_{line} and a lateral shift $\delta x = 1.5\mu$m (images and details of the line photoluminescence can be found in section VI.B and appendix B). (d-f) Corresponding intensity profiles of the two arms (black lines) and spatially resolved contrast along the x-axis (red line). The contrast was measured by fitting z-axis profiles of the interferograms with a cosine function for various positions on the x-axis. The profiles in (d-f) are limited to 10μm on both side of the origin of the x-axis, indeed for larger distances the intensity of the photoluminescence becomes too weak to obtain clear interferences. The difference of intensity for the profiles of the 2 arms comes from the beam-splitter cubes of the interferometer which do not split the beam with a perfect 50/50 ratio. This only limits the maximum reachable contrast.

(H) laser beam (with the same wavelength as the photoluminescence) through a $\lambda/2$-waveplate and a $\lambda/4$-waveplate and monitor the output polarization with a polarimeter. We then set the angle of the waveplates such that the input polarization is transformed into H, V, D, A, σ_+ and σ_-. To perform the measurements of the polarization the polarimeter is replaced by a polarized beam splitter and the set of angles are exchanged for 2 opposite polarizations ($\sigma_+ \leftrightarrow \sigma_-$ and D $\leftrightarrow$ A, H and V remaining unaffected). The polarization pattern is obtained by recording images for 2 opposite polarizations and subtracting them ($\frac{\text{H}-\text{V}}{\text{H}+\text{V}}$ for the normalized degree of polarization).

Several experimental problems can be raised at this point :

- Waveplates : if the waveplates are not perfectly flat but comport wedges, the output image will be spatially shifted when going from one set of angles to another resulting in artificial pattern in the subtraction of the images. We solve this problem by using waveplates (from LensOptics) with wedges which limits the displacement of the output beam to less than 1μm at a distance of ~1m when the waveplates are rotated. This reduces the shift to less than 300nm on the recording camera with our resolution.

- Degree of polarization : the most direct way to obtain the degree of polarization is to calculate the normalized subtraction between the photoluminescences obtained for 2 opposite polarizations. This method has the inconvenience that intensity fluctuations can easily lead to the appearance of an artificial degree of polarization. Therefore if the retrieved degree of polarization is low ($\sim 10\%$), it is impossible to differentiate between intensity fluctuations and actual polarization of the signal. In order to overcome this problem we developed a method derived from quantum optics which takes in account more than 2 opposite polarizations to reconstruct the polarization vector (this method is described in section V.B). This technique also compensate for eventual rotations of the polarization of the photoluminescence by the optics.

The results we obtained for the polarization setup are explained in section V.B

Chapter III

Macroscopic ring of dipolar excitons

In this chapter we enter in the core of our experimental results. As stated in the introduction of this manuscript, our experiments demonstrate the existence of a “gray” condensate of dipolar excitons as predicted by Monique and Roland Combescot [50]. While we think that the occurrence of such condensate is characteristic to the condensation of excitonic system (at least for GaAs/AlGaAs heterostructures) and that it will eventually be observed in other systems, the results of this thesis concern its appearance along with a particular excitonic phenomenon first reported over ten years ago : the self-organization of dipolar excitons in macroscopic fragmented rings. Therefore, we dedicate this chapter to a brief historic of previous experiments and observations on the fragmented ring and then to the characterization of the fragmented ring realized in our field-effect device.

III.A Introduction

State-of-the-art The first observation of macroscopic self-organization of dipolar excitons was simultaneously reported by the groups of L. Butov and D. Snoke[1] in 2002 [51, 52, 107]. It raised a large interest in the semiconductor community because of the intuitive idea that self-organization occurring below a temperature threshold can be related to a phase transition, notably to an eventual quantum regime [35]. Despite the fact that they worked with different heterostructures (which still present strong similarities as they both mainly studied GaAs/AlGaAs DQW with a continuous excitation

---

[1] Let us note that after this first observation the group of D. Snoke started a collaboration with a group in the Bell laboratories which performed most of the following theoretical and experimental works.

at an energy larger then the AlGaAs barrier bandgap, see [51, 89, 107, 108] for further details) they both observed the formation of a photoluminescence ring up to hundreds of microns away from the excitation spot (see fig. III.1). Concurrently to this ring was reported the appearance of localized bright spots inside or outside the ring [51, 109]. Localized bright spots had already been reported by C. Lai [110] and were interpreted [104, 111] as anti-trapping potential formed locally around current filaments. We rarely observed localized bright spots therefore we will not address this subject in this thesis. Even more strikingly, L. Butov and coworkers reported a fragmentation of their ring at low bath temperatures. We would like to stress that ring fragmentation was never observed by D. Snoke et al. or another group until the work presented here.

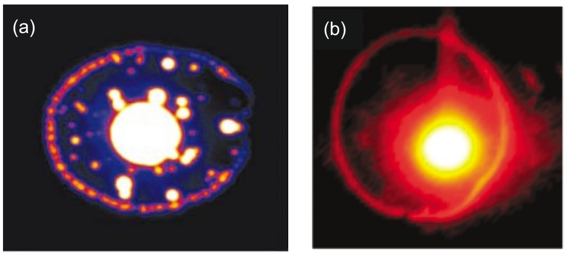

FIGURE III.1: (a) Fragmented ring and localized bright spots observed by L. Butov et al. [51]. (b) Macroscopic ring observed by D. Snoke et al. [108]. For both images the very bright (white) region inside the ring corresponds to the laser excited region.

The first interpretation for the ring formation was developed during the following years and published in [53, 108]. It relies in the charges separation and diffusion in the QW plane and was later followed by other works [54, 56, 112–114]. This interpretation can be described by the following sequence and the pictures presented in fig. III.2 (the formation mechanism is presented sequentially for clarity reasons but all processes take place simultaneously for a continuous excitation beam) :

1. A field-effect semiconductor heterostructure including a QW is electrically biased creating a flow of electrons through the structure. Some of the electrons are trapped in the QW thus forming an *a priori* homogeneous background 2D electron gas.
2. The sample is excited with a small laser beam at a wavelength above (or equal to) the bandgap of the barriers. Free carriers are then created and travel through the structure due to the applied voltage. Holes having a larger effective mass than the electrons they are more likely to be trapped in the SQW or DQW at the position of the laser excitation.
3. A fraction of the holes recombines with the background electrons leaving a large excess of holes around the position of the excitation spot.

4. Due to the repulsive electrostatic interaction, the holes are pushed away from the excitation spot while the remaining electrons are attracted towards the attractive potential created by the holes. Excitons form where the electron and hole fronts meet and when the electron and hole density is similar. When excitons recombine one can observe a photoluminescence ring.

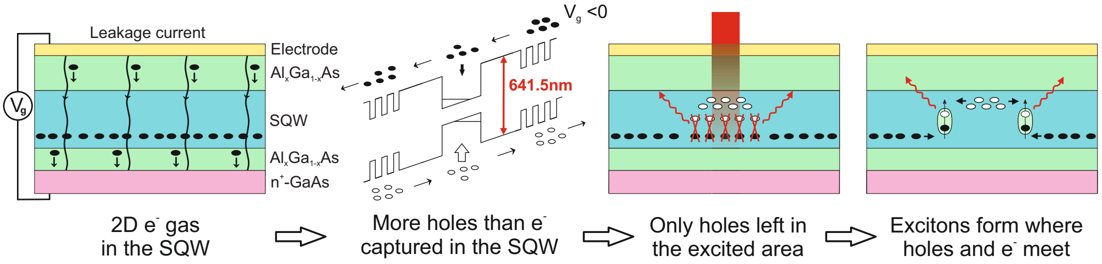

FIGURE III.2: Schema of the ring formation for our sample and experiment, the steps are described in the main text. Electrons (resp. holes) are depicted by filled (resp. empty) circles.

The photoluminescence ring then appears to be the result of a dynamical equilibrium between the holes and electrons spatial distribution and density in the QW plane. From this simple picture one can already understand what should be the main parameters which influence the characteristics of the ring. Indeed the radius, intensity and width of the ring will essentially be determined by the density and spatial profiles of the electrons and the holes which are created in the QW but also by the values of the diffusion coefficients which directly relate to the quality of the sample. The bath temperature should also play an important role since it directly affects the mobility of the free carriers in the QW plane and more generally in the heterostructure.

Having in mind this physical picture, various researchers have laid out 2D theoretical models to reproduce the formation mechanism of the ring [53, 54, 56, 108, 112–114]. In its simplest form and if $n(\mathbf{r},t)$ and $p(\mathbf{r},t)$ are the respective densities of electrons and holes, the mechanism of the charge transport in the QW plane $\mathbf{r}$ can be expressed by the following coupled diffusion equations :

$$\begin{cases} \partial_t n & = D_e \Delta n - w\, n\, p + I - \frac{n}{\tau_e} + \alpha P(\mathbf{r}) \\ \partial_t p & = D_h \Delta n - w\, n\, p + P(\mathbf{r}) \end{cases} \tag{III.1}$$

where D_e and D_h are the diffusion constants for the electrons and the holes and w the rate at which an electron and a hole bind to form an exciton. I is the source term for the electrons coming from the electric current through the structure which spread out over the entire QW plane, τ_e scales the escape of the electrons from the QW and $P(\mathbf{r})$ is the hole source localized at the excitation spot which also creates electrons with a lower rate $\alpha < 1$ ($P(\mathbf{r})$ can reduce to $P_0\delta_{\mathbf{r}}$ if we consider an infinitely small excitation spot). From these equations the theoretical expression for the radius of the ring R_{ring} and the width of the electron/hole interface W [53, 56] can be retrieved (the electrons created at the excitation spot are neglected) :

$$R_{\text{ring}} = \Lambda e^{-\frac{2\pi D_e n_0}{P_0}} \tag{III.2}$$

$$W \propto \sqrt[3]{\frac{D_h}{wI}}\sqrt[6]{\frac{D_e}{\tau_e}} \tag{III.3}$$

where $\Lambda = \sqrt{D_e\tau_e}$ is the electron depletion length while $n_0 = I\tau_e$ is the electron density without excitation. Let us note that these expressions are only valid for $R_{\text{ring}} \ll \Lambda$ (more detailed calculations for the above values can be found in [53, 56]).

The equations III.1 are very simplified and crucial processes are missing such as the drift for the carriers created by electrostatic interactions, the electrostatic potential created by the charges, the influence of the bath temperature and of course another equation dedicated to excitons. This model should thus be taken as a phenomenological description and one has to be careful when comparing its results with experimental data particularly regarding the number of parameters required. An important experiment to confirm this interpretation of the ring formation was done by both L. Butov and D. Snoke which consisted in exciting their samples with two independent laser beams and looked at the behavior of the 2 created rings as a function of the distance between the rings [53, 107]. Their observations are displayed in fig. III.3. It shows that for both experiments the shape of the rings is perturbed by the presence of the other one and the rings seem to be attracted to each others when decreasing the distance between the excitation spots. This phenomenon can be explained by considering that the electrons density in the area between the 2 rings is more strongly depleted that in the other directions. This has for effect to reduce the “pressure” for the hole fronts which can then diffuse further away from the center of the ring leading to an electron-hole interface which is displaced further out. Let us note that these experiments are very well simulated using the equations III.1. The influence of the excitation power and the applied gate voltage on the ring aspect as well as its dynamics has been extensively studied by L. Butov et al. [60] allowing them to retrieve the parameters of the equations III.1 for their sample.

The most striking feature of the macroscopic ring is certainly its fragmentation in beads observed by the group of L. Butov at low bath temperature. The relation between the structure of the sample and a possible fragmentation of the ring is far from being understood. Even more confusing is the fact that we sometimes observed fragmentation

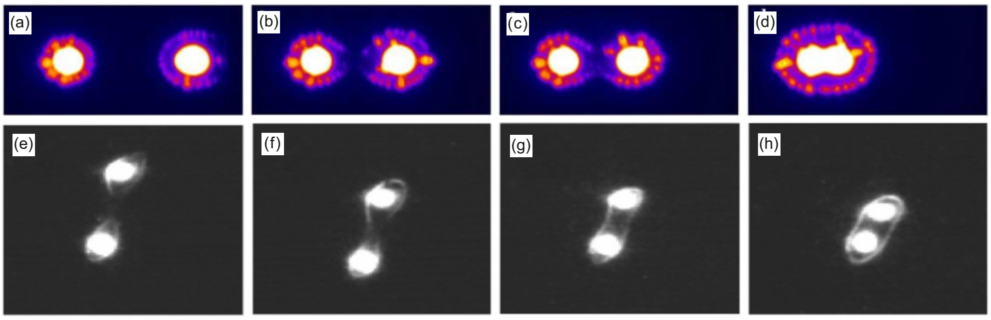

FIGURE III.3: (a-d) Photoluminescence emitted by 2 independent excitation beams (from the group of L. Butov [53]). The distance between the excited regions decreases from (a) to (d). (e-h) Same experiment performed by D. Snoke et al. (from [107]).

only in certain areas of our sample without obvious differences between the different regions. However let us already stress that the sample structure used by L. Butov and coworkers and ours differ in various important ways (for instance we study a SQW while they use a DQW) such that the fragmentation should probably not be considered as linked to a specific kind of heterostructure but in fact as a characteristic phenomenon associated to the physics of excitons when ambipolar diffusion of charges is dominant.

While the simplified equations presented previously are widely accepted to explain the formation mechanism of the ring, the processes behind the appearance of the fragmentation is still under strong debate especially to ascertain whether it signs a quantum process. Various theoretical models and approaches have been developed giving different interpretations for the ring fragmentation but a consensus has yet to be reached. The presentation of these models goes beyond the scope of this thesis and we only refer to the following references [57, 112, 113, 115, 116] for further details.

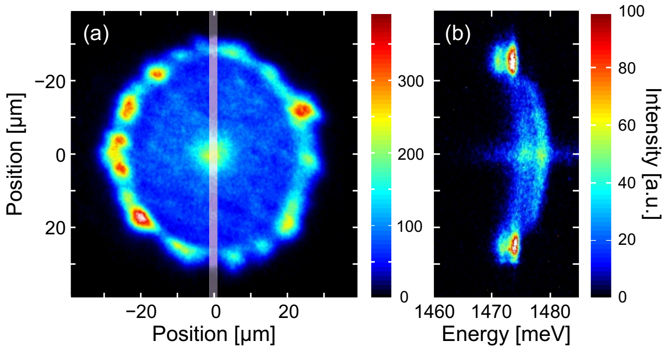

FIGURE III.4: (a) Typical image of the photoluminescence of the fragmented ring which can be produced in our sample for a bath temperature of T_b = 340mK. (b) Spatially resolved spectrum taken with the entrance slit of the spectrometer horizontally aligned with the center of the ring (corresponding to the white transparent area in (a)). The experimental conditions to obtain such data are presented in the following sections.

Our results Without further ado let us present fig. III.4 which displays a typical fragmented ring which can be produced in our sample along with a spatially resolved spectrum. In the following sections we will study the response of our ring as a function of the main experimental parameters (bath temperature, applied voltage and laser excitation power) first by analyzing the direct photoluminescence (see part III.B) and then by measuring its spectrum (see section III.C.1). This study will be completed by time-resolved measurements of the dynamics of the ring of both the direct image (see section III.B.2) and its spectrum (see section III.C.2). We will also measure the evolution of the spectrum along a radius of the ring (see section III.C.3). We now present some of the main results of this chapter.

With the direct observation of the photoluminescence of the ring we observe that the shape and the size of our ring is indeed highly dependent on the values of the excitation power and the applied voltage. The relatively small size of our ring radically differs from the rings reported in the literature (radii of 20 to 30μm in our case to be compared to radii of several hundreds of micrometers for L. Butov et al. and D. Snoke et al.). Similarly to the work of the group of L. Butov [51], we observe that the ring exhibits a more pronounced fragmentation when the bath temperature is lowered however we also observe a simultaneous contraction of the ring which has not been reported so far. Another important difference for our sample is that bringing two independent rings closer to each other does not affect their shape contrarily to the experiments shown in fig. III.3 (see appendix C).

The study of the dynamics of the direct photoluminescence allows us to retrieve the decay time of the ring. We found it to be long for a SQW but, as expected, much shorter than for other rings reported in the literature [60]. This can be easily attributed to the fact that we use a SQW while other groups study DQW heterostructures for which the overlap between the electrons and holes wavefunctions is greatly reduced. Strikingly we do not observe a contraction of the ring after the end of the excitation pulse as has been reported by L. Butov and coworkers [60].

The spectral measurements show that the photoluminescence is composed of two distinct spectral lines. By measuring the energy shift of these lines with the variation of the applied voltage we show that these lines come from quasi-particles which both present a dipolar momentum with a value consistent with the measurements performed during the characterization of the sample presented in the section II.A. This result along with the relative narrowness of the spectral linewidths lead us to conclude that the ring is formed of dipolar excitons. We attribute the line at higher energy to a pure excitonic recombination while we interpret the second line at lower energy as the results of interactions between dipolar excitons and free charges present in the QW or in its vicinity. These charges are inherent to the formation of the ring. The exact nature of the charge/exciton compound yielding this second line is not clear, however measurements show that it strongly depends on the density of free charges. We would like to note that it is the first time that such spectral characteristics are reported for a fragmented ring.

By means of the study of the dynamics of the photoluminescence spectrum we are able to obtain an estimate of the exciton density at the position of the ring and found it to be consistent with densities reported in the literature ($\sim 1 - 2.10^{10}$ cm^{-2}). We also observed a difference between the energy profiles of excitons at the position of the ring during and after the excitation pulse.

Finally we study the energy distribution of the photoluminescence along the radius of the ring. In these measurements, we report an anomalous evolution of the energy of the spectral emission on the ring and outside of it at the lowest bath temperature. Indeed we measure that the energy of the photoluminescence remains constant in this region which would indicate a uniform exciton density. In the same region the strong decrease of the intensity of the photoluminescence at the outer edge of the ring would sign on the contrary a decrease of this density. We attribute this contradiction as a first indication for the presence of a dense gas of dark excitons in the immediate vicinity of the ring.

The review of these results shows that while some characteristics of our ring are in agreement with the traditional formation mechanism of the ring presented previously, others behaviors and characteristics can not be explained by this model and differ from previous works on the fragmented ring. Some of these differences can be explained by considering that we study a different heterostructure however some of them led us to new interpretations for the formation mechanism of (at least) our ring and its fragmentation. In particular we develop the idea of the appearance of a quasi-stationary potential for excitons inherent to the formation of the ring. We think that for our sample this potential is largely responsible for the dynamics of the ring and the presence of fragments (for example it easily explains the dome-shaped profile of the photoluminescence energy in fig. III.4(b) and the absence of the ring contraction after the excitation pulse). This interpretation will be developed in chapter IV.

As a general remark our experience with this sample has shown to us that while apparently identical, different regions of the sample proved not be equivalent. Some differences can be related to the quality of the top electrodes which bias the samples, but even within a single electrode the fragmented ring can be better in certain parts of it. Additionally the experimental parameters for creating a fragmented ring were not always the same depending on the part of the sample we studied. The results presented in this chapter represent nevertheless the most common values.

III.B Direct observation of the photoluminescence

In the following sections we first describe the influence of the main experimental parameters (excitation power P_{ex}, applied voltage V_g and bath temperature T_b) on the physical properties of our fragmented ring. In a second time we study the dynamics of the ring during and after the excitation pulse. Except if stated otherwise, all data in this section and in the following sections were recorded in a 40 ns long time window 10 ns after the end of a 1 μs laser pulse at 641.5 nm with a repetition rate of 2 μs (see fig. III.5). The laser excitation beam has a gaussian profile with a FWHM of $\sim 5.3\mu$m. The photoluminescence of the ring was recorded after the pulse in order to avoid the pollution coming from the GaAs bulk emission during the pulse at the position of the excitation beam (the lifetime of the GaAs emission is less than 1 ns while the decay time of the ring is on the order of 20 ns). The objective here is not to retrieve the parameters of the equations III.1 (as was done in [60]) but rather to give the main behaviors of our ring and to determine the set of parameters necessary to produce an "optimal" ring.

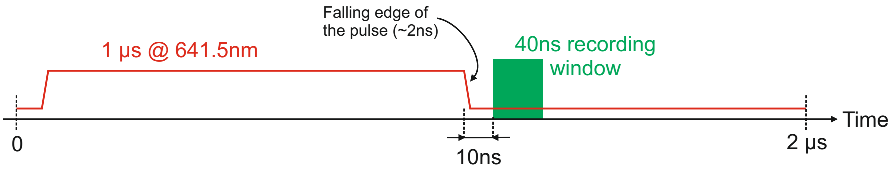

Figure III.5: Laser pulse and recording parameters.

III.B.1 Influence of the experimental parameters

III.B.1.a Excitation power

In order to study the influence of the excitation power we recorded a set of images of the photoluminescence for various P_{ex}. Some of the obtained images are displayed in fig. III.6 together with their intensity profiles along the x-axis. In fig. III.6(e) are presented the main characteristics of the ring which will be studied in more details in the next sections. R_{ring} is the radius of the ring taken from the position of the excitation spot (intensity I_{ex}) to the maximum of the ring (intensity I_{ring}). I_{min} is the minimum intensity between the excitation spot and the maximum of the photoluminescence intensity while $I_{7\mu\text{m}}$ is the intensity taken 7 μm away from the maximum of the ring. Finally the width of the ring is analyzed using the HWHM Γ_{ring} of the profile on the outside of the ring and Γ_{min} is the width of the ring at the intensity I_{min}. The evolution of these parameters with the excitation power is presented in fig. III.7 along with the intensity of the current in the sample.

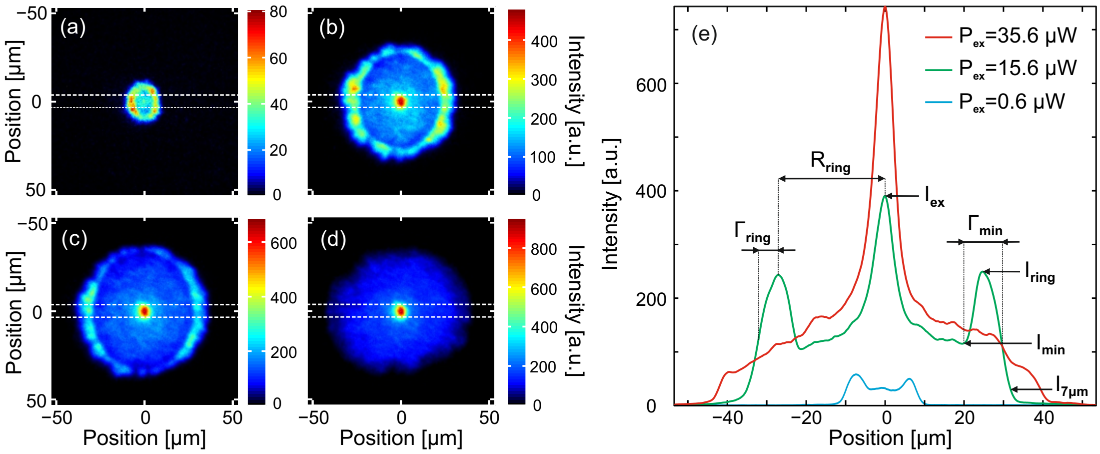

FIGURE III.6: (a-d) Photoluminescence images of the fragmented ring for various excitation power. From (a) to (d), $P_{ex} = 0.6$, 15.6, 23.6 and 35.6 μW. The data were recorded for a gate voltage of $V_g = -4.85$ V and at a bath temperature $T_b = 0.37$ K. (e) Intensity profiles along the x-axis obtained by averaging the images (a), (b) and (d) on a region of $\sim 7\mu$m along the y-axis (delimited by the dashed white lines on the images). The characteristics of the ring of particular interest are also indicated.

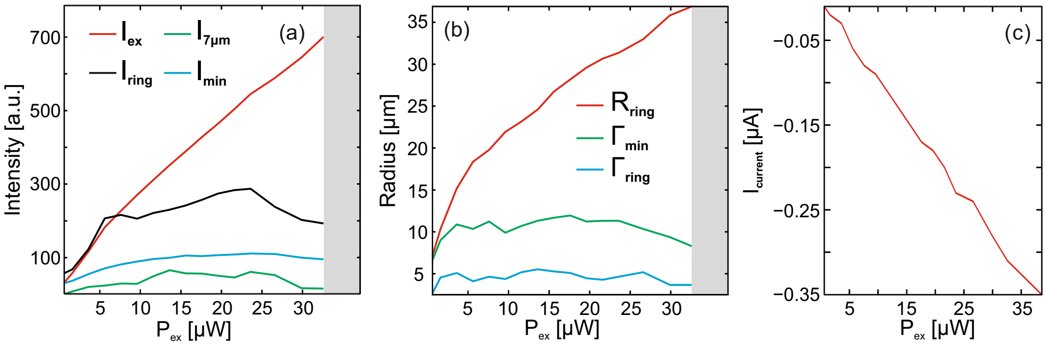

FIGURE III.7: (a-b) Evolution of the characteristics defined in fig. III.6(e) in function of the excitation power P_{ex}. The gray region is the limit above which no ring is observed. (c) Current flowing through the sample for the same variation of P_{ex}.

According to the model described by the equation III.1, raising the excitation power should lead to an increase of the hole population at the position of the laser beam ($P(\mathbf{r})$ term in the equations) which will then have to diffuse further away in order to match the density of the electrons, effectively increasing the radius of the ring. As shown in fig. III.7(b), we observe that starting from a very small ring ($R_{\text{ring}} \simeq 7\mu$m, for smaller value of P_{ex} the photoluminescence profile closely follows the one of the laser beam, i.e. no ring is produced) R_{ring} increases monotonously with the excitation power. However for $P_{ex} \gtrsim 35.6\mu$W the ring is barely distinguishable and essentially disappears in the photoluminescence background (see fig. III.6(d) and corresponding profile in (e)). This decreasing of the ring intensity is characterized by the variations of I_{ring} in fig. III.7(a) for $P_{ex} > 23.6\mu$W. This shows that above a certain excitation power, the density of electrons is not sufficient to obtain a sharp electron/hole interface. By increasing the applied voltage V_g, we increase the density of electrons which has for effect to allow exciting the structure with higher power before reaching the ring disappearance limit (see fig. III.8). Thus by simultaneously increasing V_g and P_{ex} we should in principle be able to reach very large ring radii, however we observe that above a certain gate voltage we are unable to form a ring even for a very high excitation power.

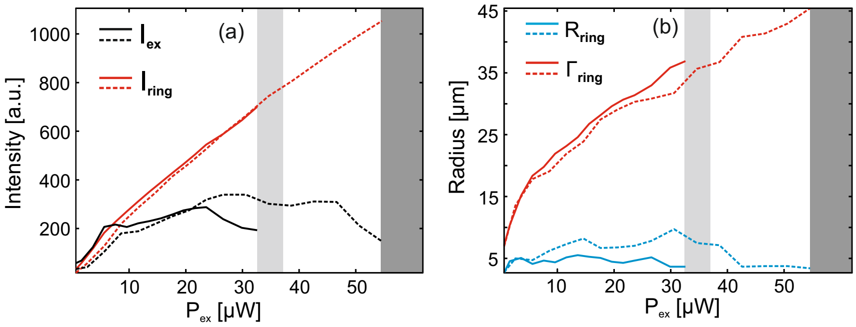

FIGURE III.8: (a-b) I_{ex}, I_{ring}, R_{ring} and Γ_{ring} in function of the excitation power P_{ex} for $V_g = -4.85$V (solid lines) and $V_g = -5.05$V (dashed lines). The light gray region is the same as in fig. III.7 while the dark gray region is the limit above which no ring is observed for $V_g = -5.05$V.

The current flowing through the structure is presented in fig. III.7(c) and increases linearly (in absolute value) with the excitation power whether or not a ring is formed. The mechanism for the ring formation requires that more holes than electrons are being captured in the QW at the position of the excitation spot. The fraction of electrons which is trapped at this position explains the very high intensity signal at the center of the ring (see figs. III.6(a-d)). This means that most of the photocreated electrons are then free to travel through the sample and account for essentially all the observed current (the current created by the gate voltage is negligible in comparison, see fig. III.10(c)). Intuitively this photocurrent should then increase the background electron density in the QW and compensate for the hole injection especially for the large value of the excitation power. However fig. III.8 shows that above a certain excitation power threshold the only way for increasing further the ring radius is to increase the gate voltage which essentially does not affect the current.

We are then led to conclude that the main effect of the gate voltage for our sample is not so much to inject the background electron gas but to control the density of electrons allowed in the QW. This interpretation is supported by the fact that, in our sample, the QW is placed very close to the back electrode ($\sim$ 100nm, see fig. II.1) and separated from the back electrode by a superlattice. This situation leads to the creation of intermediate energy states between the QW and the back electrode allowing electrons to tunnel out of the QW, this tunneling being made easier by the negative bias we apply. The distribution and quantity of these intermediate states is directly controlled by the tilt of the energy bands created by the applied voltage which therefore controls the tunneling out of the QW and the density of electrons which can be captured. Once this density is reached the remaining electrons can flow freely through the sample. This would also explain why we only observe the ring for a gate voltage much larger than commonly used in experiments on dipolar excitons : the gate voltage must be high enough to isolate the intermediate states with respect to each other and decrease the tunneling rate. Moreover this clarifies the limited size of our ring (few tens of microns for our sample against few hundreds of microns for the group of L. Butov [117]) : we initially thought that the quality of the interface of our QW was low such that the induced disorder would dramatically decrease the diffusion coefficients of the electrons and the holes. However as stated in section II.A the linewidth of the direct exciton line is extremely low ($\sim 400\mu$eV) indicating on the contrary a very good interface quality. An alternative explanation which accounts for the above discussion is to consider that since we can only form rings for a given range of applied voltage we only have access to a limited range of background electron density and therefore a limited ring radius (let us note that for example the group of L. Butov uses a DQW which is placed far from possibly disturbing structures). Understanding the role played by V_g in the equations III.1 is then very complex since it will act on both the injection rate of electrons I and the escape rate τ_e. Nevertheless the overall behavior of our ring with respect to variations of the excitation power is in good qualitative agreement with the model based on the separation of charges.

An important question to go further on the measurements which are presented in the next sections and chapters is to determine a set of parameters (V_g,P_{ex}) for which the "quality" of the ring is optimum. By quality, we mean its intensity with respect to the intensity inside the ring (which can be expressed by the ratio $I_{\text{ring}}/I_{\text{min}}$), its width and the quality of the fragmentation. One should also take in account is the photocurrent, indeed the ring resulting in a balance between charges in the QW plane we want to avoid unnecessary charges (mainly electrons) to go through the QW. Following these requirements we see on fig. III.7(a) and (b) that I_{ring}, I_{min} and $I_{7\mu\text{m}}$ steadily increase until $P_{ex} \simeq 10\mu$W and are then essentially constant while Γ_{ring} and Γ_{min} reach almost immediately a constant value. In order to minimize the current we will then choose an excitation power of $\sim 10\mu$W.

To conclude this section one can note in fig III.6 that the fragmentation and intensity of the ring are more pronounced along the x-axis than along the y-axis despite a symmetric excitation beam. We do not have a clear explanation for this phenomenon but we would like to mention that the sample was mounted such that the [110] and [1$\bar{1}$0] crystallographic axis match the x and y-axis.

III.B.1.b Applied voltage

Figs. III.9 and III.10 show images of the rings as well as intensity profiles and the parameters for a set of applied voltage V_g and an excitation power of $P_{ex} = 11.6\mu$W. As one can see, starting from a situation where no ring is present ($V_g > -4.35$ V), the ring widens monotonously (see Γ_{min} and Γ_{ring} in fig. III.10(b)) while the intensity of the ring I_{ring} rapidly increases and decreases dramatically until finally we obtain for $V_g \lesssim -5.65$V a very wide and barely distinguishable ring. From this behavior we see that increasing V_g essentially widens the ring towards the interior, indeed as shown in fig. III.9(e) the size of the ring remains essentially constant, while its maximum moves towards the center of the ring. Let us stress again that according to the equation III.2, the interface width scales as $\sqrt[3]{\frac{D_h}{wI}}\sqrt[6]{\frac{D_e}{\tau_e}}$. From the dependence of the ring on the excitation power we know that raising V_g leads to an increase of the electron density meaning that either I or τ_e (or both) increases. However this would imply a thinner ring which is not what we observe. Nevertheless one has to keep in mind that the model we use is only phenomenological and the expression for the width of the ring is only valid for $R_{ring} \ll \Lambda = \sqrt{D_e\tau_e}$, therefore without knowing exactly if we are in this situation, it is delicate to draw conclusion from the model. A possible explanation for the behavior we observe is that despite a larger electron density the holes are "kicked" out from the center with enough momentum to seep into the electron sea without being immediately captured by an electron, i.e. without forming a sharp electron/hole interface.

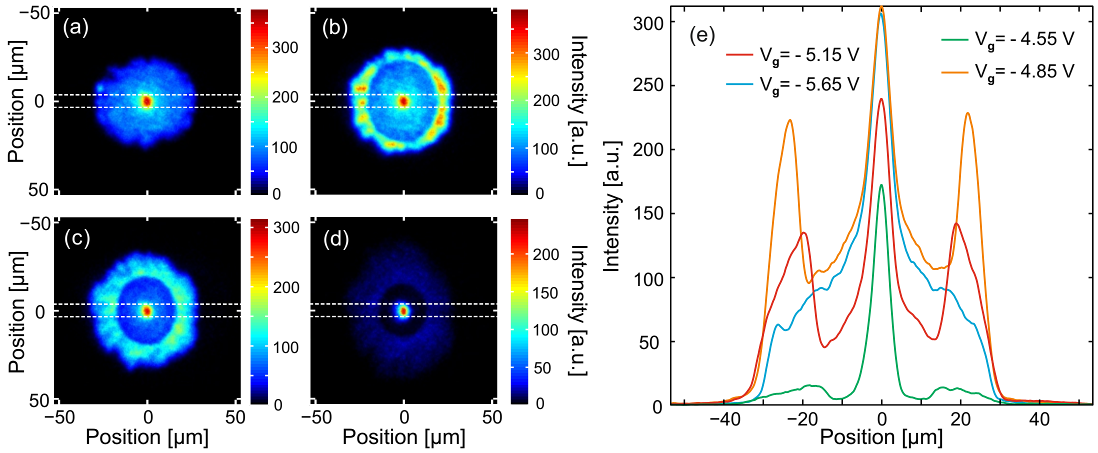

FIGURE III.9: (a-d) Photoluminescence images of the fragmented ring for various applied voltage $V_g = -4.55$, -4.85, -5.15 and -5.65 V. The data were recorded for an excitation power of $P_{ex} = 11.6\mu$W and at a bath temperature $T_b = 0.37$ K. (e) Intensity profiles along the x-axis obtained by averaging the images (a-d) on a region of 7μm along the y-axis (delimited by the dashed white lines on the images).

We see that in order to work with a ring as well defined as possible (i.e. high I_{ring} and low Γ_{ring}, Γ_{min}) the gate voltage needs to be close to the "no ring" region, therefore we will set $V_g = -4.85$V for the further experiments.

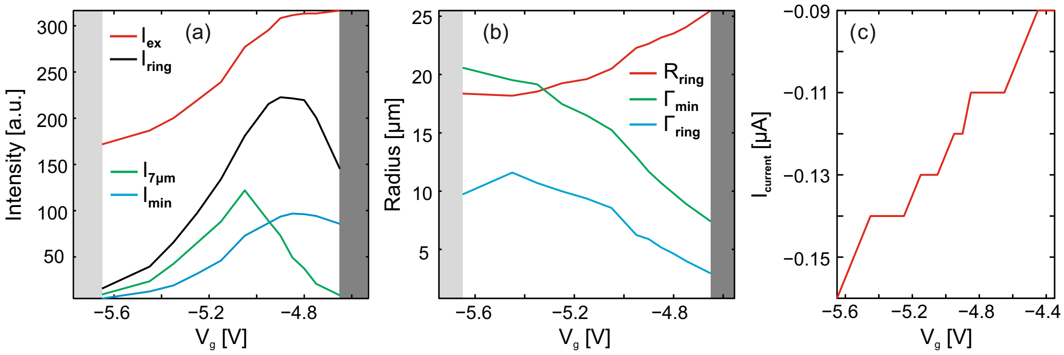

FIGURE III.10: (a-b) Evolution of the characteristics defined in fig. III.6(e) as a function of the applied voltage V_g. The dark gray region is the limit below which no ring is observed while above the light gray region there is almost no signal on the ring (width of the ring very large). (c) Current flowing through the sample for the same variation of V_g. The step-like shape of the line comes from the limited precision of the amperemeter.

III.B.1.c Bath temperature

The evolution of the ring with the bath temperature is perhaps more striking than for the excitation power and applied voltage. Indeed changing these parameters in a reasonable way does not affect the fragmentation but the situation changes dramatically when increasing T_b. As one can see in figs. III.11(a-f) raising the bath temperature leads to an increase of the radius and width of the ring (see figs. III.11(g) and III.12(b)) but more importantly causes the disappearance of the fragmentation. This effect is quite clear if we compare the intensity profiles along the ring perimeter for $T_b = 0.34$ and 7 K (see fig. III.11(h)) : the rapid oscillations which mark the fragments at low temperature vanish for $T_b = 7$ K (the large background oscillation accounts for the asymmetry of the ring intensity along the x and y-axis). Similar observations were done by L. Butov and coworkers [51, 59] however they did not report neither an increase of the ring radius nor a widening. According to the model and our interpretation we think the later effects come from a decrease of the electron density due to an increase of the activation energy of the electrons which can tunnel out of the QW more easily (τ_e decreases). In this regard increasing the bath temperature would be similar to a lowering of the gate voltage. However the behavior of the ring is very different in the 2 situations which leads to the conclusion that the overall mechanism is certainly more complex than the one described by the phenomenological model. An enhanced diffusion of the charges in the QW plane due to thermal activation is probably the dominant effect.

Throughout this manuscript we will see that the evolution of many of the characteristics of the fragmented ring with the bath temperature exhibits a change of behavior for T_b =2-3K. The first examples are here the fragmentation which is much more pronounced for $T_b \lesssim 3$K and the intensity and radius of the ring. Indeed as one can see in fig. III.12, I_{ring} and R_{ring} remain constant until $T_b \simeq 3$K and then change dramatically.

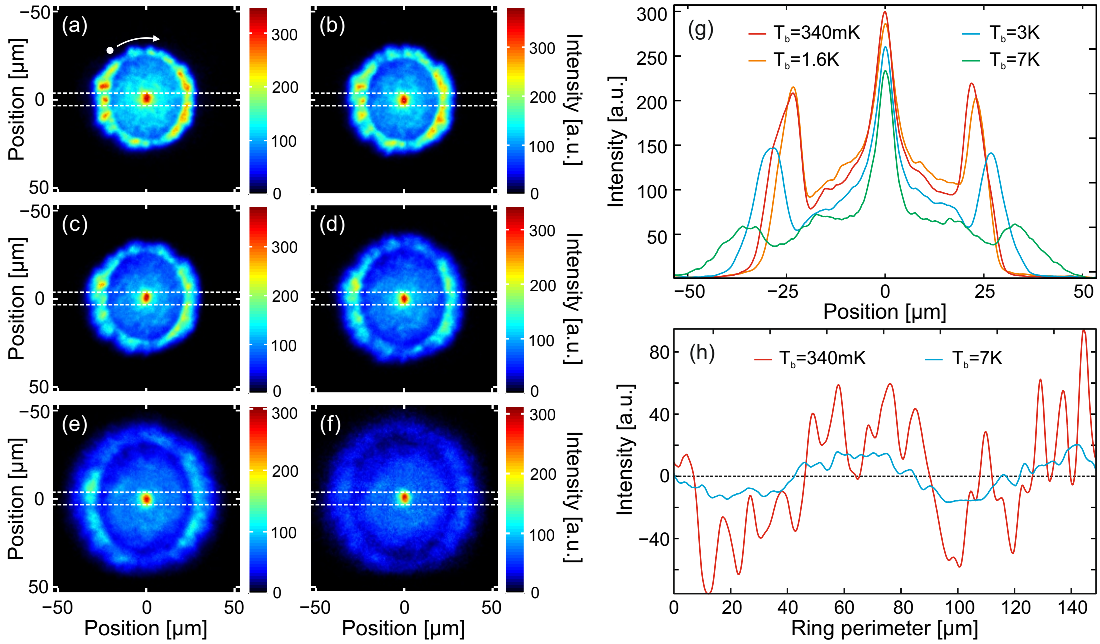

FIGURE III.11: (a-f) Photoluminescence images of the fragmented ring for various bath temperatures. From (a) to (f), $T_b = 0.34$, 1.6, 2.2, 3, 5 and 7 K. The data were recorded for an excitation power of $P_{ex} = 11.6\mu$W and a gate voltage of $V_g = -4.85$V. (g) Intensity profiles along the x-axis obtained by averaging the images (a), (b), (d) and (f) on a region of $\sim 7\mu$m width along the y-axis (delimited by the dashed white lines on the images). (h) Intensity profiles along the circumference ring for (a) and (f), the profiles have been centered around 0 and the ring perimeter for $T_b = 7$K has been rescaled with respect to the one at $T_b = 0.34$K for clarity. The white dot and arrow in (a) show the starting point and the direction at which the ring profile was taken.

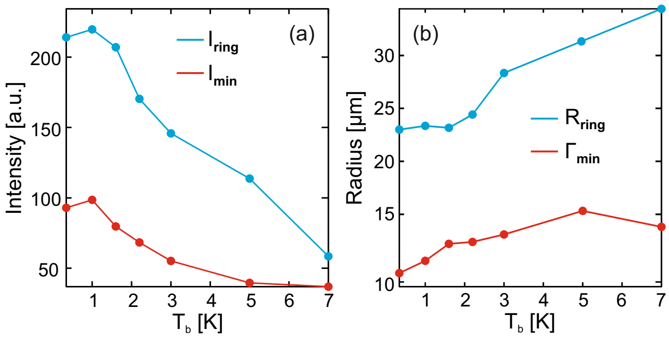

FIGURE III.12: (a-b) Evolution of some of the characteristics of the ring in function of the bath temperature T_b.

III.B.2 Dynamics : Life & death of an exciton ring

The dynamics of the ring formation was studied by L. Butov and coworkers in [60]. Starting from a strong signal at the position of the excitation spot they observed the expansion of the ring during the laser pulse up to a maximum value of the ring radius with the development of the fragmentation. After the pulse the fragmentation progressively disappears while the ring contracts and loses its circular shape until there is no ring left. Following the phenomenological model based on the ambipolar diffusion of charges, this contraction was interpreted as an increased pressure of the electrons gas when no more holes are created by the laser. Similar results and interpretation were obtained by the collaboration between D. Snoke and the Bell laboratories [118].

Fig. III.13 presents images of the ring during and after the excitation laser pulse. At the beginning of the pulse, we observe the expansion of a shapeless photoluminescence cloud around the excitation spot. This cloud then reaches a maximum expansion and a ring appears with fragments which progressively become distinguishable. The whole process takes place during the first ∼ 100ns of the laser pulse. Surprisingly, we also observe the appearance of a second ring in the center cloud when the first onsets of fragmentation appear. This ring is about half the radius of the fragmented ring and starts to expand slowly until it reaches the exterior ring and merges with it, about 500ns after the beginning of the pulse. The expansion of the interior ring can be seen in fig. III.13(l) while the solid red line profile in fig. III.14(a) clearly shows the 2 rings at the time delay 190ns. Contrarily to the experiment discussed in [60] we do not observe a contraction of the ring after the laser pulse (see fig. III.13(i-k)). In our case no changes in the general aspect of the ring can be noticed except for a decay of the intensity of the photoluminescence.

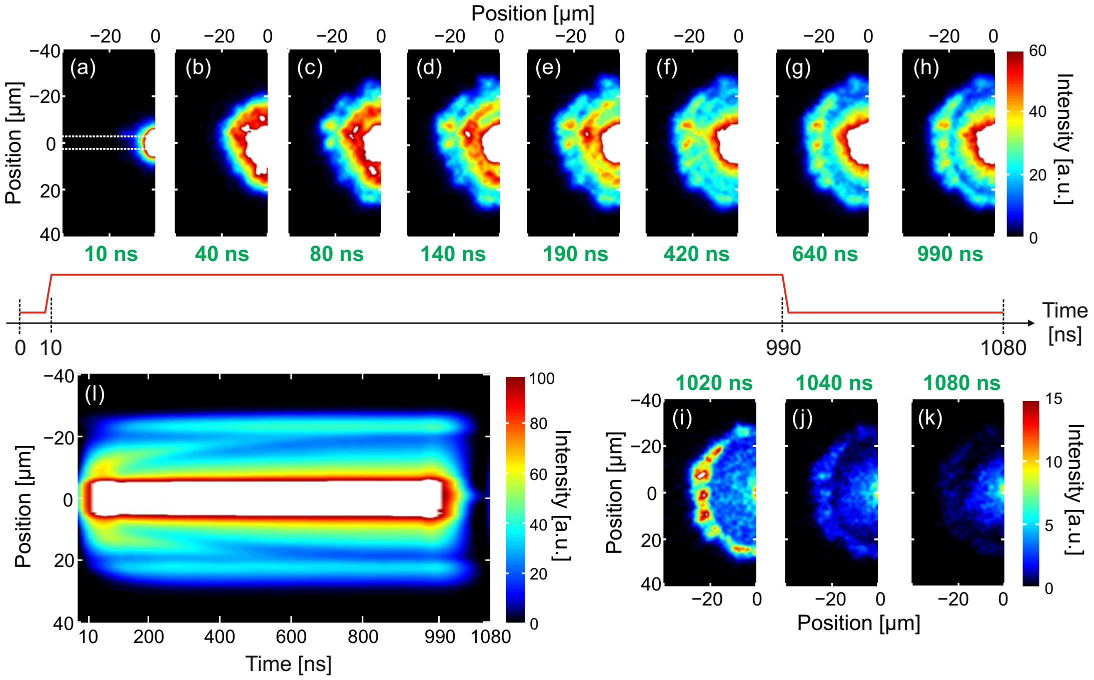

FIGURE III.13: (a-k) Images of the photoluminescence ring taken at various delays during and after the laser pulse. The images were recorded with a time window of 10ns for a pulse length of 1μs (rep. rate 2μs) and with $P_{ex} = 11.6\mu$W, $V_g = -4.85$V and $T_b = 0.37$K . (l) Evolution of the intensity profiles along the x-axis with the time delay (averaging along the y-axis delimited by the dashed white lines on the image (a)). The white saturation in most of the images comes from the very high photoluminescence signal coming from the bulk emission at the position of the excitation spot during the laser pulse.

To quantify the formation and decay times of the ring we measured the intensity of the photoluminescence at various position of the ring as presented in figs. III.14(a-b). The travel of the interior ring towards the outer ring is clearly marked by the time delayed jumps in the photoluminescence intensity. Namely this jump is first present close to the excitation spot (blue line), then halfway between the excitation spot and the outer ring (purple line) and finally at the position of the outer ring (light blue line). A steady state is reached about 600ns after the beginning of the pulse. Fig. III.14(c) presents a focus on the photoluminescence intensity after the laser pulse. The decay time at the position of the ring is about 20ns and about 8ns at the position of the excitation spot.

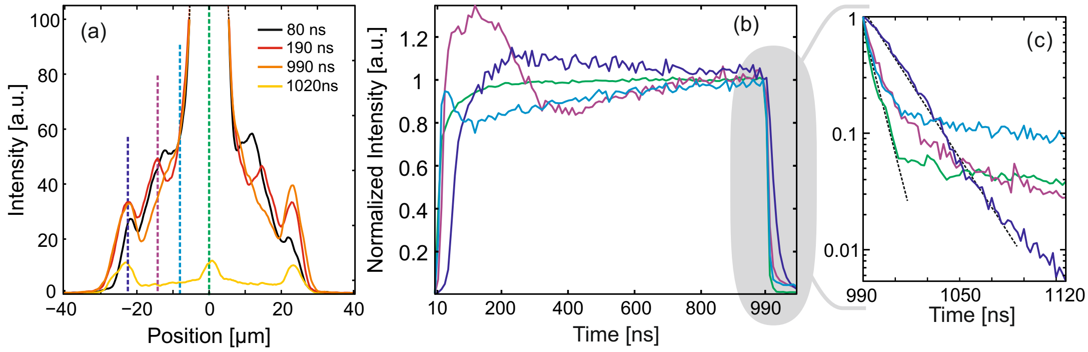

FIGURE III.14: (a) Intensity profiles along the horizontal axis for some images presented in fig. III.13 taken in the region delimited by the white dashed lines in fig. III.13(a). (b) Evolution of the intensity with the time delay for the positions given by the dashed lines in (a). The intensity profiles have been normalized to 1 for the value at the delay 990ns (end of the excitation pulse). (c) Focus of the intensity profiles of (b) after the pulse. Linear regressions of the photoluminescence decay at the position of the ring (dark blue) and at the position of the excitation spot (first part of the green line) respectively give decay times of ~ 20 and ~ 8ns. The intensity for the purple, blue and green lines is almost constant after 1010ns due to leakage of the laser pulse, which does not affect the ring profile. The photoluminescence after the pulse was recorded with time windows of 2ns in order to increase the time accuracy.

The overall dynamics of our fragmented ring occurs much faster than the one of L. Butov and coworkers (we measure a $\sim$ 20ns decay time in our case for several μs for their ring [60]), we attribute this difference to the fact that they use a DQW where the overlap of the electrons and holes wavefunctions is much lower than for our SQW. As described in the introduction to this chapter some of our results can not be explained by the sole model based on the separation of charges. However the presence of these anomalies becomes clearer if we consider the existence of a potential for excitons quasi-stationary during a pulse sequence. Precisely the measurements performed in the next chapter show that inside the ring exists a dome-shaped anti-trap potential (see section IV.A.1) which is created during the pulse and remains after the end of the laser excitation. At the same time we have observed the presence of local trapping potentials at the position of the ring and directly outside it. We can directly see that the presence of such potentials would prevent excitons to diffuse towards the interior of the ring and limit their diffusion away from the ring. This would explain why after the excitation pulse we only observe a decay of the intensity of the photoluminescence of the ring and no change in its shape. As a concluding remark, let us note that we do not have any qualitative interpretation for the origin of the temporary ring which appears inside the main ring during the laser pulse.

III.C Spectroscopy

As described in the first chapter the analysis of the spectrum of the photoluminescence gives many information on the exciton gas : the position in energy of the spectrum line informs on the density of excitons and the potential landscape while its linewidth gives a direct insight on the strength of the various phenomena leading to a homogeneous and/or inhomogeneous broadening (collisions exciton/exciton or exciton/phonon, roughness of the quantum well interfaces and interactions with free charges for instance). In the case of a spectrum presenting multiple components a thorough set of experiments usually allows one to identify the origin of the lines. To introduce the spectral measurements we first present a state-of-the-art and then an introduction to our results.

State-of-the-art Following their first observation of the fragmented ring, L. Butov and coworkers have obtained many results on the spectral characteristics of the ring, some of them are presented in fig. III.15 (results from [59, 85], the recollection does not pretend to be exhaustive). Fig. III.15(a) shows the spatially resolved spectra of a portion of the ring for different temperatures. Like us (see fig. III.13) they observe a fragmentation which becomes more and more pronounced when they lower the bath temperature until the ring fragments into individual beads. The spectrum on a bead or between two beads presents an identical single line which, for the authors, confirms the model of electrons and holes fronts forming excitons at the position of the ring. Interestingly the exciton line on the bead is blueshifted in energy with respect to the one between the beads indicating that the density of excitons is larger in the beads. This result is confirmed by fig. III.15(c) which shows the variations of the intensity and the energy of the photoluminescence along the circumference of the fragmented ring. One can see that the energy of the gas closely follows the fluctuations of the intensity when passing from bead to bead, the fragments thus signing an oscillation of the exciton density along the ring. One can notice that the spectral line is asymmetric with a longer tail towards the low energy. Such feature has been observed by another group which attributes this asymmetry to correlated behavior mediated by the dipolar interactions

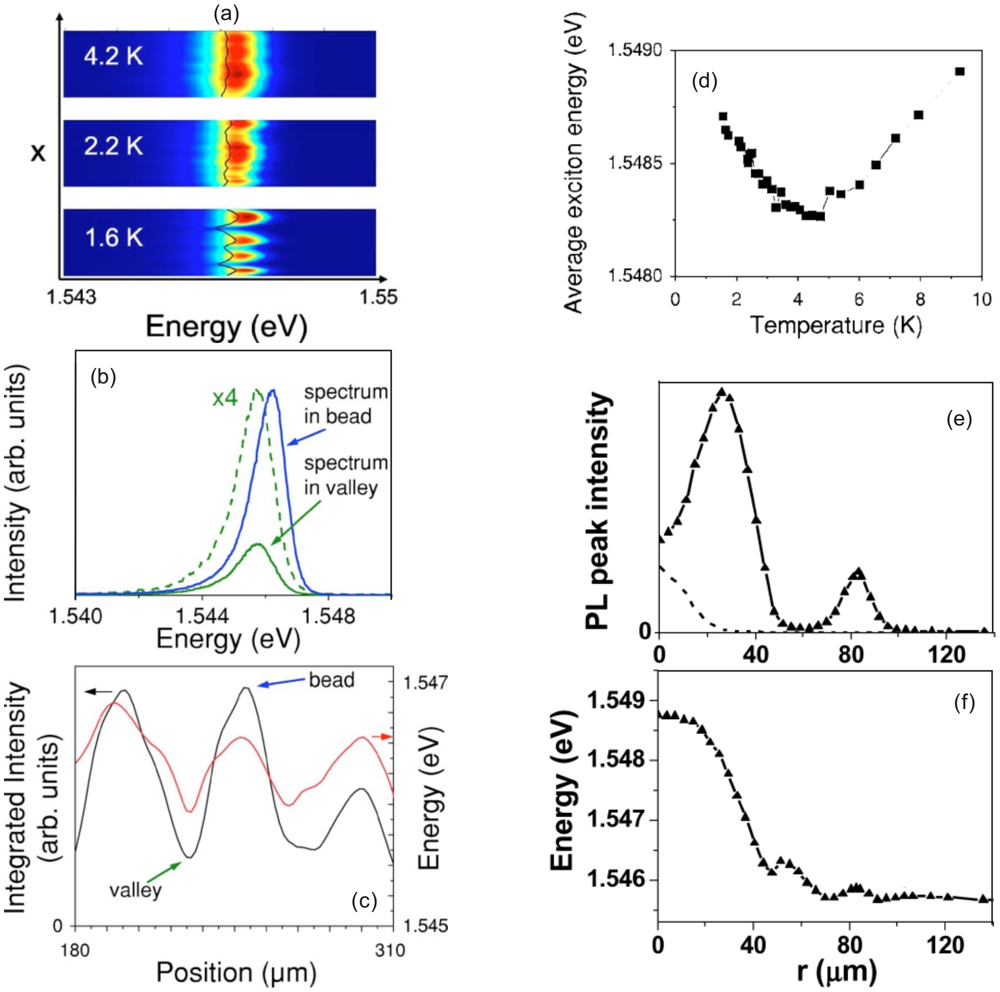

FIGURE III.15: (a) Spatially resolved spectra of aportion of the fragmented ring for various temperatures. (b) Photoluminescence spectra at the position of one of the beads (blue) and between two beads (green) at T$_b$=1.6K. (c) Integrated intensity and energy of the bottom image of (a) spatially resolved along the x direction. (d) Evolution of the averaged exciton energy at the position of the ring with the bath temperature. (e-f) Photoluminescence intensity and energy along the radius of the ring, the dashed line in (e) represent the excitation profile . Figures (a) to (d) are reproduced from [59] while (e) and (f) comes from [85].

[78]. It is difficult to assess the presence of such shape in our case since we always observe two mixed lines (however we did observe it in other experiments [73, 119]). As a final remark one can also object that two (or more) spectral lines mixed together could easily produce an overall asymmetric line if these lines were close enough to each other and with a decreasing intensity towards the low energy.

Fig. III.15(d) presents the variation of the photoluminescence energy on the ring with the bath temperature. One can see that the energy steadily increases when lowering the temperature from a minimum at T$_b$ $\sim$ 5K which is the limit above which L. Butov and coworkers do not observe a ring. This increase was interpreted as an evidence that the appearance of the fragmentation is not driven by attraction processes.

Finally the group of L. Butov measured the intensity and energy of the photoluminescence along a radius of the ring (see fig. III.15(e-f)). They observed that the energy is rapidly dropping of about 3 meV when going from the center of the ring to its inner side (the ring is marked by the intensity peak at $r \sim 80\mu$m) and then remained essentially constant except for a small peak at the position of the ring. The authors interpreted these results in terms of a slightly larger density of excitons on the ring and a much larger density when approaching the excitation spot at the center of the ring. Let us note that D. Snoke et al. [118] also measured asymmetric spectral lines (but with a longer tail towards the high energy which is more pronounced at the center of the ring) and an energy shift between the spectra at the position of the ring and its center, with the spectrum at the center of the ring lying at higher energy. This blueshift was interpreted as a band gap renormalization at the center of the ring caused by the presence of a high density of holes. Surprisingly the intensity profile in fig. III.15(e) presents a minimum at the center of the ring where the density is supposed to be the highest, the maximum of photoluminescence actually occurring $\sim 30\mu$m away from the center. This phenomenon is interpreted by L. Butov and coworkers as a sign of a local heating of the sample by the laser excitation spot which prevents excitons from decaying to the optically active minimum of the exciton dispersion effectively creating a “gap” in the intensity profile. This interpretation follows numerous works on the so-called “inner ring” which have been done by the same group [68, 104, 120–122]. However in the case of the fragmented ring and contrarily to these former studies, L. Butov et al. did not provide evidence of the photoluminescence “jump” expected at the end of the pulse if the lack of intensity at the center of the ring comes from processes of exciton thermalization. We do not observe this phenomenon in our experiments, which we attribute to the presence of free charges in the QW (indeed the theory explaining the formation of an inner-ring supposes a neutral gas which is not the case here, however we observed an inner-ring in other experiments, see [73]).

Introduction to our results Fig. III.16 serves as an introduction to the spectral measurements which will be detailed throughout the following sections. As an illustration, we show the spatially resolved spectrum of the photoluminescence with the spectrometer slit centered at the center of the ring (see fig. III.16(b) and (d)). Some of the main spectral characteristics of the ring can be seen in this image : at any point along the vertical y-axis the spectrum presents two distinct lines whose characteristics vary along the ring diameter. For example fig. III.16(e) presents the spectral profiles on the ring (green) and at the center of the ring (red) and one can already see dramatic differences especially concerning the energy position and the intensity ratio between the 2 lines at the 2 positions. The two-components spectrum can be well fitted using a

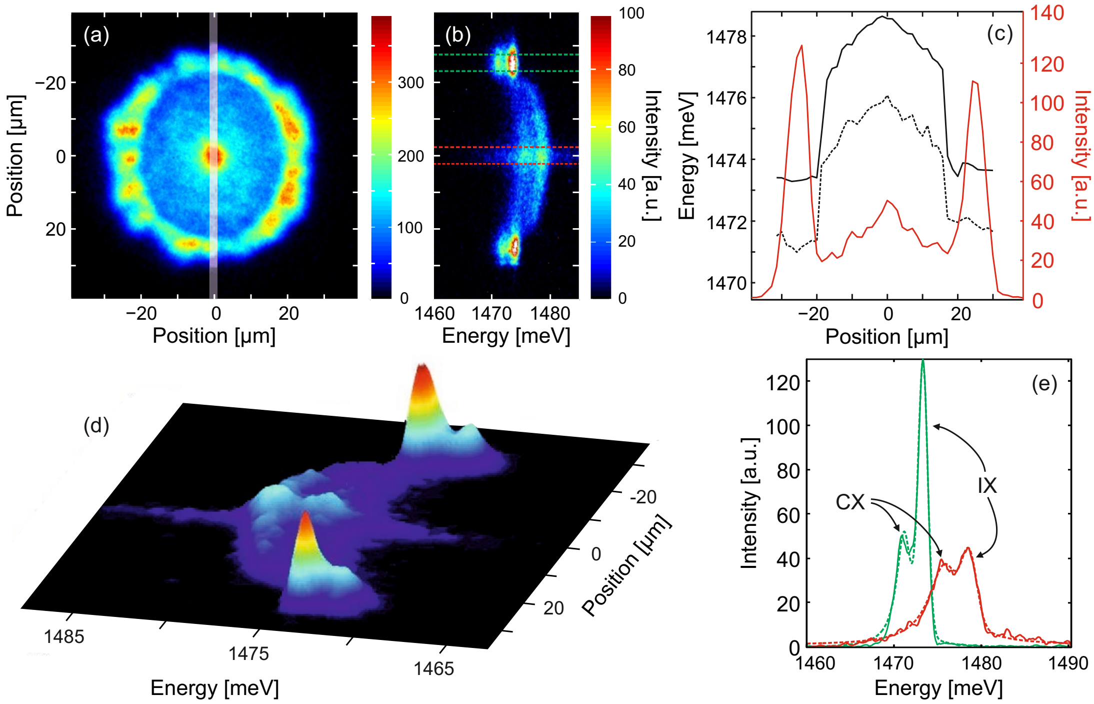

FIGURE III.16: (a) Real image of the photoluminescence ring, the white blurred region marks the position of the slit of the spectrometer (width $\sim 2\mu$m). (b) Spatially resolved spectrum (space on the vertical axis and energy on the horizontal axis) at the position on the ring marked by the white transparent region in (a). The same image is displayed with a 3D feature in (d) with the intensity on the z-axis. (e) Spectral profile on the ring (resp. at the center of the ring) solid green (resp. red) line, from the region delimited by the green (resp. red) dashed lines in (b). The spectra clearly present 2 spectral components which can be fitted by a combination of a Lorentzian function for the low energy part and a Gaussian for the high energy part in order to retrieve the main characteristics : energy position and intensity of the maximum and spectral width (FWHM). The fits are displayed with dashed line of the corresponding color. (c) Intensity (solid red line) and energy position (solid black line) of the high energy component of the spectrum resolved along the vertical axis in (b), the black dashed line displays the energy position of the low energy component of the spectrum. The measurements were performed for $T_b = 370$mK, $P_{ex} = 11.6\mu$W, $V_g = -4.85$V and during a time window of 40ns taken 10ns after a 1μs laser pulse at 641.5nm. Except if specified otherwise the same parameters are valid for all the following results and figures.

combination of a Lorentzian function for the low energy line and a Gaussian function for the high energy line. The functions used do not reflect physical processes but rather serve as tools to accurately retrieve the parameters of the lines : peak energy, spectral width and peak intensity. This analysis repeated for the spectra at different positions along the vertical axis gives fig. III.16(c) which shows the peak energy of the lines at low (dashed black) and high (solid black) energy and the peak intensity of the high energy component (solid red) along the vertical axis of fig. III.16(b).

The energy profiles present a peculiar shape with an energy essentially constant at the position of the ring and a sudden step at the inner border of the ring, the energy of the lines then steadily increasing when moving towards the center of the ring. In the following chapter we demonstrate that the dome-shaped profile of the energy inside of the ring is essentially caused by the presence of a quasi-stationary anti-trapping potential. It is not a surprise if we consider the formation mechanism of the ring : a large population of holes are injected in the QW at the position of the excitation spot (and in its vicinity due to the diffusion) and due to the negative bias these holes will place themselves at the top interface of the QW (see fig. II.2). Such an accumulation of positive charges will result in a local screening of the internal electric field inside the sample *a priori* set by the gate voltage, thus effectively decreasing its strength. Since dipolar excitons are high-field seeker we see that the injection of holes directly causes the appearance of a repulsive potential around the position of the excitation spot.

Another very peculiar behavior of the energy profile presented in fig. III.16(c) is its relative absence of variation at the position of the ring and in its outside vicinity. This behavior will be confirmed by studying the energy of the photoluminescence along the radius of the ring (see section III.C.3). This is surprising since in the same region the intensity of the photoluminescence rapidly drops which would in principle sign a strong decrease of the exciton density. As explained in the first chapter, if the potential for excitons is uniform the energy of the photoluminescence varies like the exciton density. Therefore the fact that the energy of the photoluminescence is essentially constant would indicate that the exciton density is also constant at the position of the ring and in its immediate vicinity which would be in contradiction with the variation of the intensity of the photoluminescence. This anomaly can be explained if we consider that outside the ring exists a dense gas of dark excitons which contributes to the dipolar interaction giving the energy of the photoluminescence but not to its intensity. One can immediately see the importance of such an observation. Indeed due to the small energy splitting between the bright and dark states, bright and dark excitons are normally present with a 50/50 population ratio. Therefore the imbalance of population outside the ring is a direct evidence for a Bose stimulation towards the dark sates. In order to ascertain this key result we will measure in the next chapter the potential for excitons around the position of the ring and we will confirm the presence of such dense gas of dark excitons.

As we will see in the following sections we always observe a two-components spectrum all over the ring. The study of the energy shift of these lines with variations of the applied voltage shows that both lines come from quasi-particles with dipole momentum consistent with the size of our QW and the measurements performed in Chapter 2 (see section II.A). Similar spectra have been observed in other semiconductor systems and were interpreted as the superposition of an exciton line (component at higher energy) and a line resulting from the interactions of excitons with free charges (component at lower energy) [123–126]. This interpretation is also probably valid for our sample since due to the formation mechanism of the ring we know that there are indeed free charges in the QW (and maybe also in the superlattices between the QW and the back and top contacts) and furthermore we observe that the weight, width and peak energy of the line at lower energy is highly dependent on the density of charges. We would like to stress that in the literature this second line at lower energy was often attributed to the presence of a gas of trions which are charged excitons $X^{\pm}$ ($X + e^{-} \rightarrow X^{-}$ and $X + h \rightarrow X^{+}$) [123–126]. However our experiments show that this line exhibits behaviors which do not match the description of trions. In particular we observe that the distance in energy between the 2 lines is not necessarily fixed. The exact understanding of this line and its formation goes beyond the scope of this thesis. For clarity reason the line at higher energy which we attribute to a pure excitonic state will be referred in the rest of the thesis as the "exciton line" (or IX line for indirect/dipolar exciton[1]) while the line at lower energy will be called the "exciton/charges line" (or CX line), as indicated in fig. III.16(e). Let us note that in order to ascertain the nature of the two lines it would be interesting to measure their behavior to a variation of the magnetic field in the sample as has been performed in other works [127–131]. However our cryostat was not designed to allow the application of magnetic fields to the sample.

In the following sections, we first present the evolution of the spectral characteristics of the photoluminescence of the ring with the main experimental parameters (P_{ex}, V_g, T_b). When increasing the excitation power we observe a strong blueshift of the energy of the photoluminescence as well as an increase of the difference between the energy at the position of the ring and the energy at the center of the ring. This behavior can not be explained by the sole blueshift induced by the dipolar repulsion between excitons and we interpret it as modifications of the potential landscape for excitons present inside the ring. We also see that the spectral characteristics of the exciton/charges line are strongly affected by the excitation power reenforcing the idea that the exciton/charges line does sign a charged excitonic compound. Afterward, the variation of the spectra with the gate voltage allows us to retrieve an estimation of the length of the dipolar momentum of the quasi-particles. The study of the influence of the bath temperature on the spectrum then complete the measurements of the effects of the main experimental parameters. Following the organization of the study of the direct photoluminescence, we subsequently measure the spectrally resolved dynamics of the ring which provides an estimation of the exciton density. This measurement also reveals that the spectral structure at the position of the ring is different during the excitation pulse and after it. Finally in order to obtain better details on the shape of the energy profile presented in fig. III.16(c) we accurately measure the spectral characteristics of the photoluminescence

---

[1] Let us note here that the term "indirect excitons" is widely used in the literature to describe dipolar excitons however it can be misleading since it should only be used for excitons formed in semiconductors with indirect gap. We will anyway use the acronym "IX" to comply with the familiar terminology.

along a radius of the ring. These measurements show that at the lowest bath temperature the spectra at the position of the ring and outside are very similar. In particular we confirm that their peak energy is identical.

III.C.1 Influence of experimental parameters

III.C.1.a Excitation power

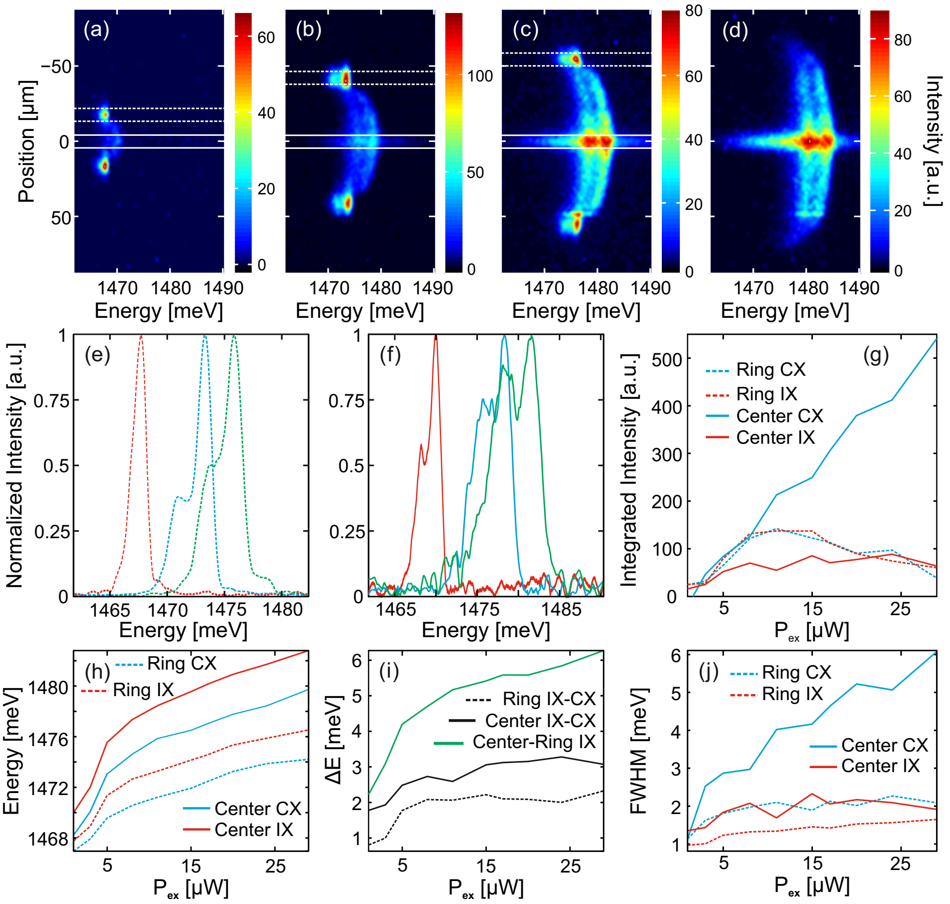

FIGURE III.17: (a-d) Spatially resolved spectra taken at the center of the ring for P_{ex} = 1.6, 11.6, 24.6 and 35.6μW. (e) (resp. (f)) normalized spectral profiles at the position of the ring (resp. at the center of the ring) for P_{ex} = 1.6 (red), 11.6 (blue) and 24.6μW (green) resulting from the region delimited by the dashed (resp. solid) white lines in (a-c). (g) Evolution of the integrated intensity with the excitation power for the exciton (IX, blue line) component of the spectra at the position of the ring (dashed) and at the center of the ring (solid). The red lines display the same information for the exciton/charges component (CX). (h) and (j) Evolution of the energy position and FWHM of the spectral components with the excitation power at the position of the ring and at its center. (i) Evolution of the energy difference ΔE between the two spectral components at the position of the ring (dashed black line) and at the center of the ring (solid black line) and between the exciton component on the ring and at its center (solid green line).

Fig. III.17 describes the evolution of the spectral characteristics of the ring with the excitation power. Similarly to the study of the direct photoluminescence (see figs. III.6 and III.7 from (a) to (d)) we find again an increase of the ring radius with P_{ex} until a value above which no ring is observed. Figs. III.17(e) and (f) present the spectra on the ring and at the center of the ring for 3 different values of P_{ex}. Interestingly one can see that at low excitation power the exciton/charges line at lower energy is not fully separated from the dipolar exciton lines resulting in a seemingly asymmetric single line (red dashed line in (e)), thus resembling the lines observed by L. Butov et al., see fig. III.15(b). At the center of the ring (in (f)), the exciton/charges line is already well marked even at low excitation power. The integrated intensities of the two lines on the ring (dashed lines) closely follow each other showing that the weight of the two lines is the same, therefore there is no transfer of intensity from the exciton line to the exciton/charges line and the more pronounced distinction between the two lines only comes from an increased separation between their peak energies. The evolution of the respective energy of the 2 lines (see (h) and (i)) at the position of the ring illustrates well this effect : the energy difference (black dashed line in (i)) between the exciton and the exciton/charges lines rapidly increases until $P_{ex} \simeq 5\mu$W and then remains constant indicating a rapid energy separation of the two lines which then stabilizes. If we now have a look in detail at the energy of the lines (blue and red dashed lines in (h)) we see that at low excitation power the exciton line energy increases more rapidly than the exciton/charges line energy which would mean that the separation comes from a rapid increase of the exciton density (which shifts the exciton line towards the high energy). After this separation the energy difference between the 2 lines remains constant but at a different energy on the ring and at its center.

Interestingly, we see that at the same time, the 2 lines shift together towards the high energy which would sign a rise of the density. Nevertheless, looking at fig. III.17(g), we see that the integrated intensity of the lines decreases after reaching a maximum at $P_{ex} \simeq 10\mu$W which is contradictory with an increase of the density. Similar observations can be made at the center of the ring where the spectra always present a clear exciton/charges line which is consistent with a larger population of free charges (holes) in the vicinity of the excitation spot. The increase of the integrated intensity of the exciton/charges line (blue solid line in (g)) is not sufficient to explain its strong blueshift : indeed the exciton line experiences the same blueshift while its integrated intensity remains essentially constant. The increase of the integrated intensity of the exciton/charges line can be partially explained by its strong broadening (blue solid line in (j)) which we attribute to a stronger interaction between the excitons and the charges as the population of holes increases. These results show that when the excitation power increases the density of charges at the position of the ring rapidly saturates while it keeps increasing inside the ring. The density profile of charges (holes) thus presents the same variation along the radius of the ring as the energy of the photoluminescence with a density density which is maximum at the center of the ring, then slowly decreases as we move towards the ring and is finally minimal at the position of the ring. This interpretation is consistent with the usual model describing the formation of the ring in terms of ambipolar diffusion of charges where a large population of holes is present near the center of the ring and where the position of the ring is marked by an almost neutral exciton gas.

Finally the energy difference between the exciton lines on the ring and at its center (green solid line in (i)) reveals an blueshift which is more pronounced at the center of the ring than on the ring (thus giving rise to the dome-shaped energy profile along the ring radius displayed in fig.III.16(c)) which can not be explained by a difference of density. Indeed such values of blueshift would theoretically indicate density of excitons extremely large (essentially in the range where we would expect the appearance of electron-hole plasma, i.e. a Mott transition [129]) which is contradictory with the narrow spectral linewidths measured (see (j)). These results support our interpretation of the presence of an anti-trap potential inside of the ring which would account for the additional blueshift. Our explanation for the formation of this potential as a product of the screening of the electric field by the holes is also confirmed by the above results on the energy variations of the photoluminescence.

III.C.1.b Applied voltage

Fig. III.18 describes the evolution of the spectral characteristics of the ring with the applied voltage V_g. The evolution of the integrated intensity displayed in (g) shows that on the ring both exciton/charges and exciton lines reach a maximum for $V_g \sim -5.9$V and that at this V_g the ratio between the 2 components is also minimum with a dominating excitons line. This indicates that around this value of the applied voltage we maximize both the ring photoluminescence and the charge neutrality at the ring position, which confirm the range for the value of V_g used for the experiments. Interestingly the peak energy for both spectral components at both positions presents a linear evolution with the applied voltage. This behavior is typical of dipolar excitons in biased quantum well. Indeed, as seen in the first chapter, due to the tilting of the energy bands by the electric field created by V_g electrons and holes are being pushed apart to the opposite sides of the quantum well. Excitons will therefore exhibit an electric dipole oriented perpendicularly to the quantum well plane with a dipole length d corresponding to the distance along the z-axis between the electron and the hole. The interaction between the internal electric field $\mathbf{E}$ and the exciton dipole $\mathbf{d}$ thus reads : $E_X = -\mathbf{d} \cdot \mathbf{E} = -ed.E_z$

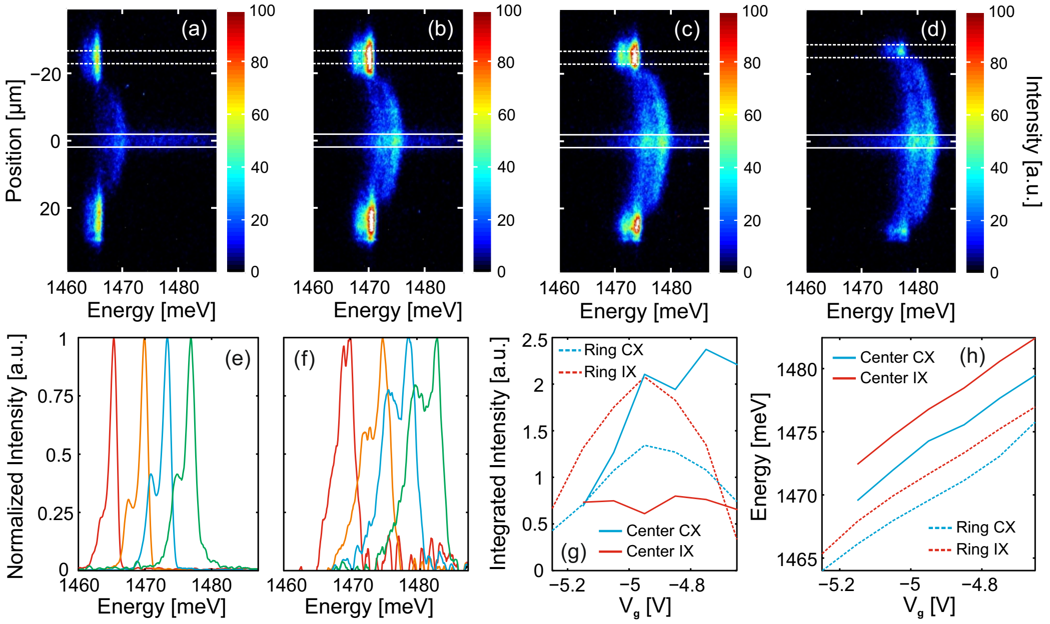

FIGURE III.18: (a-d) Spatially resolved spectra taken with the spectrometer slit aligned with the center of the ring, from left to right $V_g = -5.25$, -5.05, -4.85 and -4.65 V. (e) (resp. (f)) normalized intensity profiles at the position of the ring (resp. at the center of the ring) for the spectra in (a-d) (same ordering left to right), the vertical averaging is delimited by solid (resp. dashed) white lines in (a-d). (g-h) Evolution of the integrated intensity and peak energy of the spectral components with the applied voltage at the position of the ring (dashed lines) and at the center of the ring (solid lines), the exciton and exciton/charges components are respectively represented in red and blue. The lower boundary in V_g for the lines for the center of the ring is -5.15, indeed for lower value of V_g the spectra become structureless and noisy which prevents satisfying fitting. Linear regressions of the lines in (h) give electric dipole lengths in the same range : $d = 18.1 \pm 1.1$ nm.

with E_z the component of the electric field along the z-axis which directly relates to V_g through $E_z = V_g/l$, $l = 1\mu$m being the thickness of the sample. We thus obtain that the energy of the exciton gas decreases with the increase of the absolute value of the applied voltage (let us recall that dipolar excitons always align alongside the internal electric field such that the interaction is negative, see fig. II.2) and the peak energy of the photoluminescence experiences a redshift. Using the above formula, the measurements in fig. III.18(h) allow us to retrieve the value of the exciton dipole length d by simply applying a linear regression. We found that for all spectral components and positions on the ring, d is in the range of 18.1 ± 1.1 nm, i.e. the expected order of magnitude for a 25nm-wide quantum well.

This result has two important significations : first we are now certain that the photoluminescence we observe comes from dipolar excitons and that dipolar excitons accounts for all the signal all along the ring and its interior. Secondly we see that the exciton/charges compound exhibits the same electric dipole that the excitons which is in agreement with an interacting exciton/charges compound. Let us note that since varying the gate voltage affects the ring and therefore the charges distribution, we can not exclude that scanning V_g also affects the internal value of the electric field. This would disrupt the previous measurements of the exciton dipole where we assume a direct and linear relation between the gate voltage and the electric field. However since we observe a linear dependance of the peak energy with V_g both on the ring and inside it although the charges distribution is very different we can conclude that if there are some additional effects of the gate voltage on the internal electric field, these are probably not dominant.

III.C.1.c Bath temperature

Fig. III.19 presents direct images of the photoluminescence ring with the corresponding spatially resolved spectra for various bath temperatures. In order to increase the statistics and to measure accurately the spectral profiles (in particular for the high bath temperature for which the spectrum is low in signal and structureless) we recorded spectral images at two different positions on the ring by aligning the spectrometer slit successively at the center of the ring (spectral images #.2) and at the position of the ring (spectral images #.1). The spectral profiles recorded by averaging along the vertical position (dashed and solid white lines on the spectral images) are presented in fig. III.19(e-h) and the evolution of their characteristics with the bath temperature is shown in fig. III.20 along with the variation of the ring radius.

In fig. III.20(b) we see that both spectral components at both positions present redshifts between 1 and 1.5 meV when increasing T_b which would indicate, if the potential is constant, a loss of exciton density corresponding to a density at the lowest temperature of $\sim 1-2.10^{10}\text{cm}^{-2}$ (see calibration curves in fig. I.5). However as we have seen previously the energy shift of the spectral lines is probably highly dependent on the charges distribution and density (especially in the quantum well and at the Schottky interfaces, one also has to mention the modification of the bandgap of the QW with the temperature as shown in the section II.A) which blur the measurement. Therefore this redshift can only give a very rough estimation of the exciton density which needs to be confirmed by other methods.

Interestingly, we observe in fig. III.20(a) and (c) that the spectral width and the integrated intensity for both spectral components at both positions experience dramatic changes for $T_b \gtrsim 2\text{K}$ which corresponds to the temperature for which the ring radius starts to increase (green line). This would indicate that the system changes regime and constitute another example of characteristics of the ring presenting dramatic changes for $T_b \gtrsim 2\text{K}$, as already observed during the direct analysis of the photoluminescence. The

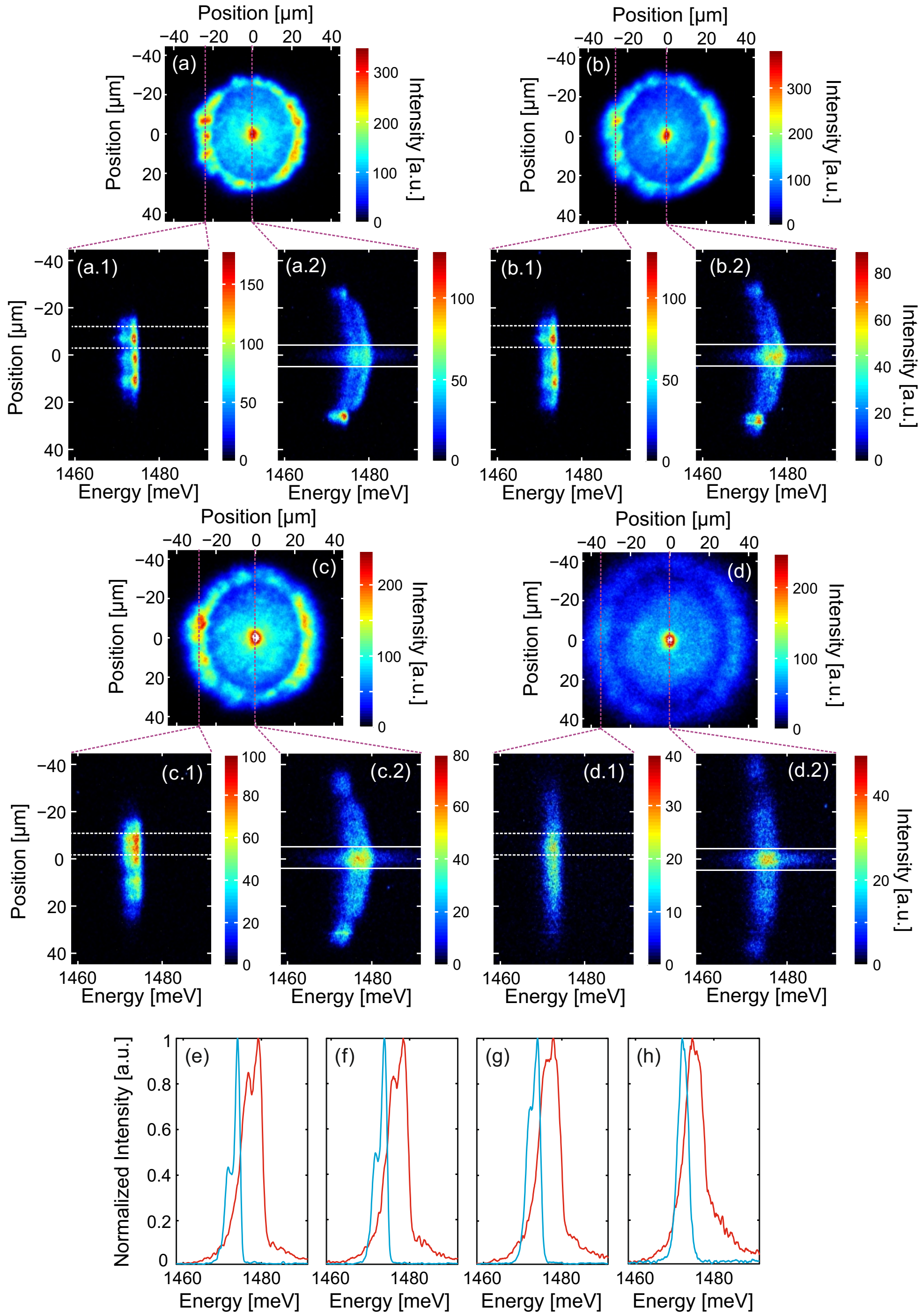

Figure III.19: (a-d) Direct images of the ring photoluminescence for various bah temperatures. From (a) to (d), T_b = 0.34, 2.2, 3 and 7K. At each temperature, two spatially resolved spectra were recorded with the spectrometer slit centered at the position of the ring (#.1) and at the center of the ring (#.2). (e-h) Spectral profiles for the above mentioned bath temperatures (i.e. from (e) to (h), T_b = 0.34, 2.2, 3 and 7K) at the position of the ring (blue line, spatial averaging marked by the white dashed lines in the (#.1) spectral images) and at the center of the ring (red line, spatial averaging marked by the white solid lines in the (#.2) spectral images).

increase of the spectral width with the bath temperature is quite common in excitonic systems and usually signs a homogeneous broadening due to increased elastic collisions

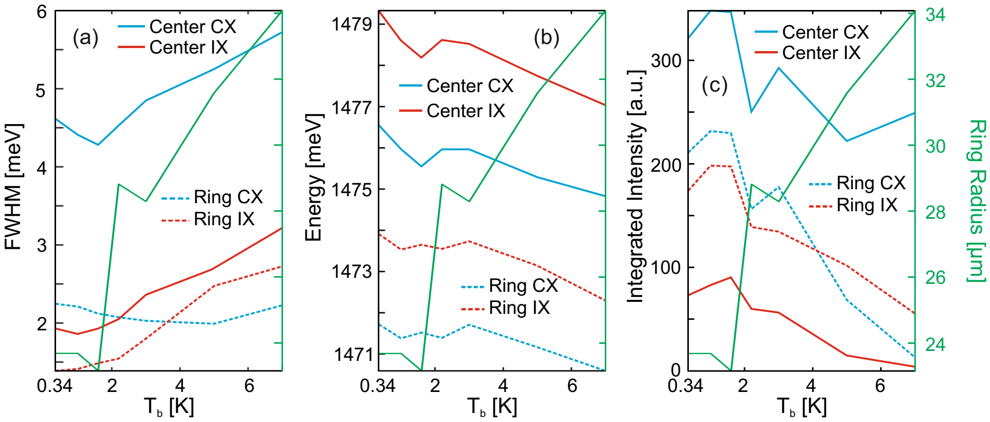

Figure III.20: (a-c) Evolution of the spectral width, peak energy and integrated intensity with the bath temperature at the position of the ring (dashed lines) and at the center of the ring (solid lines), the exciton and exciton/charges components are respectively represented in red and blue. The solid green line in each figure shows the evolution of the ring radius for the same variation of T$_b$.

with the phonon bath, between excitons and between excitons and the free charges in the quantum well [78, 88, 90–92]. The strong drop of the integrated intensities when the bath temperature increases confirms the loss of signal which has been previously seen on the measurements of the direct photoluminescence (see fig.III.12). Thanks to the variation of the spectral width we know that this drop is related to a strong diminution of the optically active population of excitons (indeed the broadening of the lines we observe should yield on the contrary an increase of the integrated intensity). This would indicate an increase of the non-radiative processes allowing excitons to recombine without emitting a photon. Another (non-exclusive) interpretation is that due an increase of the activation energy with the bath temperature, less charges can be captured and stay trapped in the QW thus reducing the maximum population of excitons in the QW.

III.C.2 Spectrally resolved dynamics

Fig. III.21 presents spatially resolved spectra of the photoluminescence during and after the laser pulse. The spectral images were taken with the spectrometer slit aligned with the center of the ring. Due to the very strong emission from the GaAs bulk at the position of the laser spot it is not possible to study the spectral profiles at the center of the ring during the laser pulse. This can only be done after the laser pulse but the spectral profiles remain nevertheless noisy, which only allows one a rough measurement of the peak energy of the exciton line. Additionally, the spectra on the ring can only be obtained after a delay of ∼ 200ns which is limited by the formation time of the ring. As a general remark we would like to stress for these measurements the length of the recording window had to be shortened in order to obtain a good time resolution.

This combined to the inherent loss of signal due to the use of a spectrometer cause the intensity reaching the recording camera to be fairly low. Unfortunately the limited time allowed at the lowest bath temperature prevented us to compensate this loss of signal with an increased exposure time. This explains why the statistics of the data is not optimum.

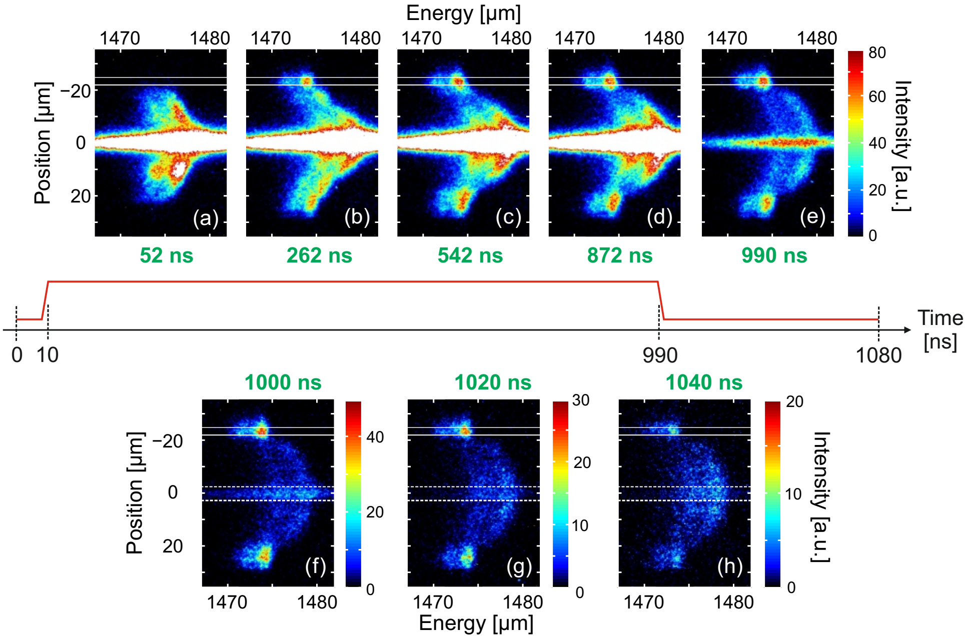

FIGURE III.21: (a-h) Spatially resolved spectra with the spectrometer slit aligned with the center of the ring taken at various delays during and after the laser pulse. The images were recorded with a time window of 10ns for a pulse length of 1μs (rep. rate 2μs) and with $P_{ex} = 11.6\mu$W, $V_g = -4.85$V and $T_b = 0.34$K. The solid (resp. dashed) white lines in (a-h) (resp. f-h) mark the limits for the spatial averaging to retrieve the spectral profiles at the position of the ring (resp. at the center of the ring). The white saturation in most of the images comes from the very high photoluminescence signal from the bulk emission at the position of the excitation spot during the laser pulse. This signal effectively blurs the spectrum at the center of the ring during the excitation pulse.

From the measurement of the dynamics of the integrated intensities presented in figs. III.22(d) and (e) we see that both exciton/charges and exciton lines increase steadily until reaching a stationary value at a delay which corresponds to the establishment of a quasi-steady-state for the ring. After the laser pulse the decay time for both spectral components is essentially the same and is similar to the one obtained for the dynamics of the direct images of the ring (see figs III.14(b) and (c)). Interestingly while the ratio between the exciton and exciton/charges integrated intensities increases during the formation of the ring (first 600ns in (d)) thus signing a preponderance of the exciton line, we see that this ratio invert ∼ 40ns after the end of the laser pulse probably indicating an increase of the electrons in the quantum well. This is not surprising since while these charges were compensated by the flux of holes during the laser pulse, this compensation disappears after the pulse allowing the electrons to diffuse towards the ring. In figs. III.22(b) and (c) we can observe that both peak energies and spectral widths remain constant during the excitation pulse but experience rapid changes after the pulse. Indeed while the spectral width of the exciton line sharpens of about 0.5meV, the spectral width of the exciton/charges line broadens by about 1meV.

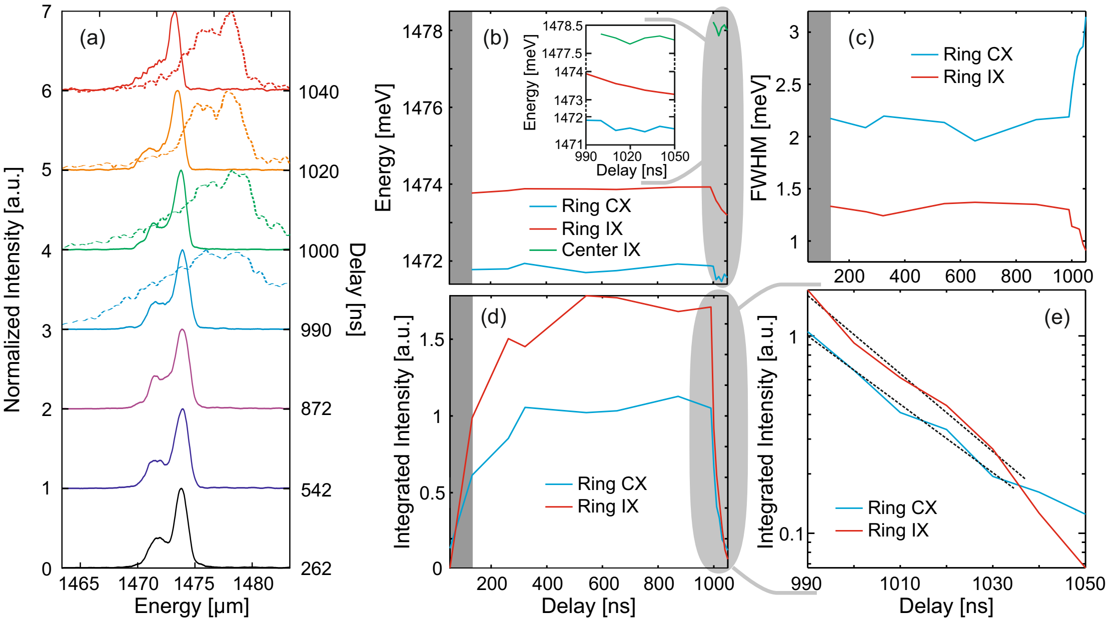

FIGURE III.22: (a) Spectral profiles for the spectral images displayed in fig. III.21 at the position of the ring (solid lines) and at the center of the ring (dashed lines). The spectral profiles have been normalized to 1 and shifted vertically for clarity. (b-d) Peak energy, spectral width and integrated intensity of the spectral components during and after the laser pulse at the position of the ring, the exciton and exciton/charges lines are respectively marked in red and blue. The dark gray region in (b-d) corresponds to the delays where the ring is not yet fully formed and therefore no accurate measurements on the spectra can be made (for a detailed dynamics of the ring formation refer to fig. III.13). (b) additionally displays the peak energy of the exciton line at the center of the ring after the pulse. The inset shows a focus on the peak energy variations after the excitation pulse. (e) Focus on the evolution of the integrated intensities after the laser pulse. Linear regressions for delays between 990 and 1030 ns give decay times of $\sim$ 19ns for the exciton/charges line and $\sim$ 18ns for the exciton line.

The evolution of the peak energy is of particular interest since it allows us to estimate the exciton density. Indeed, as seen in the first chapter, the energy shift of an exciton line directly relates to the exciton density due to the dipolar repulsion between the excitons (if we neglect other effects like the modification of the internal electric field or the presence of free charges). However, to measure the exciton density one needs a reference value for the peak energy when the exciton gas is sufficiently dilute to neglect the dipolar interactions. This can be solved if we consider the photoluminescence of the ring a long time after the laser pulse. At some delay time the intensity from excitons is so weak that we can estimate that we have reached the dilute gas regime, at which point the value of the peak energy can serve as a reference and a blueshift of the line indicates an increase of density. If we apply this technique to our measurement we see that starting from the lowest energy at the delay 1050ns the exciton line experiences a blueshift of about 800μeV when going backwards towards the end of the laser pulse (red line in fig. III.22(b)). This would indicate an exciton density of $\sim 1.3 \times 10^{10}\text{cm}^{-2}$ according to the calibration presented in fig.I.5.

This value for the density has to be considered carefully, indeed due to the very weak signal far from the pulse we are probably not able to measure the value of the lowest peak energy leading to an underestimation of the density. This limitation is particularly true if we consider the presence of dark excitons which have a longer lifetime and can contribute to the dipolar interaction during a time longer than we can estimate by only looking at the photoluminescence. Finally a time-dependent potential landscape for excitons after the pulse can lead to both an over or an underestimation of the exciton density by altering the reference energy. This effect can be estimated to some extent by observing that the peak energy of both the exciton/charges line on the ring and the exciton line at the center ring (resp. blue and green line in fig. III.22(b)) stays essentially constant after the pulse. This would indicate that the charges density remains the same for a few tens of ns (at least $\sim$ 40ns if we consider the evolution of the integrated intensities on the ring) and thus does not fundamentally affect the exciton potential energy. In the following chapter (see in particular the section IV.A.4) we will measure precisely the density and potential distribution.

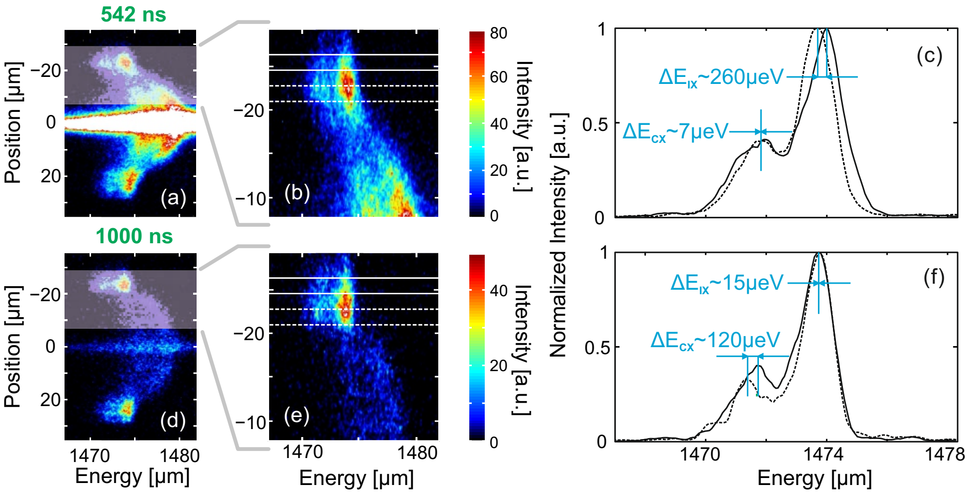

FIGURE III.23: (a) and (d) Spatially resolved spectra at 2 different delays : 542ns (during laser pulse) and 1000ns (10ns after laser pulse). (b) and (e) Focus of the white transparent region of (a) and (d). (c) (resp. (f)) Spectral profiles taken by averaging along the vertical axis on the focus (b) (resp. (e)) : the dashed (resp. solid) black line comes from the area delimited by the white dashed (resp. solid) lines in (b) and (e). ΔE_{IX} and ΔE_{CX} are the peak energy differences between respectively the exciton lines and the exciton/charges lines of the dashed and solid black spectral profiles. The energy differences were obtained by fitting the lines with a combination of Lorentzian and Gaussian functions, however our spectral resolution to measure peak energies is limited to $\sim$ 50μeV therefore the retrieved energy differences are not necessarily significant.

To conclude on the dynamics of the spectral components of the ring let us examine fig. III.23 which shows an additional difference between the situation during the laser pulse and after it, this time concerning the density of excitons and free charges at the position of ring. First of all let us consider the distribution of the energy of the photoluminescence during and after the pulse. During the pulse we see that the energy profile for the exciton line at the position of the ring presents a redshift when moving outwards the ring (see figs. III.23(b) and (c)). This redshift can be quantified and we find a energy shift of $\Delta E_{\mathrm{IX}} \sim 260\mu\mathrm{eV}$ between the inner part of the ring and its outer part (i.e. the regions delimited respectively by the dashed and solid white horizontal lines in figs. III.23(b) and (e)). Similar measurements for the exciton line after the pulse reveals no such redshift. Indeed in figs. III.23(e) and (f), one can see that the fits of the spectral lines give an energy shift of $\Delta E_{\mathrm{IX}} \sim 15\mu\mathrm{eV}$ which is not significant since the spectrometer we use only has a spectral accuracy of $\sim 50\mu\mathrm{eV}$ for the distinction of peak energies. If the potential for excitons is uniform and quasi-stationary in this region, these results reveal that during the pulse the density of excitons on the ring is slowly decreasing when moving outwards the ring while it is uniform after the pulse. This difference could be attributed to a constant input of excitons at the position of the ring during the pulse, while after the pulse excitons diffuse and their density distribution homogenizes.

If we now perform the same analysis for the exciton/charges line we observe an opposite behavior for the variations of the peak energies. Indeed, while the value of the peak energy of this line is uniform during the pulse ($\Delta E_{\mathrm{CX}} \sim 7\mu\mathrm{eV}$ which is negligible), we observe that after the excitation pulse, the exciton/charges line slightly shifts towards the high energy when moving outwards the ring. This blueshift is limited ($\Delta E_{\mathrm{CX}} \sim 120\mu\mathrm{eV}$) but significant. In the section dedicated to the evolution of the spectral characteristics with the excitation power (see section III.C.1.a), we have seen that changes of the peak energy of the exciton/charges line indicate a variation of the density of free charges. Thus the results presented here reveal that after the pulse the population of free charges increase when moving outwards the ring. This observation is confirmed by the spectral measurements on the fragmented line (see appendix B).

III.C.3 Energy of the photoluminescence along the radius of the ring

In the introduction to the spectroscopic measurements (see fig. III.16(c)) we have seen that the energy profile of the photoluminescence presents surprising variations with a dome-shaped towards the high energy inside the ring and an essentially constant energy at the position of the ring and outside it. As already mentioned we attribute the dome-shaped profile to the presence of a potential for the excitons and we will confirm this interpretation in the next chapter. The variation of the energy around the position of the ring is very significant. Indeed, as previously discussed, if the potential for the excitons is constant in this region, the fact that the energy is constant while the intensity drops indicates the presence of a dense gas of dark excitons. These observations were done on an energy profile which was retrieved from a single spatially resolved spectrum at the center of the ring. This effectively limits the accuracy of the measurement particularly outside the ring where the intensity is very low.

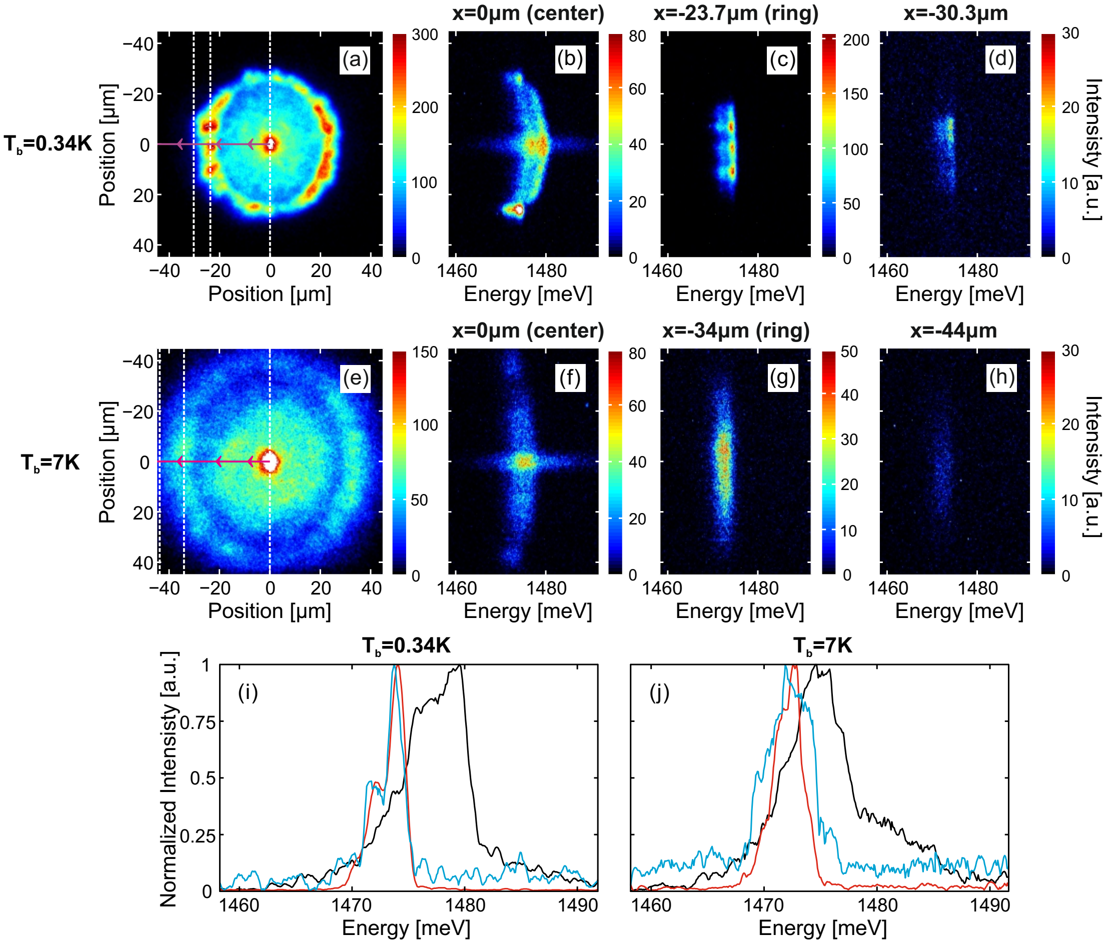

FIGURE III.24: (a) Direct image of the photoluminescence of the ring at $T_b = 340$mK. (b-d) Spatially resolved spectra respectively taken with the entrance slit of the spectrometer aligned at the center of the ring (b), at the position of the ring (c) and $\sim 6\mu$m away from it. The positions are indicated by the white vertical dashed lines in (a). (e-h) Same as (a-d) for a bath temperature of 7K. Since at this temperature the radius of the ring is larger than for $T_b = 340$mK, the positions on the ring where the spectral images are taken have been moved accordingly. The data were recorded with a 40ns window 10ns after the end of the excitation pulse with $P_{ex} = 11.6\mu$W and $V_g = -4.85$V (like in the previous experiments). (i-j) Normalized spectral profiles at the origin of the vertical axis (same ordinate than the center of the ring). The spectra in (i) (resp. (j)) correspond to the spectral images (b-d) (resp. (f-h)) with the black line being the spectrum at the center of the ring, the red line the spectrum at the position of the ring and the blue line the spectrum outside the ring.

In order to refine our observations, we measured spatially resolved spectra with the entrance slit of the spectrometer aligned at various positions along a horizontal radius of the ring (see purple arrowed lines in figs. III.24(a) and (e)). This allowed us to adapt the exposure time of our camera to the photoluminescence intensity in order to obtain enough statistics, which is particularly critical outside the ring. Figs. III.24(a-h) present direct images of the photoluminescence together with spatially resolved spectra taken at various distances to the center of the ring for two bath temperature. From these spectral images we extracted spectral profiles averaged over a small region around the ordinate corresponding to the center of the ring. These profiles are shown in figs. III.24(i-j). At the lowest bath temperature we observe the now familiar (see e.g. figs III.17 and III.19) energy shift between the spectrum at the center of the ring and the spectra around the position of the ring due to the dome-shaped potential inside the ring. The most striking result is that the spectra at the position of the ring and $\sim 6\mu$m outside of it (resp. red and blue profiles in fig. III.24(i)) are remarkably similar and in particular the energies of the peaks are essentially the same. Normally this would indicate that the exciton gas is the same in a large region surrounding the ring, however the intensity of the photoluminescence is more than 10 times smaller $\sim 6\mu$m outside of the ring than at the position of the ring (the spectra are normalized for an easier comparison but the measurements presented in the next paragraph confirm the drop of intensity). Such a loss of intensity would be in principle attributed to a strong decrease of the density of excitons which would affect both the value of the peak energy and the linewidth of the lines (indeed an increase of density is usually associated with a homogeneous broadening of the spectral line [88, 91, 92]). The situation changes for $T_b = 7$K where the spectra on the ring and outside of it (resp. red and blue profiles in fig. III.24(j)) are very different.

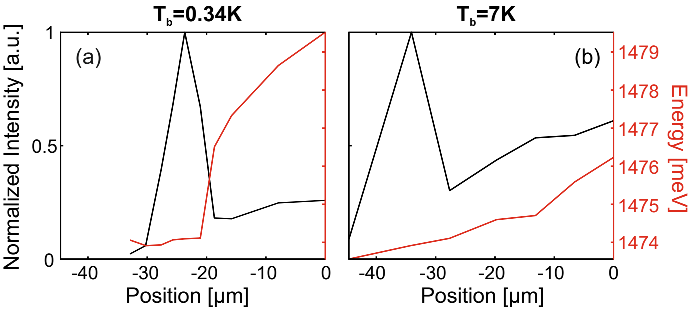

FIGURE III.25: (a) Evolution of the intensity (black) and peak energy (red) of the exciton line along the radius of the ring. The intensity profile is normalized with respect to its highest value which corresponds to the position of the ring. The 0 of the abscissa marks the center of the ring and the graduation the distance away from it (along the left radius of the ring as shown by the arrowed purple lines in figs. III.24(a) and (e)). (b) Same as (a) for a bath temperature of 7K.

By recording such spectra at various distances from the center of the ring along its left radius (see purple arrowed lines in figs III.24(a) and (e)) we were able to obtain the precise evolution of the peak energy and intensity of the exciton line. These variations are presented in fig. III.25. The intensity profiles are normalized with respect to their maximum values which correspond to the position of the ring. The results at the lowest bath temperature confirm the observations done in fig. III.16(c) and reminded in the beginning of this section. Indeed we see that the peak energy of the exciton line is essentially constant up to $\sim 10\mu$m outside the ring while at the same time the peak intensity is divided about ten-fold. We also find again the dome-shaped profile of the energy inside the ring. Interestingly, the situation for $T_b = 7$K is completely different with the energy profile presenting a smooth decrease all along the radius of the ring. This observation would indicate that both the potential and the density profiles along the radius of the ring are highly dependent on the bath temperature. The measurements of the next chapter confirm this interpretation and in particular we found that at high bath temperature the dense gas of dark excitons is not present anymore.

The procedure used in this section is the most direct but is limited since we still have problems of statistics which prevent us to perform a complete analysis of the spectral characteristics along the radius of the ring (we could only retrieve accurately the peak energy and intensity of the exciton line). As seen throughout this section dedicated to the spectroscopy, in order to increase the statistics and the accuracy of the analysis of a spectrum profile, we have to average the spatially resolved spectrum along the vertical axis over a given area (this is particularly important when the signal is low and/or noisy which is the case for the photoluminescence outside the ring). This of course supposes that the averaging is done over a region with homogeneous spectral characteristics. However in the case of a photoluminescence with circular symmetry, the vertical cut by the entrance slit of the spectrometer induces that the resulting spatially resolved spectrum will include spectral information of photoluminescence coming from different distances to the center of the ring, which can lower the accuracy of the averaging. This is particularly the case when we are interested on spectral characteristics along the radius of the ring where we can only average the spectral images over a very small region.

A possible approach to overcome this problem is to change the geometry of the system by creating vertical fragmented lines. Indeed in this case the averaging can be done over a much larger region since all points are at equal distance from the excitation spot. The properties of these fragmented lines are reviewed in the section VI.B.1 and in the appendix B but let us stress here that they are very similar to these of the fragmented ring. In particular, the spectral characteristics along the “radius” of the fragmented line (i.e. along the direction perpendicular to the one of the linear-shaped excitation beam) show that the energy of the photoluminescence presents a dome-shaped profile inside the fragmented lines similar to the one of the fragmented ring. Moreover we also measure a constant energy at the position of the fragmented line and outside of it. This geometry being more convenient, we were able to retrieve detailed information on the spectral characteristics, as presented in appendix II.C. In particular we obtain that the region of constant energy (and constant exciton density if the potential is uniform) is also a region where the density of charges is minimal. If we consider that the fragmented lines and ring display the same physics then we can imagine that this region of minimum density of charges also exists in the case of a fragmented ring. In the next chapter we will confirm these results by using a different technique based on a pump-probe laser sequence to probe the energy of the photoluminescence and the potential for excitons. The main advantage of this method is that it gives information in regions where the photoluminescence intensity is normally too low to perform an accurate direct spectroscopy. It will in particular allow us to measure precisely the potential for excitons and to ascertain the presence of a dense gas of dark excitons in the outside vicinity of the ring.

To complete these considerations on the spectral characteristics of the photoluminescence outside the ring we performed time-interferometric measurements. As explained in section II.B.2.a, this method can provide information on the weight ratio between the exciton/charge and exciton lines as well as on their linewidths (but not on their peak energy). The results obtained with this method are detailed in appendix A. Our main finding is that the exciton line is the narrowest at the position of the ring, but that we can also find regions of narrow linewidth outside the ring. We therefore confirm with an alternative experimental technique the main characteristics obtained by direct spectroscopy.

III.D Conclusion

In this chapter we have studied the basic characteristics of our fragmented ring. We have seen in particular that while some of these characteristics are consistent with previous experiments, our observations lead us to conclude that the photo-excitation yields a potential for the excitons, and that a dense gas of dark excitons coexists with a weak gas of bright excitons in the outside vicinity of the ring. The latter observation is of particular importance. Indeed as explained in the first chapter, the bright and dark excitonic states are separated by a small energy splitting, with the dark states laying at lower energy. Thus, in a classic situation, the thermal activation energy is sufficient to allow a 50/50% population ratio between the bright and dark excitons, yielding a thermal exciton gas. However in the case of a Bose-Einstein condensate, the condensation must occur in the dark states at lower energy, yielding a higher population of dark excitons. Therefore, demonstrating the existence of a larger population of dark excitons is a direct evidence for a Bose stimulation towards the dark states and that the exciton gas has entered a quantum regime.

As mentioned in this chapter the direct spectroscopy of the photoluminescence is not sufficient to ascertain the presence of a dense gas of dark excitons. Indeed, this approach can not differentiate between the two main contributions to the energy of the photoluminescence, namely the amplitude of the dipolar interaction between excitons (which signs their density) and the interaction of dipolar excitons with the internal electric field. In the previous sections we have seen that a signature of a large population of dark excitons is a strong decrease of the intensity of the photoluminescence in a region of uniform density of exciton. Therefore being able to separate the two contributions to the energy of the photoluminescence is of the utmost importance in order to prove that we have indeed an uniform density of excitons. In order to obtain this information we performed the pump-probe experiments described in the following chapter.

Chapter IV

Spectral signature of a "gray" condensate of excitons

The previous chapter has shown that various physical properties of the ring can not be explained solely by the model based on the ambipolar diffusion of charges. In particular spectral anomalies have led us to conclude that the photo-excitation used to create the fragmented ring also controls the electrostatic confinement for excitons through the injection of an excess of free charges. As explained in the first chapter, the energy of the photoluminescence E_X is mainly the result of the interaction between the excitons and the electric field inside the sample which reads $V_X = -\mathbf{d} \cdot \mathbf{E}$, and the dipolar repulsion between excitons U_X, which is related to the density of exciton. Unfortunately these 2 contributions are indiscernible in experiments relying on direct spectroscopy such as these performed in the previous chapter. Thus it is required to quantify the potential landscape in order to evaluate the density of excitons. In order to separate the two contributions we used a pump-probe experiment with 2 excitation pulses at 2 different wavelengths. This method rests upon the injection of a uniform and very low density of dipolar excitons by a wide probe beam. The wavelength of the probe beam is set such that it only creates excitons and does not affect the potential (in particular the probe beam only injects a very limited amount of free charges and it can not create a fragmented ring). These excitons will therefore only interact with the potential and the value of the energy of their photoluminescence indicates the value of the potential at-a-glance over large areas. The technical details of the pump-probe experiment are presented in the next section.

Thanks to this technique we were able to obtain crucial information which allowed us to complete our picture of the physics of the fragmented ring. First of all we prove the existence of an electrostatic potential confining the excitons. We demonstrate that the emergence of this potential comes from the injection of free charges inherent to the formation of the ring (see section IV.A.2). These charges can be found at various positions in the sample and their presence modulates the internal electric field created by the applied voltage V_g. At the lowest bath temperature the decay time of the potential induced by the excess of charges is very long, in fact the potential is quasi-stationary over a time larger than our repetition rate (2μs, see section IV.A.3). The profile of the potential in the case of the fragmented ring is particularly interesting and is presented in the section IV.A.4. While the dome-shaped variation inside the ring does not come as a surprise considering the energy profiles of the photoluminescence, we also observe the presence of a confinement potential which extends from the inner edge of the ring towards up to $\sim 5-10\mu$m outside the ring. The measurement of the potential then allows us to measure accurately the density of excitons at the position of the ring and outside of it and our findings confirm the presence of a dense gas of dark excitons outside the ring. We would like to stress that this confinement is not systematically present outside the ring which indicates that the potential landscape in the vicinity of the ring is probably very irregular.

To ascertain this last observation we modified the pulse sequence such that the probe beam now injects dipolar excitons only at the center of the potential created by the fragmented ring (see section IV.B). As explained in the previous paragraph, the probe beam can not create fragmented ring on its own. However when the potential associated with the fragmented ring is present, we observe that the diffusion of excitons on this potential yields a photoluminescence pattern very similar to the one of fragmented ring. This is a strong indication that the fragmentation is partially caused by the modulation of the potential along the circumference of the ring.

IV.A Pump-probe measurements

Pump-probe techniques have been shown as a powerful toolbox to reveal complex dynamics such as the formation of the fragmented ring. These techniques are very common for quantum optics measurements with cold atoms or trapped ions and its use on solid-state systems cover a large domain from spintronics to the study of Faraday rotation. This method has however rarely been used to measure the potential and density profiles in a system of dipolar excitons [62, 72]. It relies on an excitation pulse which creates the phenomenon which we want to study, and in a second time on an additional pulse to record the state of the system. In our case we want to measure the potential landscape $V_X = -\mathbf{d} \cdot \mathbf{E}$ arising from the interaction between the electric dipole of excitons and the electric field inside the sample. This electric field is the result of various influences : the overall gate voltage V_g, the charges at the metal-i and $i-n$ interfaces, the presence of charges in the QW or in the superlattices due to the formation mechanism of the ring and to electrostatic impurities from the sample growth. From this list one can realize that characterizing precisely the effect of each of these contributions is probably impossible. This imposes necessary simplifications in order to interpret the formation of the potential.

An important requirement for the pump-probe experiment is that the probe pulse does not affect the excitonic system but solely allows a qualitative reading of the electric field in the QW plane. This implies that the probe pulse must not disturb the ring formation and the exciton potential and thus mainly creates excitons and only a very small number of charges (if none at all). These excitons will interact with the electric field and allow a direct reading of V_X. We want to know the potential for excitons in the QW, therefore it would be preferable that the probe pulse only creates excitons in the QW. In order to meet the previous requirements we used a probe pulse at a wavelength of 790nm which corresponds to an energy only larger than the bandgaps of the GaAs QW and the GaAs bulk. We also want the density of excitons injected to be very small in order to avoid an energy blueshift due to the dipolar repulsion which would blur the reading of the potential and to prevent the diffusion of excitons which could accumulate locally and reach a too high density. A solution to overcome this issue is to excite simultaneously an area larger than the ring diameter, for example with a long linear-shaped vertical excitation beam (an essentially one-dimensional pattern is sufficient since we can only record spectra along the vertical slit of the spectrometer). Finally we want to measure the pure potential profile, thus the probe pulse must start at a delay after the pump which ensures that all excitons created by the pump excitation have recombined. Therefore reading the potential can only work if the potential has a lifetime which is significantly larger than the one of the photoluminescence of the ring (i.e. $\sim$ 20ns). We will see that a wide linear-shaped excitation beam at a wavelength of 790nm meets all these requirements.

The following section covers the characterization of the photoluminescence created by a vertical linear excitation at 790nm. Then we study the effect of a spatially large pump pulse at 641.5nm on the photoluminescence of the probe (see section IV.A.2). Our data show that the excitation at 641.5nm does create a potential for excitons through the injection of free charges. We find that charges are situated in the Schottky interfaces and in the QW where they screen the overall electric field produced by the gate voltage. In order to pace the way to measure the potential created along with the ring we measure the decay time of the potential (see section IV.A.3) and find it to exceed the length of the usual repetition rate (2μs) at the lowest bath temperature. Finally we measure the potential which arises along with the ring formation (see section IV.A.4). The results show the presence of a trapping potential at the position of the ring at the lowest bath temperature which disappears when the temperature increases. These measurements allow us to retrieve the profile of the exciton density and confirm the existence of a condensed gas of dark excitons in the exterior vicinity of the ring.

IV.A.1 Characterization of the probe pulse

To start the characterization, we study the behavior of the photoluminescence created by a weak linear-probe probe beam at 790nm with the gate voltage V_g, as shown in fig. IV.1. The direct image of the photoluminescence produced by the linear excitation beam at 790nm is displayed in fig. IV.2(b). As it is the case with the beam at 641.5nm (see section II.A) we observe the presence of a built-in voltage of ~ -1V for which the peak energy and the spectral width are minimum while the peak intensity is maximum (thick dots in figs. IV.1(e-f)). However the behavior of the spectrum when lowering the gate voltage differs dramatically. Indeed while the spectral line of the photoluminescence strongly broadened with the excitation at 641.5nm for $V_g < -1$V (see fig. II.4), illuminating at 790nm only leads to a moderate increase of the spectral width which even decreases for $V_g \lesssim -3$V. Moreover this temporary broadening can be related to the apparition of a now-familiar second spectral component at lower energy (see blue spectral profile in fig. IV.1(d)) which essentially disappears at lower gate voltages. In particular in the region where we usually form a ring (i.e. $-5 \leq V_g \leq -4$) the spectral line presents a single component (see red profile in fig. IV.1(d)), thus signing a very weak population of free charges. Finally a linear regression of the variation of the peak energy for $-5 \leq V_g \leq -3.5$V gives a dipole length of ~ 13.4nm which is very close to the value found during the characterization of the sample with the excitation at 641.5nm ($d \sim 12.2$nm see fig.II.4) and the dipole momentum of excitons in the ring ($d \sim 18.1$nm see fig.III.18, as explained in the section III.C.1 this value of the dipole momentum is to be considered with precautions due to the unknown effect of the gate voltage on the free charges which might alter the electric field). This means that the interaction with the electric field will be essentially the same whatever the wavelength we use to create excitons which is not surprising since the length of the dipole mainly depends on the size of the QW and on the interactions between the free carriers and the gate voltage.

From the previous measurements we know that for $-5 \leq V_g \leq -4$V, excitons created by the probe have an adequate dipole length and that the exciton/charges line is minimal. This last results is confirmed by the evolution of the spectra with the excitation power, as shown in fig. IV.2. Indeed, as presented in fig. IV.2(e), we see that the integrated intensity of the exciton line is superior than the one of the exciton/charges line for $P_{\mathrm{ex}}(790) \leq 0.5\mu$W. As stated in the introduction to this section, we want to

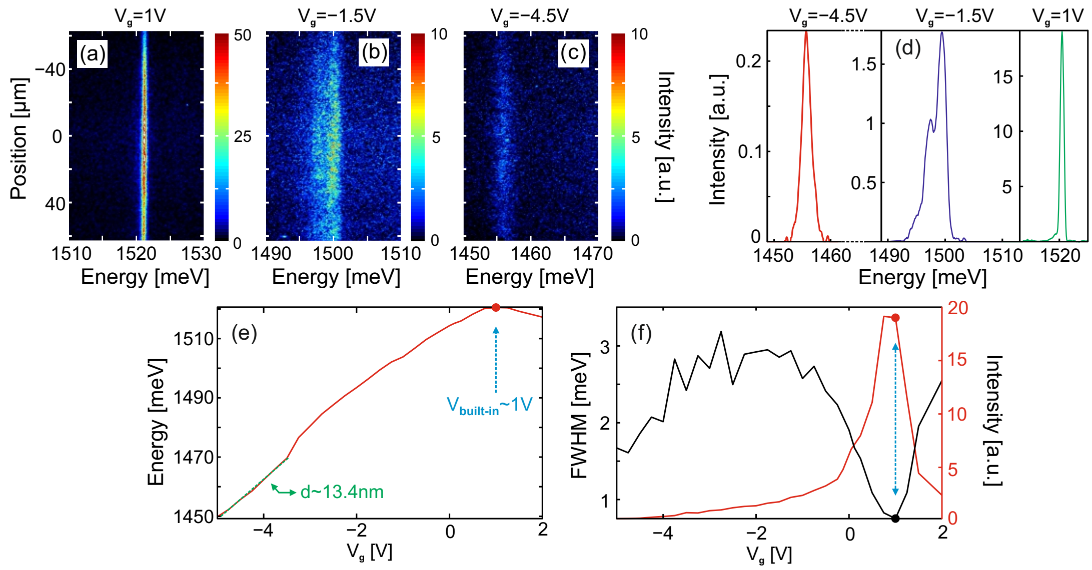

FIGURE IV.1: (a-c) Spatially resolved spectra at 3 different gate voltages. The entrance slit of the spectrometer is aligned at the center of the photoluminescence created by a vertical linear-shaped excitation beam at 790nm with excitation power $\sim 1.5\mu$W. The data were recorded with a window of 200ns matching the length of the laser pulse with a repetition rate of 500kHz, $T_b = 340$mK. (d) Spectral profiles of the spectral images (red profile ↔ (c), blue profile ↔ (b), green profile ↔ (a)). (e-f) Peak energy, peak intensity and spectral width of the spectral profiles for a set of V_g. The thick dots mark the characteristics for $V_g = -V_{\text{built-in}} \sim 1$V. The green line in (e) is a linear regression of the variation of the peak energy for $-5 \leq V_g \leq -3.5$V, giving a dipole length of ~ 13.4nm.

use a probe with a sufficiently low power such that there is essentially no blueshift coming from the dipole-dipole repulsion. According to fig. IV.2(f), this is the case for $P_{\text{ex}}(790) \leq 0.5\mu$W which means that below this excitation power the effect of the exciton density on the photoluminescence energy is negligible.

The purpose of the pump-probe experiment is to measure the potential confining the excitons. Practically, this is achieved by placing the vertical probe beam in the region of interest on the sample (in most cases the middle of the photoluminescence pattern created by the pump pulse). Then the probe photoluminescence is aligned with the entrance slit of the spectrometer thus obtaining a spatially resolved spectrum. The variation of the spectral characteristics along the vertical axis can then be retrieved by studying slices of the spectral images at various vertical positions (in our case slices are $\sim 1\mu$m wide). The results of such analysis for the spectral image in fig. IV.2(c) is presented in fig. IV.2(d). We see that along the vertical axis the integrated intensity can fluctuate up to 40% which means that despite our best effort the beam shape of the probe is not perfectly homogeneous vertically. At the same time the peak energy fluctuates of $\sim 500\mu$eV. Knowing the amplitude of the energy fluctuations is important since we want to be able to discriminate energy variations induced by the probe beam and fluctuations of the exciton confining potential. However for this data the fluctuations of

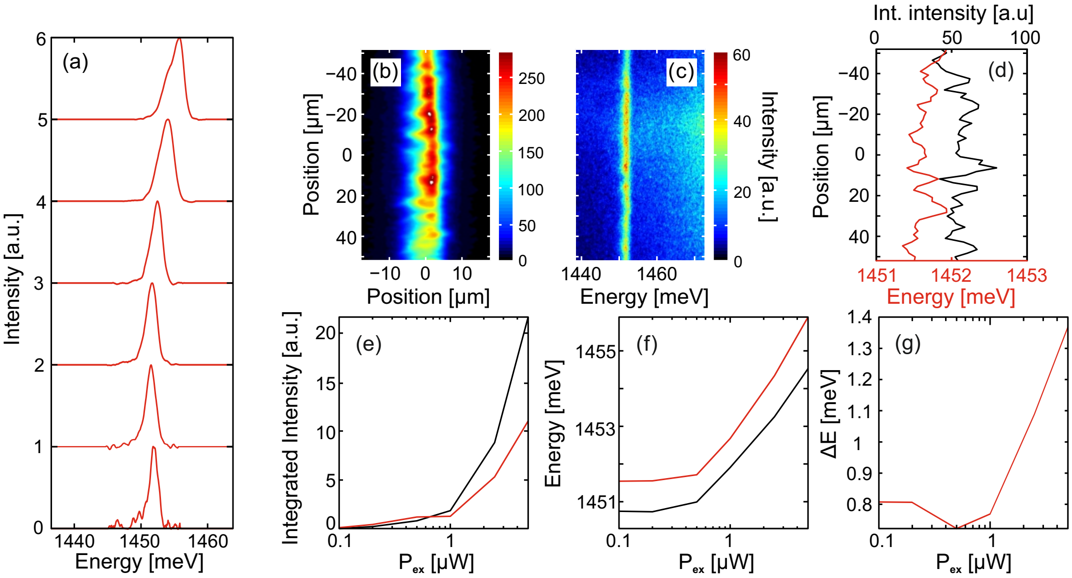

FIGURE IV.2: (a) Spectral profiles for $P_{\text{ex}}(790) = 0.1$, 0.2, 0.5, 1, 2.5 and 5μW (from bottom to top), $V_g = -4.95$V and $T_b = 0.34$K. Experimental conditions are the same as in fig. IV.1. (b) Direct image of the photoluminescence (c) Spatially resolved spectra for $V_g = -4.95$V and $P_{\text{ex}}(790) = 0.5\mu$W. (d) Variation of the peak energy (red) and integrated intensity of the photoluminescence (black) of (c) along the vertical axis. (e-f) Evolution of the integrated intensity and peak energy with the excitation power of the exciton (red) and exciton/charges (black) spectral components obtained from the spectral profiles in (a). (g) Evolution of the difference ΔE between the peak energies of the exciton and exciton/charges lines with the excitation power ($\Delta E = E(\text{IX}) - E(\text{CX})$).

the integrated intensity are not correlated with the ones of the peak energy which should be the case if the energy variations were the results of local density fluctuations. This means that the energy variations are likely to be the sign of the electrostatic disorder in the QW which modulates the overall electric field created by the gate voltage.

It is important to note that whatever the gate voltage or the excitation power is, we do not measure any current flowing through the sample (within our resolution of 0.01μA) and strikingly we are never able to form a ring with the excitation at 790nm (see section IV.B, this effect have also been observed by the group of D. Snoke [132]). These two features indicate that at this wavelength the effects of free charges are not dominant or at least that we can not enter the regime of charge separation. Finally, fig. IV.2(g) shows that the difference between the peak energy of the 2 spectral components depends on the excitation power. Similar observations have been done in the previous chapter (see for instance the sectionsIII.C.3 and III.C.1.a) and were attributed to a modification of the density of free charges. This proves that above a given excitation power ($P_{ex} > 1\mu$W) an excitation at 790nm also injects free charges in the sample, probably directly in the QW. However we can not neglect the possible injection of a very limited population of charges at lower excitation power. In the next section we will see that this is indeed the case. Nevertheless the absence of the energy shift for $P_{ex} \leq 1\mu$W proves that this population is too small to affect the potential landscape.

IV.A.2 Study of a simple situation

In the previous section we obtained the proper parameters for the probe pulse. Before using the pump-probe technique on the fragmented ring, we want to study a simpler situation which will allow us to determine the effect of the pump pulse on the sample more easily. To do so we excite the sample with a large circular pump beam at 641.5nm (diameter $\sim 80\mu$m). The probe beam is aligned at the center (horizontally and vertically) of the pump beam and has a vertical extension of $\sim 120\mu$m. In order to keep the pulse parameters identical to the ones used to create the ring we use a 1μs-long pump pulse with a 500kHz repetition rate. In order to isolate as much as possible the population of excitons created by the pump and the probe we set a delay of 200ns between the end of the pump pulse and the beginning of the probe pulse. According to the characteristic time of the decay of the photoluminescence measured for the ring (see sections III.B.2 and III.C.2), this delay is sufficient to ensure that all excitons from the pump have recombined before we create new excitons with the probe. We record the photoluminescence of the probe with a window matching the length of the probe pulse in order to maximize the statistics while keeping a very low excitation power.

IV.A.2.a First observations

Fig. IV.3 displays the pulse sequence and the spatially resolved spectra for the various on/off states of the probe and pump pulses, together with the corresponding variations of the peak energy along the vertical axis.

One can see that the distribution of the energy of the photoluminescence created by the sole pump pulse (red line in fig. IV.3(e), $P_{\text{ex}}(790) = 0$) exhibits a dome-shaped profile which extends over the diameter of the beam with a maximum energy at a vertical position matching the one of the peak intensity of the pump (black profile). Let us note that this energy profile is identical if the probe pulse is on (data not shown) which confirms that the probe pulse has no effect on excitons created by the pump pulse. If the pump pulse is switched off ($P_{\text{ex}}(641.5) = 0$), the energy distribution of the photoluminescence of the probe is essentially flat (purple line in fig.IV.3(e)) as we have measured in the previous section. Now if we measure the energy distribution of the probe photoluminescence when the pump pulse is on we obtain a completely different profile (orange line in fig. IV.3(e)). Indeed the whole energy distribution is blueshifted by $\sim$ 14meV with an additional blueshift at the position of the pump beam such that the

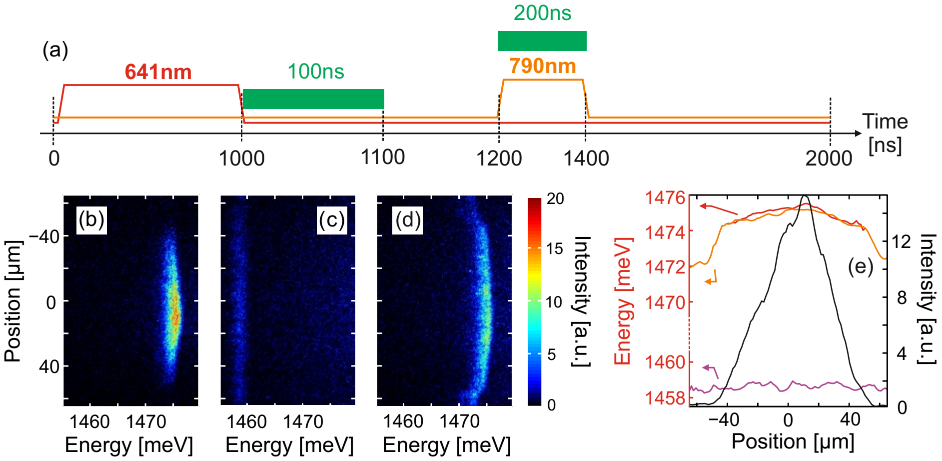

FIGURE IV.3: (a) Schema of the pulse and recording sequence. (b) Spatially resolved spectrum of the center of the photoluminescence created by a wide circular laser beam at 641.5nm, the data was taken with a 100ns window directly after the laser pulse (represented by the first green square in the pulse sequence, $P_{\text{ex}}(641.5) \sim 5\mu\text{W}$ and $P_{\text{ex}}(790) = 0$). (c) idem for the photoluminescence created by a vertical linear-shaped laser beam at 790nm, the data was taken with a 200ns window matching the laser pulse (represented by the second green region in the pulse sequence, $P_{\text{ex}}(790) \sim 1.5\mu\text{W}$ and $P_{\text{ex}}(641.5) = 0$). (d) same as (c) with both laser pulses on ($P_{\text{ex}}(790) \sim 1.5\mu\text{W}$ and $P_{\text{ex}}(641.5) \sim 5\mu\text{W}$). For all data $V_g = -4.25\text{V}$ and $T_b = 0.34\text{mK}$. (e) Evolution of the peak energy along the vertical axis for the spectral images (b-d) with red line ↔ (b), orange line ↔ (d) and purple line ↔ (c). The black line is the variation of the peak intensity along the horizontal axis for the spectral image (b).

energy distribution of the probe essentially matches the one of the pump. This striking result leads to interesting conclusions.

First of all since no exciton from the pump are left when the probe pulse starts, it means that the pump pulse changes the electrostatic landscape for excitons for a very long time, and indeed the energy distribution of the probe photoluminescence does not significantly varies if we move the probe pulse further away from the pump pulse (at least atthe lowest bath temperature). Actually the modification of the potential lasts so long that excitons created by the next pump pulse will also experience it, thus leading to a identical potential quasi-stationary along a pulse sequence. We can therefore understand that the dynamics of excitons of the pump pulse is far from simple since the pulse which creates them also produces (and maintains) the potential they explore. This proves the usefulness of the pump-probe experiment which allows to isolate the two processes.

The second important conclusion is the heterogeneity of the potential which indicates two different effects of the pump pulse on the potential. Indeed at the position of the pump beam the energy distribution of the probe photoluminescence closely follows the one of the pump photoluminescence. However this similarity immediately stops where the intensity of the pump drops to zero (i.e. at the edge of the dome), which means that the additional blueshift is created locally at the position of the pump beam.

Moreover since the intensity profile of the pump photoluminescence is much narrower than the energy distribution we are led to think that whatever created the dome-shaped must experience lateral diffusion towards the edge of the photoluminescence. In this experiment where the pump excitation is low this diffusion is not very important since the modification of the potential does not extend further away from the limit of the pump beam. Let us also note that since the dome-shaped profile is essentially the same for the pump and probe photoluminescence energy distribution, the energy of the pump photoluminescence is largely dominated by the shape of the potential and that the blueshift due to the density is negligible. Finally we see that outside the limit of the pump photoluminescence the energy of the probe signal is still at much higher energy (~ 1472meV) than for the situation with the pump beam off (~ 1458meV). Thus the pump pulse also creates a homogeneous potential outside the excitation spot of the pump beam. Indeed measurements done with a pump beam very far away from the probe beam on the sample (data not shown) show that the distribution of the energy of the probe photoluminescence is completely flat at the same background value (i.e. ~ 1472meV). Therefore this background potential is likely to be present along the entire electrode extension.

IV.A.2.b Effect of the pump beam power

In order to study more precisely the formation mechanism of the potential, we now measure the probe photoluminescence for a set of pump excitation power. The results of this experiment are presented in fig. IV.4. When increasing $P_{\mathrm{ex}}(641.5)$ we see in figs. IV.4(e) and (l) that the photoluminescence energy of the probe experiences a steady blueshift both at the position of the pump excitation and outside, however the increase of the blueshift is faster at the position of the pump beam which has for effect to amplify the dome-shaped pattern of the potential. Strikingly the blueshift at both positions is immediate as soon as the pump pulse is switched on and this even for a mean excitation power as low as $P_{\mathrm{ex}}(641.5) = 50$nW which is surprising since the pump beam is extremely wide. The variation of the current flowing through the sample does not seem to be correlated with the energy shift since is it essentially negligible for $P_{\mathrm{ex}}(641.5) \lesssim 1\mu$W and then only starts to increase. The only changes in the spectral characteristics is a sudden increase of the integrated intensity of the exciton spectral line at the position of the pump beam. Another change in the spectral characteristics occurs for $P_{\mathrm{ex}}(641.5) \gtrsim 10\mu$W where the difference between the peak energy of the 2 spectral components of the probe photoluminescence increases at the position of the pump beam along with a sharp increase of the exciton/charges line integrated intensity.

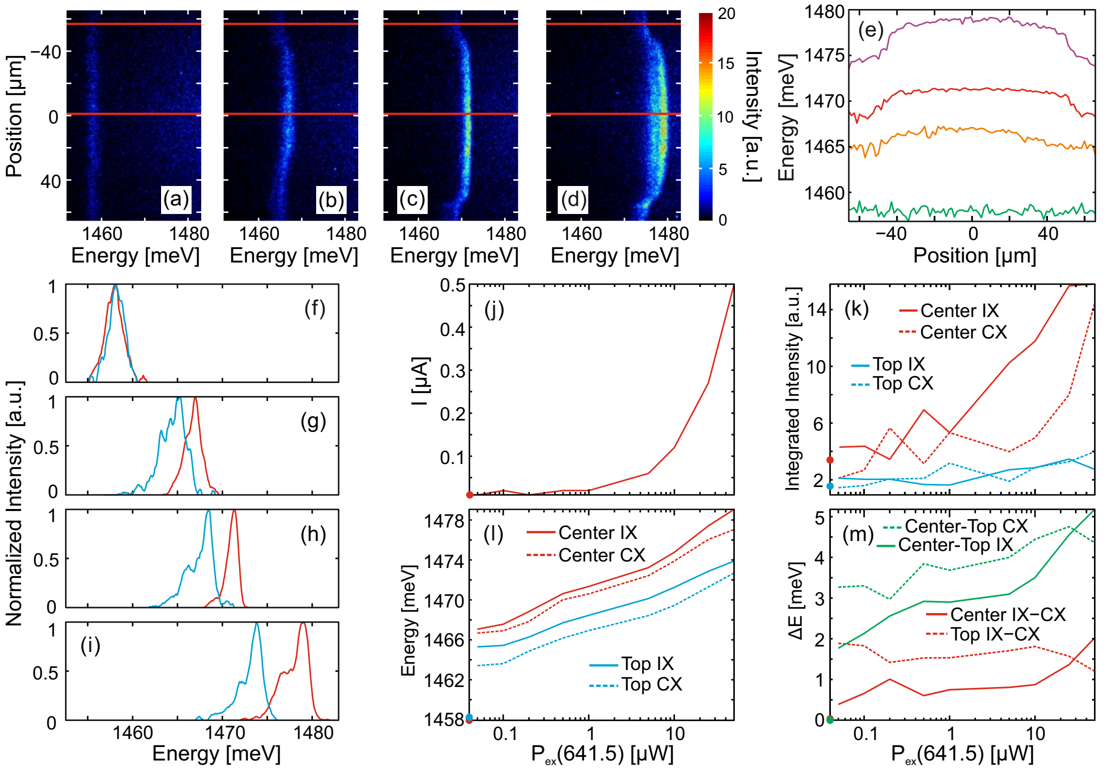

FIGURE IV.4: (a-d) Spatially resolved spectra of the photoluminescence from the 790 linear excitation for various excitation powers of the 641.5nm pulse, for all data $P_{\mathrm{ex}}(790) \sim 1.5\mu\mathrm{W}$ and $V_g = -4.3\mathrm{V}$ while from left to right $P_{\mathrm{ex}}(641.5) = 0$, 0.1, 1 and 50$\mu$W. (e) Evolution of the peak energy along the vertical axis for the spectra images (a-d), bottom to top profiles corresponding to (a) to (d). (f-i) Spectral profiles from (a-d). Red (resp. blue) profiles are taken along the top (resp. bottom) red horizontal lines in (a-d). (j) Evolution of the intensity of the current through the sample with the excitation power at 641.5nm. (k-l) Variation with $P_{\mathrm{ex}}(641.5)$ of the integrated intensity and peak energy of the IX line (solid lines) and CX lines (dashed lines), for the two vertical positions indicated by the horizontal lines in (a-d) with the red (resp. blue) lines corresponding to the marker at the center (resp. at the top) of the images. (m) Evolution of various peak energy differences with $P_{\mathrm{ex}}(641.5)$, namely green solid line $\Delta E = E(\mathrm{IX,center}) - E(\mathrm{IX,top})$, green dashed line $\Delta E = E(\mathrm{CX,center}) - E(\mathrm{CX,top})$, red solid line $\Delta E = E(\mathrm{IX,center}) - E(\mathrm{CX,center})$, red dashed line $\Delta E = E(\mathrm{IX,top}) - E(\mathrm{IX,top})$. In (j-m) the thick dots correspond to the value for $P_{\mathrm{ex}}(641.5) = 0$ which cannot be included in the logarithmic scale. Additionally for $P_{\mathrm{ex}}(641.5) = 0$ the spectral profiles only presents a single component (see (f)), thus there is no distinction between the IX and CX lines. The pulse and recording sequences are the same as in fig. IV.3.

IV.A.2.c Formation mechanism of the potential

The previous experimental results allow us to give an interpretation of the formation mechanism for the potential landscape. First of all since the blueshift outside the position of the pump beam occurs all along the area defined by the surface electrode we can attribute it to an effect of the photocurrent. We are then led to consider the background homogeneous blueshift and the additional blueshift leading to the formation of the dome-shaped potential as two independent phenomena. The magnitude of the background blueshift and the fact that it occurs even for a very small excitation power of the pump is quite characteristics of sudden modification of the overall electric field created by the gate voltage (this modification is equivalent to a decrease of almost 1V of V_g). The most direct way for it to happen is an alteration of the charge density at the Schottky interfaces (metal-i at the top of the sample and $i-n$ at the bottom). Indeed as we have seen with the built-in voltage, these interfaces exhibit local trapping potentials for the free carriers. This is particularly the case at the bottom of the sample where the close proximity of the superlattice to the $i-n$ interface probably increases the density of states.

To be more precise, a decreasing of the gate voltage would be linked to an increase of the electron density at this interface. As described previously since the effect is homogeneous the electrons must be brought there by the photocurrent. Though we do not measure a significant photocurrent for $P_{\mathrm{ex}}(641.5) \lesssim 1\mu$W it does not mean that there is no photocurrent at all (our current measurement is limited to 0.01μA). The limited value of the photocurrent could indicate that most of the electrons of the photocurrent progressively fill the bottom Schottky interface leading to a decrease of the gate voltage and preventing a build-up of the photocurrent. The photocurrent increase for $P_{\mathrm{ex}}(641.5) > 1\mu$W seems to indicate that the states at the interface are then full allowing the electrons to flow through the sample. The picture is however more complex since the background blueshift of the photoluminescence keeps increasing for $P_{\mathrm{ex}}(641.5) > 1\mu$W which means that an excess of electrons are still screening the applied gate voltage. The filling of the QW or of the bottom superlattice with electrons could account for this behavior. Practically it is essentially impossible to discriminate when each of these effects starts to influence the electric field and both probably contribute simultaneously to the blueshift.

Contrarily to the background blueshift the dome-shaped pattern is localized at the position of the pump beam. From the previous interpretation this potential feature should be considered as an additional blueshift which superimposes itself to the homogeneous one. The fact that this additional potential is localized leads us to think that it may be caused by holes photocreated by the pump excitation. Indeed the holes having a heavier effective mass than the one of the electrons they are much more easily captured at a vertical position along the sample growth direction and also diffuse much less in the lateral direction (let us also note that the holes being almost immediately captured they do not contribute to the current). There are essentially 3 places where the holes could accumulate and screen the overall electric field: states created at the top Schottky interface, the top superlattice and the upper part of the QW. Similarly to the electrons none of these positions can be excluded and they probably all can contribute. The presence of holes at the top Schottky interface can be justified with the same argument as for the electrons. Indeed, switching on the pump beam immediately creates a small dome-shaped pattern even for an almost insignificant excitation power.

Interestingly, we have seen that at the position of the pump beam, the difference between the peak energy of the two spectral components of the probe photoluminescence starts to increase for $P_{\text{ex}}(641.5) > 10\mu\text{W}$ (see fig. IV.4(m)). At the same time, the integrated intensity of the exciton/charges line also strongly increases (see fig. IV.4(k)). If we recalled the results of the sections III.C.3 and III.C.1.a these observations sign a strong increase of the population of free charges in the QW. The integrated intensity of the exciton line shows a similar behavior but for $P_{\text{ex}}(641.5) > 1\mu\text{W}$. In the section dedicated to the characterization of the probe photoluminescence, we have determined that a limited injection of charges directly in the QW by the excitation at 790nm can not be discarded. If we now consider that a large density of charges can also build-up in the QW due to the action of the pump pulse (in particular holes at the position of the pump beam) then the charges created by the probe pulse can recombined with some of these charges, effectively leading to an increase of the photoluminescence intensity of the exciton line only at the position of the pump beam. Thus these observations prove that the pump beam causes a local injection of holes in the QW, and probably also a homogeneous population of electrons through the photocurrent. Let us note that such hypothesis is exactly the mechanism which usually describes the formation of the ring with the exception that we probably have also a build-up of charge density at the Schottky interfaces (and also maybe in the superlattices).

As a final remark for these paragraphs we would like to point out that the fluctuations of the energy of the probe photoluminescence along the vertical axis are greatly reduced when the pump pulse is on (compare vertical energy profiles in fig. IV.4(e)). As discussed previously the bare potential exhibits fluctuations due to the presence of localized electrostatic impurities which create local potential minima. When additional charges are injected they will in priority be trapped in these minima effectively compensating for them and we will end up with a much more homogeneous and flatter potential. Thus the amplitude of the fluctuations of the energy of the probe photoluminescence when the pump probe is off should not be considered as a limitation of the resolution when measuring the potential landscape. The limitation is in fact given by the precision of the spectrometer i.e. $\sim 50\mu\text{eV}$ for measuring peak energy.

IV.A.3 Decay time of the potential

As mentioned previously the scan of the delay between the pump and the probe pulses at the lowest bath temperature does not show any changes of the potential created by the pump pulse. We then must conclude that the injected charges have a lifetime which is superior to the delay between 2 pump pulses (i.e. 2μs with the repetition rate of 500kHz) creating a quasi-permanent potential landscape. In order to study the lifetime of these charges we lowered the repetition rate to 50kHz to increase the time window. The information obtained by this experiment will be critical to study of the fragmented ring therefore we set the experimental conditions in order to produce a ring (small pump beam of FWHM$\sim 6-7\mu$m and higher excitation power).

The results of this experiment are displayed in fig. IV.5. To compensate the loss of signal on the recording camera we increased the length of the probe pulse to 1μs and recorded its photoluminescence with a window matching the length of the pulse. For the same reason, we also had to increase the probe beam excitation power to value for which there is a small diffusion of the probe excitons. Thus we can not neglect a possible additional blueshift due to the higher exciton density, however this may only create a small positive offset of the energy photoluminescence but not a modification of its overall dynamics. The gate voltage also had to be changed compared to the previous experiment to obtain a decent ring shape. The minimum delay between the 2 pulses is set to 100ns in order to ensure that no excitons from the pump pulse are left when the probe pulse starts.

Scanning the delay between the pump and the probe pulses reveals that the potential does experience changes when moving away from the pump pulse. More precisely for $T_b = 0.34$mK (see fig. IV.5(i)) the energy outside the position of the pump beam jumps slightly over the first 4-5μs and then increases linearly. As for the dome-shaped part of the potential, its energy presents an exponential decrease (with a characteristic time of $\sim 2.2\mu$s) during the same time and then also present a linear increase with a rate similar to the one of the background potential. It is important to note that even if the energy at the position of the pump beam decreases, it never levels down to the potential outside which means that even at the maximum delay we still have a dome-shaped potential. Therefore even if part of the hole density creating the dome-shaped potential is decaying, another part has a lifetime which is long enough to ensure a remaining quasi-stationary potential. From our measurements we can assume that these holes have a decay time much larger than 20μs. As explained previously holes can be present at various positions in the sample and from the dynamics of the potential we are led to conclude that they are present at least in 2 different places where they have 2 different decay times : a short one of $\sim 2.2\mu$s and a much longer one superior to 20μs. The dynamics of the spectral width at $T_b = 0.34$mK at the position of the pump beam (see fig. IV.5(l)) also presents a fast decay consistent to the one of the energy. This would indicate that the density of charges in the QW is rapidly dropping after the end of the pump pulse and we can consider that the fast decay of the potential corresponds to a recombination

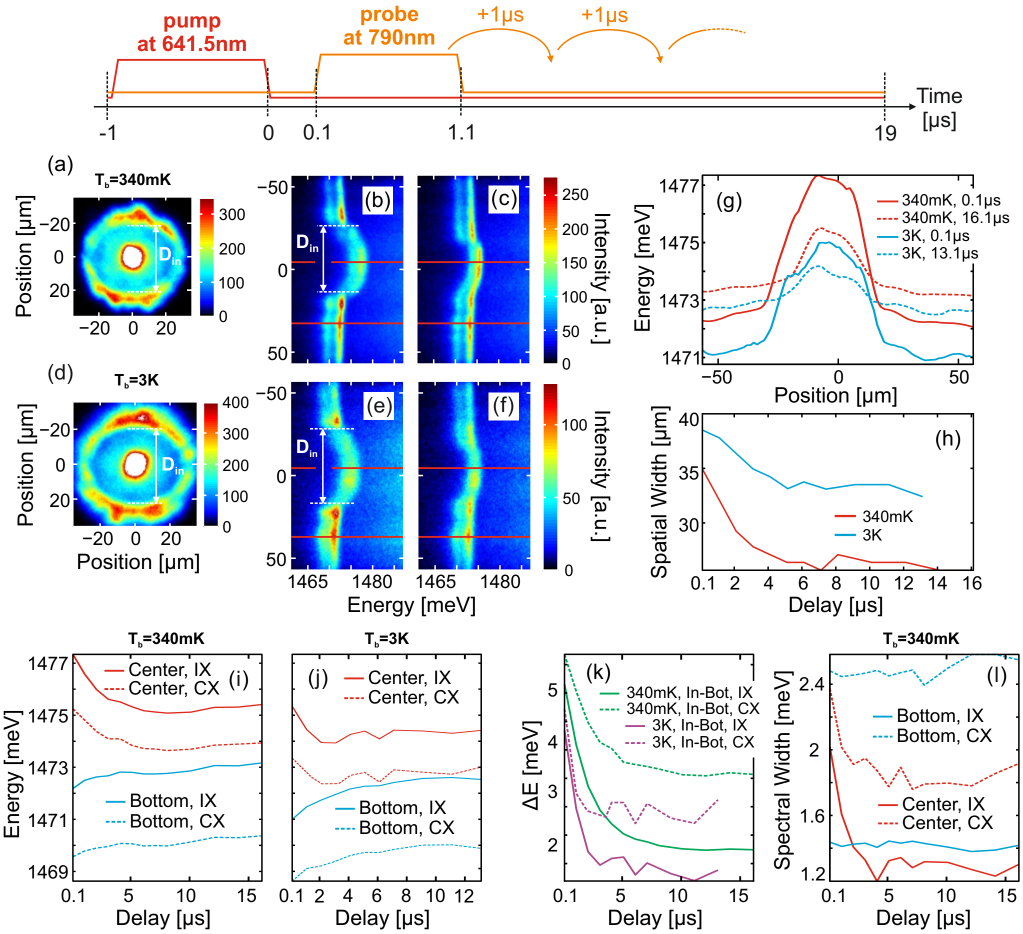

FIGURE IV.5: Pulse sequence : the pump pulse at 641.5nm lasts 1μs, the probe pulse at 790nm also lasts 1μs and is moved by step of 1μs. The reference for the delays is taken at the end of the 641.5nm pulse. The repetition rate is 50kHz. Data of the probe are recorded with a window of 1μs matching the 790nm pulse and $P_{\text{ex}}(790) = 1\mu$W. (a) Direct photoluminescence image of the ring for T$_b$ = 340mK, $P_{\text{ex}}(641.5) = 1.6\mu$W (pump pulse with a gaussian shape of FWHM$\sim 6\mu$m in order to create the ring) and $V_g = -4.45$V. The data was recorded with a window of 40ns directly after the 641.5nm pulse. (b-c) Spatially resolved spectra of the photoluminescence from the probe at 0.1 (b) and 16.1 (c) μs from the 641.5nm pulse. The image (a) is scaled such that the inner diameter of the ring D_{in} is the same on (a) and (b). (d-f) Same as (a-c) for T$_b$ = 3K. (g) Peak energy variation along the vertical axis of the spectral images (b-c) (resp. solid and dashed red profiles) and (e-f) (resp. solid and dashed blue profiles). (h) Dynamics of the spatial width of the vertical peak energy profiles plotted in (g) for T$_b$ = 0.34 and 3K. (i-j) Evolution with the delay of the peak energy of the 2 spectral components (IX $\leftrightarrow$ solid lines and CX $\leftrightarrow$ dashed lines) for two vertical positions marked by the red horizontal lines in (b-c) and (e-f) (red lines $\leftrightarrow$ center marker, blue lines $\leftrightarrow$ bottom marker), for T$_b$ = 0.34 and 3K. (k) Dynamics of various peak energy differences at the 2 bath temperatures : green lines (resp. purple) for T$_b$ =340mK (resp. 3K) with solid line $\Delta E = E(\text{IX}, \text{center}) - E(\text{IX}, \text{bottom})$, dashed line $\Delta E = E(\text{CX}, \text{center}) - E(\text{CX}, \text{bottom})$. Exponential decay fits on the lines give characteristic times of $\sim 2.2\mu$s for T_b =340mK and $\sim 0.8\mu$s for T$_b$ =3K. (l) Evolution of the spectral width of the 2 spectral components at the 2 spatial positions for T_b =340mK, the color code is the same as for (i-j).

of the holes present in the QW. Interestingly we see that the spatial extension of the dome-shaped potential at T$_b$ = 0.34mK is also decreasing during the first 4-5μs towards a constant value (see fig. IV.5(g) and (h)). This indicates than while the overall hole density is dropping, its spatial extension is also shrinking. If we recall that the QW also presents a dominant population of electrons outside the position of the pump probe, we can envisage that the electrons are attracted towards the hole concentration and slowly "gnaw" the edges of the hole distribution.

In the previous discussion we have ignored the electrical characteristics of the sample and their effects on the photocurrent. Indeed the sample exhibits a structure resembling the one of a capacitor (among others : a photodiode, a resistor,...). Thus one could conceive that the dynamics of the current through the structure is complex. In particular we have already established that most of the current is created by the pump pulse such that if the sample behaves as a capacitor a transient photocurrent could remain after the pump pulse. Such current would not be measured since our actual experimental set-up only allows us to monitor a steady current. We tried to perform a time-resolved current measurement (using a transimpedance amplifier), however the fact that the back of the sample is not electrically isolated from the mass of the cryostat prevented us to do it. Such experiment would require another type of sample structure and therefore will be left for further studies. Nevertheless the presence of a transient current is conceivable and would result in a continuous and spatially homogeneous injection of electrons in the sample for some time after the pump pulse. This additional supply of electrons would definitely influence the potential and in particular could explain the decay of the hole density and the small and rapid increase of the background potential directly after the pump pulse. It is surprising to note that contrarily to its dome-shaped part, the background component of the potential does not show any decrease towards the energy of the probe photoluminescence without any pump pulse. This indicates that the electrons responsible for the background have a very long decay time.

After the study of the dynamics of the potential at the lowest bath temperature, we now increase the bath temperature to 3K. At this temperature three main differences can be observed : an overall decrease of the amplitude of both parts of the potential (the background is lower in energy of about 1meV and the amplitude of the dome is also lower of about 1 meV), a larger spatial extension and a faster decrease of the potential at the position of the pump beam (the characteristic decay time is $\sim 0.8\mu$s). A higher bath temperature has two effects (among others) on the system : first of all it enhances the lateral diffusion of the charges in the QW (and in any other two-dimensional plane). This would explain the larger spatial extension of the dome potential created by the holes diffusing further away from the position of the pump beam. The second effect is a higher thermal activation energy which would diminish the trapping efficiency of the charges thus effectively lowering the density of the trapped charges. The amplitude of the screening of the electric field created by the gate voltage would then decrease which would result in a lower potential. The higher activation energy could also probably explain the faster decrease of the dome-shaped potential. Let us finally note that the amplitude of the decrease of the energy of the dome potential is lower at 3K than at 340mK, the same effect can be observed for the drop of the spatial extension which also presents a longer decay time. We do not have a clear explanation for these observations which may result from a lower density of holes in the QW at 3K.

At 3K, we measured a characteristic time of $\sim 0.8\mu$s. However since our time resolution is 1μs (the length of the probe pulse and the recording window) this decay time is likely to be inferior to this value. This means that for a bath temperature of 3K or more (and maybe less) the decay time might be short enough to affect the dome-shaped potential even at a repetition rate of 500kHz leading to a potential landscape which is no longer quasi-stationary. We would then have to deal with the problem of a measuring a potential which varies with the delay and therefore retrieving the exciton density might be more problematic.

From all the previous discussions one can see that the formation of the potential and its evolution is a very complex problem and we do not pretend to fully comprehend it here. In particular we do not have an explanation for the slight linear increase of the potential after the first 5μs. Let us also note that the difference between the peak energy of the 2 spectral components is almost twice smaller at the position of pump beam than away from it (and this at the 2 bath temperatures). This surprising observation confirmed the idea that the spectral line at lower energy signs the presence of a complex exciton/charges compound.

To conclude this study of the dynamics of the potential we would like to emphasize that the fragmented ring created at a repetition rate of 50kHz is of much less good quality than at 500kHz (fragments less well-defined). As seen previously one of the differences between the 2 repetition rate is that at 50kHz the amplitude of the dome-shaped has the time to decrease before the next pump pulse. We are then led to conclude that the shape of the potential has a great influence on the formation of the ring and in particular on its fragmentation. The most obvious influence is that a higher potential at the position of the pump beam would enhance the lateral diffusion of excitons away from the laser spot but one can not exclude a more complex scenario.

As a last remark, during the study of the dynamics of the ring in the sections III.B.2 and III.C.2 we were surprised by the fact that the ring does not contract after the pump pulse as observed by L. Butov et al. [60]. The measurements performed in this section now allow us an explanation. Indeed the typical decay time of excitons in our ring is $\sim$ 20ns i.e. much shorter than the decay time of the potential. Excitons would therefore experience a permanent potential barrier which prevents them to diffuse towards the interior of the ring. To go further we could even ask ourselves if in our case the creation of ring is not essentially dominated by the diffusion of excitons on this dome-shaped potential and only secondarily as the result of the meeting of diffusion fronts of electrons and holes as it was usually explained. Interestingly the (only) data presented by the group of L. Butov on the variation of the energy of the photoluminescence along the radius of the ring (see fig. III.15(f)) is quite similar to our own observations and while they interpreted this profile as a result of the blueshift induced by the density profile of excitons, it is legitimate to ask if their system is not also influence by the presence of a photo-induced potential controlling the exciton confinement. As a concluding remark we would like to point out that none of the theoretical models developed to explain the formation of the photoluminescence ring includes the effect of the screening of the gate voltage by the injected charges, which is, in our opinion (and considering the results of our experiments), a key ingredient.

IV.A.4 Accurate measurement of the potential and the density of excitons

The previous sections gave us many information on the effect of the pump beam on the formation mechanism and lifetime of the potential landscape confining excitons. We now return to usual experimental parameters (500kHz repetition rate, small pump beam) in order to study with accuracy the potential and density profiles of excitons in the regime where the fragmented ring is formed. We will see that at the lowest bath temperature the potential can be divided in three parts :

- Inside the ring we observe as expected a dome-shape profile with very sharp edges and an amplitude of $\sim$ 5meV.
- Around the position of the ring we can sometimes observe a confinement potential with a depth of $\sim 1-1.5$meV which extends from the edge of the dome profile up to $\sim 10\mu$m outside the position of the ring. The presence of this trapping potential is not systematic and we had to measure several different ring in order to reproduce the results presented in this section. This does not mean that the presence of confinement potentials is uncommon. The reason is rather due to the characteristics of our experimental setup. Indeed in order to measure the energy of the probe photoluminescence, the vertical linear probe beam and the entrance slit of the spectrometer are both aligned vertically and horizontally at the center of the ring. Therefore we can only explore a limited spatial extension of the potential along the horizontal axis and since we have *a priori* no idea of the shape of the

potential, we need to find a ring which exhibits a confinement potential at the proper position.

- Further away from the ring the potential can present significant fluctuations.

Knowing the potential profile allows us to measure with accuracy the density of excitons. As explained previously in order to ascertain the presence of a dominant fraction of dark excitons we need to find a region where the density is uniform while the intensity of the photoluminescence presents strong variations. Strikingly the most significant evidences for the presence of a dense gas of dark excitons are found within the confining potentials. Indeed in this region we obtain that the density of exciton is essentially uniform while the intensity of the photoluminescence can be divided up to ten-fold. When the bath temperature is increased, the amplitude of dome-shaped profile of the potential decreases while its edges become less and less sharp and its extension increases, which explains the rise of the radius of the ring. At the same time the confining part of the potential disappears and the variations of the density of excitons closely follow the one of the intensity of the photoluminescence such that there are no more evidence of a dense gas of dark excitons. We also observe that when the bath temperature increases, the whole potential experiences an energy shift towards the lower energies, at was reported in the previous section.

IV.A.4.a Introduction to the measurements

Before presenting the experimental results we would like to introduce some notations which will help for the interpretation of the results and also to describe the experimental procedure which slightly differs from the previous measurements. In the following paragraphs, we note V_X the energy due to the interaction between dipolar excitons and the internal electric field, while U_X is the energy of the exciton gas resulting from the dipolar interaction. We recall that the value of U_X is a direct indication of the value of the exciton density n_X (see first chapter). Let us note that V_X being given by $-\mathbf{d}\cdot\mathbf{E}$, the potential is negative. Therefore what we should actually consider is the energy offset compared to a reference value, which could be for example the energy of the probe photoluminescence with the pump pulse switched off (see figs. IV.3 and IV.4) or the bandgap energy of the QW, but since we are only interested in the variations of the potential this distinction is not relevant.

As seen in the previous section, the potential confining excitons presents a decay time such that its value and shape can be modified during the 2μs-duration of a pulse sequence, in particular at high bath temperatures. To overcome this problem we implemented the pulses and recording protocol displayed in fig. IV.6. Namely we record two

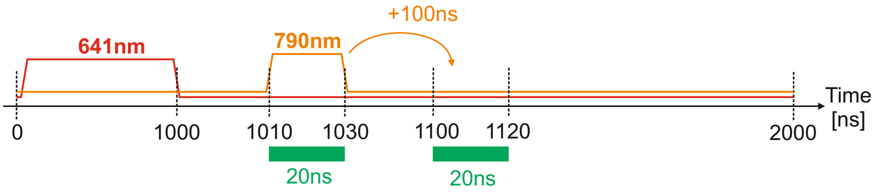

Figure IV.6: Pulse and recording sequence. Two spatially resolved spectra are recorded with a 20ns window matching the duration of the probe pulse at 790nm. The probe pulse is set to start respectively 10 and 100ns after the end of the pump pulse for the two data.

spatially resolved spectra with a window of 20ns corresponding to the duration of the probe pulse. The two spectral images are recorded for probe pulses starting respectively 10ns and 100ns after the end of the pump pulse. We can then measure the variations of the peak energy of the exciton line along the vertical z-axis ($z = 0$ marks the vertical center of both the ring and the probe beam). In this condition the energy of the photoluminescence $E_X(z,t)$ is the sum of the energy of excitons created by both the pump and probe pulse and reads $E_X(z,t) = U_X^{\text{pump}}(z,t) + U_X^{\text{probe}}(z,t) + V_X(z,t)$, t being the delay time after the end of the pump pulse (t = 10ns and 100ns for the two spatially resolved spectra).

This expression is very general and can be simplified. Firstly, since the excitation power of the probe beam is set at a very low value, the density of excitons created by the probe pulse can be neglected and $U_X^{\text{probe}}(z,t) \sim 0$. Then we know that the extension of the probe beam exceed the one of the pattern of the fragmented ring such that there are regions outside the ring where we have information on the energy of the photoluminescence thanks to the probe beam but where the density of excitons created by the pump pulse is negligible. Thus we can write $U_X^{\text{pump}}(|z| > z_{\text{edge}}, t) = 0$, where z_{edge} marks the maximum vertical extension of the pump photoluminescence. For $|z| > z_{\text{edge}}$, the energy of the photoluminescence is then directly given by $V_X(z,t)$. With the recording sequence presented in the previous paragraph we can estimate that the potential profile given $V_X(z,t)$ does not have time to vary between the two measurements such that $V_X(z, t = 10\text{ns}) = V_X(z, t = 100\text{ns})$, even at high bath temperatures. This assessment can be easily verified by superposing the energy profiles recorded at the two delays. Indeed if the potential does not vary then at any time we should find that $U_X^{\text{pump}}(|z| \geq z_{\text{edge}}, t) + V_X(|z| \geq z_{\text{edge}}) = V_X(|z| \geq z_{\text{edge}})$, practically this means the energy profiles at the two delays should coincide starting from a given distance from the ring. Finally, 100ns after the end of the pump pulse, we can expect that all excitons created by the pump pulse (i.e. all excitons forming the fragmented ring) have recombined, such that $E_X(z, t = 100\text{ns}) = V_X(z)$ and the energy of the photoluminescence directly gives the variations of the potential. If all these considerations are satisfied (and we will see that this is the case for the measurements presented in this section) then the profile of the energy resulting from the dipolar interaction for $t = 10\text{ns}$ is given by $U_X^{\text{pump}}(z, t = 10\text{ns}) = E_X(z, t = 10\text{ns}) - E_X(z, t = 100\text{ns})$. Thanks to the relation between this energy and the density of excitons we can obtain the profile of the exciton density for $t = 10\text{ns}$.

The level of details of this discussion may seem overly complex compared to the analysis of the previous sections, however we would like to recall that in these sections we were only interested in the potential confining the excitons. The final goal of this section is to retrieve the density profile of excitons and this requires more precautions.

IV.A.4.b Results

Fig. IV.7 presents the spatially resolved spectra recorded 10 and 100ns after the end of the pump pulse and the corresponding profiles of the peak energy and intensity of the exciton spectral line for 3 different bath temperatures. First of all, for all temperatures we can see that the energy profiles at both delays coincide at a given distance outside the ring (see dashed and solid energy profiles in figs. IV.7(a.4), (b.4) and (c.4)). As explained in the previous section, this means that the potential is quasi-stationary between these 2 delays. The second important prerequisite for a simple interpretation of the results was that no exciton created by the pump pulse is left at delay 100ns. We see that indeed, for all temperatures, the intensity of the photoluminescence at the position of the ring has been divided by more than 10 which means that most of the photoluminescence comes from excitons created by the probe pulse (see dashed and solid black lines in figs. IV.7(a.4), (b.4) and (c.4)). According to the considerations presented in the previous section, these observations imply that the energy profile at 100ns (red dashed lines in fig. IV.7) directly gives the exciton potential landscape in the plane of the QW. Therefore the difference of the energy profiles between the two delays gives the spatially resolved strength of the dipolar interaction at 10ns from which we can estimate the profile of the density of exciton at this delay.

The most striking result of these measurements is the presence of a confining potential which can be seen on the left part of the ring in fig. IV.7(a.4) (blue transparent area, corresponds to the lower part of the ring). It extends from the edge of the dome-shaped potential to outside the ring (i.e. from the abscissa $z \sim -18$ to $-37\mu\text{m}$). Interestingly we see that in this region, the bottom of the trapping potential and the profile of the energy at 10ns (solid and dashed red lines in fig. IV.7(a.4)) are essentially flat which means that the intensity of the dipolar interaction and the density of excitons are uniform. The difference of energy is $\sim 1.2\text{meV}$ which corresponds to a density of $\sim 1.7 \times 10^{10}\text{cm}^{-2}$ (see calibration curve in fig. I.5). Additionally the profiles of the potential and of the

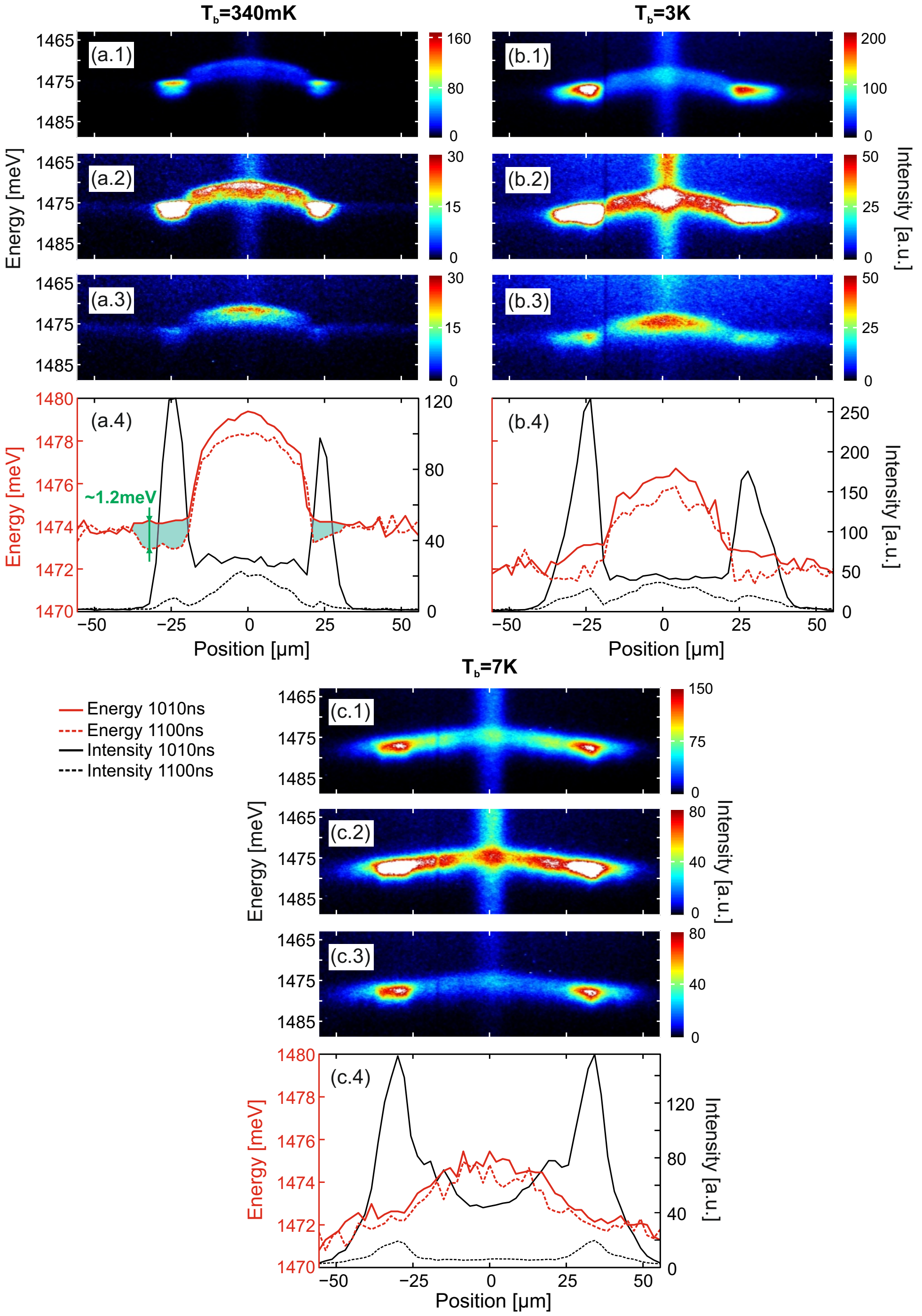

FIGURE IV.7: (a.1) and (a.3) Spatially resolved spectra recorded with the probe pulse starting respectively 10 and 100ns after the end of the pump pulse, $T_b = 340$mK (see pulse sequence in fig.IV.6). (a.2) Same as (a.1) with a different color scale which enhances the probe photoluminescence outside the ring. (a.4) Evolution of the peak energy (red lines) and intensity (black lines) of the exciton line along the horizontal axis for the spatially resolved spectra presented in (a.1) (solid lines) and (a.3) (dashed lines) (the spectral images have been rotated of 90 degrees for clarity but the value of the abscissa corresponds to the position along the vertical axis z of the photoluminescence). (b) and (c) and corresponding columns : same as (a) for $T_b = 3$ and 7K. For all temperatures $P_{ex}(641.5) = 10.4\mu$W, $P_{ex}(790) = 70$nW and $V_g = -4.2$V.

energy at 10ns coincide starting from the outer edge of the trapping potential. This indicates that the trapping potential is perfectly filled and no exciton of the fragmented ring diffuses further away (Appendix C presents measurements where a confining potential is over-filled). Now that we have a very accurate estimation of the density, we can analyze the distribution of the intensity of the corresponding photoluminescence (solid black line). And we see that while the density is constant, the intensity of the photoluminescence is divided by ten which confirms the presence of a dominant population of dark excitons directly outside the ring. As mentioned several times throughout this thesis, a dominant population of dark excitons directly signs a Bose stimulation towards the dark states. Therefore the previous results implies that the region comporting the ring and its outside vicinity exhibits a phase separation with a thermal gas of bright and dark excitons with a 50/50 population ratio at the position of the ring and a quantum gas with a dominant population of dark excitons in its vicinity. Let us note that in the outside vicinity of the ring, even if the exciton population is dominated by dark excitons, bright excitons are also present yielding to a "gray" gas of excitons.

The formation of a "gray" condensate next to a thermal gas of excitons in the same confinement potential can seem surprising since in principle nothing differentiates the exciton gas at the position of the ring to the one in the outside vicinity of it. However one has to consider that during the excitation pulse (and also probably for some time after the excitation pulse), excitons are being constantly injected at the position of the ring due to the abrupt fall of potential at the inner edge of the ring. These excitons will thus have a high kinetic energy which yields a local heating of the exciton gas at the position of the ring (or at least we can imagine that these excitons will perturb the exciton gas at the position of the ring, similarly to the turbulence at the bottom of a waterfall). From this perturbed exciton gas, excitons will diffuse towards the outer edge of the confining potential (for example helped by the dipolar repulsion), cooling down to the lattice temperature in the process. Therefore we will end up with a cold and dense gas of excitons which can then undergo Bose-Einstein condensation. As a conclusion we can see that the distribution of excitons in the naturally formed confining potential is very similar to the situation where we would directly inject excitons on one side of an artificial trap (for example created by a pattern of electrodes on top of the sample) with a laser beam and collect thermalized excitons at the opposite side of the trap [1]. Let us also note that in a two-dimensional system, Bose-Einstein condensation can only occur in a confined environment. Therefore it is in a sense reassuring and significant that the confining potential and the quantum gas of dark excitons are found together.

---

[1] This picture depicted the injection of excitons due to their diffusion from the dome-shaped potential towards the region of the ring. Alternatively we can consider the model based on the ambipolar diffusion of charges which says that excitons form at the position of the ring where the electrons and holes fronts meet. The formation of excitons will result in a liberation of their binding energy which will locally heat the exciton gas.

Interestingly, if we examine the right part of the ring, we see that while the energy profile at 10ns is constant the potential is slowly increasing until the two profiles coincide (other blue transparent region in fig. IV.7(a.4), corresponds to the top of the ring). This indicates that the density of excitons is not uniform in this region and that its variation closely follows the fast decrease of the intensity. Therefore there is no dominant population of dark exciton in this region. Similar observations can be done on the profiles for the two higher bath temperatures. This would then indicate that excitons can only condense into the dark states at the lowest bath temperature and in specific area along the circumference of the ring, for instance where an adequate confinement is present. With the pump-probe experiment used in this chapter, we can only probe the potential landscape and the distribution of density along a single axis (i.e. the vertical axis corresponding to the slit of the spectrometer) and it would be interesting to know the lateral extension of the confinement potential. To complete the map of the potential we could imagine to repeat the above experiment with a linear probe beam slightly translated horizontally in order to probe the vicinity of the trapping potential. However we have to take in account that finding such potentials is not easy (not because they are unusual but because of the limitations of our experimental set-up) and that the recordings themselves take such a long time that we would not be able to perform enough measurements to retrieve a map of the potential due to our limited available time at the lowest bath temperature.

The fact that we observe two different confining potentials at the opposite side of the ring indicates that the formation of the fragmented ring yields the creation of a certain number of various confinement with different shapes, extensions and depths distributed along the circumference of the ring. In the next chapter we validate the presence of the quantum gas of dark excitons by measuring the spatial coherence and the polarization of the photoluminescence. We found that these characteristics can be found in localized regions in the outside vicinity of the ring which would confirm the existence of local trapping potentials where condensation can occur. Additionally, the analysis of the map of the phase of the $g^{(1)}$-function performed together with the shift-interferometry experiments will provide an independent indication of the link between the presence of trapping potentials and islands of long-range spatial coherence.

When the bath temperature increases we notice an overall redshift and smoothing of the potential, which has for results that at 7K the potential presents a large Gaussian-like shape. We already observed these phenomena in the previous section IV.A.3 and there were interpreted as an overall lower density and a higher lateral diffusion of the charges which creates the potential.

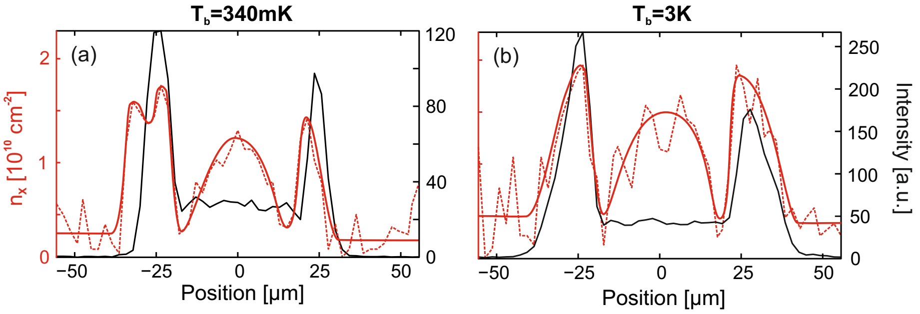

Figure IV.8: (a) Profiles of the density of excitons (dashed red line) and the intensity of the photoluminescence (solid black line) along the horizontal axis defined in fig. IV.7 at T$_b$ = 0.34K. The intensity profile is the same as in fig. IV.7(a.4) while the density profile was obtained by the correspondence between the density of excitons and the strength of the dipolar interaction given by the absolute value of the subtraction of the energy profiles in fig. IV.7(a.4), as defined by the calibration curve in fig. I.5. The thick solid red line is a guide for the eyes for the density profile. (b) Same as (a) for the data presented in fig. IV.7(b.4) at T$_b$ = 3K.

Let us note that the presentation of the above results would be simpler if we could directly plot the distribution of the exciton density. With our experiment the density profile at t = 10ns can be obtained by subtracting the energy profiles at the two delays which gives the strength of the dipolar interactions $U_X^{\text{pump}}(z, t = 10\text{ns}) = |E_X(z, t = 10\text{ns}) - E_X(z, t = 100\text{ns})|$. The value of $U_X^{\text{pump}}(z, t = 10\text{ns})$ can then be associated to the density of excitons by using the theoretical curve presented in fig. I.5. However one has to keep in mind that the energy profiles are quite noisy and subtracting them tends to amplify the local fluctuations, which can render the resulting density profile very difficult to interpret. Nevertheless, we performed the analysis for T$_b$ = 0.34 and 3K and the results are presented in fig. IV.8 (at 7K, the resulting profile exhibits too large fluctuations). We added guide-for-the-eyes to the density profiles in order to clarify their variations.

Around the position of the ring, we can see that the variations of the density profiles confirm the previous observations done in fig. IV.7. Namely, on the left of the ring at the lowest bath temperature, we see that while the density presents a maximum at the position of the ring (maximum of intensity), it also exhibits a peak at high value directly outside the ring where the intensity is essentially negligible. On the left of the ring at the same temperature and on both side at T$_b$ = 3K, the variations of the density and of the intensity are very similar : we observe for both a maximum at the position of the ring and a strong decrease when moving outwards the ring. Interestingly we see that inside the ring, the density is maximum at the center of the ring and strongly drops when moving towards the inner edge of the ring. This behavior is consistent with the dome-shaped potential in this region : excitons are injected at the position of the excitation spot (i.e. the center the ring), then they diffuse away from it due to the double effect of the shape of the potential and the dipolar repulsion, finally the diffusion is enhanced at the inner edge of the ring by the presence of the abrupt fall of the potential effectively creating an exciton depleted region directly before the ring. As mentioned previously, the fluctuations of the energy profiles at $T_b = 7K$ prevented us to plot a clear enough density profile. We can nonetheless observe that all along the radius of the ring, the two energy profiles remain essentially parallel, indicating that sudden and strong modifications of the density such as the ones observed at the lowest bath temperatures do not exist here. The density is then more or less uniform along the diameter of the ring. The averaged value of the strength of the dipolar interaction indicates a density inferior to 1.10^{10}cm^{-2} which is significantly smaller than the values observe at lower temperatures. This agrees with the previously observed decrease of the intensity of the photoluminescence of the ring at higher bath temperatures (see section III.B.1.c).

Interestingly, the previous measurements have shown that at 3K we do not observe a condensed gas of dark excitons. This observation can be interpreted two ways which are not mutually exclusive : first we know that Bose-Einstein condensation can only occur below a critical temperature determined by the density of bosons. The profiles of the density of excitons presented in fig. IV.8 show that the value of the density at the position of the ring is not fundamentally different at T_b =0.34 and 3K. The absence of the dense gas of dark excitons at 3K could then indicate that the exciton gas is above the critical temperature. Alternatively we see that the shape of the confining potentials strongly vary between 0.34 and 3K. Thus we could imagine that the characteristics of the confining potential is a determinant factor for the formation of a "gray" condensate of excitons. This interpretation is supported by the fact that at $T_b = 0.34K$ we are able to observe two different confining potentials (on both side of the ring) which are not equivalently adequate to the appearance of a dominant population of dark excitons.

To conclude this section, we would like to review the results we obtained on the same experiment with an alternative pulse sequence and a different fragmented ring. Details for various bath temperatures (0.34, 1.5, 3 and 7K) can be found in the appendix C. In this experiment we directly record the energy and intensity profiles of the pump photoluminescence after the pump pulse and measure the potential landscape later on. A study similar to the one presented in the previous paragraphs can be performed, and in particular, for $T_b = 0.34K$, we observe again the presence of a confinement potential (this time on the top of the ring). The comparison between the variations of the density and the intensity of the photoluminescence also demonstrates the presence of a dense gas of dark excitons outside the ring. Interestingly, for $T_b = 1.5K$ this trapping potential is still present but has a lower depth. At the same time the density of excitons is not uniform anymore and slowly decreases when moving outwards the ring. In the same region the intensity of the photoluminescence does not exhibit spectacular variations, meaning that the dense gas of dark excitons is not present anymore. As a consequence these observations confirm that both the presence of a dominant fraction of dark excitons and the characteristics of the confining potential are strongly dependent on the bath temperature. Finally at the two highest temperatures the data show that the potential landscape has changed between the two recording delays, therefore we can not conclude on the distribution of the density of excitons. This last result proves that the pulse sequence used in this section, despite being more complex, is more adequate to the study of the fragmented ring since it allows conclusive measurements for all bath temperatures.

As a last remark we would like to develop on the consequence of the presence of the confining potential on the distribution of free charges. In the previous chapter (see e.g. sections III.C.3 and III.C.2), we have observed that in the QW the density of free charges is minimum at the position of the ring and in the outside vicinity of it. Thanks to the measurements of the potential landscape we are now able to give further details on the distribution of the charges. Indeed a trapping potential for excitons is also a trapping potential for holes but an anti-trap for electrons [133] due to their opposite electrostatic charges [1]. Therefore the limited population of charges around the position of the ring in the QW can only be holes while electrons are confined to the exterior of the trapping potential.

IV.B Filling the potential

We have shown that the potential landscape created together with the ring can exhibit relatively deep traps. We actually observed that such potentials can be found in various shapes, sizes and depths along the circumference of the ring. The potential landscape around the position of the ring would then be very complex. A possible experiment to test its profile is to fill this potential with excitons and observe the distribution of the photoluminescence. Indeed if the potential landscape displays local traps, excitons will accumulate in these regions and the intensity of the photoluminescence should reflect the structure of the potential. The results of the experiment presented in this section show precisely this behavior and strikingly we will see that the pattern obtained by filling the potential is remarkably similar to the pattern of the fragmented ring.

---

[1] If we consider two positions $x_{1,2}$ in QW plane such that the interaction V_X between dipolar excitons and the internal electric field is $V_X(x_1) < V_X(x_2)$ (i.e. presence of a trapping potential in x_1). Then since $V_X = -\mathbf{d}\cdot\mathbf{E} < 0$, we obtain that $|\mathbf{E}(x_1)| > |\mathbf{E}(x_2)|$. Thus considering that $\mathbf{E}(x)$ is given by $\mathbf{E} = -\partial_x \phi(x)$, where $\phi(x)$ is the internal electrostatic potential, the previous equations give $\phi(x_1) < \phi(x_2)$. The interaction between charges and the electrostatic potential are respectively $V_{\text{hole}}(x) = +e.\phi(x)$ and $V_{\text{electron}}(x) = -e.\phi(x)$. Considering the evolution of $\phi(x)$ between x_1 and x_2, we obtain that a trapping potential for excitons is also a trapping potential for holes but an anti-trap for electrons.

IV.B.1 Direct observations

At the lowest bath temperature, we have seen that the potential landscape is quasi-stationary and considering the geometry of our system, we decided to inject excitons at the center of the potential (i.e. the center of the ring) using a small excitation beam at 790nm (FWHM $\sim 6-7\mu$m). An excitation with a wavelength at 790nm should in principle only create excitons in the QW, while injecting a minimum amount of charges and therefore not modify the potential landscape. The pulse corresponding to this beam was set to a duration of 200ns starting 100ns after pulse creating the potential (i.e. the pump pulse) in order to ensure that all excitons injected by the pump have recombined. A schema of the pulse sequence is presented in fig. IV.9(a). In figs. IV.9(c-h) we present the photoluminescence patterns which can be observed after the pulse at 790nm depending on its excitation power. We recorded images at the same excitation power when the pulse at 641.5nm was switched on (see figs. IV.9(c-e)) and off (see figs. IV.9(f-h)). As a comparison we also present the photoluminescence pattern of the fragmented ring directly after the pump pulse (see fig. IV.9(b)).

First of all, as mentioned in the section IV.A.1, a sole pulse at 790nm can not create a fragmented ring pattern (see figs. IV.9(f-h) for which the pulse at 641.5nm is switched off) and we only observe a symmetric and smooth repartition of the photoluminescence whose extension depends on the quantity of injected excitons i.e. the value of the excitation power. The regularity of the pattern is confirmed by the variations of the normalized profiles of the intensity of the photoluminescence along the vertical axis (blue lines in figs. IV.9(i-k))). For the same measurements with the pump pulse switched on the situation changes dramatically. Indeed, while at the lowest excitation power the only differences are an increase of the spatial extension and of the overall intensity of the photoluminescence (see fig. IV.9(f)) and red and blue profiles in fig. IV.9(i))), for $P_{ex} = 7\mu$W the photoluminescence pattern displayed in fig. IV.9(d) is remarkably similar to the one of the fragmented ring measured after the pump pulse (see fig. IV.9(b)). The resemblance is confirmed by the almost perfect overlap of the intensity profiles displayed in fig. IV.9(j) (red and black curves). If we keep increasing the excitation power, we observe that the photoluminescence located at the position equivalent to the one of the fragmented ring gains in intensity and expands further away while keeping its fragmented aspect (see fig. IV.9(e)). The comparison of the corresponding intensity profile with the one of the fragmented ring (see black and red lines in fig.IV.9(k)) shows that both exhibit an increase of the intensity at the inner edge of the ring with similar shape and amplitude, however the photoluminescence created by the 790nm extends much further away from the position of the ring.

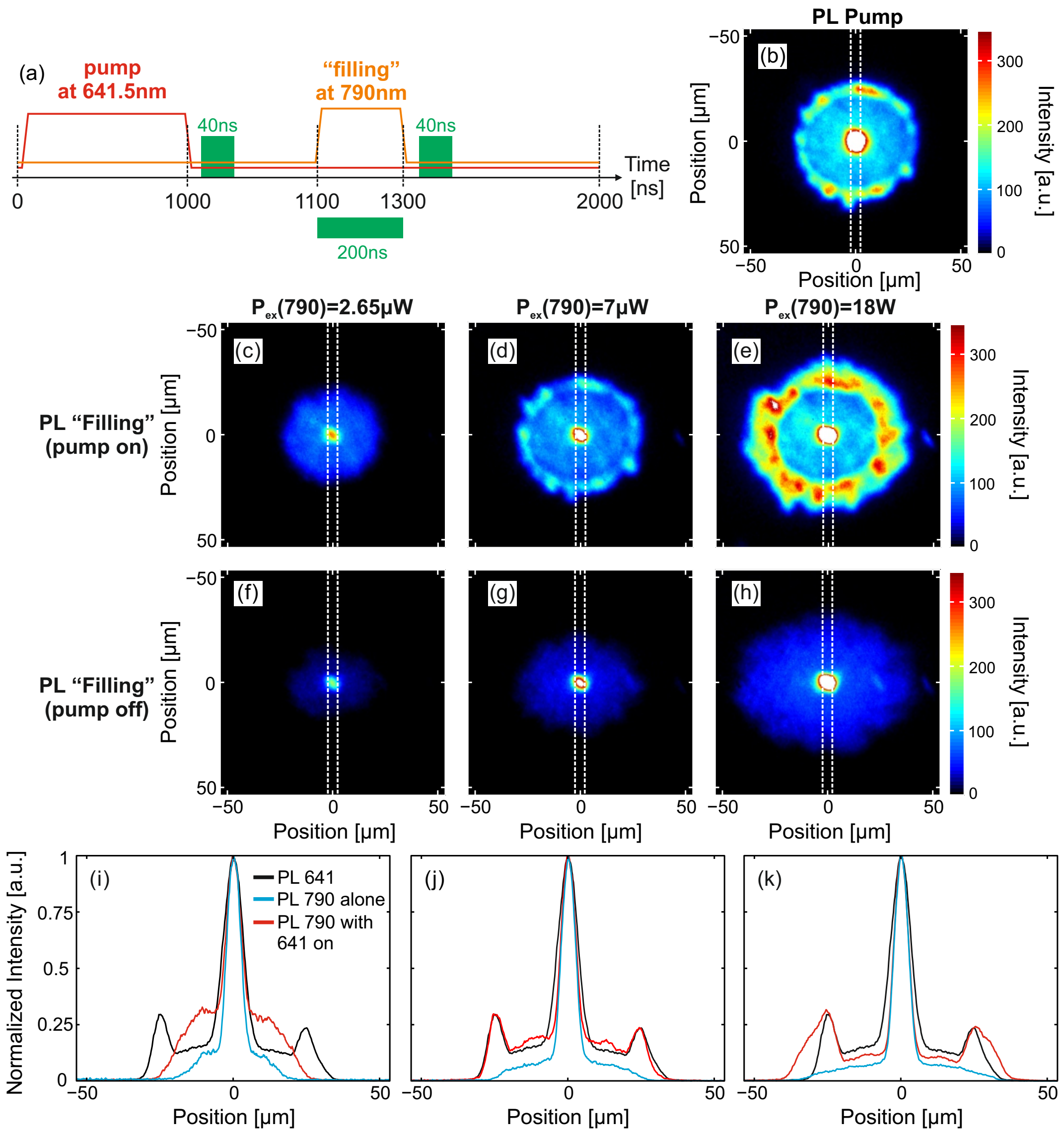

Figure IV.9: (a) Pulse and recording sequence. (b) Direct image of the photoluminescence of the fragmented ring recorded with a 40ns-long window starting 10ns after the end of the excitation pulse at 641.5nm (indicated by the first green rectangle in the pulse sequence). (c-h) Direct images of the photoluminescence created by the excitation pulse at 790nm, recorded with a 40ns-long window 10ns after the pulse at 790nm (indicated by the third green rectangle in the pulse sequence). For the data (c-e) the pump pulse at 641.5nm was switched on and $P_{ex}(790) = 2.65$, 7 and 18μW from left to right. Same for data (f-h) except that the pump pulse was switched off. (i) Normalized profiles of the intensity of the photoluminescence along the vertical axis averaged horizontally in the area marked by the vertical dashed white lines in the images. The black, red and blue lines respectively correspond to the images (b), (c) and (f). (j-k) Same as (i) except for the red and blue lines which respectively correspond to the images (d) and (g) in figure (j) and to the images (e) and (h) in figure (k). The increase of the intensity of the photoluminescence at the center of the profiles (and of the images) corresponds to the strong emission of the bulk GaAs at the position of the excitation beams. For all data $P_{ex}(641.5) = 11.3\mu$W (when on), $V_g = -4.2$V and $T_b = 340$mK.

We will now interpret the photoluminescence pattern created by the pulse at 790nm by considering the potential landscape yielded by the pump beam at 641.5nm and which was measured in the previous section. We know that around the center of the ring, the potential exhibits a dome-shaped profile which slowly decreases when moving towards the position of the ring. Such a potential will have for effect to enhance the diffusion of excitons away from the excitation spot. This explains the difference of the spatial extension of the photoluminescence depending if the potential is present or not, as can be seen by comparing the blue and red profiles in figs. IV.9(i-k). The difference in intensity has already been observed in the section IV.A.2 and we use the same interpretation here. Namely, we know that an excitation pulse at 790nm inject some charges, particularly at high excitation power (see section IV.A.1, the effect is amplified here since we use a much smaller excitation beam). Since the potential is due to the presence of excess charges (in particular holes for the dome-shaped part), the additional intensity can be linked to the recombination of some of these charges with the ones injected by the pulse at 790nm.

When we increase the excitation power, we also inject more excitons. Due to the dipolar repulsion between excitons which enhances their diffusion, excitons will eventually reach the edge of the dome and fall towards the position of ring. At this location they will explore a distinct potential where they can accumulate in local traps. Strikingly we see that for $P_{ex} = 7\mu$W we have injected just enough excitons such that the resulting photoluminescence pattern is almost identical to the one recorded after the pump pulse. This is a clear evidence that the potential landscape around the position of the ring is highly complex. Moreover this resemblance would indicate that the formation and location of the fragments are largely due to the potential landscape since we are able to form a fragmented ring with an excitation beam which would normally not allow it. This observation has a very importance consequence, indeed the self-organization of the photoluminescence of the ring in fragments at the low bath temperature is often interpreted as the sign of a phase transition towards a quantum regime [57, 116]. In our experiment, we see that the appearance of this fragmentation is the result of the diffusion of excitons in a complex potential landscape and thus quantum processes are not involved. We can therefore ask ourselves if this conclusion should be extended to other experimental and theoretical works present in the literature. When we increase the bath temperature we have seen that the potential landscape becomes more regular (in particular we note the disappearance of the confining potential, see previous section) which would explain the vanishing of the fragmentation. If we keep increasing the excitation power we can imagine that excitons eventually overfill the local trapping potentials and keep diffusing away from the position of the ring, which is what we observe for the last excitation power in fig. IV.9.

IV.B.2 Spectral information

To complete the study of the direct photoluminescence, we measure spatially resolved spectra of the photoluminescence created by the small beam at 790nm for various excitation power. As usual, the entrance slit of the spectrometer is aligned at the center of the ring. Spectral images are shown in figs. IV.10(c-e). In order to interpret these data we also record the spatially resolve spectrum of the photoluminescence after the pulse at 641.5nm (see fig. IV.10(a)). An additional point of comparison is given by the measure of the potential obtained by recording the photoluminescence created by a vertical linear-shape beam at 790nm with very low excitation power, as performed in the section IV.A.2. As usual the linear beam is aligned vertically and horizontally at the position corresponding to the center of the ring and its photoluminescence is recorded with a window matching the 200ns duration of the pulse. The resulting spectral image is displayed in fig. IV.10(b). Let us note that the linear and small beams at 790nm are independent and that their respective photoluminescences are being recorded independently in order to avoid perturbations between the measurements (the small beam is switched off when the photoluminescence created by the linear beam is been recorded and reciprocally).

The purpose of these measurements is not to provide detailed analysis of the energy and intensity profiles of the photoluminescence as it has been done in the previous sections. We will therefore limit the study to the variation of the peak energy and intensity of the exciton line at two different positions, namely at the positions corresponding to center of the ring and to the ring itself (the positions are displayed by the white dashed lines in figs. IV.10(a-e)). Fig. IV.10(f) shows the evolution of these energies with the excitation power of the small beam (the corresponding evolution of the intensity is displayed in fig. IV.10(g)), while the values of the energies for the potential and the photoluminescence after the pulse at 641.5nm are displayed by horizontal dashed lines.

First of all, as a general observation, we see that the overall shape of the spectra resulting of the filling of the potential by the small beam at 790nm is very similar to the one of the fragmented ring. This is particularly the case for the spectral image shown in fig. IV.10(f)) which corresponds to the excitation power $P_{ex} = 7\mu$W for which the direct images of the photoluminescence were almost identical (see figs. IV.9(a) and (d)). This confirms that excitons created by the small beam at 790nm and the ones created by the beam at 641.5nm explore a very similar potential. However, at the center of the ring, one can see that the energy of the photoluminescence created by the small beam ("PL 790") is always lower than the energies of the potential and the fragmented ring (resp. "PL 790 probe" and "PL 641", see upper half of fig.IV.10(f)). This is surprising since in principle the energy can not be lower than the potential. We attribute this

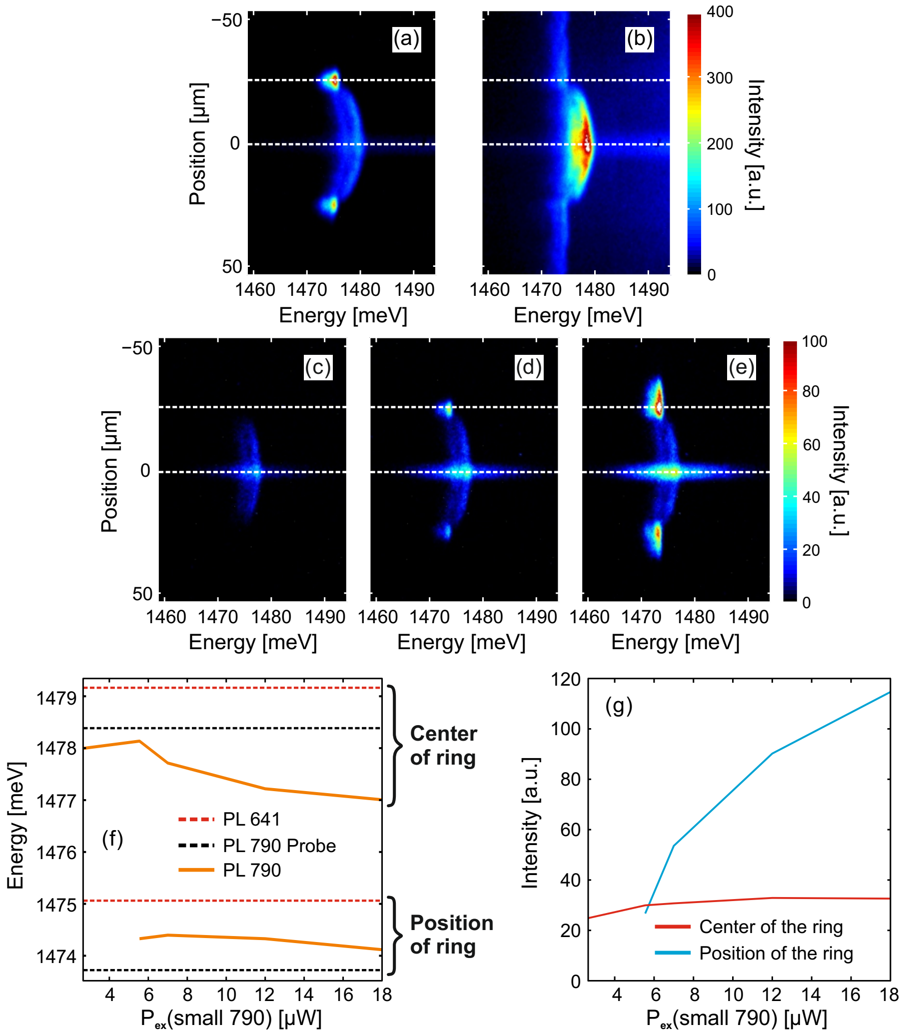

FIGURE IV.10: (a) Spatially resolved spectrum taken with the entrance slit of the spectrometer aligned at the center of the photoluminescence presented in fig. IV.9(b). (c-e) Same as (a) for the images (c-e) in fig. IV.9 (i.e. from left to right $P_{ex}(790) = 2.65$, 7 and 18μW and $P_{ex}(641.5) = 11.3\mu$W). (b) Spectrally resolved spectrum of the photoluminescence created by a vertical linear beam aligned horizontally and vertically with the center of the ring. The data was recorded with a window matching the length of the pulse at 790ns, corresponding to the second green rectangle in the schema of the pulse sequence displayed in fig. IV.9(a), in this case $P_{ex}(790) = 200$nW. (f) Oranges lines : evolution of the peak energy of the exciton line of the photoluminescence with the excitation power of the small beam at 790nm, taken at two positions along the vertical axis on the spectral images (c-e) (marked by the white horizontal dashed line in the spectral images (c) to (e) and named "PL 790"). The red (resp. black) horizontal dashed lines mark the value of the peak energy of the exciton line at the two same positions for the spectral image (a) (resp. (b)) and are named "PL 641" (resp. "PL 790 probe"). (g) Evolution of the peak intensity of the exciton line of the photoluminescence with the excitation power of the small beam at 790nm. The blue line (resp. red) corresponds to the position of the upper white dashed line (resp. white dashed line at the center vertically). The curves corresponding to the position of the ring in (f) and (g) only start for $P_{ex}(\text{small } 790) \gtrsim 6\mu$W since for lower excitation powers no photoluminescence can be observed at this position. Experimental parameters are identical to the ones in fig. IV.9.

energy difference to a modification of the potential induced by the small beam at 790nm (we recall that the potential is measured independently). Indeed, we know that this pulse can inject charges which can recombine with the ones left by the pump excitation. This would cause a decrease of the amplitude of the dome-shaped part of the potential. Increasing the excitation power will then have for effect to inject more charges which will further lower the potential. This interpretation is confirmed by drop of the energy at the center of the ring when the excitation power is increased. At the same time the intensity at this position remains essentially constant as shown by the red curve in fig. IV.10(g), which means that the redshift of the energy can not be the result of a lower density of excitons.

If we now consider the situation at the position of the ring (see lower half of fig. IV.10(f)), we see that the energy of the photoluminescence created by the small beam at 790nm slightly decline when the excitation power is increased and stays between the energies corresponding to the potential and the fragmented ring. If we consider that the potential remains constant, this would indicate that the density of excitons is dropping at the position of the ring. This is unexpected because we would have anticipated on the contrary that the density of excitons would increase as more and more excitons are being injected and diffuse to this region. The strong increase of the intensity with the excitation power contradicts this counter-intuitive behavior and shows that it is not the result of a limitation of the density by the exciton diffusion away from the ring. In the previous paragraph we have seen that the small beam at 790nm affects the potential and we can imagine that this effect is probably not limited to the sole center of the ring. In particular, if the potential experiences an overall redshift in energy as the excitation power is increased, then this redshift could compensate the blueshift of the spectral line signing an increase of the density of excitons. In this case we can not conclude on the variation of the density since a stable reference point for the energies is missing.

To conclude this section, we have seen that the fragmentation of the ring is most likely the results of a complex potential landscape around the position of the ring. The previous experiments show that in principle we should be able to fill this potential and to see how excitons explore the potential and accumulate in local traps. However in order to measure precisely these effects we need to know the modifications induced by the injection of excitons (and especially of additional charges) by the filling pulse on the potential landscape created together with the fragmented ring. Such analysis goes beyond the scope of this thesis. We could for example imagine to use an excitation at a lower energy (higher wavelength) in the hope to inject less charges. Another possibility in the spirit of the work presented in this chapter would be to use a sequence with three pulses : the first one at 641.5nm creates the ring and the potential landscape, then later on another pulse at 790nm (or at another wavelength) injects excitons and finally a last pulse with a linear beam-shape (also at 790nm) measures the modified potential landscape.

As a general remark, being able to tune the density of excitons at the position of the ring would be of great advantage for experiments studying fragmented rings. Indeed the experiments reported in this thesis show that the potential landscape created along with the formation of such ring is favorable to the appearance of quantum gases of excitons. The problem is that the mechanism behind the generation of this potential potential landscape also effectively sets the density of excitons. Therefore we can not explore the relation between the density and the emergence of the quantum regime, which would provide an important additional proof of Bose-Einstein condensation. It is our conviction that an improved version of the experimental procedure described in this section could provide the proper tools to investigate this effect. As a matter of fact, it would already be interesting to carry out the measurements performed in the next chapter (long-range spatial coherence and polarization) on the photoluminescence patterns observed in this section with the simple pulse sequence (such experiments goes beyond the scope of this thesis). If we observe the same kind of results then we would know that the formation of a quantum gas of excitons is directly dependent on the potential landscape. The evolution of these results with the excitation power of the "filling" pulse could then provide a first idea of the dependency to the density of excitons. Negative observations could either indicate that the modifications of the potential by the "filling pulse" are too important, or that an adequate density can not be reached, or finally that additional processes occurring along with the formation of the fragmented ring are necessary to allow for the formation of a quantum gas of excitons.

IV.C Conclusion

In this chapter, the extensive use of pump-probe spectroscopy allowed us to measure the potential landscape which appears together with the formation of the fragmented ring. While the processes behind the formation of this potential are probably too complex to be determined accurately, we showed that the injection of free charges by the laser excitation can provide a viable explanation. Indeed, the presence of charges can easily lead to a modulation of the internal electric field created by the applied voltage. Our measurements confirm that the potential presents an anti-trap dome shape inside the ring. More surprisingly, we can sometimes observe local confinement potentials around the position of the ring. We were then able to retrieve accurately the distribution of the exciton density and we observed that depending on the shape and depth of the local traps, dense gases of dark excitons can form in the outside vicinity of the ring. As explained throughout this thesis the presence of a dominant fraction of dark excitons is a direct proof that the gas of excitons has entered a quantum regime. In order to ascertain this quantum nature we measure in the next chapter the spatial coherence and the polarization of the photoluminescence.

Interestingly, by filling the potential landscape with an additional laser pulse we were able to reproduce the photoluminescence pattern of the fragmented ring, even though this excitation can normally not produce a fragmented ring. This result seems to indicate that the fragmentation of the ring is at least partially caused by the diffusion and local accumulation of excitons in the very complex potential landscape present along the circumference of the ring.

As a general remark, it is our conviction that the model based on the sole ambipolar diffusion of free charges is not sufficient to explain the formation of fragmented rings and that the diffusion of excitons in the potential landscape plays an important (if not dominant) role (at least for our sample).

Chapter V

Quantum coherence and polarization of a “gray” condensate of excitons

In the previous chapter, we have seen that in the exterior vicinity of the ring, the exciton gas can exhibit a dominant population of dark excitons which suggests the presence of a Bose-Einstein condensate. In order to ascertain the presence of this quantum gas we measure two of the characteristics inherent to the formation of an exciton condensate : long-range spatial coherence and linear polarization. To probe these features we first present shift-interferometry measurements (see section V.A). This experiment reveals the presence of islands of macroscopic spatial coherence outside of the ring i.e. in the region where we measured the dense gas of dark excitons. We will see that the interpretation of the phase of the $g^{(1)}$-function in term of motion of excitons can highlight the potential landscape. In particular, the regions presenting a large degree of spatial coherence are found together with specific variations of the phase of the $g^{(1)}$-function which are consistent with the presence of a confining potential. Subsequently, we measure the dynamics of the interference contrast and find it to be larger after the excitation pulse. Finally, we study the polarization of the photoluminescence (see section V.B) and find a significant degree of linear polarization in the “gray” region outside the ring. These results confirm the presence a “gray” condensate of excitons in agreement with the predictions of Monique and Roland Combescot [50]. To conclude this chapter we compare our results to similar experiments performed by the group of L. Butov.

V.A Spatial coherence

The purpose of this section is to measure the spatial coherence of the photoluminescence by setting a lateral shift between the two outputs of the Mach-Zehnder interferometer. Details on the interferometer can be found in section II.B.2 while considerations on the expected behavior of the first-order correlation function for this experiment are presented in section II.B.2.b. In the following sections we will first measure the variation of $g^{(1)}$-function with the lateral shift for various bath temperatures in order to obtain the evolution of the coherence length. In a second time we record maps of the value of the $g^{(1)}$-function at a fixed lateral shift. Finally we study the dynamics of the value of the interference contrast.

V.A.1 Calibration and coherence length measurement

To measure the spatial coherence of the photoluminescence we performed experiments similar to the ones for the time-interferometry but this time with $\delta t = 0$. First of all, we need to calibrate the interferometer in term of lateral shift and try to retrieve the coherence length of the exciton gas. Figure V.1 presents normalized interferograms of a region of the ring at two different bath temperatures. One can already see than when increasing δx the fringes with the highest contrast can be found outside of the ring and only at the lowest temperature. In order to quantify this behavior, we measured the contrast in given regions of the interferograms (indicated by the vertical red lines) by fitting a vertical profile with a cosine function whose amplitude gives an averaged value of $\left|g^{(1)}(\mathbf{r}, \delta x, 0)\right|$ for the vertical region considered (see equation II.4). This of course supposes that the contrast is homogeneous vertically such that its spatial variation essentially depends on the distance to the center of the ring. If this is not the case the measured contrast is likely to be underestimated. We could in principle measure maps of the contrast for a set of δx and have a much more accurate spatial definition of the contrast, however such map requires a long time to acquire and since we only have a limited time at the lowest temperature we preferred to do the experiments as described above since they can be performed in a single shot. For the same reasons, the interferometer phase was not stabilized for these measurements since realigning the stabilization for each δx is too time consuming. This partially explains the relatively low maximum contrast. Additionally, we voluntarily lowered the distance between the fringes (larger α) in order to increase the spatial resolution (we need less fringes in the vertical profiles to perform an accurate fit) which has the effect of slightly worsen the interferometer alignment. The experimental conditions are the same as in the chapter

3 : the data are recorded with a 40ns window starting 10ns after the end of the 1μs-long pulse at 641.5nm, the repetition rate being 2μs. The excitation power and applied voltage are respectively 11.6μW and -4.85V.

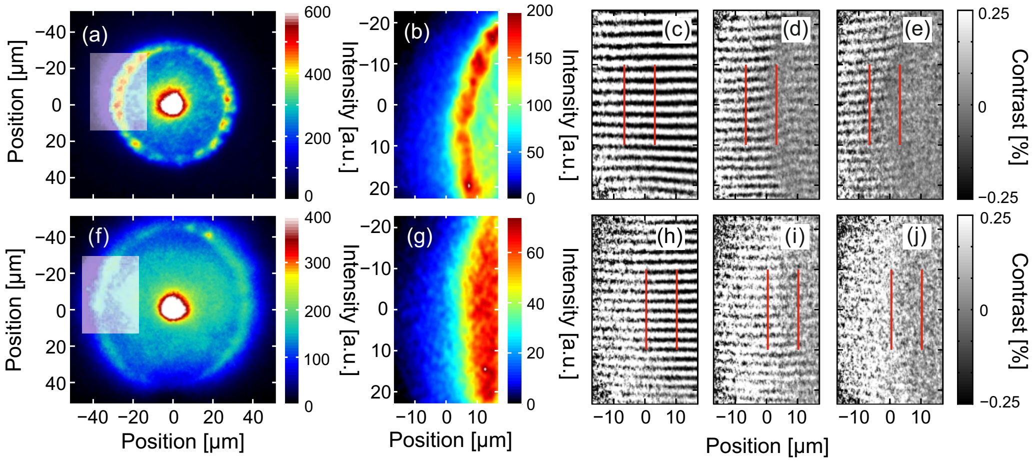

FIGURE V.1: (a) Direct images of the photoluminescence at $T_b = 370$mK. (b) Photoluminescence of one of the arm of the interferometer, corresponding to the white transparent region in (a). (c-e) Normalized interferograms of the photoluminescence in (b) for lateral shifts of $\delta x = 0$, 1.4 and 2.4μm (from left to right). The red lines represent the region on the ring and 10μm outside it at which vertical profiles are retrieved in order to calculate an averaged contrast using a cosine fit. (f-j) Same as (a-e) for $T_b = 7$K.

The results of the experiment are presented in fig. V.2. As one can see in figs. V.2(a-b), the variations of the contrast with the lateral shift for both positions at $T_b = 7$K and on the ring at $T_b = 370$mK are essentially identical : starting from the maximum of the contrast for $\delta x = 0$ at around 40% the contrast rapidly drops lower than 5% for $\delta x \gtrsim 2\mu$m. By contrast, outside the ring at $T_b = 0.37$K the drop is much less pronounced and the contrast remains relatively high over a longer range of δx. Fits of the experimental points with the absolute value of the $g^{(1)}_{\text{obs}}$-function (see eq. II.23) are shown with dashed and solid lines in fig. V.2(a-b) while the obtained coherence lengths ξ can be found in the table V.2(d). For both positions at $T_b = 7$K, the retrieved ξ are very small (as expected for a thermal gas) and thus the exponential decay do not contribute to the convolution product : $g^{(1)}_{\text{obs}}$ and the variation of the contrast solely reflect the point-spread function (PSF) of the experimental system. Therefore the fitting of the data for $T_b = 7K$ allows us to calibrate the PSF and we obtain an optical resolution of $\sim 1.5\mu$m which is in agreement with the characteristics of the set-up (see section II.B.1).

Using this value we can fit the experimental points for $T_b = 340$mK. On the ring we obtain a coherence length which is in the order of magnitude of the de Broglie wavelength, however $\sim 10\mu$m outside the ring we measure $\xi \sim 1.3\mu$m i.e. much larger than the de Broglie wavelength ($\lambda_{\text{dB}}(T_b = 370\text{mK}) \sim 260$nm). Thus the photoluminescence presents

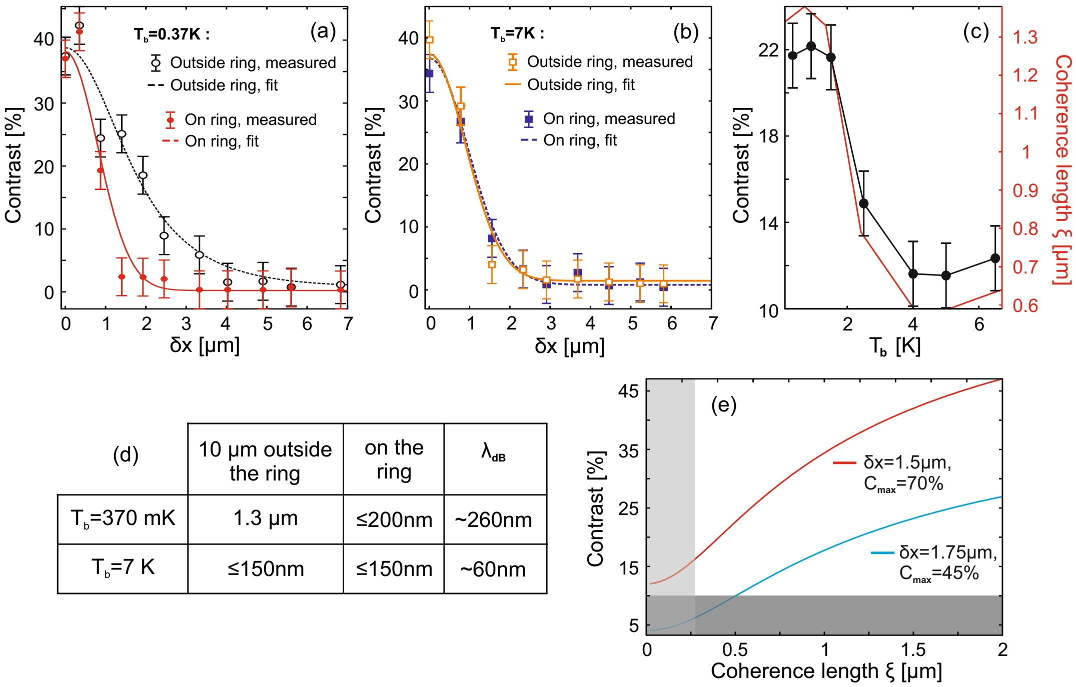

(d)	10 μm outside the ring	on the ring	λ_{dB}
T_b=370 mK	1.3 μm	≤200nm	~260nm
T_b=7 K	≤150nm	≤150nm	~60nm

FIGURE V.2: (a) Interference contrast of the area marked by the vertical red lines in fig.V.1 as a function of the lateral shift δx for $T_b = 370$mK. Measurements done at the position of the ring (red filled circle) and $\sim 10\mu$m outside the ring (black empty circle). (b) Same as (a) for $T_b = 7$K (filled and open squares respectively). Solid and dashed lines in (a) and (b) show the best fit our theoretical model to the experimental data. (c) Variation of the contrast $\sim 10\mu$m outside the ring as a function of T_b for $\delta x = 1.75\mu$m (black dots). The red line shows the corresponding evolution of the coherence length obtained with the blue curve in (e). (d) Values of the coherence length obtained with the fitting model for each bath temperatures and positions with respect to the ring. The thermal de Broglie wavelengths λ_{dB} at both temperatures are also shown. (e) Evolution of the contrast with the coherence length according to the fitting model used for 2 different sets of parameters. In red (resp. blue) $\delta x = 1.5\mu$m (resp. 1.75μm) and the value of the contrast for $\delta x = 0$ is $C_{\text{max}} = 70\%$ (resp. 40%). The transparent light gray area extends until the value of the de Broglie wavelength for $T_b = 0.34$K while the darker gray transparent area marks the contrast threshold below which no interpretation can be made.

long-range spatial coherence in the outside proximity of the ring which is a clear evidence of the presence of a quantum gas of excitons.

As explained previously these measurements only give an averaged value of the contrast and therefore of the coherence length. In order to get a better spatial definition, we performed scans of the interferometer phase to directly obtain maps of the degree of coherence. The optimum way to obtain maps of the coherence length would then be to measure the contrast maps for a set of δx and to fit the $g^{(1)}_{\text{obs}}$-function for each spatial point. The problem is that measuring a single map can take up to 2 hours and we only have 6 hours measurement time at the coldest temperature, therefore we would not be able to acquire a complete set within the available time. We do not have the same issue at warmer temperature however a whole set of measurement with various temperatures would take several days without the guarantee of having the exact same experimental conditions (for instance the same ring) between one day and the next. A possible method to overcome this problem is to reverse the formula used for the fit (i.e $g^{(1)}_{\text{obs}}$, see eq. II.23) and obtain the coherence length for a given contrast value.

The resulting curve will depend on the optical resolution, the lateral shift and the maximum value of the contrast. Fig.V.2(e) shows such plots for two sets of $(\delta x, C_{\text{max}})$, where we used the value of the optical resolution retrieved in the previous experiments at $\text{T}_b = 7\text{K}$. It is important to note that this method presents 2 limitations (represented by the two transparent gray areas in fig.V.2(e)) for low coherence length and low contrast. Indeed, as explained in section II.B.2.b, for $\xi \lesssim \lambda_{\text{dB}}(T_b = 0.34\text{mK})$ the exponential decay does not influence the $g^{(1)}_{\text{obs}}$-function which is then solely given by the Point Spread Function and the optical resolution. This effectively limits the minimum measurable coherence length. The second limitation comes from retrieving the contrast value by fitting a noisy profile with a cosine function. Indeed, as explained in the second part of the section II.B.2.b, when the random fluctuations are in the order of magnitude of the cosine amplitude we expect to observe, such fit will always give a value for the amplitude which can easily go up to 10%. Thus, below this threshold, we can not distinguish an artificial contrast value from an actual degree of coherence and therefore we can not extract a value of the coherence length. Comparing the 2 curves in fig.V.2(e), one can see that in order to obtain the maximum resolution for the coherence length optimizing both δx and C_{max} is critical. In order to obtain a higher C_{max} we decreased the distance between the interference fringes (by lowering α) since the spatial resolution given by small distances between the fringes is not a problem with the method relying on the scan of the interferometer phase (in principle we do not even need fringes but their presence is a very convenient tool for the interferometer alignment). Choosing a proper value for δx can be done by studying the two fits in fig.V.2(a) where we see that the maximum difference between the curves occurs for values of δx between ~ 1.5 and $2\mu\text{m}$. In order to maximize the value of the contrast for large coherence length we set δx at $1.5\mu\text{m}$.

Phase transitions usually go along with strong variations of order parameters with experimental conditions. For the phase transition from a classical to a quantum gas (particularly for a Bose-Einstein condensate) the evolution of the coherence length with the bath temperature is usually a strong indicator. In order to investigate this variation, we measured the contrast of the interferences $\sim 10\mu\text{m}$ outside the ring for a lateral shift of $1.75\mu\text{m}$. The results are displayed in fig.V.2(c) along with the corresponding values of the coherence lengths obtained from the calibration curve in fig.V.2(e). One can notice that the contrast at high temperature remains relatively large which would correspond to a coherence length larger than de Broglie wavelength we expect to find at these temperature (and which we did measure for T$_b$ = 7K). This should not be interpreted as the presence of extended coherence but rather, as explained previously, as the inaccuracy of the cosine fit when the contrast value is low. Strikingly one can see that the contrast and the coherence length rapidly drop for $T_b \gtrsim 2$K which is a strong indication of a phase transition from a classical gas to a "gray" condensate of excitons.

V.A.2 Advanced interferometry at fixed lateral shift

To unambiguously demonstrate the regime of macroscopic spatial coherence, we measured maps of the degree of coherence for various bath temperatures and ring realizations for a lateral shift of $\delta x = 1.5\mu$m and a maximum contrast of $C_{\max}(\delta x = 0) \simeq 70\%$. The results of this experiment for T$_b$ = 0.34K are displayed in fig. V.3. The experimental procedure has been described in section II.B.2 and we will only briefly remind it here. In order to obtain the g$^{(1)}$-function all over the photoluminescence, we vary the phase $\phi = 2\pi\delta l/\lambda_{\text{stab}}$ of the interferometer. The effect of the phase shift can be seen in the normalized interferograms in figs. V.3(b-d), where the fringes slip vertically. The relative phase shift between the interferograms is retrieved by fitting a vertical profile (taken along the vertical blue line) with a cosine function whose argument reads : $q_\alpha z + \varphi_{\mathbf{r};\delta x,0} + \phi$. Since the term $q_\alpha z + \varphi_{\mathbf{r};\delta x,0}$ does not vary between the interferograms, the result of the cosine fit gives us both q_α and ϕ ($\varphi_{\mathbf{r};\delta x,0}$ is considered as a fixed phase). Then the variations of the contrast with ϕ at a given spatial point (x, z) of the interferograms (see fig. V.3(e)) is also a cosine function which can be fitted by $I_{\text{int}}(x, z; \delta x, 0) = \cos\left(q_\alpha z + \varphi_{\mathbf{r};\delta x,0} + \phi\right) \left|g^{(1)}\left(x, z; \delta x, 0\right)\right|$. Repeating this process over the whole photoluminescence allows us to retrieve the corresponding maps of the contrast of the fringes (i.e. the amplitude of the previous cosine function $\left|g^{(1)}\left(x, z; \delta x, 0\right)\right|$, which is also the degree of spatial coherence), of the relative error of the contrast and of the phase of the previous cosine function $(q_\alpha z + \varphi_{\mathbf{r};\delta x,0})$, as shown in fig. V.3(f-h).

V.A.2.a General observations

As expected from the measurements of the previous sections, the map of the contrast reveals a maximum of degree of coherence $\sim 7\mu$m outside the ring (see fig. V.3(f)). The position of this maximum is illustrated by looking at the respective profiles of the contrast and photoluminescence intensity along the horizontal axis at a given vertical position (see in fig. V.3(i)). Importantly, we see that when moving towards the exterior of the ring and after a well-marked maximum the contrast substantially decreases in a region where the relative error is not yet too high. This confirms that the extended spatial coherence is only located in the vicinity of the ring and does not extend further

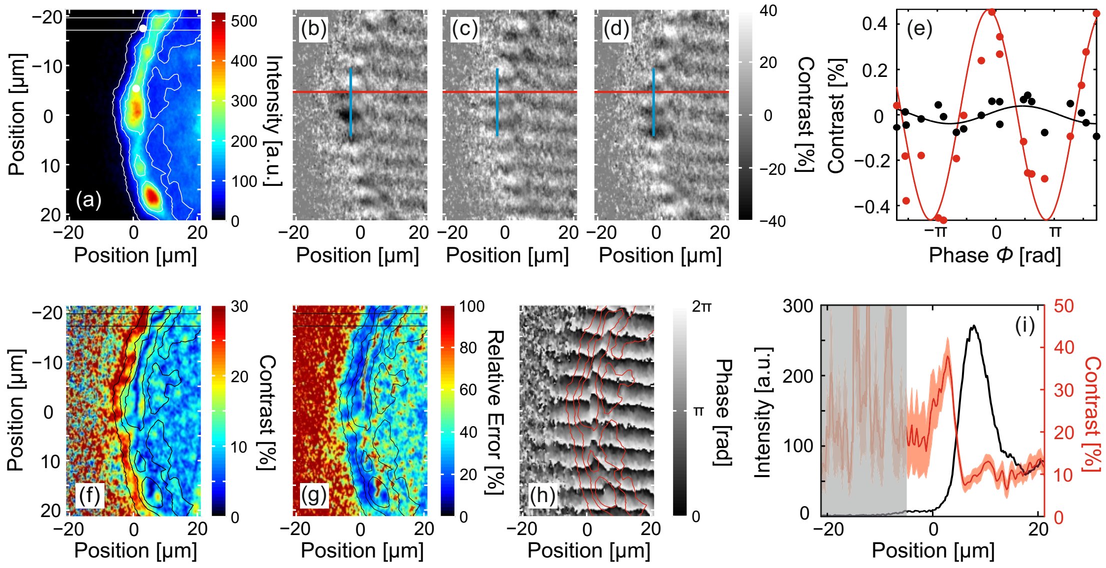

Figure V.3: (a) Direct photoluminescence coming from one of the interferometer arm for $T_b = 0.34$K, the white lines are isointensity contour lines for intensities of 20, 100 and 200. (b-d) Normalized interferograms of the photoluminescence (a) for $\delta x = 1.5\mu$m and various phases ϕ between the 2 arms : from left to right 0, π and $\pi/2$ (the horizontal red line is a guide for the eyes to follow the slip of the interference fringes). The phase ϕ is measured for each interferogram by fitting the contrast profile along the z-axis (blue line in (b-d)) with a cosine function. (e) Evolution of the contrast of the fringes with the phase of the interferometer at 2 positions on the photoluminescence : outside the ring (red dots) and at the position the ring (black dots), the positions are marked by the white dots in (a). Fitting the evolution with a cosine function (solid red and black lines) gives the amplitude of the contrast and the phase at a given position. (f-h) Contrast, relative error of the contrast and phase maps obtained by fitting the contrast fluctuations with the interferometer phase at each point of the photoluminescence. The black (f-g) and red (h) lines are the same contour lines as in (a). (i) Contrast (red) and intensity (black) profiles along the horizontal axis in the area delimited by the white (a) and black (f-g) horizontal lines. The transparent red area represents the error for the contrast due to the cosine fit while the gray transparent area shows the region outside the ring where the relative error is $\sim$ 100% at the vertical position the profiles are taken.

away. Our experiments thus show that we only observe long-range spatial coherence in a region where the intensity of the photoluminescence can be up to 10 times less than on the ring which confirms the hypothesis of a quantum gas with a dominant population of dark excitons. At the position of the ring and inside of it the contrast is about 10% which is consistent with the threshold we defined for a lower limit of meaningful contrast (see the second part of the section II.B.2). Interestingly the map of the degree of spatial coherence (see fig. V.3(f)) shows that the regions of high contrast are organized in small “islands” apparently randomly placed and in particular not correlated in position with the fragments of the ring. It is very enlightening to compare these findings to the observations of confining potentials in the previous chapter. Indeed let us recall that we could only observe the “gray” condensate of excitons in specific confining potentials. While we could not measure the lateral size of the potential along the circumference of ring, the section where we try to fill the potential shows that the potential landscape is highly irregular, such that these adequate potentials are likely to be of limited extension. Therefore it is not surprising that we only observe size-limited "islands" of long-range spatial coherence : this indicates that excitons can only condense in small and adequate regions of the potential landscape.

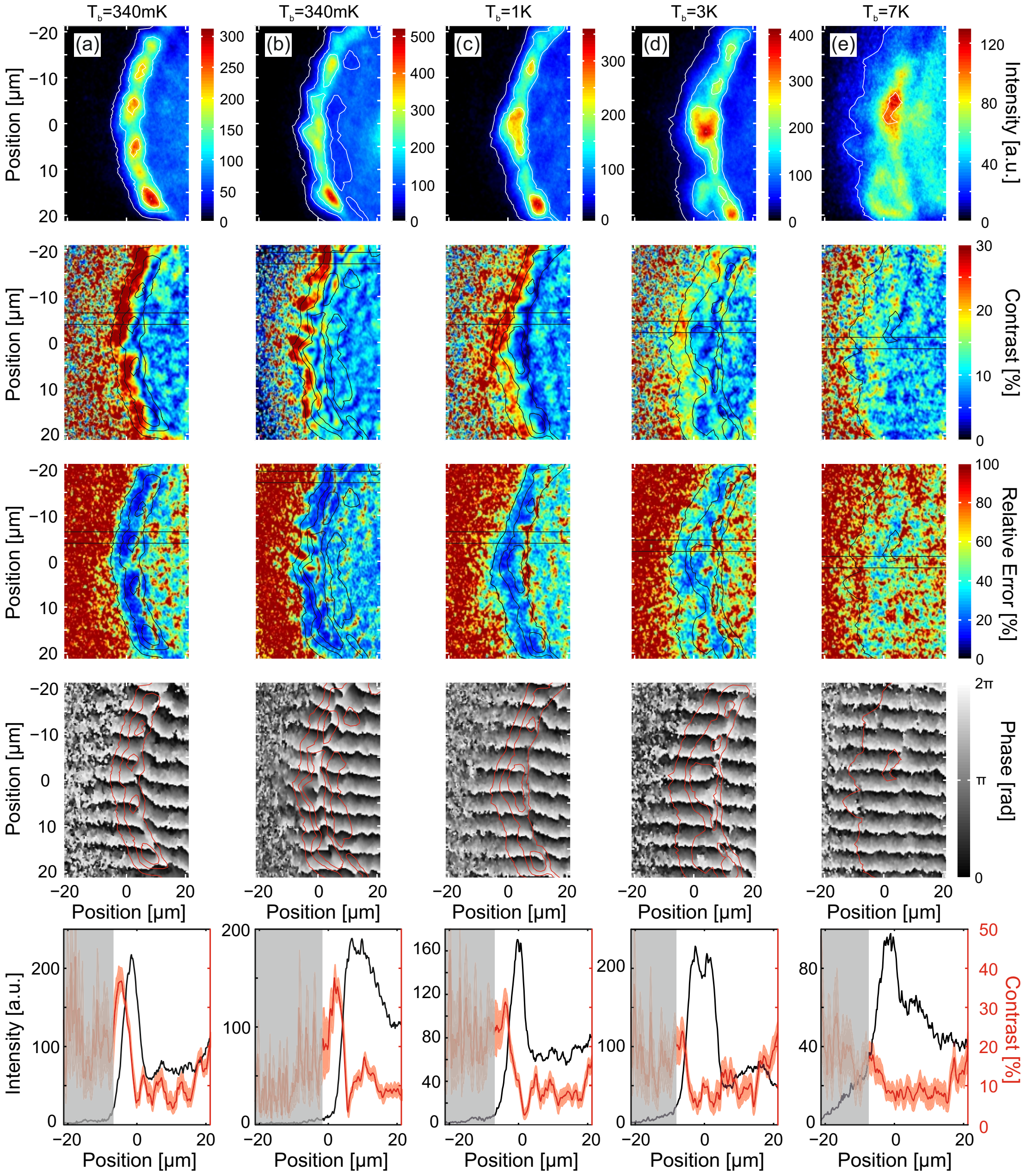

FIGURE V.4: (a) and first column from top to bottom : One-arm photoluminescence image, contrast map, relative error map, phase map, contrast and intensity profiles taken in the horizontal region marked by the horizontal black lines with the corresponding contrast error and 100% relative error transparent areas. The data were taken with the same experimental parameters as in fig.V.3 but at a different position on the sample. (b) and corresponding column : same as (a) at another point on the sample. (b-e) and corresponding columns : same as (a) but for various bath temperatures.

Fig. V.4 presents other measurements for 2 other positions on the samples at $T_b = 0.34$K (first two columns) and at the same position for other bath temperatures (the other experimental parameters such as gate voltage and excitation power always remain identical). By comparing the maps of the contrast at the lowest temperature we see that we always observe a qualitatively similar distribution of the degree of coherence with localized maxima outside the ring and low contrast on the ring and inside it. This proves that the phenomenon we observe is not specific to an area of the sample but is characteristic to our system. The location and contrast value of the islands (and the overall shape of the ring) are however different which show that positions on the sample are not fully equivalent and affect the ring and its characteristics. This is consistent with the observations of the previous chapter which show that the confining potentials adequate for the condensation of excitons can be found at various positions along the circumference of the ring depending on its shape. As seen on the contrast maps, increasing the bath temperature rapidly leads to both a homogenization and a drop of the contrast towards an essentially flat distribution at the background contrast value for $T_b \sim 7$K. Let us note that for most of the bath temperatures the contrast presents a minimum right at the inside edge of the ring (see deep blue stripe on the contrast maps) which coincides with a disruption of the fringes as can be seen on the phase maps.

The evolution of the degree of spatial coherence both on the ring and outside with the bath temperature is displayed in fig. V.5(a). Outside the ring the contrast presents a step-like shape with a discontinuity for $T_b \sim 2$K while on the ring the contrast remains essentially constant. Thanks to the calibration of the coherence length shown in fig. V.2(e), we can plot the corresponding coherence length outside the ring which presents an even more pronounced step. This is consistent with the previous measurements (see fig. V.2(c)) and confirms that the exciton gas outside the ring experiences a transition to a quantum gas with extended spatial coherence at $T_b \lesssim 2$K. It has to be noted that retrieving representative values of the contrast for the different temperatures is not trivial due to the heterogeneous distribution of the contrast value, especially at the lowest temperatures. In order to obtain a more general display of the localization and variation of the degree of coherence we modified the color scale of the contrast maps with the aim of emphasizing the regions where the coherence length is larger than 1μm (i.e. the contrast is larger than $\sim 34\%$) by marking them in red, while the areas with lower degree of coherence are rendered visually unattractive. As shown in fig. V.5(c-g), the resulting maps are striking with "islands" of macroscopic coherence length which are extremely well localized next to the ring and completely disappear for $T_b > 1$K. The small red dots further away from the ring are to be ignored since they are located in regions with a very large relative error. Interestingly, the size of the islands of extended

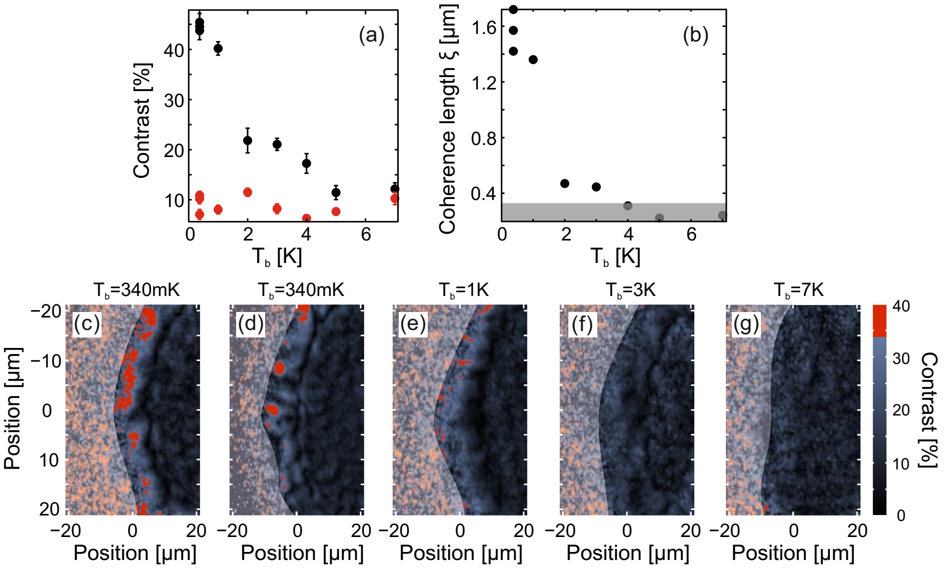

FIGURE V.5: (a) Evolution of the contrast value with the bath temperature, retrieved from the contrast maps in figs. V.3 and V.4. The contrast at each temperature is a representative value of the degree of coherence which can be find outside the ring (black dots) and on the ring (red dots). (b) Evolution of the coherence length ξ with the bath temperature for the points outside of the ring presented in (a). The coherence lengths were obtained using the red curve presented in fig. V.2(e). The transparent gray area represents the region where the model used to make the link between coherence length and contrast value is not valid ($|g^{(1)}| \lesssim 15\%$). (c-g) Contrast maps at various bath temperature (same as fig.V.4). The particular color scale aims to emphasize the region of the photoluminescence where $\xi > 1\mu$m which corresponds to a degree of coherence larger than $\sim 34\%$ (see red curve in fig. V.2(e)). The transparent white area represent the regions outside the ring for which the relative error of the contrast value is $\sim 100\%$, (see error maps in fig. V.4)

spatial coherence has the same order of magnitude as the measured coherence length (area of the islands between 1 and 4 μm^2 for a ξ up to 1.5μm). This is in agreement with the general consideration on the g$^{(1)}$-function presented in the section II.B.2.b where we show that the coherence length is limited by the size of the wavefunction of the condensate. Considering the small size of the islands it is therefore not surprising that the coherence length is limited.

Thanks to the the pump-probe experiment we were able to obtain an estimation of the density of excitons outside the ring, namely between 1 and 2.10^{10}cm^{-2}. This means that a typical island contains a few hundreds of excitons. It would be interesting to know the fraction of condensed excitons in this population. However because of the small value of the coherence length (and the size of the islands) we can not resolve the plateau in the variation of the first-order correlation function which would give the fraction of condensate (see fig.II.12(a) and section II.B.2.b).

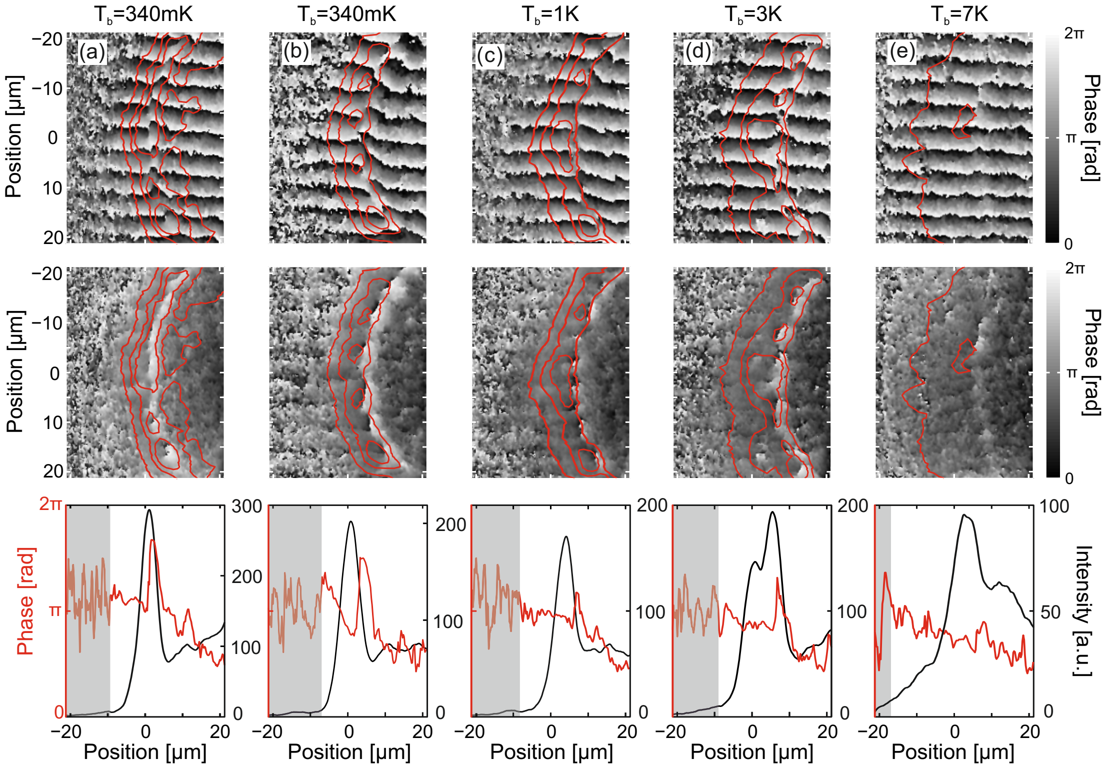

FIGURE V.6: (a) and corresponding column from top to bottom : map of the phase of the cosine fit, map of the phase of the $g^{(1)}$-function, phase and intensity profiles along the horizontal axis at the ordinate 0 on the vertical axis. The red lines on the maps are the contour lines of the photoluminescence and the gray transparent area on the profile plot marked the region where the relative error of the fit is $\sim 100\%$. (b-e) and corresponding columns : same as (a) for various bath temperatures (and position on the sample for the second $T_b = 340$mK).

V.A.2.b Analysis of the phase maps

To continue the study of the results of the shift-interferometry, let us analyze the phase maps with a method similar to the one used for the time-interferometry measurements. From the equation II.4 describing the interferograms, we know that the position of the fringes for a lateral shift δx is given by $q_\alpha z + \varphi_{\mathbf{r},\delta x,0}$ ($\delta t = 0$). Thus, the situation is considerably simpler than for the time-interferometry since in this case only the period of the fringes depends on the energy of the photoluminescence (through $q_\alpha = 2\pi/\lambda \sin\alpha$). One should note that the phase of the interferometer ϕ used to performed the scan also depends on λ since $\phi = 2\pi\delta l/\lambda$ where δl is the small path-length difference between the two arms of the interferometer. However since we only scan the fringes of a few wavelengths, δl is at maximum of the order of a few micrometers. This means that small variations of λ between two different points $\mathbf{r}$ of the photoluminescence will only result in small fluctuations of the period of the cosine function used to fit the variations of the contrast along ϕ. Therefore the effect of the dependency of ϕ in λ is negligible and will not affect the overall phase distribution. Additionally, the fluctuations of the energy of the photoluminescence over the radius of the ring is limited to a maximum of 4 meV (see sections III.C.3 and IV.A.4) which induces a fluctuation of the period of the fringes of a few percents maximum. Therefore extracting the phase of the $g^{(1)}$-function is just a matter of demodulating the phase map with respect to $q_\alpha z$, with a q_α which can be considered as uniform. The resulting maps of the value of $\varphi_{\mathbf{r},\delta x,0}$, i.e. the phase of the $g^{(1)}$-function, are displayed in fig.V.6.

As one can see on the profiles along the horizontal axis displayed in the last row in fig.V.6, at all temperatures $\varphi_{\mathbf{r},\delta x,0}$ steadily increases when moving from the center of the ring towards its exterior, presents a peak right before the ring and then remains essentially constant (except for the second map at $T_b = 0.34$K). Interestingly if we compare the profiles for the different temperatures, the peak amplitude drops when the bath temperature increases until its disappearance at $T_b = 7$K. The bump in the value of the argument of the $g^{(1)}$-function is located at same position of the fringes disruption we observe on the phase maps. This phase disruption is not without reminding the similar pattern observed on the phase maps of the time-interferometric measurements and which was linked to a sudden change in the photoluminescence energy as explained in the appendix A.

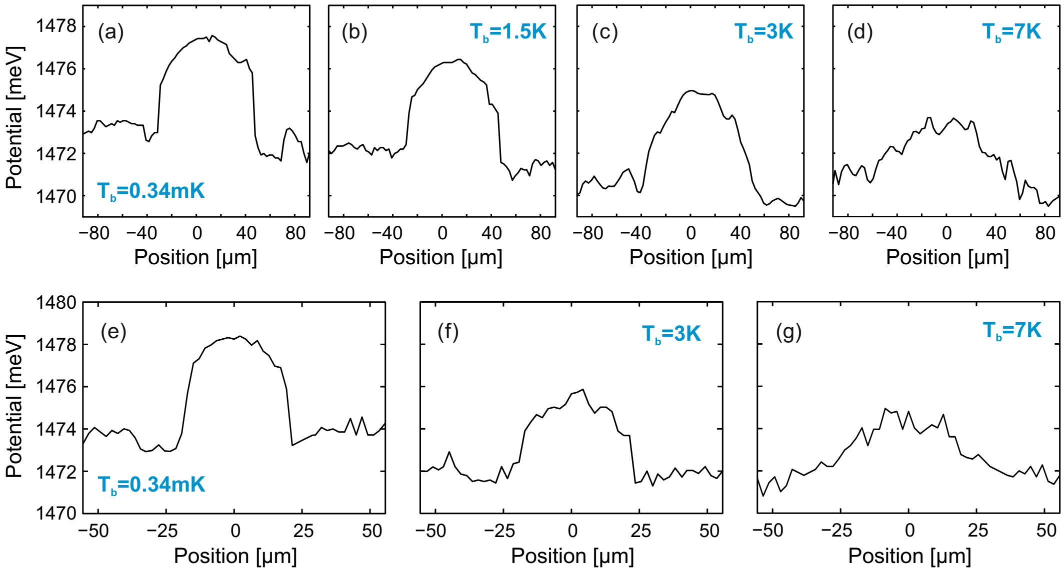

FIGURE V.7: Profiles of the potential landscape measured by the pump-probe experiments. Profiles (a-d) come from the appendix C, while (e-g) are from the section IV.A.4.

For a pure lateral shift we have seen in the section II.B.2 that the phase of the $g^{(1)}$-function can be related to the exciton velocity along the x-axis through the formula

$$\varphi_{\mathbf{r},\delta x} = \frac{M_X V_x(\mathbf{r})\delta x}{\hbar} \tag{V.1}$$

We will see that this relation provides a good ground in order to explain the variation of the phase of the $g^{(1)}$-function. The velocity can be affected by essentially 2 phenomena : the presence of a potential and a high density of the excitons which enhances their diffusion particularly due to the strong dipolar repulsion between them. Potentials inherent to the formation of the ring have been presented in section IV.A.4 and in appendix C for various bath temperatures and are showed again in fig. V.7. From their various shapes we can get an idea of the variation of the velocity of excitons along a radius of the ring. Starting from the center of the ring the potential slowly decreases until a cliff of high amplitude at the inner edge of the ring. Accordingly the velocity and the phase of the $g^{(1)}$-function would slowly increase and present a strong discontinuity at the position of the potential cliff. Since the amplitude of the potential decreases with the bath temperature the amplitude of the discontinuity for the velocity and the phase should decline accordingly.

This behavior is precisely the one we observe for the variation of the profiles of $\varphi_{\mathbf{r},\delta x}$ displayed in the last row in fig. V.6. One can note that since excitons are being created in a relatively small region at the position of the excitation spot, we can imagine that the high density of excitons at the center of the ring enhances the velocity at this position such that the phase should also present a discontinuity. Unfortunately our maps do not cover the center of the ring therefore we can not assess the behavior of the phase at this position. When excitons "fall" from the potential cliff they acquire a high velocity and therefore we would expect the velocity and the phase to remain at a high value at the position of the ring and further away from it. However this is not what we observe, indeed after a sharp increase the phase immediately drops down to a value similar to the one before the discontinuity. We do not have a clear explanation for this. We could imagine that the continuous flow of excitons at this position could create a kind of turbulence which suddenly stop them, similarly to the bubbling at the bottom of a waterfall. Additionally one can consider the effect of the strong dipolar repulsion due to the local accumulation of excitons at the position of the ring which creates an effective potential barrier. This interpretation is reinforced by the fact that the ring corresponding to a maximum of intensity most of the excitons at this position have relaxed towards the bottom of the dispersion band and thus have a very small momentum which is consistent with a low velocity. In the previous discussion we have only considered the displacement of excitons created at the position of the laser beam. However we have to keep in mind that excitons can also be directly created at the position of the ring according to the usual formation mechanism of the ring (excitons are also probably created inside the ring due to the presence of remaining electrons). This additional influx of excitons is very likely to influence the velocity distribution at the position of the ring.

Finally, after the peak of the phase value and moving further away from the ring, the phase can present distinct variations depending on the bath temperature (see phase profiles in fig. V.6) and the position with respect to the ring (see fig. V.8). As displayed in fig. V.7 the potential landscape can also exhibit different shapes ranging from simple features like slowly decreasing ramps or potential traps to much more complicated ones. Moreover if we consider that the high concentration of excitons at the position of the ring will enhance the diffusion, we can imagine that the exciton dynamics of in this region is probably very complex such that the velocity distribution can present many different behaviors. Therefore we will not try to interpreter all these phase profiles but we will focused on the phase profile which seem to emerge along with a high degree of spatial coherence.

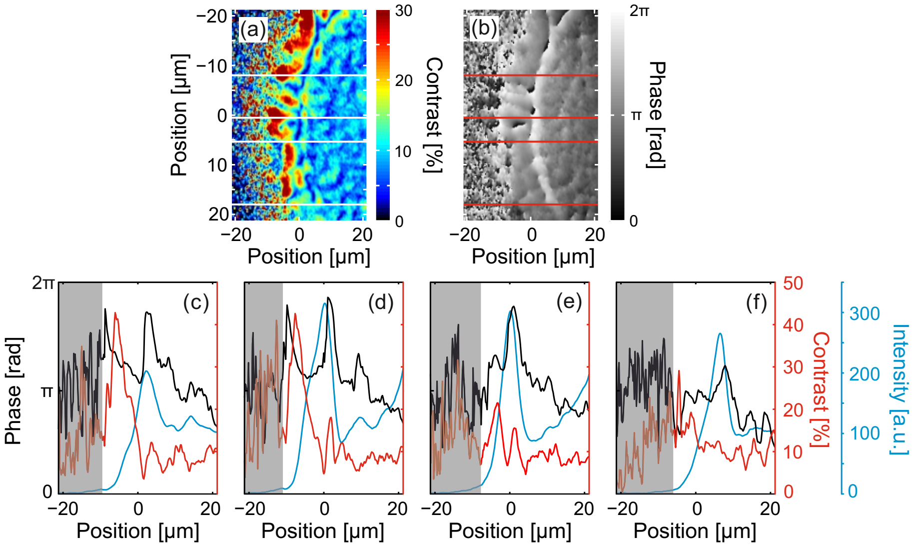

Figure V.8: (a) Map of the interference contrast (from the column (b) in fig.V.4). (b) Corresponding map of the phase of the $g^{(1)}$-function. (c-f) Profiles along the horizontal axis of the contrast (red), photoluminescence intensity (blue) and $\varphi_{x;\delta x}$ (black) at the vertical positions indicated by the white and red horizontal lines in (a) and (b) (plots from left to right correspond to the lines from top to bottom on the maps). The gray transparent areas mark the region outside the ring where the relative error of the contrast is $\sim 100\%$.

In fig. V.8, one can see that the regions of high contrast seems to be correlated to a particular variation of the phase. The contrast, intensity and phase profiles along the ring radius for two of the clearest of these regions are presented in figs. V.8(c) and (d). As seen previously, in the regions with long-range spatial coherence, the maximum of contrast is located in the exterior vicinity of the ring. Interestingly we see that the drop of contrast when moving further away from the ring is associated with another discontinuity of $\varphi_{\mathbf{r},\delta x,0}$, in particular the minimum of contrast coincides with a drop of the phase. On the contrary in the regions where the contrast is essentially homogeneous along the horizontal axis (see figs.(e) and (f)) no additional discontinuity of the phase of the $g^{(1)}$-function is observed. Similar behaviors are observed for the maps at the lowest bath temperatures (see for example fig. V.6(b)) and in particular no such discontinuity is observed for higher T_b (see fig. V.6). If we interpret the phase variations as fluctuations of the velocity of excitons in the regions of high contrast, we see that after the discontinuity at the inner edge of the ring the velocity rises again with a more or less steep slope depending on the data until it suddenly drops back. As discussed previously this increase could be associated to a corresponding shape of the potential or the strong repulsion between exciton at the position of the ring (or both). However a sudden drop of velocity is likely to be associated with the presence of a potential wall which stops excitons. Such potential wall is not surprising since we measure confining potentials. Therefore these measurements show a direct link between the presence of long-range coherence of the photoluminescence and specific variations of the phase of the $g^{(1)}$-function. This confirms with an independent method the relation between condensates of excitons and confining potentials.

Let us note that the lateral shift δx of the interferometer was done along the x-axis which means that the fluctuations of the phase of the $g^{(1)}$-function only reflect the exciton velocity along the horizontal axis. Thus we can only obtain information on the potential along the horizontal direction. This is probably not very important since due to the geometry of the ring, the velocity of excitons is likely to be oriented along the radius of the ring and we examine a small portion of the ring such that the radii of the ring do not present a strong angle with respect to the horizontal axis. Nevertheless this effectively limits the study of the fluctuations of the phase of the $g^{(1)}$-function and possible conclusions on the potential along the vertical direction. Interestingly, the measurement of the phase of the $g^{(1)}$-function allows us an estimation of the velocity of excitons along the x-axis. Indeed, eq. V.1 shows that $V_x = \hbar\varphi_{\mathbf{r},\delta x}/M_X\delta x$. If we examine the phase profiles in figs. V.8 and V.6, at the lowest bath temperature, we see that the maximum phase jump occurs at the inner edge of the ring, i.e. at the position of the abrupt fall of the potential. The amplitude of the phase jump at this position is at maximum between $\pi/2$ and π, which gives a velocity of $0.5 - 1 \times 10^5$cm/s. This velocity is lower than the velocity of the sound in GaAs $v_s \sim 3.4 \times 10^5$cm/s [104], indicating that the transport of excitons in the edges of the dome-shaped potential is not ballistic.

The comparison between these velocities is important. Indeed for an exciton velocity larger than the speed of sound, we expect a decrease of the scattering processes between excitons and phonons which could lead to a conservation of the coherence and polarization of the excitons over large distances. These effects have been studied theoretically for instance in [134, 135]. Let us note that in our case the maximum fluctuations of the phase of the $g^{(1)}$-function occur at the inner edge of the fragmented ring, thus the maximum velocity of excitons is found in this region and is still lower than the speed of sound. Therefore we can reasonably conclude that our results are not affected by eventual ballistic effects, in particular since in this region we do not measure a large degree of spatial coherence. Another interesting comparison is the velocity acquired by an exciton falling from a potential cliff of height $\Delta E \sim 4$meV (which is typically what we measured in the previous chapter at the lowest bath temperature, see fig.V.7). If we consider a direct conversion of potential energy ΔE in kinetic energy (i.e. $\Delta E = M_X V_x^2/2$, which is a very rough approximation), we obtain a velocity of $\sim 9.10^6$cm/s. This calculation therefore shows on the contrary a ballistic transport, however we would probably need a more complete diffusion model in order to estimate the velocity gained by excitons falling from a potential cliff of a given height.

To conclude this section, we would like to stress that we are fully aware that the above discussion relies on the hypothesis of a relation between $\varphi_{\mathbf{r},\delta x,0}$ and the velocity for excitons. This statement should be backed up with thorough theoretical calculations (which can not be found in the literature to the best of our knowledge) and further experiments (one could for instance imagine to map the phase of the $\mathrm{g}^{(1)}$-function for a set of well-known potential landscapes). However this goes beyond the scope of this thesis.

As a final remark we would like to point out that the phase of the $\mathrm{g}^{(1)}$-function can be in principle directly extracted from normalized interferograms by performing a two-dimensional Fourier transform. This method has been successfully used to show the presence of vortices in exciton-polariton systems [34, 98]. Exciton-polariton condensates exhibit much higher contrast value when performing shift-interferometry due to very large coherence length therefore the interferograms usually present very well defined interference fringes. Our interferograms not having this level of quality it was more precise to use the phase given by the scan of the interferometer.

V.A.3 Dynamics of the spatial coherence

As seen in sections III.C.2 and III.B.2 dedicated to the dynamics of the photoluminescence, the pattern of the exciton ring varies depending on the time delay with respect to the excitation pulse. The first phase is the expansion of the ring at the beginning of the pulse towards a quasi-stationary configuration which forms the second phase and lasts until the end of the pulse. Finally the last phase starts right after the laser pulse and includes the decay of the photoluminescence. It is therefore interesting to measure the evolution of the contrast with the delay to see if we observe connections between the degree of spatial coherence and the various phases the ring goes through. Let us recall here that the previous measurements where recorded after the laser pulse with a time window of 40ns. Thus in order to increase the time resolution particularly after the pulse we lowered the time acquisition to 10ns (which has the inconvenient of lowering the statistics and the quality of the data). Fig. V.9 presents the photoluminescence coming from one arm of the interferometer along with the corresponding normalized interferograms at various time delays and for $\delta x = 1.6\mu$m. From these interferograms, we extracted the value of the contrast at 3 horizontal positions with respect to the ring by fitting the vertical contrast profile with a cosine function. As we explained in the previous section, this method presents several limitations but due to the time constraints we could not measure maps of the contrast or full contrast variations with δx.

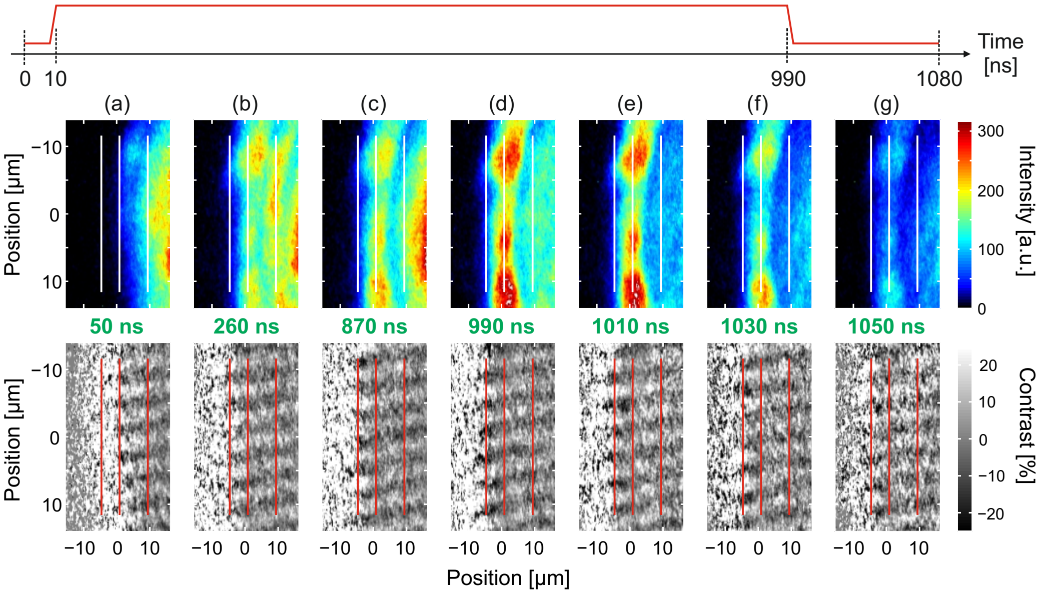

FIGURE V.9: (a-g) Images of the photoluminescence coming from one arm of the interferometer at various delay during and after the laser excitation pulse along with the corresponding normalized interferograms for $\delta x = 1.6\mu$m. The vertical lines marks the regions (from right to left : in the ring, at the position the ring and $\sim 7\mu$m outside the ring when the quasi-stationary extension of the ring is established) where the contrast values were retrieved by fitting the vertical contrast profiles. The data were recorded with a time window of 10ns for $T_b = 0.34$K. The field of view towards the center of the ring is limited due to a spatial filtering necessary to cut the strong photoluminescence of the bulk GaAs at the position of the excitation beam during the laser pulse.

In fig. V.10(a) are shown the evolutions of the degree of spatial coherence with the time delay at the three positions. As one can see at the position of the ring and inside of it the contrast remains essentially constant during and after the pulse, the values being within the range of the background noise (i.e. in the range of the threshold of 10% described in the previous section). Interestingly the behavior of the contrast $\sim 7\mu$m outside the ring is very different, namely from a low contrast value during the pulse the degree of coherence suddenly jumps up directly at the end of the pulse and then stays constant. This indicates a strong increase of the long-range spatial coherence after the excitation pulse and is consistent (not in value but in general) with the measurements of the previous section taken after the pulse where we only measured extended spatial coherence outside the ring. It is not very clear why the spatial coherence increases after the laser pulse, although previous observations can provide some explanations and confirm that the conditions for the exciton gas at the position of the ring are different during and after the excitation pulse :

- During the measurements of the photoluminescence dynamics (see fig. III.14(c)), we observed a fast intensity decay inside the ring. This means that even if the ring reaches a quasi-stationary state during the excitation pulse, at the same time charges and excitons are constantly injected which can perturb the exciton gas at the position of the ring, these perturbations rapidly vanishing after the pulse.
- We measure a strong decrease of the spectral width of the exciton line after the laser pulse (see fig. III.22(c)).
- The study of the dynamics of the spectral characteristics of the ring performed in the section III.C.2 shows that the energy profile at the position of the ring is not the same during and after the excitation pulse (see fig. III.23). In particular this would indicate that the density and/or the potential around the ring is different during and after the pulse.

Surprisingly, we see that the contrast value seems to remain constant for a relatively long time after the pulse though we know that the density of the exciton gas strongly decreases during the same period (the energy of the photoluminescence decreases of about 1meV, see fig. III.14(b)). We would then expect a plateau and then a decreasing of the contrast since the transition from a classical to a quantum gas can in principle only occur above a density threshold. This density threshold is for sure reached or exceeded right after the pulse since we observe extended spatial coherence but since the density then decreases we would expect the contrast to drop accordingly after a given delay. However let us stress that we have no precise idea of the actual density of the exciton gas for a given ring and of the density threshold, thus we do not really know at which delay the exciton density would be lower than the density threshold. Finally for large delays after the pulse, we have to face a major challenge which is to measure interferences of a low intensity signal and thus a very low signal over noise ratio. This effect can be seen on the data points which have increasing error bars when the delay increases after the pulse. Therefore it is risky to draw conclusion concerning the contrast value for large delays and to actually observe this behavior would require more precise measurements such as maps of the contrast.

In order to conclude this section we would like to get back to the artificial interference contrast which can appear if the studied photoluminescence pattern is too narrow,

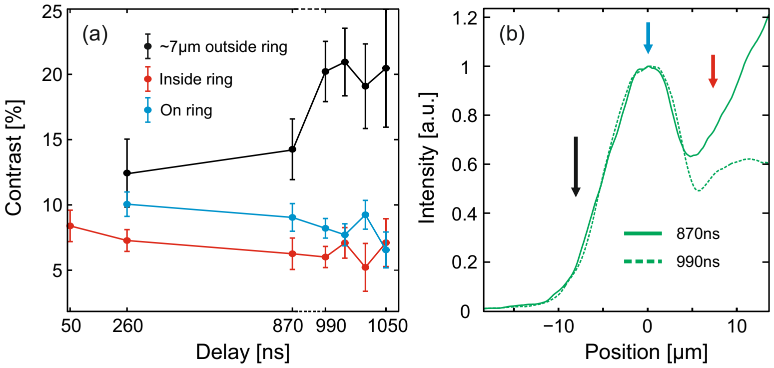

FIGURE V.10: (a) Evolution of the contrast with the delay at the three positions with respect to the ring marked by the vertical lines in fig.V.9. The time scale after the pulse (delays larger than 990ns) is stretched in order to increase the visibility. There are no black and blue data points at delay 50ns, since the ring has not yet reached its steady-state regime and no photoluminescence is present at the corresponding positions. (b) Horizontal intensity profiles for 2 delays during (870ns) and after (990ns) the excitation pulse taken at the ordinate 0 on the vertical axis of the images in fig.V.9. The colored arrows correspond to the horizontal positions of the data shown in (a).

as explained in the second part of section II.B.2.b. The previous measurements provide us with various ring shapes and contrast values which can be compared to assess this effect. For instance if we plot intensity profiles along the horizontal axis at delays during and after the pulse (see fig. V.10(b)) we see that outside the ring the profiles are identical. Thus according to the idea formulated by H. Stolz and cowokers [95] the artificial interference pattern should give the same value for the contrast at both delays, however this is not what we measured which is a direct proof that the extended spatial coherence we observe is more than just an experimental artifact.

V.B Polarization

In the previous section we measured the existence of a quantum gas of excitons with macroscopic spatial coherence in the vicinity of the ring. As explained in the first chapter, a "gray" condensate of excitons would result in a coherent superposition of the 2 exciton bright/dark states such that the emitted photoluminescence is linear polarized. In the following section, we thus examine the polarization of the photoluminescence.

V.B.1 Direct Measurements

As described in section II.B.3, using a combination of quarter- and half-waveplates and a polarized beam splitter, we record the intensity of the photoluminescence of the ring along the main polarization axis : I_{H}, I_{V}, I_{D}, I_{A}, I_{σ^+} and I_{σ^-}. We can then process the images for two orthogonal polarizations to obtain a map of the degree of polarization along a given polarization axis (for instance $P_{\mathrm{HV}} = (I_{\mathrm{H}} - I_{\mathrm{V}})/(I_{\mathrm{H}} + I_{\mathrm{V}})$). The resulting maps for $T_b = 0.34$ and 4K are displayed in fig. V.11.

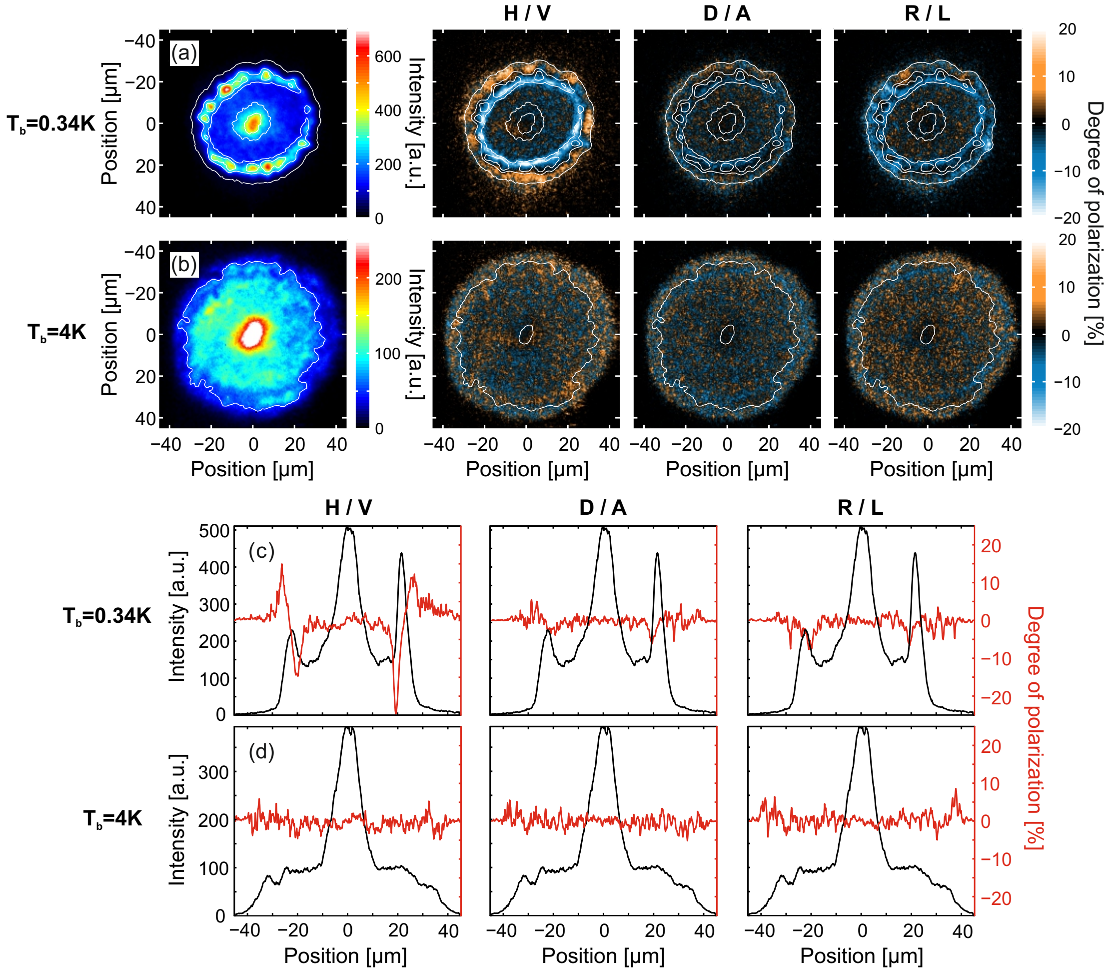

FIGURE V.11: (a) and corresponding row : Direct image of the photoluminescence of the ring for $T_b = 340$mK, normalized polarization map for $P_{\mathrm{HV}} = (I_{\mathrm{H}} - I_{\mathrm{V}})/(I_{\mathrm{H}} + I_{\mathrm{V}})$, P_{DA} and P_{RL}. Blue and gold colors are associated to orthogonal polarizations. Recording and pulse scheme parameters are identical to the ones of the previous section with $V_g = -4.08$ and $P_{\mathrm{ex}}(641.5) = 11.5\mu$W. The white lines on the maps are iso-intensity contour lines for 50, 300 and 500. (b) and corresponding row : same as (a) for $T_b = 4$K. (c) and corresponding row : polarization and intensity profiles along the vertical axis at abscissa 0 on the horizontal axis for the photoluminescence and polarization maps at $T_b = 340$mK. (d) and corresponding row : same as (c) for $T_b = 4$K.

At the lowest bath temperature, we measure a polarization which is dominantly linear along the horizontal and vertical axis (see first row fig. V.11). The regions of high degree of horizontal polarization are organized in islands at the exterior vicinity of the ring. Interestingly, we also observe a high vertical degree of polarization homogeneously distributed directly inside the ring. This region also exhibits σ^- polarization at a lower degree. When increasing the bath temperature, the degree of polarization drops very rapidly and as shown in the second row in fig. V.11, no polarization is left at 4K. The comparison between the intensity and polarization profiles along a ring diameter is presented in figs. V.11(c-d) and corresponding rows. One can see that the maximum of the horizontal polarization outside the ring can be found at the same distance from the ring as the maximum of spatial degree of coherence while the vertical polarization is placed at the inner side of the ring, i.e. the position of the potential cliff measured in the previous chapter.

These measurements show that the degree of polarization is very low $\sim 10-15\%$. Multiple reasons can explained this. First of all we have to consider our excitonic system. Indeed the establishment of a dominant polarization is a delicate process which requires a coherent superposition of the bright states without any disturbances which could induce a random mixing. It is in this sense much more delicate than the long-range spatial coherence where all states can interfere with the others. Let us also note that the calculations of M. Combescot et al. leading to a dominantly linear polarization are based on the assumption that the two dark states are degenerate [50]. If it is not the case the nature of the resulting polarization state is likely to be more complex. Finally, we do not expect a fully condensed exciton gas which means that the polarization from the condensate is mixed with the unpolarized light of the thermal part of the gas. We also observed that the presence of a dominant polarization is highly dependent on the ring shape but without any clear relation between the two (data not shown). On the contrary the presence of long-range spatial coherence was more robust.

To conclude on perturbing effects on the polarization, we have to take in account the disturbances caused by the experimental setup. Indeed optics are never perfectly neutral with respect to the polarization and can yield to rotations of the polarization axis. In order to overcome these problems we decided to implement an analyzing technique very commonly found in quantum optics but which, to the best of our knowledge, has never been applied to excitonic systems. This technique is presented in the following section where we use it to analyze the previous measurements with more accuracy.

V.B.2 Maximum likelihood method

We will only give a light description of this method, further details can be found in [136, 137]. The general idea is to reconstruct the density matrix of an unknown polarization state with a defined set of measurements. To do so we note the polarization as a vector $\mathbf{r}$ whose components $(r_{\mathrm{H}}, r_{\mathrm{D}}, r_{\mathrm{R}})$ give the degree of polarization over the Horizontal-Vertical (H-V), Diagonal-Antidiagonal (D-A) and Right-Left Circular (R-L) bases. These components are often viewed as coordinates on the Poincaré sphere (see fig. V.12(c)). The vector $\mathbf{r}$ being normalized, all polarization states must lie inside or on the sphere where $||\mathbf{r}|| = 1$ represents pure polarized states and $||\mathbf{r}|| = 0$ a completely unpolarized state. To determine the polarization of a state four measurements are required : three to determine the relative values on each base and a fourth to determine the normalization. In our case we chose to use the intensity given by the measurements performed previously over the V, H, D and R polarizations (i.e. I_{V}, I_{H}, I_{D}, $I_{\sigma+}$). From these values we can reconstruct the polarization state. However since our measurement is subject to statistical fluctuation of the intensity which could blur the polarization or yield an unphysical result, we use a maximum likelihood technique in order to estimate a physical density matrix that would most likely produce the measured data.

Applying this method to all the points of the photoluminescence image allows us to retrieve maps of the values of the polarization components $(r_{\mathrm{H}}, r_{\mathrm{D}}, r_{\mathrm{R}})$. Let us note that this technique is particularly adapted to filter the effects of the perturbations caused by optics to the polarization states. Indeed optics usually cause modifications along a single polarization axis without their equivalent on the other axis, as would be the case for a physical change of the polarization state. Thus the non-physical part of the polarization will be easily discarded since we consider measurements over multiple axis at the same time.

The results of this technique are presented in fig. V.12 where we plot maps of the total degree of polarization $||\mathbf{r}||$, the values of the components of the polarization vector (r_H, r_D, r_R) for the data obtained in the previous experiment (see fig. V.11) and the profiles of the photoluminescence intensity and polarization components along the vertical axis. As we can see the effect of the density matrix reconstruction is quite spectacular with a strong increase of the overall degree of polarization and of the spatial resolution of the regions of high degree of polarization. Therefore the observations are essentially the same as the ones of the previous section. We can confirm that outside the ring the polarization is dominantly horizontal and distributed in islands. At the same positions, the polarization exhibits a small positive component along the right circular and diagonal axis. At the interior vicinity of the ring the polarization is homogeneously distributed and dominantly vertical with small degrees of A and L polarization.

As stated previously, one of the advantage of the method is to precisely know the position of the polarization vector in the Poincaré sphere. In particular if we limit ourselves to the linear polarization (i.e. $\mathbf{r}_{\mathrm{linear}} = \mathbf{r}_{\mathrm{H}} + \mathbf{r}_{\mathrm{D}}$ in the $r_{\mathrm{R}} = 0$ plane), we can infer the orientation of the linear polarization. Indeed, since we observe in the same region polarizations along the H-V and D-A axis this means that the resulting polarization is linear with an angle with respect to the H-V axis. This angle θ_{linear} can be calculated and reads :

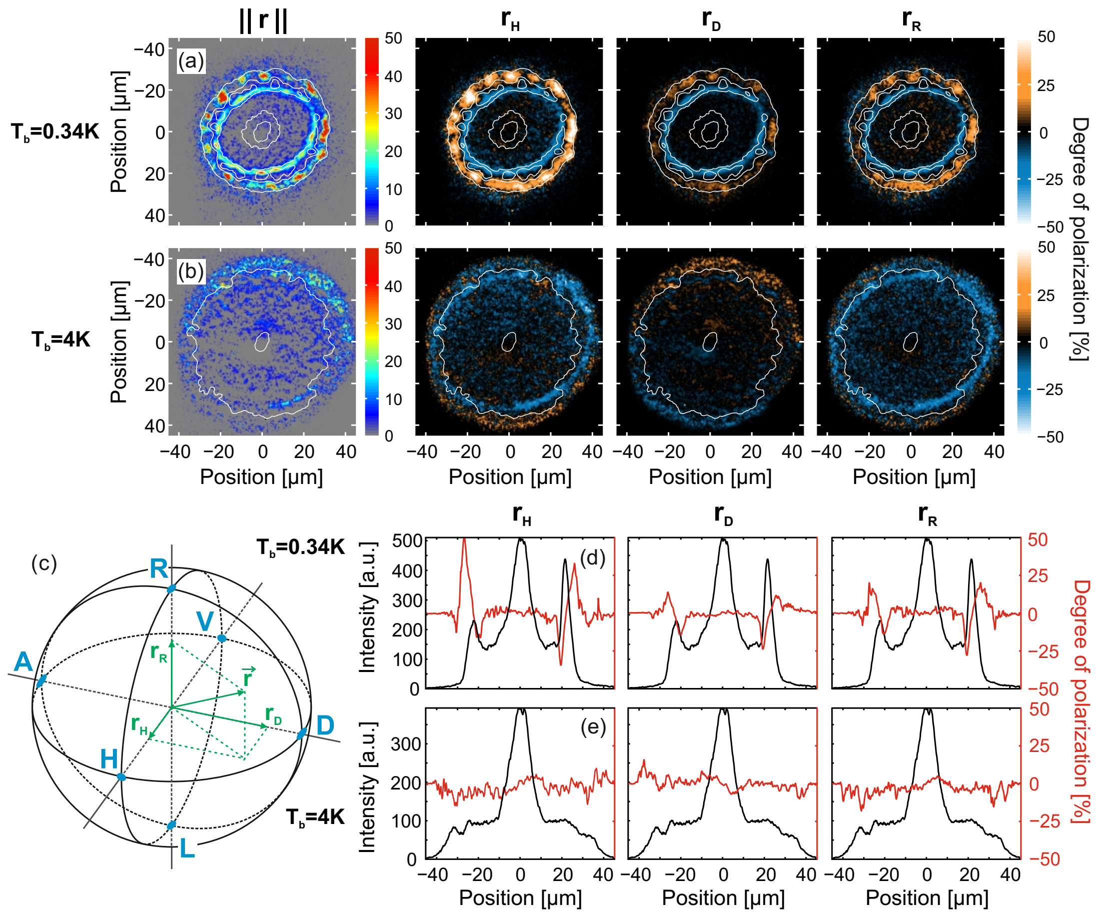

FIGURE V.12: (a) and corresponding row : maps of the value of the norm of the polarization vector $||\mathbf{r}|| = \sqrt{r_\mathrm{H}^2 + r_\mathrm{D}^2 + r_\mathrm{R}^2}$ and its three coordinates r_H, r_D and r_R for $T_b = 340$mK. The white lines on the maps are the same iso-intensity contour lines used in fig. V.11. (b) and corresponding row : same as (a) for $T_b = 4$K. (c) Poincare sphere with a polarization vector $\mathbf{r}$ and its 3 coordinates r_H, r_D and r_R along the HV, DA and RL axis. (d) and corresponding row : polarization coordinate and intensity profiles along the vertical axis at the abscissa 0 on the horizontal axis for the polarization coordinate maps at $T_b = 340$mK. (e) and corresponding row : same as (d) for $T_b = 4$K.

$$\theta_\mathrm{linear} = \mathrm{sign}\, ||\mathbf{r}_D|| \,.\, \mathrm{acos}\left(\frac{||\mathbf{r}_H||}{||\mathbf{r}_\mathrm{linear}||}\right)/2 \tag{V.2}$$

where $\theta_\mathrm{linear} = 0$ indicates the H direction, sign $||\mathbf{r}_D||$ serves to discriminate the A and D half-parts of the linear plane and the division by 2 accounts for the fact that the physical angle between the H and D polarization is $\pi/4$ and not $\pi/2$ as it is the case in the Poincaré sphere representation. If we calculate the corresponding map of θ_linear (data not shown), we found that the linear part of the polarization outside the ring is almost fully horizontal while inside the ring the angle is $\sim 0.8\pi/2$ meaning that the linear polarization is not perfectly vertical. At high temperature we found again that even with the maximum likelihood technique the photoluminescence outside the ring is unpolarized while only a small degree of polarization remains inside the ring.

The presence of polarization inside the ring is puzzling and we do not fully comprehend it. A possible explanation is associated to the potential cliff which occurs at the same position. Indeed a standard exciton gas exhibits a linear polarization due to the superposition of the two bright states as long as the spin coherence in maintained namely if no dephasing processes occur (such as collisions between excitons or between excitons and phonons) [138, 139]. In usual experiments, this coherence time is very short such that the polarization is almost immediately lost, leading to the emission of unpolarized photoluminescence. From this we can conceive that excitons falling from the top of the potential cliff could acquire a high velocity which might allow them to conserve temporarily the polarization [135]. Outside the ring we measured the presence of linear polarization with a relatively high degree as theoretically predicted. This observation and the previous measurements showing long-range spatial coherence at the same position confirm the existence of a quantum gas of exciton in the exterior vicinity of the ring.

V.C Comparison with the results of L. Butov et al.

As mentioned in the introduction to this manuscript, the group of L. Butov probed both the spatial degree of coherence and the polarization of their fragmented ring (the experimental methods are identical to the ones presented in this thesis except for the interferometer which is not stabilized). Some of their results are presented in fig. V.13 while further details can be found in [61, 134].

Figs. V.13(a-c) show the direct photoluminescence, normalized interferograms and a map of the amplitude of the interference contrast for a large portion of the fragmented ring and its interior. The results are very impressive and high values of the contrast can be found in the vicinity of the ring and around localized bright spots inside the ring. A focus on a portion of the fragmented ring and the corresponding measurements are displayed in figs. V.13(d-h). L. Butov et al. observed long-range spatial coherence on each side of the fragments with a strong maximum $\sim 15\mu$m outside (see black profiles in fig. V.13(h)). Analysis of the evolution of the interference contrast with the lateral shift give a coherence length as high as 2.5μm. As the bath temperature is increased, the contrast drops dramatically and no extended coherence is left at 8K (see fig. V.13(g) and blue profiles in fig. V.13(h)).

Interestingly, the respective evolutions of the value of the contrast and the intensity of the photoluminescence across the fragmented (see fig. V.13(h)) at the lowest bath temperature are very similar to the ones we presented in the section dedicated to the shift-interferometry (see for instance figs.V.3(i), V.4 and V.8(c-f)). Indeed we both

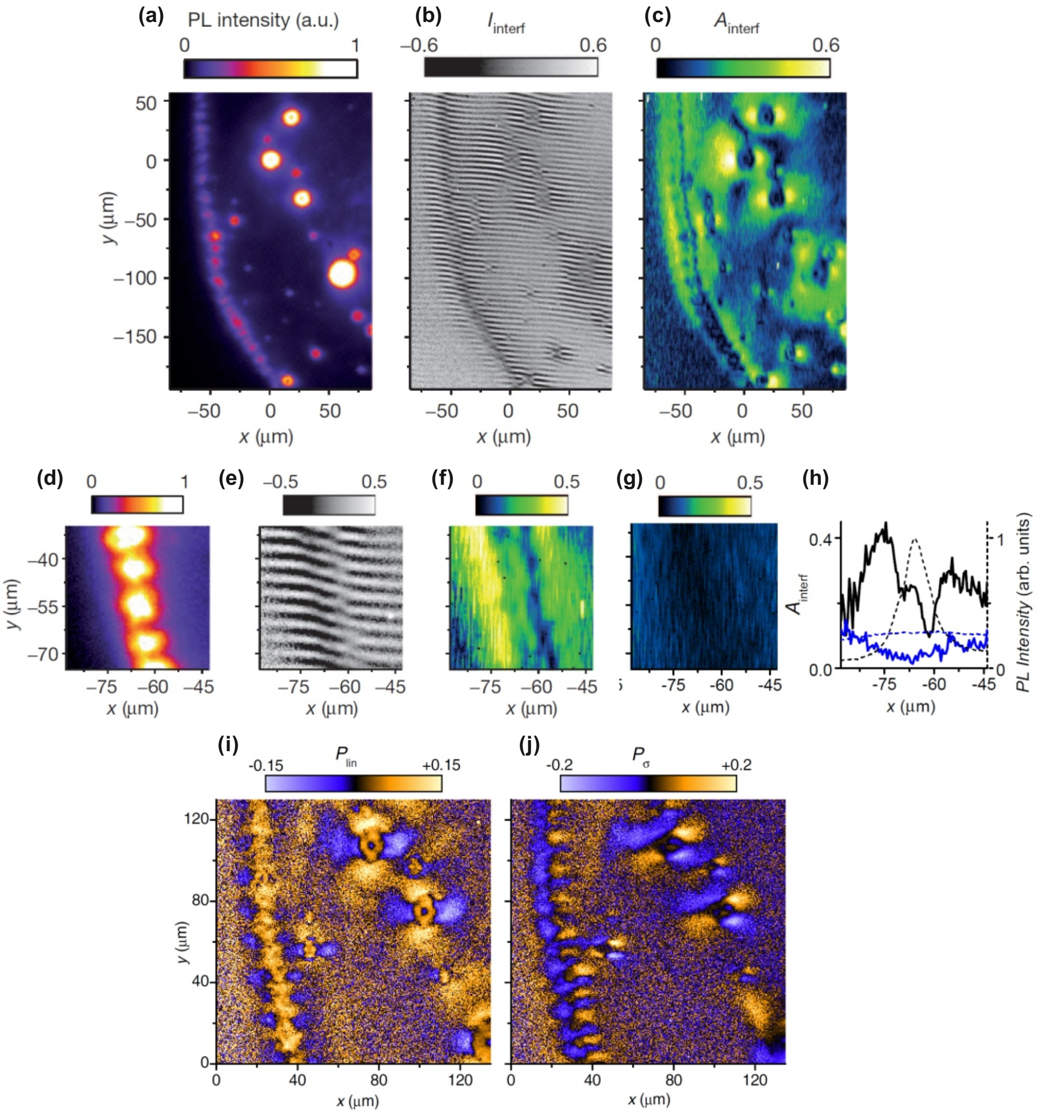

Figure V.13: (a) Photoluminescence pattern of the fragmented ring. (b) Normalized interferogram for a lateral shift of $\delta x = 2\mu$m. (c) Map of the amplitude of the interference contrast of (b). (d-f) Same as (a-c) for a focus on a part of the fragmented ring. (g) Same as (f) at high bath temperature. (h) Variation of of the amplitude of the interference contrast (solid lines) and the intensity of the photoluminescence (dashed lines) for two bath temperature (0.1 and 8K resp. black and blue lines) along the horizontal axis across the portion of the fragmented ring presented in (d). Pattern of linear (i) $P_{\text{lin}} = (I_{\text{H}} - I_{\text{HV}})/(I_{\text{H}} + I_{\text{V}})$ and circular (j) $P_{\sigma} = (I_{\sigma^+} - I_{\sigma^-})/(I_{\sigma^+} + I_{\sigma^-})$ polarization of the photoluminescence. All data were recorded with a continuous excitation at 633nm and a bath temperature of 0.1K, except for (g) for which the bath temperature is 8K. (a-h) are extracted from [61] while (i-j) are from [134].

observe a maximum of contrast outside the ring, even if L. Butov et al. do not measure an organization in "islands". Their interpretation of their results is however very different from ours. Specifically, following theoretical work [57], they attribute the fragmentation of the ring as a direct evidence of a quantum behavior and the fragments as sources for coherent excitons.

The polarization pattern measured by L. Butov and coworkers differ significantly from ours. Indeed, as presented in figs. V.13(i-j), they observe an intricate pattern of both circular and linear polarizations. These patterns have been interpreted in terms of coherent exciton transport away from the fragments and spin-orbit coupling [61, 134, 135]. Our experiments, which do not reveal such phenomena, are performed in a single quantum well with an energy splitting between bright and dark excitons much larger than in bilayer heterostructures. Since this energy splitting plays a key role in selecting the specific condensate which is formed, it is reasonable to conclude that experiments performed in single and double quantum wells probe distinct regimes.

Let us note that the group of L. Butov has put a particular emphasis on the analysis of the characteristics of the localized bright spots inside the fragmented ring. In particular the highest coherence length and degree of polarization were observed in the vicinity of these spots [61], along with fork-like dislocations of the interference fringes and strong dependence of the polarization pattern to modification of the magnetic field [134]. The localized bright spots were therefore interpreted as the cause of vortices and sources of coherent excitons creating spin currents. We only rarely observe such bright spot in our sample therefore these were not discussed in this manuscript.

To conclude this section, we would like to point out that the group of L. Butov never produced measurements of neither the potential landscape nor the distribution of density. In our opinion the lack of such results constitutes of major drawback to their interpretation of the phenomena associated to the formation of a fragmented ring.

V.D Conclusion

In this chapter we have presented the results of experiments designed to probe the quantum nature of the exciton gas. Thanks to the shift-interferometry, we observe at the lowest bath temperature the presence of “islands” of long-range spatial coherence with coherence lengths much larger than the de Broglie wavelength. The spatial coherence disappears for higher bath temperatures and the variation of the coherence length with the temperature confirms the existence of a phase transition from a thermal to a quantum gas for $T_b \lesssim 2$K. The region of high degree of coherence are always situated in the exterior vicinity of the ring where we measured a dense gas of dark excitons. We also presented a link between the phase of the $g^{(1)}$-function and the potential for excitons which confirm the observations done in the last chapter showing that the islands of quantum gas can only form in regions where trapping potentials are adequate. In a second part we measured the polarization of the photoluminescence and found it to be dominantly linear and organized in islands in the exterior vicinity of the ring. All these results are in agreement with the presence a “gray” condensate of excitons outside the ring.

Chapter VI

Overall conclusion and outlook

VI.A Conclusion

In this thesis we have presented the first observation of the self-organization of dipolar excitons in fragmented ring patterns apart from the group of L. Butov. Contrarily to this group, our fragmented is formed in a wide single quantum well. We have shown an extensive analysis of the dynamics and of the behavior of the ring with respect to the main experimental parameters by examining both the direct photoluminescence and its spectrum. While we observe that some of the physical characteristics of the ring well agree with the currently dominant theoretical model based on the ambipolar diffusion of charges, our ring also exhibits unusual properties. Among these are an increase of the diameter of the ring with the bath temperature, an absence of apparent perturbations when two fragmented rings are moved close to each other, an absence of contraction of the ring after the end of the excitation pulse and a very peculiar variation of the energy of the photoluminescence along the radius of the ring. These anomalies have led us to conclude that a potential landscape for excitons is created together with the ring.

By using a pump-probe pulse technique we were then able to separate the contributions to the energy of the photoluminescence in order to measure independently the exciton potential landscape and the spatial profile of the exciton density. Let us stress that it is the first time that such measurements are performed for systems of dipolar excitons and that these should be compulsory for any accurate discussion on the exciton density. Thus we have shown that the potential confining excitons is highly inhomogeneous and quasi-stationary and results of the modulation of the internal electric field by free charges injected by the same excitation beam which creates the fragmented ring. At the lowest bath temperatures, this modulation yields a strong anti-trap potential inside the ring and more strikingly, a trapping potential which extends from the inner edge of the ring until up to $\sim 5-10\mu$m outside of it. Further measurements confirm that the potential landscape along the circumference of the ring is complex and can exhibit traps with various shapes and depths. In particular our measurements show that the fragmentation of the ring in beads seems to be the result of the local trapping of excitons in confining potentials.

These measurements allowed us to compare the variations of the exciton density to the distribution of the intensity of the photoluminescence. We have shown trapping potentials where the density of excitons is high despite a very low intensity of the photoluminescence. This observation constitutes a direct evidence for the existence of an excitonic gas with a dominant population of dark excitons. Dark and bright excitons are normally present with the same population ratio due to the small energy splitting between the bright and dark states, with the dark states lying at the lowest energy. The observation of the dense gas of dark excitons can therefore only be explained by the presence of a "gray" condensate which is mostly composed of dark excitons, but also present a smaller fraction of bright excitons coherently coupled to the dark ones. In adequate confining potentials distributed along the circumference of the ring, we thus observe the coexistence of a thermal gas of excitons at the position of the ring while directly outside can be found the "gray" condensate. We attribute this phase separation to the complex hydrodynamics of excitons falling from the anti-trap potential towards the ring which locally disrupts the gas of excitons at the position of the ring. Excitons can then diffuse to the opposite edge of the confining potential, thus cooling down and undergo Bose-Einstein condensation. When the bath temperature is increased, we have shown that the potential landscape is modified and in particular does not exhibit confining potential. At the same time we do not observe the presence of a dense gas of dark excitons. This confirms the strong link between the characteristics of the confining potential and the possibility to form a "gray" condensate of excitons.

To probe the quantum nature of the exciton gas we measured the degree of spatial coherence and the polarization pattern of the photoluminescence. At the lowest bath temperature, our measurements reveal the existence of "islands" of long-range spatial coherence (up to 10 times the de Broglie wavelength) located in the outside vicinity of the ring. These islands rapidly disappear while the coherence length drops when the bath temperature increases. The interpretation of the phase of the first-order correlation function in terms of exciton transport then gave us an independent confirmation of the necessity to have a confining potential in order to be able to observe long-range spatial coherence. Finally we probed the polarization of the photoluminescence and found it to be dominantly linear outside the ring.

Overall we have then observed the presence of a dense gas of excitons in a confining potential with a dominant population of dark excitons which exhibits a macroscopic spatial coherence and a dominantly linear polarization. These observations are in full agreement with the prediction of a "gray" condensate of excitons as developed by Monique and Roland Combescot. Let us note that this observation has probably been made easier by the fact that we studied a SQW for which the energy splitting between the bright and dark states is larger than for previously studied samples which mainly include DQW.

Throughout the thesis we have observed that many physical properties of our fragmented ring experience dramatic changes when the bath temperature reaches ∼2K, among these are the radius and intensity of the ring, the peak energy and spectral width of the spectrum, the quality of the fragmentation, the presence of confining potentials, the coherence length and the degree of polarization. This strongly suggests a phase transition towards the quantum regime when the bath temperature is lowered below this critical temperature.

As a general remark our findings emphasize the critical role played by free charges which are inherent to the formation of the fragmented ring. This role is especially important for the appearance of the potential landscape. Let us note that the implications of such potential on the formation mechanism of the fragmented ring have largely been underestimated or ignored in theoretical studies.

As mentioned previously, the works presented in this thesis constitutes the first observation of a fragmented ring outside the group of L. Butov. Like them, we observe long-range spatial coherence and polarization patterns at low bath temperature. It is therefore natural to compare our results. Already, we can say that the fact that we observe similar characteristics for a different heterostructure (for example we study a SQW while they work with a DQW) would indicate that the formation of fragmented pattern of photoluminescence could be a general behavior of dipolar excitonic systems (let us note that the group of V. Timofeev also reported fragmented photoluminescence patterns but in an electrostatic trap, see e.g.[27, 28]). However, our results have led us to an interpretation of the phenomena associated with the formation of a fragmented ring which strongly differs with the one formulated by L. Butov et al. and most of the existing theoretical models on this subject. Apart from the fundamental importance of the qualitative reproduction of physical results by different experimental works, this underlines the interest of having various groups studying a seemingly similar system (a direct comparison can be made with the not-so-distant debate on the observation of a condensate of exciton-polaritons).

As a personal comment I would like to say that I was initially skeptical about the conclusions of our results. Indeed all the experiments presented in this thesis were performed on different rings, at different positions on the sample and spanned over a very long period (almost 2 years). Thus I was a bit disappointed that our experimental setup could not allow us to obtain the same observations during a single set of measurements for a unique fragmented ring, which for me would have proven the validity of all the different results. However while writing this manuscript, I realized that our work should be considered with a different point of view. Namely I have found on the contrary quite extraordinary that we managed to obtain results which all point in the same direction despite the various methods used and the relative disparity of the experimental conditions. This convinced me that we have observed a phenomenon which goes beyond possible "lucky" shots and that the possibility to create a "gray" condensate of excitons is indeed an intrinsic characteristic of our sample.

A natural evolution of this work would be to vary the density of excitons around the position of the ring while conserving the same potential landscape. This would in principle allow us to observe the phase transition of a thermal gas of excitons towards a quantum regime, which would be a very important confirmation of Bose-Einstein condensation. However, as mentioned in the chapter dedicated to the pump-probe experiments, the formation of an adequate potential landscape effectively sets the physical properties of the fragmented ring and in particular the distribution of excitons. This system therefore presents an intrinsic limited degree of control. Thus, even if the formation of the fragmented ring seems to be favorable to the formation of a condensate of exciton, it is very likely that in order to obtain the necessary experimental control over a system of excitons, the approach relying on tailored potential landscape for example by using pattern of electrodes is more promising to reach a decisive control over Bose-Einstein condensation of excitons, such as has been the case for cold atoms.

Incidentally and to continue on the engineering of potential, one of the consequences of our work on the fragmented ring is the possibility to create potential landscape by injecting free charges. This effect has already been investigated by the group of V. Timofeev [72] and our group [62] and as a conclusion of this manuscript, the two following sections show how the shaping of an excitation beam can lead to unusual fragmented photoluminescence patterns and the possibility to optically create interesting potential landscapes.

VI.B Outlook

VI.B.1 Fragmented line

Our initial interest in illuminating our sample with a linear excitation beam at 641.5nm was to examine the possibility of creating fragmented patterns with alternative geometries. Linear-shaped laser beams can easily be produced by using cylindrical lenses which expand the originally small Gaussian-shaped beam along a given direction, depending on the orientation of the lenses. The beam is modified outside the cryostat and is then projected on the sample through the microscope objective (see schema of the experimental setup in fig. II.6) resulting in a linear excitation (along the horizontal or vertical axis).

Fig. VI.1 presents the photoluminescence pattern created by a vertical linear excitation (marked by the white transparent area in fig. VI.1(a)) at the lowest bath temperature, as well as a profile of the intensity of the photoluminescence along the horizontal axis. The first observation is that indeed, a linear excitation creates linear-shaped photoluminescence patterns on each side of the excitation beam and these lines exhibit a fragmentation along the vertical direction. The deformation of the photoluminescence pattern at its two vertical extremities is the direct consequence of the imperfection of the excitation. Indeed while engineering an overall linear excitation beam is relatively easy, obtaining an illumination uniform and homogeneous over a large distance on the sample is not. Nevertheless one can see that vertically the photoluminescence is globally invariant by translation over a region of $\sim 80\mu$m (except for the fragmentation of course). The formation mechanism of the fragmented line is then similar to the one of the fragmented ring if we consider the linear excitation beam as a juxtaposition of small excitation spots along the vertical axis.

In appendix B, we investigate the physical properties of the fragmented lines with respect to variations of the excitation power and the applied voltage. The results show behaviors which are very similar to those of the fragmented ring. A natural interrogation would be then to know how far the similitude between the two systems goes and if, despite a different geometry, the fragmented lines exhibits all the properties observed for fragmented rings. We do not have definitive answers for these questions as we did not repeat all experiments on the fragmented lines. Thus we will only review some of our observations. Let us note that a possible equivalence between the two geometries is important from an experimental point of view which was another motivation for the implementation of the fragmented lines. Indeed, most of our measurements rely on analysis along the vertical or horizontal axis of the photoluminescence (for example the entrance slit of the spectrometer is vertical, the outputs of the Mach-Zehnder interferometer are

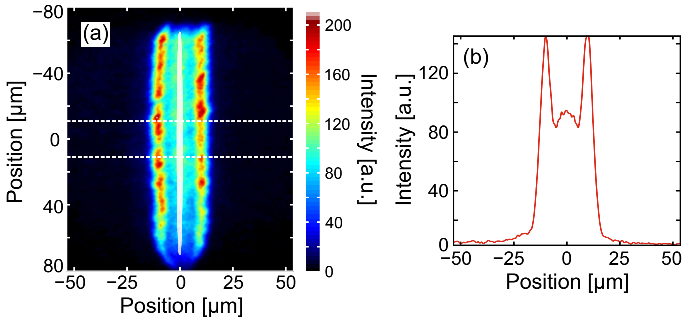

Figure VI.1: (a) Direct image of the photoluminescence created by a linear excitation beam at 641.5nm. The excitation beam is aligned vertically along the white transparent area. The data was recorded with a 40ns window 10ns after the end of the 1μs-long laser pulse (repetition rate is 2μs), $P_{ex} = 100\mu$W, $V_g = -5$V and T$_b$ = 0.34K. (b) Profile of the intensity of the photoluminescence of (a) along the horizontal axis, the signal is averaged along the vertical axis in the region delimited by the dashed white lines in (a).

shifted horizontally and more generally we record the photoluminescence with a CCD camera where the pixels are organized in a matrix) which are rendered more complex by the circular shape of the fragmented ring. An equivalent system with a translational invariance along a single axis would then be of great advantage.

As a first observation on the similarities/differences between the two geometries, one can see that the fragments for the lines are globally smaller and less well-defined. In appendix B, we present measurements of the spectral characteristics of the photoluminescence of the fragmented lines along their "radius" (i.e. along the horizontal axis perpendicular to the direction of the excitation beam). This experiment illustrates well the advantage of studying a system with a linear invariance. Our findings have already been discussed in section III.C.3 together with the spectrum along the radius of the fragmented ring. We found that for the two systems the characteristics are analogous which would led to conclude that a potential landscape for excitons is also present in the case of fragmented lines and exhibits the same overall shape as the one of the fragmented ring. This would indicate that trapping potentials could also be present around the position of the fragmented line together with a dense gas of dark excitons. However we did not repeat the pump-probe measurements for the linear geometry thus we do not know if these resemblances extend this far. We also probed the degree of spatial coherence by performing shift-interferometry. The contrast values we obtain are generally not high enough to conclude on the presence of long-range spatial coherence. Therefore the possibility of forming quantum gas of excitons with a linear excitation beam remains an open question.

In appendix B, we present the photoluminescence pattern created by two vertical linear excitation beams for various distances between them. Interestingly we see that moving the two patterns closer from each other does not seem to affect them (similar measurements with fragmented rings lead to the same observation, data not shown). In particular we do not observe an "attraction" or an opening of the patterns as has been observed by the groups of L. Butov and D. Snoke (see fig. III.3). This would indicate that the formation of our fragmented ring is dominated by the diffusion of excitons in the potential landscape rather than by the formation of excitons where the two traveling fronts of charges meet, as described by the model based on the ambipolar diffusion of charges.

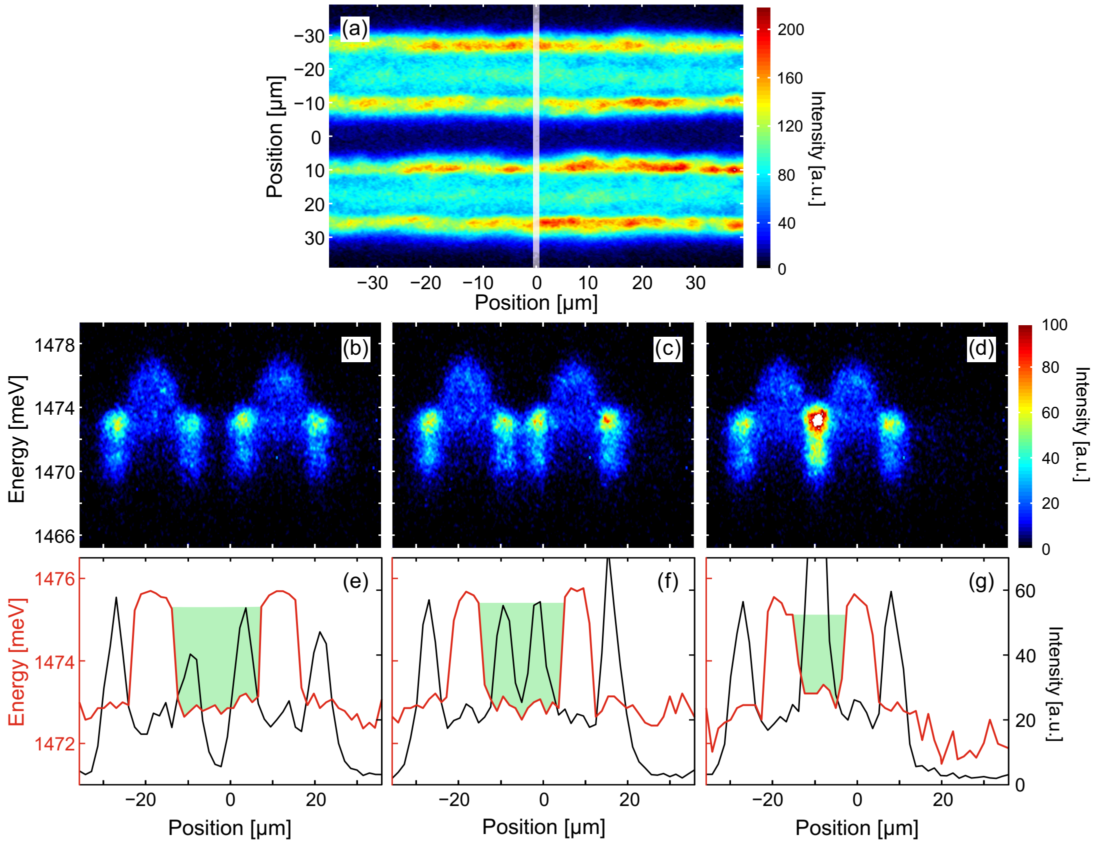

FIGURE VI.2: (a) Direct image of the photoluminescence created by two identical linear excitation beams aligned horizontally. (b-d) Spatially resolved spectra of photoluminescence patterns such as the one shown in (a) for various distances between the excitation beams. The entrance slit of the spectrometer is then perpendicular to the excitation beams as indicated by the white transparent area in (a). From (b) to (d) the distances between the two closest fragmented lines (as described in fig. B.3) are respectively ∼12, 7.5 and 0μm. (e-g) Variation of the peak energy (red) and intensity (black) of the exciton line along the horizontal axis (which corresponds to the position along the vertical slit of the spectrometer) of the spectral images (b-d). Experimental parameters are the same as the ones described in fig. VI.1 with the same excitation power for each linear excitation beam.

To conclude this section, let us examine fig. VI.2(a) which shows the photoluminescence pattern produced by two linear excitation beams aligned horizontally. Figs. VI.2(b-d) then present the spatially resolved spectra of the photoluminescence (the entrance slit of the spectrometer is perpendicular to the axis of the lines) for 3 different distances between the two closest (inner) fragmented lines. From these spectra we extracted the corresponding profiles of the peak energy and intensity of the exciton line along the vertical axis, as shown in figs. VI.2(e-g). As indicated previously, the variations of the profiles are very similar to the ones observed for the fragmented ring (see for instance fig. III.4(c)). This means that inside each of the fragmented lines pattern is present a dome-shaped potential which acts as a barrier for excitons. Thus, as shown by the green transparent areas in figs. VI.2(b-d), the combination of two linear excitation beams results in the creation of a deep confining potential channel whose vertical width can be reduced by moving the beams closer to each other. Of course the effective potential landscape would need to be characterized properly (for example with a pump-probe experiment) but these observations show the possibility of engineering optically quasi-stationary potential landscapes. This technique could provide an interesting alternative/complement to the modulation of the internal electric field by micro-patterned electrodes. These potentials could then be filled by an additional non-perturbing laser pulse.

VI.B.2 Ring excitation

Fig. VI.3(a) presents a fragmented pattern with another geometry. In this case we illuminated the sample with a ring-shaped excitation beam created by shaping the laser beam with an axicon lens. The resulting photoluminescence exhibits two concentric fragmented rings (in the image only the inner fragmented ring is shown, the outside ring as well as the position of the excitation beam are cut by optics of the experimental setup).

Fig. VI.3(c) shows the corresponding spatially resolved spectrum recorded with the entrance slit of the spectrometer aligned horizontally with the center of the excitation ring (as indicated by the white transparent rectangle in fig. VI.3(a)). We then retrieved the profiles of the peak intensity and energy of the exciton line along the vertical axis (see black solid lines in figs. VI.3(e) and (f)). As expected the energy of the photoluminescence presents a bump at the position of the ring excitation which extends towards the inner fragmented ring, thus indicating the presence of a potential barrier. We can then see that by adjusting the radius of the ring excitation beam we can produce hollow traps of various extensions.

The photoluminescence pattern created by the ring excitation being quite large we decided to add an additional small excitation beam at the center of it. We then obtain concentric fragmented rings, as shown in fig. VI.3(b). Fig. VI.3(d) displays the corresponding spatially resolved spectrum while the red lines in fig. VI.3(e-f) presents

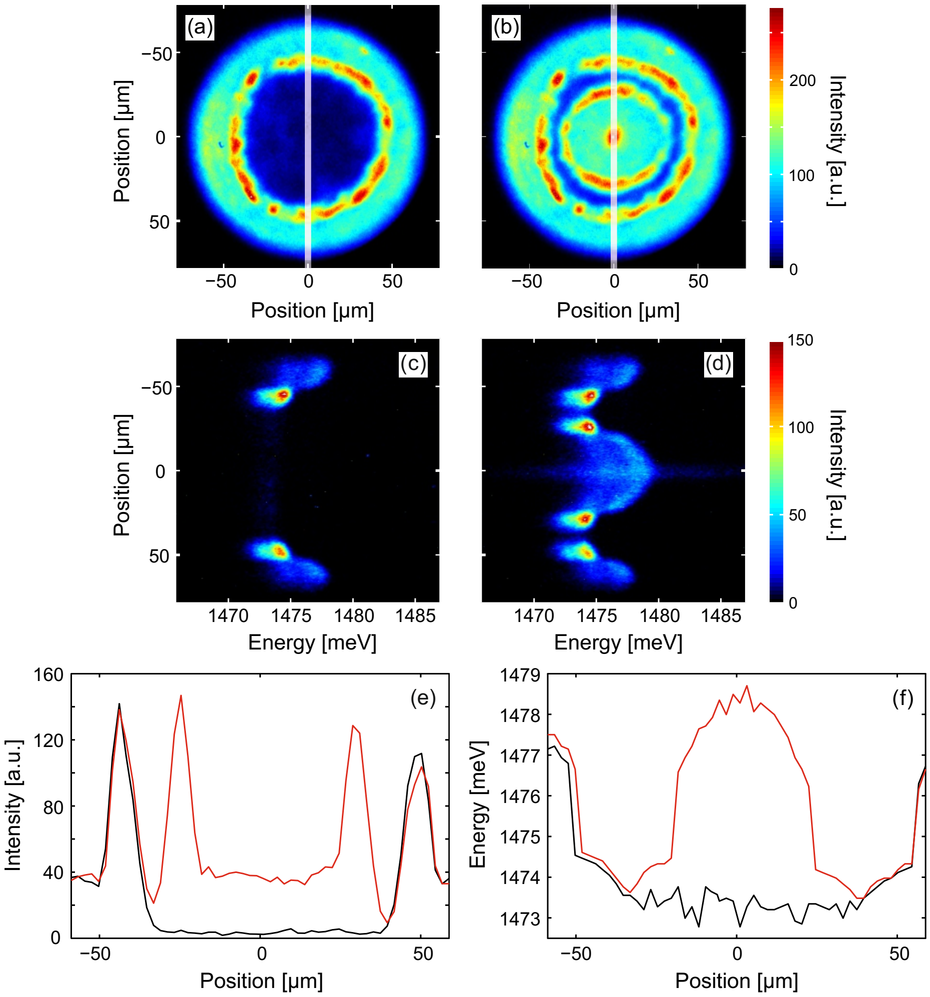

FIGURE VI.3: (a) Direct image of the photoluminescence created by a circular excitation beam at 641.5nm (only the inner fragmented ring appears in the image). (b) Same as (a) but with an additional fragmented ring created by an independent small excitation beam at 641.5nm aligned at the center of the circular excitation beam. (c-d) Spatially resolved spectra of the photoluminescence patterns shown in (a-b) taken with the entrance slit of the spectrometer aligned horizontally at the center of the circular excitation beam (as indicated by the white transparent rectangles in (a) and (b)). (e) Profiles of the peak intensity of the exciton line along the vertical axis from the spectral images (c) and (d) (resp. black and red solid lines). (f) Same as (e) for the peak energy of the exciton line. The data were recorded at $T_b = 340$mK.

the variations of the peak intensity and energy of the photoluminescence along the vertical axis. Similarly to the previous section, the comparison between the red and black profiles in fig. VI.3(e-f) shows that adding the fragmented ring does not affect the pattern created by the circular excitation. If we examine the energy profile we see that the potential now exhibits a wide potential barrier at the center. By varying the sizes of the inner fragmented rings we can therefore create a ring trap.

As a conclusion we have seen in the two previous sections that different curvatures of the excitation beam can yield fragmented photoluminescence patterns of various geometries. However, the consequences of the different geometries on the physical properties and formation mechanism of these patterns, notably the presence of “gray” condensate of excitons, have yet to be determined.

Appendix A

Fourier transform spectroscopy

Here are presented the time-interferometric measurements. As explained in section II.B.2.a, the purpose of these experiments is to obtain a direct and at-a-glance insight of the spectral distribution of the photoluminescence. In principle, this method should allow us to know the ratio between the integrated intensities of the exciton/charges and exciton spectral components and the energy of the photoluminescence at once all over the ring without the need of a spectrometer. We will see that even if the results are not as clear as one could expected, we do manage to obtain phenomenological conclusions. In particular we confirm that the narrowest exciton spectral line can be found at the position of the ring but more interestingly also in spatially limited regions in the outside vicinity of it. All the data presented in this section were recorded with the pulse sequence presented in fig. III.5 and with the following experimental parameters : $P_{ex} = 11.7\mu$W and $V_g = -4.7$V.

I.A Calibration of the interferometer

First of all, to calibrate our interferometer and to check the accuracy of the set-up, we measured normalized interferograms for various delay δt between the 2 arms. The results for $T_b = 0.37$ and 7K are presented in fig. A.1 and we can already notice that the fringes contrast is more robust with increasing δt at $T_b = 0.37$K than at $T_b = 7$K. From these interferograms we extracted the value of the interference contrast at 2 positions with respect to the ring (on the ring and inside it as marked by the red lines in fig. A.1) by fitting profiles of the contrast along the vertical axis with cosine functions. The amplitude of the fit then gives an average value of the contrast in this region. Of course, this technique presupposes that the contrast does not strongly vary in the region of study. The resulting evolutions of the contrast with δt at the 2 positions and the 2 temperatures

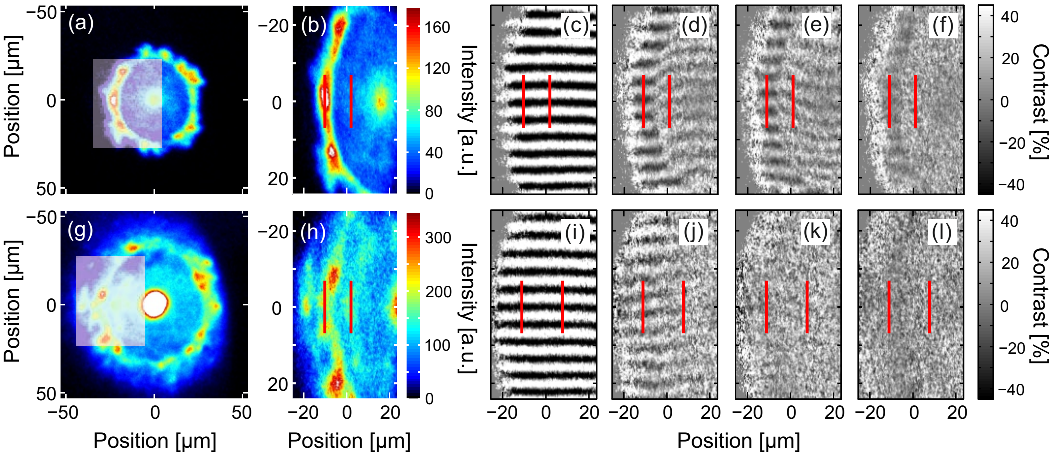

FIGURE A.1: (a) Direct image of the photoluminescence ring at $T_b = 0.37$K. (b) Direct photoluminescence coming from 1 arm of the interferometer, due to the limited size of the mirrors in the interferometer we can only analyze a portion of the ring which is indicated by the white transparent region in (a). (c-f) Normalized interferograms for the photoluminescence (b). From left to right $\delta t = 0.02$, 0.88, 1.38, 2.72 ps (with a resolution of ±0.03ps). The red lines marks the positions (on the ring and in midway between the ring and its center) where the contrast and the spectra presented in fig. A.2 were retrieved. (g-l) Same as (a-f) but for $T_b = 7$K.

are shown in fig. A.2. We superposed these experimental points with normalized Fourier transforms of spectra taken at the corresponding positions and as expected we obtain a very good agreement. From these curves we see that setting the interferometer for instance at $\delta t = 1.5$ps efficiently filters the component with large spectral width (i.e. the exciton/charges line) and following the basic example presented in section II.B.2.a, the value of the measured contrast directly relates to the ratio of the integrated intensity between the exciton/charges and the exciton lines.

As we have seen in chapter 2 and in fig. A.2(a), the characteristics of the spectral lines dramatically varies along the radius of the ring and when the bath temperature increases. In particular, the ratio between spectral widths can change such that the influence of the spectral widths in the formula between the contrast and the integrated intensity ratio can not be neglected. Thus, obtaining an accurate ratio of the integrated intensities using time-interferometry would require to perform spectroscopic measurements to know the spectral characteristics effectively making the interferometric method useless (but it could prove to be a very efficient tool for simpler systems). Therefore this method can in practice not be applied to retrieve specific numbers but should rather be used to obtain a general idea of the spectral distribution.

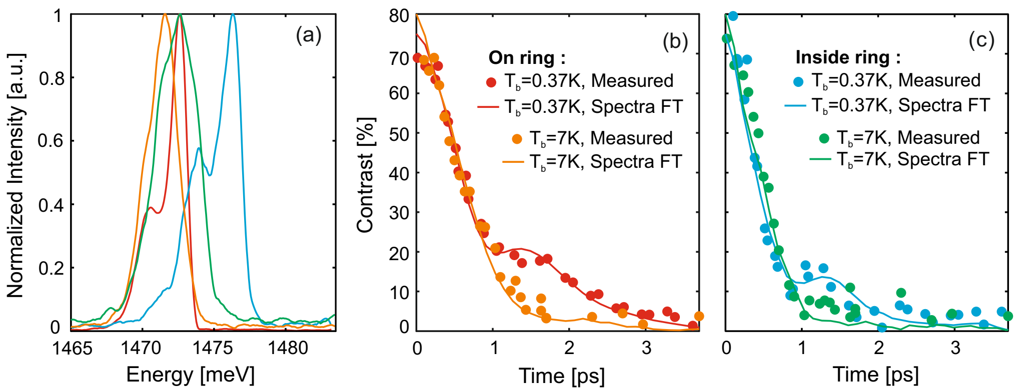

FIGURE A.2: (a) Spectral profiles at the positions indicated by the red lines in fig. A.1 namely red profile (resp. orange) at the position of the ring and blue (resp. green) in midway between the ring and its center for $T_b = 0.37$K (resp. $T_b = 7$K). (b-c) Solid lines : Fourier transforms of the spectra presented in (a), the color code is the same. The Fourier transform amplitudes were scaled according to the maximum of the interference contrast for $\delta t \sim 0$ i.e. 75%. The thick dots represent the value of the interference contrast for various δt measured by fitting with a cosine function the interference fringes on the normalized interferograms along the vertical lines showed in fig. A.1.

I.B Advanced interferometry at fixed path length difference

I.B.1 Introduction and direct results

In order to obtain directly the map of the contrast, we set $\delta t = 1.5$ps and vary the phase $\phi = 2\pi\delta l/\lambda_{\text{stab}}$ of the interferometer. This is done by stabilizing the path length difference between the two arms of the interferometer for various δl, as explained in section II.B.2. The effect of the phase shift can be directly observed on the normalized interferograms in figs.A.3(b-d), where fringes slip vertically. The relative phase shift between the interferograms can be calibrated by fitting a vertical profile (taken along the vertical blue line) with a cosine function whose argument reads in principle : $q_\alpha z + \phi_t + \varphi_{\vec{r};0,\delta t} + \phi$. However since $\phi_t = 2\pi c\delta t/\lambda$ is fixed and $\varphi_{\vec{r};0,\delta t}$ does not depend on ϕ (which is not entirely true since $\delta t = 2\pi\delta L/\lambda$ and we actually vary δL by δl when we scan the phase. Nevertheless since $\delta L \gg \delta l$, we can probably neglect the influence of δl on $\varphi_{\vec{r};0,\delta t}$), the result of the cosine fit gives us both q_α and ϕ. Then the variations of the contrast at a given spatial point (x, z) of the interferograms with ϕ (see fig. A.3(e)) is also a cosine function which can be modeled as $I_{\text{int}}(x, z; 0, \delta t) = \cos\left(q_\alpha z + \phi_t + \varphi_{\vec{r};0,\delta t} + \phi\right) \left|g^{(1)}(x, z; 0, \delta t)\right|$. Repeating this process over the whole photoluminescence allows us to retrieve maps of the degree of time coherence (amplitude of the previous cosine $\left|g^{(1)}(x, z; 0, \delta t)\right|$), of its relative error and of the phase of the previous cosine function, as shown in fig. A.3(f-h).

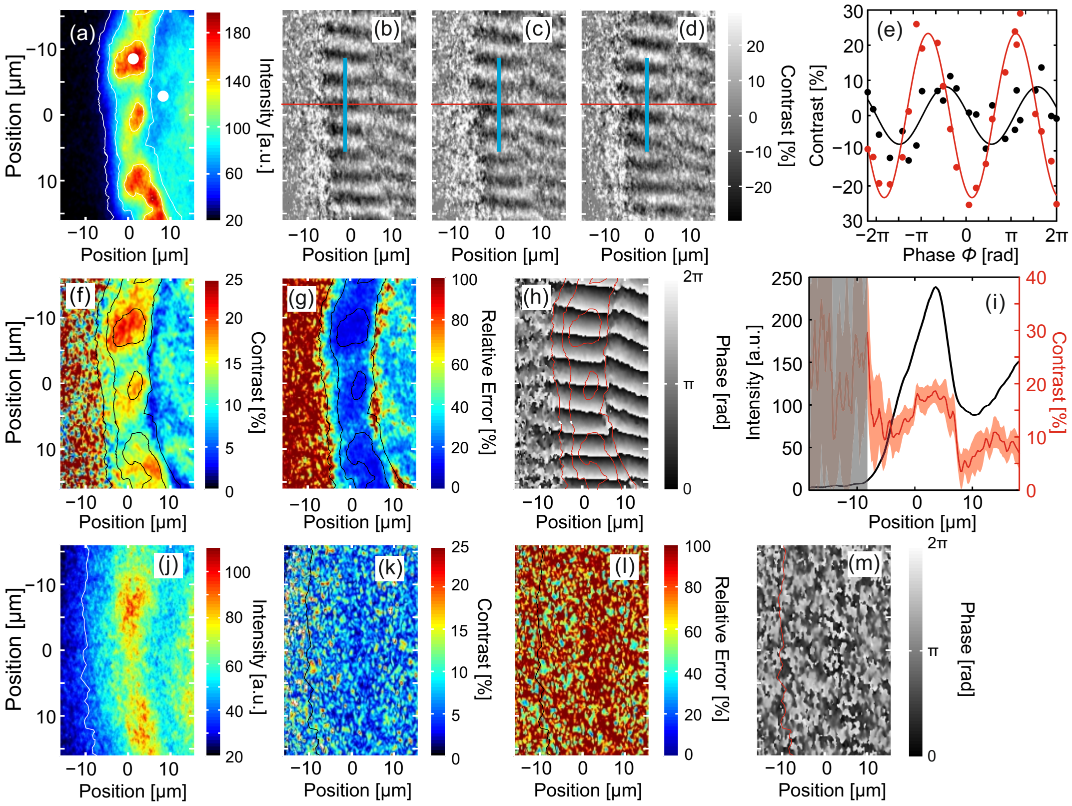

Figure A.3: (a) Direct photoluminescence coming from one of the interferometer arm for $T_b = 0.37$K, the white lines are isointensity contour lines for intensities of 20, 100 and 200. (b-d) Normalized interferograms of the photoluminescence (a) for $\delta_t = 1.5$ps and various phases ϕ between the 2 arms : 0, $\pi/2$ and π (the horizontal red line is a guide for the eyes to follow the slip of the interference fringes). The phase ϕ is measured for each interferogram by fitting the contrast profile along the z-axis (blue line in (b-d)) with a cosine function. (e) Evolution of the contrast of the fringes with the phase of the interferometer at 2 positions on the photoluminescence : at the position of the ring (red dots) and inside the ring (black dots), the positions are marked by the white dots in (a). Fitting the evolution with a cosine function (solid red and black lines) gives the amplitude of the contrast and the phase at a given position. (f-h) Contrast, relative error of the contrast and phase maps obtained by fitting the contrast fluctuations with the interferometer phase at each point of the photoluminescence. The black (f-g) and red (h) lines are the same contour lines indicated in (a). (i) Contrast (red) and intensity (black) profiles along the horizontal axis for a vertical position at $z \simeq -8\mu$m. The transparent red area represents the error for the contrast due to the cosine fit, while the gray transparent area marks the region outside the ring for which the relative error is $\sim 100\%$. (j-m) Direct photoluminescence, contrast, relative error and phase maps for $T_b = 7$K.

As expected from the direct spectral measurements, we have a maximum of contrast at the position of the ring indicating that the exciton line is there narrower and/or have a higher weight compared to the exciton/charges line. This is better visualized by overlapping the intensity profile and the value of the contrast along the ring radius as shown in fig.A.3(i). Interestingly on the ring itself we see that at the position of the fragments the contrast is maximum but that the correspondence is not perfect. Indeed regions of high contrast can be found between the beads and more surprisingly also outside the ring (see fig. A.3(f)). These observations have important implications. This is in particular the first time we manage to observe that the fragments exhibit characteristics which differs from the rest of the ring (but these differences are much less pronounced than for the experiments of L. Butov et al., see introduction to section III.C). This difference are confirmed by the study of the spectrum of a fragmented line (see appendix B). Thanks to the direct spectral measurements presented in section III.C.3, we already know that the spectra on the ring and outside it are very similar but these measurements were lacking spatial resolution. With the time-interferometry experiment, we are not only able to ascertain that some spectral characteristics (linewidths and weight ratios) are identical on the ring and outside of it with another method, but one also see that outside the ring, narrow linewidths can only be found in limited regions (see fig. A.3(f)). This is not without reminding the small islands of long-range spatial coherence observed in the section V.A.2 and is in agreement with the intuitive idea that a condensed gas of excitons should exhibit a narrow linewidth. To conclude this first part on the analysis of the map of contrast, we performed the same interferometric analysis for the ring at $T_b = 7$K (last row in fig.A.3) and we only obtained a background noise for the contrast map indicating that, as expected, there is no narrow spectral width component left at high bath temperature.

I.B.2 Analysis of the phase map

To carry on the analysis of the maps of the contrast we would like to focus on the peculiar aspect of the map of the phase at low temperature. Indeed as one can see in fig.A.3(h), the distribution of the phase presents a disruption at the interface between slightly tilted iso-phase values at the position of the ring and more tilted fringes in the interior of the ring. The theoretical expression of the phase $q_\alpha z + \phi_t + \varphi_{\vec{r};0,\delta t}$ (see eq.II.4) enlightens the structure of the phase map. Indeed the $q_\alpha z$ term creates horizontal patterns closely resembling the ones of the interference fringes. However one has to keep in mind that $q_\alpha = 2\pi \sin(\alpha)/\lambda$ and $\phi_t = 2\pi\delta L/\lambda$, therefore if the photoluminescence is emitted at different wavelengths along the ring and its interior, these terms will create fluctuations of the phase and disturb the positions of the fringes.

If we now recall the profile of the peak energy of the photoluminescence along the ring diameter (see e.g. fig. III.16(c)), we know that the energy of the photoluminescence is highly non uniform. Thus, in principle, analyzing the curvature of the fringe pattern should gives us a map of the photoluminescence energy without the need of a spectrometer. Following this idea, we first neglect the phase of $g^{(1)}$-function $\varphi_{\vec{r};0,\delta t}$ and try to reproduce a part of the phase map (focus shown in fig. A.4(b)) by applying the energy profile shown in red in fig. A.4(f) to the phase formula. We obtain the simulated phase

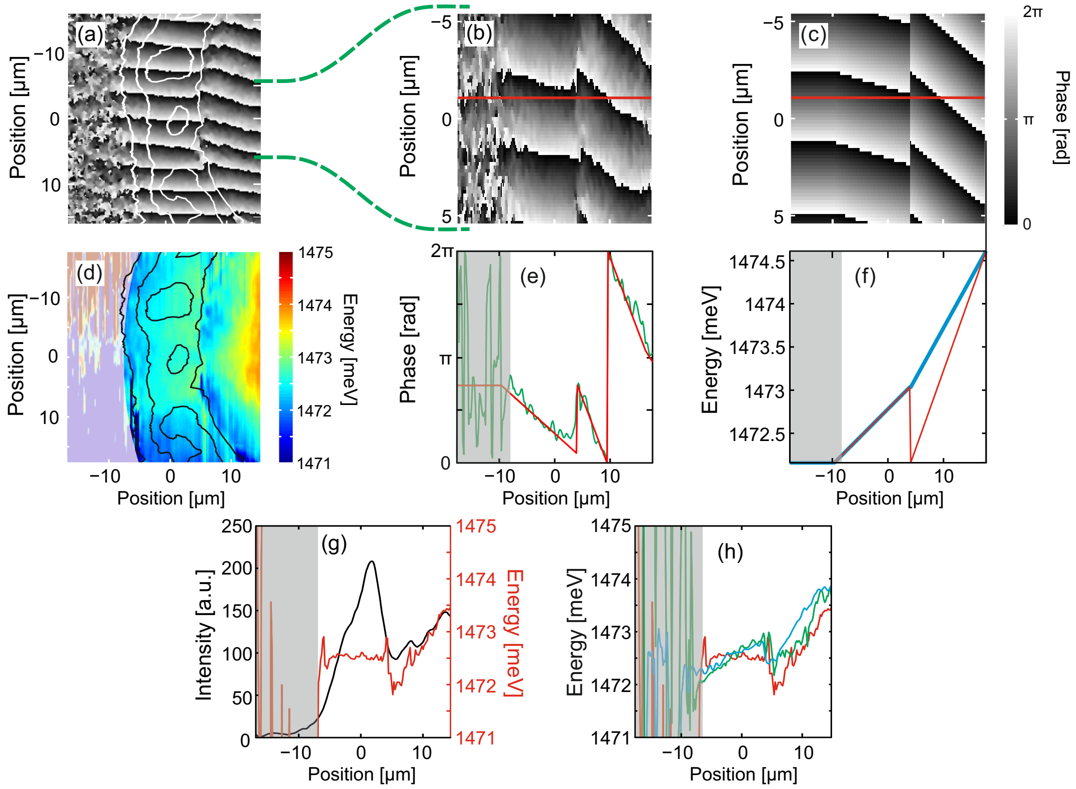

Figure A.4: (a) Map of the phase of the cosine fit (same as in A.3(h)). (b) Focus on the center part of (a). (c) Simulation of a phase map for the energy profile along the horizontal axis described with the solid red line in (f). In (f), the solid blue line shows a energy profile more continuous. (e) Measured (green) and simulated (red) phase profile along the horizontal axis at the position given by the red line in (b) and (c). (d) Map of the energy of the photoluminescence computed from the phase map (a). (g) Intensity of the photoluminescence (black, from fig. A.3(a)) and energy profiles (red) along the horizontal axis for $z \simeq 0\mu$m in (d). (h) Profiles of the energy of the photoluminescence at various vertical positions in (d) : $z \simeq -10$, 0 and 10μm. The white transparent in (d) and gray areas in (e-h) mark the region outside of the ring for which the phase is too random and noisy to perform an accurate analysis.

map presented in (c) where the fringes depends on z through the $q_\alpha z$ term and on x through λ in $(q_\alpha z + \phi_t)$. As one can see in (e) the used energy profile creates a simulated phase profile (red curve) which matches very well the real phase profile (green line). Due to the invariance of the phase by 2π multiplication, the same matching can be obtain for various range of energy such that one actually needs a spectroscopic measurement (on the ring for instance) to calibrate the energy range. If we apply a similar procedure for the whole phase map (a) we obtain fig. A.4(d).

Horizontal cuts from the map A.4(d) are presented in (g) while (h) shows the energy profiles along the ring radius. First of all, one can see that inside the ring we found again an energy of the photoluminescence which is decreasing towards the ring as seen in fig.III.16(c) (which reminds of the dome-shaped profile observed for instance in fig. III.16(c)). Interestingly, we also observe that the profile of the energy at the position of the ring and outside it can present different variations depending on the position along the ring circumference (see fig. A.4(h)). If we recall that the energy of the photoluminescence depends on both the exciton density (in this case only "real" excitons and not the exciton/charges compound since only their spectral component is filtered by the interferometer) and the potential landscape, we see that regions with different potential/density landscapes can exist depending on the position along the ring. We have therefore confirmed with an alternative method that the potential/density distribution outside the ring is complex as observed with the pump-probe experiments presented in chapter IV.

At this point a few remarks have to made about the precision of the phase analysis which strongly alter the above results. Indeed according to the above study, the energy profile presents a sudden drop at the interface between the ring and its interior. This would indicate a strong loss of density or a potential well which was not observed with the spectroscopic measurements. This is disturbing and in order to explain this anomaly we have to recall that in the previous analysis we have neglected the effect of the phase of the $g^{(1)}$-function. This simplification is probably too strong and for example it can be easily shown that if we start with a more regular energy profile (see thick blue line in fig.A.4(f)) adding a inhomogeneous additional phase through $\varphi_{\vec{r};0,\delta t}$ can lead to the same phase map. In order to take in account the phase of the $g^{(1)}$-function, we would need to relate its behavior with physical processes of the exciton gas.

For example, in the introduction to the Mach-Zehnder interferometer (see section II.B.2), we have seen that in the case of a collective movement of the exciton gas, the phase of the $g^{(1)}$-function can be related to the velocity $\mathbf{V}(\mathbf{r})$ of exciton through the expression : $\varphi(\mathbf{r}, \delta t) = M_X V^2(\mathbf{r})\delta t/2\hbar$. This influence of physical (classical) processes on the phase of the $g^{(1)}$-function is for sure not negligible in our case. Indeed, in chapter 4, we measure the potential landscape for excitons (see section IV.A.4), and find that it exhibits an abrupt fall at the inner edge of the ring, thus we can imagine that excitons inside the ring will fall towards the ring with a high velocity. Therefore we can imagine that the variations of the phase of the $g^{(1)}$-function are far from trivial and can not safely be neglected. The problem is that including this effect to the previous analysis will result in an extremely complex situation since the wavelength and the phase of the $g^{(1)}$-function effects on the characteristics of the interference fringes are fully mixed up. We will therefore not try to interpret further the phase map.

The situation is simpler for the phase of the interferograms given by the shift-interferometry. Indeed in this case $\phi_t = 0$, such that the phase of the cosine function reduces to $q_\alpha z + \varphi_{\vec{r};\delta x,\delta t=0}$ (see section V.A.2). Additionally, we see that the dependency of the $q_\alpha z$ term to the energy of the photoluminescence can be neglected (see section V.A.2). Thus, the position of the interference fringes is solely determined by the phase of the $g^{(1)}$-function which renders the interpretation of the phase map much easier.

To conclude this section we have seen that while theoretically possible, actually retrieving information on the spectral characteristics of the photoluminescence and on the phase of the temporal $g^{(1)}$-function by using time-interferometry is very challenging since both are intrinsically linked in the measurement, adding to the already complex nature of our system which includes multiple spectral components and very inhomogeneous photoluminescence energy. Nevertheless we were able to confirm with an other method that outside the ring, one can find regions with spectral characteristics similar to these on the ring.

Appendix B

Complements on the fragmented line

In this appendix, we present additional results on fragmented photoluminescence pattern created by illuminating the sample with a linear excitation beam at 641.5nm. We first see that the behavior of these fragmented lines with respect to the excitation power and the applied voltage is very similar to the one of the fragmented ring. We then examine the evolution of the photoluminescence pattern created by two independent linear excitation beams when the beams are moved closer to each other. We observe that the two sets of fragmented lines do not perturb each other, which contrasts with analogous experiments performed by the groups of D. Snoke and L. Butov. Finally we measure the spectral characteristics of the fragmented lines along the direction perpendicular to the one of the excitation beam. We find that the evolution of the spectra along the "radius" of the line resembles the one of the fragmented ring with a dome-shaped profile inside the fragmented lines and an energy essentially uniform around the position of the fragments. The favorable geometry allows us to study the spectral characteristics with a greater precision and in particular we observe that the density of free charges is lower at the position of the fragmented lines and in their outside vicinities. All the data presented in this appendix were recorded with the pulse sequence presented in fig. III.5 and at a bath temperature of 340mK.

II.A Influence of experimental parameters

In this section we examine the behavior of the photoluminescence pattern created by a linear excitation beam with respect to variations of the excitation power and the applied voltage. The objective is to compare phenomenologically these behaviors to those observed for the fragmented ring (see section III.B.1).

First of all, fig. B.1 displays the photoluminescence pattern for various values of the excitation power. We can see that starting from almost indistinct lines on each side of the linear excitation beam (at the abscissa 0 on the images), the "radius" of the lines (i.e. the distance between the positions of the excitation beam and the exterior lines) progressively increases while the intensity of the lines rises and the fragmentation develops. However for $P_{ex} = 200\mu$W, the fragmented lines disappear, leaving only a shapeless photoluminescence pattern with a maximum of intensity at the position of the excitation line. Similarly to the fragmented ring, varying the value of the applied voltage also changes the value of the excitation power above which no fragmented lines can be observed.

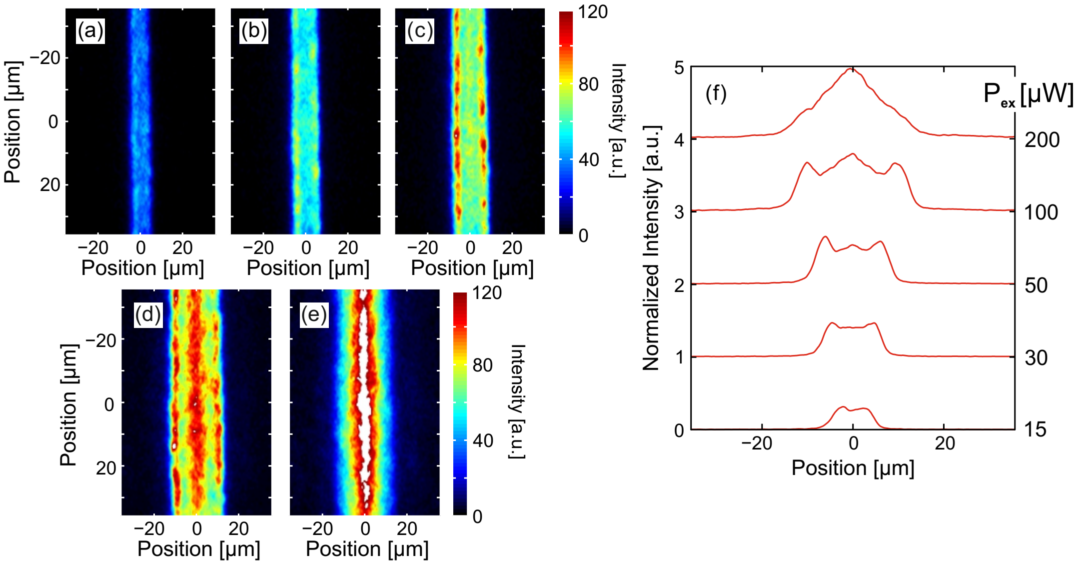

FIGURE B.1: (a-e) Direct images of photoluminescence created by a vertical linear excitation beam, $V_g = -4.8$V. From (a) to (e) the excitation power is respectively 15, 30, 50, 100 and 200μW. (f) Profiles of the intensity of the photoluminescence of the images (a-e) along the horizontal axis.

Fig. B.2 displays the variations of the fragmented lines with the applied voltage, which are very similar to these of the fragmented ring presented in fig. III.9. One can see that for $V_g = -5.6$V, the photoluminescence exhibits exterior lines and the maximum of intensity is at the position of the excitation line. Increasing V_g causes the fragmented lines to appear and gain in intensity. At the same time the lines widens towards the interior. Above -4.6V, the intensity of the whole photoluminescence rapidly drops until no signal can be observed.

To continue the comparison with the fragmented ring, we studied the behavior of the fragmented lines with the bath temperature and we observed once again that the

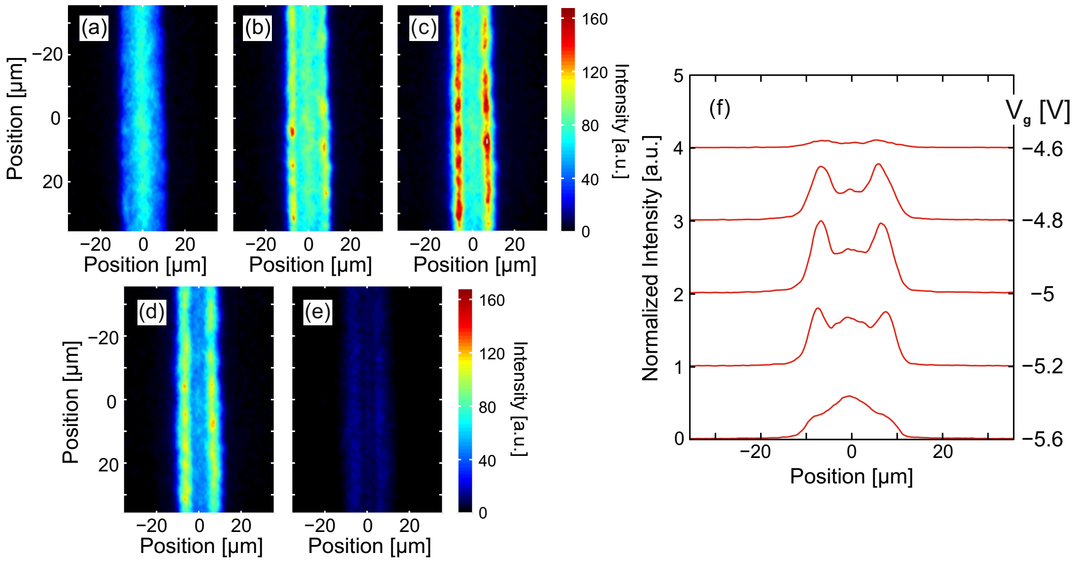

FIGURE B.2: (a-e) Direct images of photoluminescence created by a vertical linear excitation beam, $P_{ex} = 70\mu$W. From (a) to (e) the applied voltage is respectively -5.6, -5.2, -5, -4.8 and -4.6V. (f) Profiles of the intensity of the photoluminescence of the images (a-e) along the horizontal axis.

"radius" of the lines increases with the bath temperature. The fragmentation is also better defined at the lowest temperatures and rapidly disappears when the sample is warmed up. Let us note that the dynamics of the fragmented line presents overall characteristics very similar to these of the fragmented ring (data not shown), in particular the fragmented lines do not contract after the laser pulse.

Finally, if we have a look at the spectrum of the fragmented lines, one can see in figs. VI.2(b-d) and B.4 that the photoluminescence presents two distinct spectral components and that the distribution in energy strongly resemble the one of the fragmented lines. A study of the shift of the energy with the applied voltage reveals that these components also comes from compounds which exhibits an electric dipole momentum consistent with the one measured for the fragmented ring.

As a conclusion we see that the physical properties of the fragmented lines are near identical to those of the fragmented ring. We would then led to think that the formation mechanism is probably the same for the two geometries. To highlight a difference would require a much more detailed set of measurements which we leave for further studies.

II.B Photoluminescence created by two linear excitation beams

In order to validate the model based on the ambipolar diffusion of charges both the groups of L. Butov and D. Snoke performed experiments consisting in bringing closer two photoluminescence rings created by two independent excitation beams. Their results are shown in fig. III.3. They observed that when the excitation beams are brought closer, the rings seem to be attracted by each other resulting in an expansion of each ring towards the other. Upon further decreasing of the distance, the two rings merge to form eventually an oval-shaped photoluminescence pattern. These observations were interpreted as a depletion of the electron density in the region between the two rings, such that the holes injected at the position of the excitation beams can travel further away before recombining with the electrons and form excitons. We decided to reproduce this experiment with our sample with fragmented lines and our results are presented in fig. B.3.

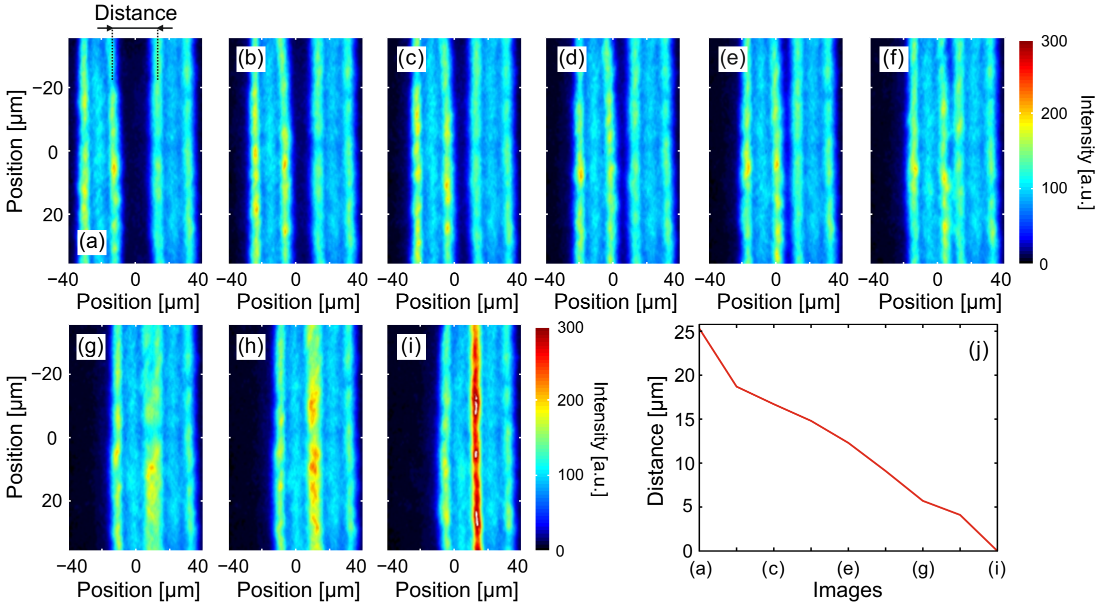

Figure B.3: (a-i) Direct images of the photoluminescence created by two identical vertical excitation beams aligned vertically at various distances from each other. The images were recorded with $P_{ex} = 97\mu\text{W}$ and $V_g = -5.2\text{V}$, the excitation power being the same for both linear excitation beams. (j) Distance between the inner fragmented lines for the images (a-i), as indicated in (a).

Strikingly we do not observe any significant modification of the photoluminescence when the linear excitation beams are brought closer to each other, except for an increase of the intensity of the photoluminescence when the two inner fragmented lines are superposed. Upon further decrease of the separation, the middle fragmented line loses intensity and eventually disappears (the two excitation lines are then essentially superposed). Let us note that similar experiments done with fragmented ring gives the same observations (data not shown), except that we eventually observe a merging of the two fragmented rings. At this moment the photoluminescence exhibits an “eight”-like shape with an increased intensity in the corners.

The interpretation of these observations is facilitated if we consider the profiles of the energy of the photoluminescence displayed in figs. VI.2(e-g). Indeed, these profiles indicate that the dome-shaped potentials inside the fragmented lines (and equivalently inside the fragmented rings) are not modified when the two linear excitation beams are brought closer. The global potential landscape is then equivalent to the sum of each potentials leading to a quasi-one dimensional confining potential between the two excitation lines. Excitons which explore this potential landscape will then accumulate at this position and form the middle fragmented line. If the excitation lines are brought closer this confining potential eventually disappear and we obtain a wider dome-shaped potential. The situation is the same for the fragmented ring except that due to the circular symmetry the sum of the two potentials will create a saddle-shaped potential. Excitons will then be able to diffuse away from the pass created between the two excitation beams and accumulate at each end of the pass, which explains the increased intensity of the photoluminescence in the corners of the “eight”-shape.

These observations have two important consequences which are the same whether we consider the fragmented ring or lines. Firstly, the potential inside the fragmented ring only depends on the spatial organization of the holes injected at the position of the excitation spot and not on the background electrons in the QW. However, we can imagine that the complex repartition of electrons and holes in the region surrounding the ring could be responsible for the formation of the local confining potentials we observed with the pump-probe experiments. In order to confirm this hypothesis we could for example examine with precision eventual changes in the repartition and location of the fragments when the fragmented ring are brought closer from each other. The second consequence is that the formation of our ring is largely dominated by the diffusion of excitons injected at the position of the excitation spot in the potential landscape. The formation of excitons at the position of the ring as the result of the recombination of electrons and holes traveling in opposite directions would thus only be secondary. The natural conclusion of these observations is that a model solely based on the ambipolar diffusion of charges is largely insufficient to explain the formation mechanism of our ring.

II.C Detailed spectroscopy

As explained in section VI.B.1, by illuminating the sample with a linear-shaped excitation beam we were able to produce fragmented lines. If we set these lines to be vertical one can immediately see the advantage for spectroscopic measurements. Indeed if we consider that the spectral characteristics only depend on the distance to the excitation spot and are essentially invariant along the fragmented line, we will be able to average the spatially resolved spectrum over a relatively large vertical region hence increasing the statistics. Similarly to the experiments presented in section III.C.3, we measure spectral information along the direction perpendicular to the line (the "ring radius") by aligning the entrance slit of the spectrometer at various distances with respect to the center of the fragmented lines (i.e. the position of the excitation line). The relevance of this method supposes that the spectral characteristics remain the same along the line, particularly between the beads and the valley. We will see that it is not exactly the case however the differences are small enough to guarantee the validity of our measurement.

Although drawing conclusions for the ring from experiments on the line can seem to be daring since the geometries are different, many characteristics are identical. For example we found again the two-components spectrum, a dome-shaped profile of the energy inside the fragmented line and an energy which is constant when moving outwards the fragmented line. The interest in the linear geometry is that we can now extract more information from the spectra thanks to an increased statistics and this at larger distance from the excitation line. In particular the behavior of the spectral line at low energy corresponding to the exciton/charges compound indicates that the density of free charges is larger inside the fragmented lines (as was the case for the fragmented ring, see section III.C.1.a) but also $\sim 6-7\mu$m outside them (we had a first evidence of this last result when studying the dynamics of the spectrum of the photoluminescence, see section III.C.2). We then have the confirmation that, like the fragmented ring, the region including the fragmented lines and its immediate outside vicinity presents the minimum concentration of free charges.

Fig. B.4 presents a direct image of the photoluminescence of the fragmented line, a spectrally resolved image taken on the fragmented line, characteristics of the 2 spectral components along the "line radius" as well as some spectra. First of all, one can see in figs. B.4(c) and (f) that while the exciton/charges line is always dominant along the "line radius", the exciton/charges and exciton lines have almost the same weight over a distance larger than the fragmented line. This signs a minimum density of charges in the QW for a region of a width of almost 10μm. This interpretation is confirmed by the spectral widths variations. Indeed the FWHM of the exciton/charges line is larger both inside and outside the line which we attribute to an increase of the interaction between

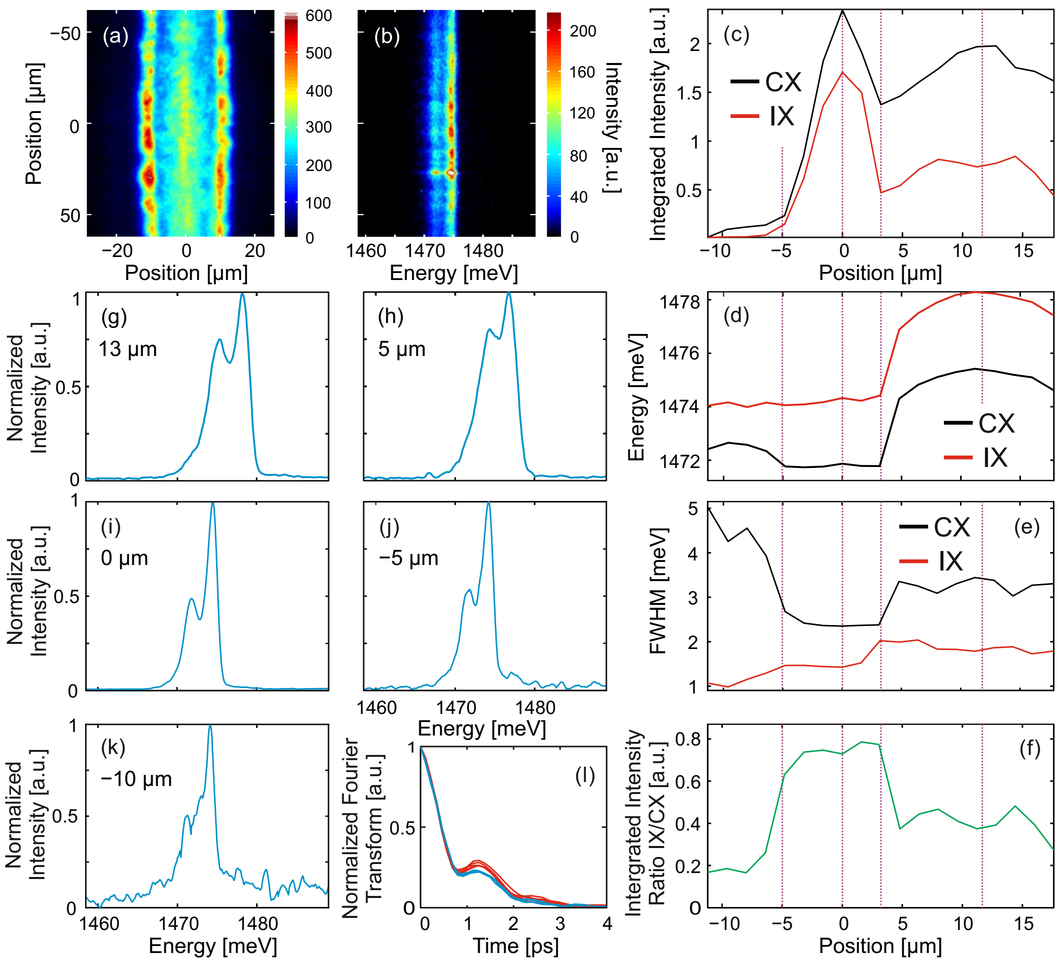

FIGURE B.4: (a) Direct photoluminescence of the fragmented lines for $T_b = 0.37$K, $P_{ex} = 112\mu$W and $V_g = -5.25$V. (b) Spatially resolved spectrum with the entrance slit of the spectrometer centered on the left fragmented line in (a). (c-f) Integrated intensity, peak energy, spectral width and integrated intensity ratio for the 2 spectral components (exciton/charges line in black and exciton line in red). The data were obtained by measuring spatially resolved spectra at various distances from the center of the fragmented line (distances are measured with respect to the origin at the position of the left fragmented line in (a)). The purple vertical dashed line are markers for the spatial positions. (g-k) Spectral profiles at various distances from the fragmented line. (l) Normalized Fourier transform of spectral profiles taken on the beads (red lines) and between the beads (blue lines) in the spectral image (b).

dipolar excitons and free charges. Finally the exciton/charges line presents a blueshift in energy outside of the fragmented line when the distance to it is larger than $\sim 6-7\mu$m. The results presented in the section dedicated to the influence of the excitation power on the spectrum (see section III.C.1.a) showed that the difference in energy between the exciton/charges and exciton lines depends on the density of free charges, therefore the region extended from -5 to 5μm is indeed a region of low density of free charges. The presence of charges inside the fragmented lines and of a lower density of free charges at the position of the fragmented lines should not come as a surprise if we recall the formation mechanism of the ring (and which is probably the same for the fragmented lines). What is more interesting with these measurements is that for the first time we established the existence of a high density of free charges outside the fragmented lines, which can be linked to the presence of the background electron gas described by the model relying on the ambipolar diffusion of free carriers. We also see that the region of low density of charges extends further away outside the fragmented line.

Similarly to the fragmented ring, the variation of the peak energy of both the exciton/charges and exciton lines (see fig. B.4(d)) is very peculiar. As we have seen before (see fig. III.16(c)) the peak energy is maximum at the position of the excitation beam (abscissa $\sim 12\mu$m) then slowly decreases towards the fragmented line until an abrupt fall of about 4 meV right before the line. Similarly to the ring, we attribute this to the screening of the internal electric field by free carriers resulting in a potential for excitons. Interestingly we see that after the sudden drop, the energy of both exciton/charges and exciton spectral lines remain exactly the same (within our spectral resolution) up to $\sim 5\mu$m away from the fragmented line, which is extremely surprising since at the same time the integrated intensity is divided by more than 10-fold. In principle, a drop of intensity of this magnitude is associated with an equivalent drop of energy. If the potential is homogeneous in this region it would mean that the density of excitons is constant over a large area which extends from the inner edge of the fragmented line until $\simeq 5\mu$m outside the maximum of the line. As explained throughout this manuscript, we interpret this anomaly as the presence of a dense gas of dark excitons in the vicinity of the fragmented lines. We recall that dark excitons contribute to the overall blueshift signing the dipolar interaction between excitons but being optically inactive they do not appear in the photoluminescence. Nevertheless in order to confirm this interpretation we need to measure the shape of the potential.

Such measurements for the fragmented ring are presented in section IV.A.4 and the results show evidences of the presence of confinement potentials extending from the edge of the dome-shaped potential to a certain distance away from the position of the ring. If we consider that the fragmented ring and line patterns exhibit similar characteristics we can imagine that such trapping potentials are also present in the case of the fragmented lines. The location of this confinement potential would then coincide with the region of low charges density and of uniform exciton density.

In order to obtain a better idea of the spectral differences between the beads and the valley of the fragmented line, we retrieved spectral profiles at various positions along the vertical axis in the spatially resolved spectrum presented in fig. B.4(b). The corresponding Fourier transforms are shown in fig. B.4(l) where the blue lines corresponds to the spectra in the valleys while the red lines corresponds to the beads. The differences are better marked with Fourier transform due to the very small variations of the spectral characteristics between the beads and the valleys. Indeed if we perform a two-components fit on the spectra of two adjacent bead/valley which present the most differences we obtain results which only differs within our experimental resolution. For instance the linewidth difference of the exciton/charges and the exciton lines are respectively of ~ 0.05 and ~ 0.07meV and the difference of the integrated intensity ratio (IX/CX) is only of $\sim 3\%$. The difference of the peak energy between the exciton lines is negligible however this difference for the exciton/charges lines would indicate a slightly larger density of charges in the valley. Such small fluctuations justify that we can average the spectral profile over the vertical axis and that we only can observe variation using Fourier transform of the spectra, which is a much more accurate measurements for small fluctuations (we also observed a difference on the map of the contrast of the time-interferometry, see appendix A and particularly fig. A.3(f)).

Appendix C

Other measurements of the exciton confinement potential

Here, we present additional measurements of the potential landscape and the density distribution obtained with an alternative pulse sequence and for a different fragmented ring compared to the experiment presented in section IV.A.4. The idea is to use a simpler pulse and recording sequence. To this aim, the duration of the probe pulse was set to 200ns and started 200ns after the end of the pump pulse. The probe photoluminescence was recorded with a window matching the length of the probe pulse while the photoluminescence of the fragmented ring was recorded with a 40ns-long window starting 10ns after the end of the pump pulse (see the pulse sequence in fig. C.1(a)). As usual the entrance slit of the spectrometer and the linear probe beam are aligned vertically and horizontally with the center of the fragmented ring. In this case $E_X^{\mathrm{probe}}(z, t = 200 - 400)$ (i.e. the energy profile of the probe photoluminescence) is directly equal to the potential landscape $V_X(z, t = 200 - 400)$, while the energy profile of the photoluminescence after the pump pulse $E_X^{\mathrm{pump}}(z, t = 10)$ is the sum of $V_X(z, t = 10)$ and $U_X^{\mathrm{probe}}(z, t = 10)$ (same notations as in section IV.A.4).

The results of this experiment are presented in fig. C.1. First of all one can see that for $T_b = 0.34$ and 1.5K, the energy profiles of the probe photoluminescence and of the fragmented ring coincide at large distances outside the ring (the extension of the energy profile for the photoluminescence after the pump pulse is limited due to the absence of signal far away outside the ring). Accordingly, at these temperatures $V_X(z, t = 200 - 400) = V_X(z, t = 10)$ such that the potential landscape is quasi-stationary. As a consequence the difference between the energy profiles $E_X^{\mathrm{probe}}(z, t = 200 - 400)$ and $E_X^{\mathrm{probe}}(z, t = 10)$ directly gives the variation of the strength of the dipolar interaction between excitons and therefore the distribution of the exciton density.

On both sides of the ring for $T_b = 0.34\text{K}$ (see fig. C.1(b.3)), we can observe the presence of confinement potentials. On the right side of the ring (blue transparent area), the variations of the two energy profiles are similar hence indicating that the density of excitons is uniform in this region. The profile of the intensity of the photoluminescence shows on the contrary a strong decrease outside the ring which would indicate a drop of the density. Similarly to the results presented in section IV.A.4, these contradictory behaviors prove the presence of a dominant population of dark excitons and therefore of a quantum gas of excitons in the outside vicinity of the ring. The difference in energy in this region is $\sim 1.3\text{meV}$ which corresponds to a density of excitons of $\sim 1.7 \times 10^{10}\text{cm}^{-2}$ (consistent with the measurements presented in the section IV.A.4). Interestingly, if we examine the same region at 1.5K (see fig. C.1(c.3)), we see that the confining potential is still present but with a lower depth ($\sim$ 1meV). Moreover the variations of the two energy profiles are not similar anymore and the profile of the intensity of the photoluminescence does not exhibit a strong drop. Thus we conclude that the dense gas of dark excitons is not present anymore (or least is not dominant). This difference between the two bath temperatures shows that both the presence of large fraction of dark excitons and the characteristics of the confining potential are strongly dependent on the temperature.

For the region on the right side of the ring and at the two lowest bath temperatures, the confining potential was perfectly filled as indicated by the superposition of the two energy profiles precisely at the outer edge of the trapping potential. If we now examine the left part of the ring for $T_b = 0.34\text{K}$ we see that while a confining potential is also present the two energy profiles only start to coincide at a larger distance from the outer edge of the potential. This means that in this region the trapping potential is not deep enough to contain all excitons such that some of them can diffuse further away from the ring. Therefore we see that the potential landscape outside the ring can present various shapes and depths inducing distinct distributions of the exciton density.

At the two highest temperatures the data show that the two energy profiles do not coincide away from the ring which indicate that the potential landscape has changed between the two recording delays (i.e. $V_X(z, t = 200 - 400) \neq V_X(z, t = 10)$). Therefore we can not conclude on the distribution of the density of excitons. This last result proves that the pulse sequence used in this appendix is not adequate to study the fragmented ring when the potential is varying on a timescale larger than $\sim 100 - 200\text{ns}$. This is the reason why we changed the pulse and recording sequence (see section IV.A.4), thus allowing conclusive measurements for various bath temperatures.

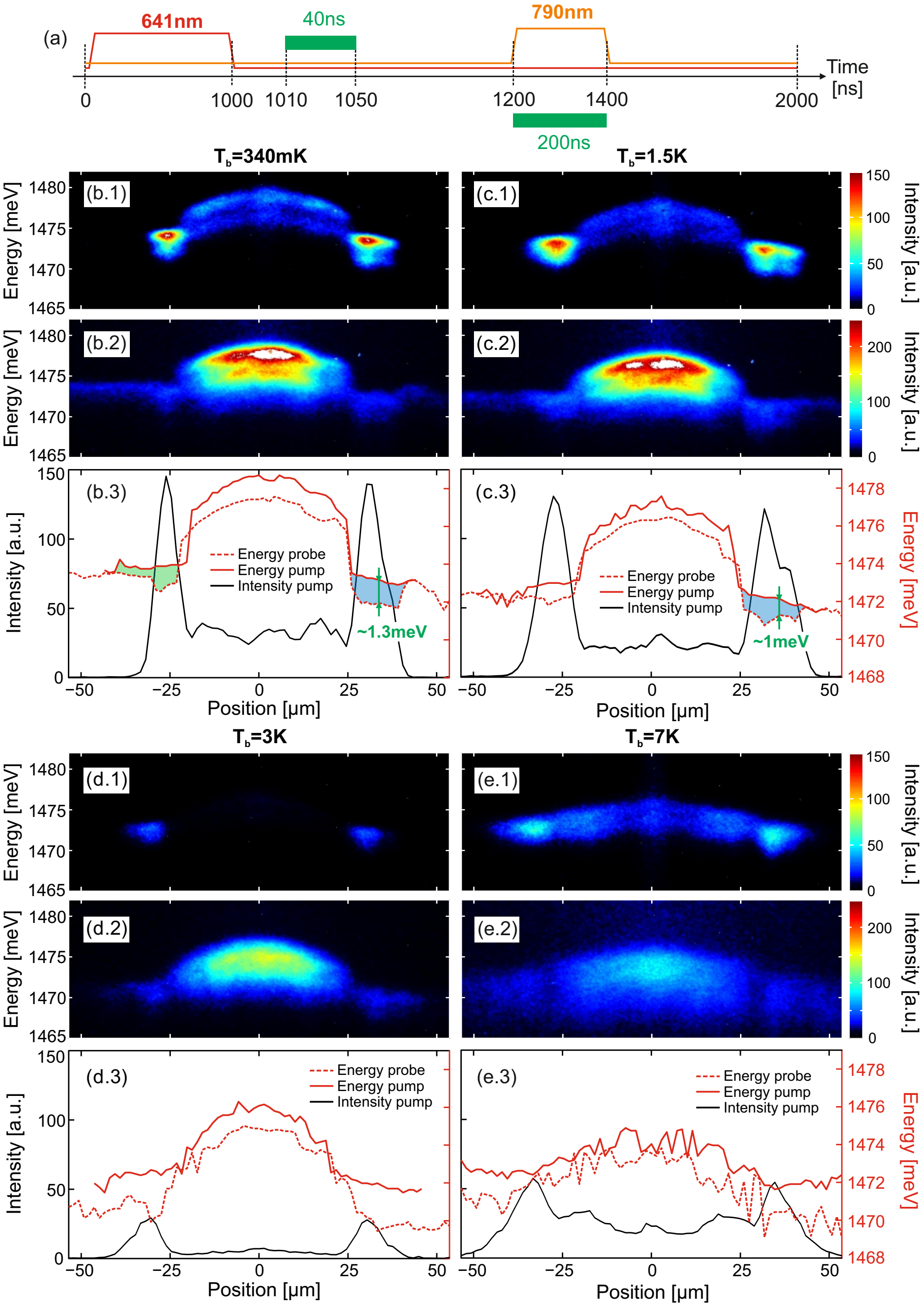

FIGURE C.1: (a) Schema of the pulse and recording sequence. (b.1) Spatially resolved spectrum of the photoluminescence created by the pump pulse recorded with a 40ns window starting 10ns after the end of the pump pulse (first green rectangle in the schema of the pulse sequence). (b.2) Spatially resolved spectrum of the probe photoluminescence recorded with a window matching the probe pulse (second green rectangle in the pulse sequence). The spectral images have been rotated by 90 degrees for clarity, the value of the abscissa corresponds to the position along the vertical axis given by the slit of the spectrometer. (b.3) Variation of the peak intensity of the exciton line of the pump photoluminescence (black line, from (b.1)) along the horizontal axis, the peak energy of the exciton line of the pump and probe photoluminescences are respectively represented by the solid and dashed red lines (resp. from (b.1) and (b.2)). For these measurements $T_b = 340$mK. (c-e) and corresponding columns show the same measurements for bath temperatures of 1.5, 3 and 7K. For all temperatures $P_{\mathrm{ex}}(641.5) = 18\mu$W, $P_{\mathrm{ex}}(790) = 200$nW and $V_g = -4.3$V.

Bibliography

[1] Bose, S. Plancks gesetz und lichtquantenhypothese. *Zeitschrift fur Physik* **26**, 178–181 (1924).

[2] Einstein, A. Quantentheorie des einatomigen idealen gases: Zweite abhandlung. *Sitzungber. Preuss. Akad. Wiss* **3** (1925).

[3] Anderson, M. H., Ensher, J. R., Matthews, M. R., Wieman, C. E. & Cornell, E. A. Observation of bose-einstein condensation in a dilute atomic vapor. *Science* **269**, 198–201 (1995).

[4] Davis, K. B. *et al.* Bose-einstein condensation in a gas of sodium atoms. *Physical Review Letters* **75**, 3969–3973 (1995).

[5] Bloch, I., Dalibard, J. & Zwerger, W. Many-body physics with ultracold gases. *Reviews of Modern Physics* **80**, 885–964 (2008).

[6] Blatt, J. M., Böer, K. W. & Brandt, W. Bose-einstein condensation of excitons. *Physical Review* **126**, 1691–1692 (1962).

[7] Moskalenko, S. A. Reversible optico-hydrodynamic phenomena in a nonideal exciton gas. *Sov Phys-Sol State* **4**, 199 (1962).

[8] Keldysh, L. V. & Kozlov, A. N. Collective properties of excitons in semiconductors. *Soviet Journal of Experimental and Theoretical Physics* **27**, 521 (1968).

[9] Chang, L. L., Esaki, L. & Tsu, R. Resonant tunneling in semiconductor double barriers. *Applied Physics Letters* **24**, 593 (1974).

[10] Dingle, R., Wiegmann, W. & Henry, C. H. Quantum states of confined carriers in very thin $\mathrm{Al}_x\mathrm{Ga}_{1-x}\mathrm{As}$-GaAs- $\mathrm{Al}_x\mathrm{Ga}_{1-x}\mathrm{As}$ heterostructures. *Physical Review Letters* **33**, 827–830 (1974).

[11] Lozovik, Y. E. & Yudson, V. I. A new mechanism for superconductivity: pairing between spatially separated electrons and holes. *Soviet Journal of Experimental and Theoretical Physics* **44**, 389 (1976).

[12] Miller, D. A. B. *et al.* Band-edge electroabsorption in quantum well structures - the quantum-confined stark effect. *Physical Review Letters* **53**, 2173–2176 (1984).

[13] Miller, D. A. B. *et al.* Electric field dependence of optical absorption near the band gap of quantum-well structures. *Phys. Rev. B* **32**, 1043–1060 (1985).

[14] Hammack, A. T. *et al.* Excitons in electrostatic traps. *J. Appl. Phys.* **99**, 066104 (2006).

[15] High, A. A., Novitskaya, E. E., Butov, L. V., Hanson, M. & Gossard, A. C. Control of exciton fluxes in an excitonic integrated circuit. *Science* **321**, 229–231 (2008).

[16] High, A. A. *et al.* Trapping indirect excitons in a GaAs quantum-well structure with a diamond-shaped electrostatic trap. *Physical Review Letters* **103**, 087403 (2009).

[17] High, A. A. *et al.* Indirect excitons in elevated traps. *Nano Letters* **9**, 2094–2098 (2009).

[18] Gärtner, A., Holleitner, A. W., Kotthaus, J. P. & Schuh, D. Drift mobility of long-living excitons in coupled GaAs quantum wells. *Applied Physics Letters* **89**, 052108 (2006).

[19] Gärtner, A., Prechtel, L., Schuh, D., Holleitner, A. W. & Kotthaus, J. P. Micropatterned electrostatic traps for indirect excitons in coupled GaAs quantum wells. *Phys. Rev. B* **76**, 085304 (2007).

[20] Rapaport, R. *et al.* Electrostatic traps for dipolar excitons. *Phys. Rev. B* **72**, 075428 (2005).

[21] Schinner, G. J. *et al.* Confinement and interaction of single indirect excitons in a voltage-controlled trap formed inside double InGaAs quantum wells. *Physical Review Letters* **110**, 127403 (2013).

[22] Rapaport, R. & Chen, G. Experimental methods and analysis of cold and dense dipolar exciton fluids. *Journal of Physics Condensed Matter* **19**, C5207 (2007).

[23] High, A. A. *et al.* Condensation of excitons in a trap. *Nano Letters* **12**, 2605–2609 (2012).

[24] Dremin, A. A., Timofeev, V. B., Larionov, A. V., Hvam, J. & Soerensen, K. Phase diagram of the bose condensation of interwell excitons in GaAs/AlGaAs double quantum wells. *Soviet Journal of Experimental and Theoretical Physics Letters* **76**, 450–455 (2002).

[25] Gorbunov, A. V. & Timofeev, V. B. Collective behavior of interwell excitons laterally confined in GaAs/AlGaAs double quantum wells. *Physica Status Solidi C* **2**, 871–876 (2005).

[26] Timofeev, V. B., Gorbunov, A. V. & Larionov, A. V. Long-range coherence of interacting bose gas of dipolar excitons. *Journal of Physics Condensed Matter* **19**, C5209 (2007).

[27] Timofeev, V. B. & Gorbunov, A. V. Bose-einstein condensation of dipolar excitons in double and single quantum wells. *Physica Status Solidi C* **5**, 2379–2386 (2008).

[28] Timofeev, V. B., Gorbunov, A. V. & Demin, D. A. Bose-einstein condensation of dipolar excitons in lateral traps. *Low Temperature Physics* **37**, 179–187 (2011).

[29] Weisbuch, C., Nishioka, M., Ishikawa, A. & Arakawa, Y. Observation of the coupled exciton-photon mode splitting in a semiconductor quantum microcavity. *Physical Review Letters* **69**, 3314–3317 (1992).

[30] Imamoglu, A., Ram, R. J., Pau, S. & Yamamoto, Y. Nonequilibrium condensates and lasers without inversion: Exciton-polariton lasers. *Phys. Rev. A* **53**, 4250–4253 (1996).

[31] Richard, M. *et al.* Experimental evidence for nonequilibrium bose condensation of exciton polaritons. *Phys. Rev. B* **72**, 201301 (2005).

[32] Kasprzak, J. *et al.* Bose-einstein condensation of exciton polaritons. *Nature* **443**, 409–414 (2006).

[33] Deng, H., Weihs, G., Santori, C., Bloch, J. & Yamamoto, Y. Condensation of semiconductor microcavity exciton polaritons. *Science* **298**, 199–202 (2002).

[34] Lagoudakis, K. G. *et al.* Observation of half-quantum vortices in an exciton-polariton condensate. *Science* **326**, 974– (2009).

[35] Manni, F., Lagoudakis, K. G., Liew, T. C. H., André, R. & Deveaud-Plédran, B. Spontaneous pattern formation in a polariton condensate. *Physical Review Letters* **107**, 106401 (2011).

[36] Amo, A. *et al.* Superfluidity of polaritons in semiconductor microcavities. *Nature Physics* **5**, 805–810 (2009).

[37] Amo, A. *et al.* Polariton superfluids reveal quantum hydrodynamic solitons. *Science* **332**, 1167– (2011).

[38] Galbiati, M. *et al.* Polariton condensation in photonic molecules. *Physical Review Letters* **108**, 126403 (2012).

[39] Abbarchi, M. *et al.* Macroscopic quantum self-trapping and josephson oscillations of exciton polaritons. *Nature Physics* **9**, 275–279 (2013).

[40] Balili, R., Hartwell, V., Snoke, D., Pfeiffer, L. & West, K. Bose-einstein condensation of microcavity polaritons in a trap. *Science* **316**, 1007– (2007).

[41] Lai, C. W. *et al.* Coherent zero-state and π-state in an exciton-polariton condensate array. *Nature* **450**, 529–532 (2007).

[42] Utsunomiya, S. *et al.* Observation of bogoliubov excitations in exciton-polariton condensates. *Nature Physics* **4**, 700–705 (2008).

[43] Amo, A. *et al.* Collective fluid dynamics of a polariton condensate in a semiconductor microcavity. *Nature* **457**, 291–295 (2009).

[44] Sanvitto, D. *et al.* Persistent currents and quantized vortices in a polariton superfluid. *Nature Physics* **6**, 527–533 (2010).

[45] Combescot, M., Betbeder-Matibet, O. & Combescot, R. Bose-Einstein condensation in semiconductors: The key role of dark excitons. *Physical Review Letters* **99**, 176403 (2007).

[46] Combescot, M. & Leuenberger, M. N. General argument supporting bose-einstein condensate of dark excitons in single and double quantum wells. *Solid State Communications* **149**, 567–571 (2009).

[47] Amand, T. *et al.* Spin quantum beats of 2D excitons. *Physical Review Letters* **78**, 1355–1358 (1997).

[48] Blackwood, E., Snelling, M. J., Harley, R. T., Andrews, S. R. & Foxon, C. T. B. Exchange interaction of excitons in GaAs heterostructures. *Phys. Rev. B* **50**, 14246–14254 (1994).

[49] Viña, L. Spin relaxation in low-dimensional systems. *Journal of Physics Condensed Matter* **11**, 5929–5952 (1999).

[50] Combescot, R. & Combescot, M. “Gray” BCS condensate of excitons and internal josephson effect. *Physical Review Letters* **109**, 026401 (2012).

[51] Butov, L. V., Gossard, A. C. & Chemla, D. S. Macroscopically ordered state in an exciton system. *Nature* **418**, 751–754 (2002).

[52] Snoke, D., Denev, S., Liu, Y., Pfeiffer, L. & West, K. Long-range transport in excitonic dark states in coupled quantum wells. *Nature* **418**, 754–757 (2002).

[53] Butov, L. V. *et al.* Formation mechanism and low-temperature instability of exciton rings. *Phys. Rev. Lett.* **92**, 117404 (2004).

[54] Snoke, D. *et al.* Moving beyond a simple model of luminescence rings in quantum well structures. *Journal of Physics Condensed Matter* **16**, 3621 (2004).

[55] Rapaport, R. *et al.* Mechanism of exciton emission ring pattern in doped quantum wells. *Physica Status Solidi Applied Research* **201**, 655–660 (2004).

[56] Haque, M. Ring-shaped luminescence pattern in biased quantum wells studied as a steady-state reaction front. *Phys. Rev. E* **73**, 066207 (2006).

[57] Levitov, L. S., Simons, B. D. & Butov, L. V. Pattern formation as a signature of quantum degeneracy in a cold exciton system. *Phys. Rev. Lett.* **94**, 176404 (2005).

[58] Yang, S., Hammack, A. T., Fogler, M. M., Butov, L. V. & Gossard, A. C. Coherence length of cold exciton gases in coupled quantum wells. *Phys. Rev. Lett.* **97**, 187402 (2006).

[59] Yang, S., Mintsev, A. V., Hammack, A. T., Butov, L. V. & Gossard, A. C. Repulsive interaction in the macroscopically ordered exciton state in GaAs/$\mathrm{Al}_x\mathrm{Ga}_{1-x}\mathrm{As}$ coupled quantum well structures. *Phys. Rev. B* **75**, 033311 (2007).

[60] Yang, S., Butov, L. V., Levitov, L. S., Simons, B. D. & Gossard, A. C. Exciton front propagation in photoexcited GaAs quantum wells. *Phys. Rev. B* **81**, 115320 (2010).

[61] High, A. A. *et al.* Spontaneous coherence in a cold exciton gas. *Nature* **483**, 584–588 (2012).

[62] Alloing, M., Lemaître, A., Galopin, E. & Dubin, F. Optically programmable excitonic traps. *Scientific Reports* **3**, 1578 (2013).

[63] Shilo, Y. *et al.* Particle correlations and evidence for dark state condensation in a cold dipolar exciton fluid. *Nature Communications* **4** (2013).

[64] Sivalertporn, K., Mouchliadis, L., Ivanov, A. L., Philp, R. & Muljarov, E. A. Direct and indirect excitons in semiconductor coupled quantum wells in an applied electric field. *Phys. Rev. B* **85**, 045207 (2012).

[65] Mathieu, H. & Fanet, H. *Physique des semiconducteurs et des composants électroniques* (Dunod, 2009).

[66] Kittel, C. *Introduction to Solid State Physics* (Wiley, 2004).

[67] Ivanov, A. L., Littlewood, P. B. & Haug, H. Bose-einstein statistics in thermalization and photoluminescence of quantum-well excitons. *Phys. Rev. B* **59**, 5032–5048 (1999).

[68] Ivanov, A. L. Thermalization and photoluminescence dynamics of indirect excitons at low bath temperatures. *Journal of Physics Condensed Matter* **16**, 3629 (2004).

[69] Schinner, G. J. *et al.* Electrostatically trapping indirect excitons in coupled $\mathrm{In}_x\mathrm{Ga}_{1-x}\mathrm{As}$ quantum wells. *Phys. Rev. B* **83**, 165308 (2011).

[70] Rapaport, R., Chen, G. & Simon, S. Analysis of trapped quantum degenerate dipolar excitons. *Applied Physics Letters* **89**, 152118 (2006).

[71] Chen, G. *et al.* Artificial trapping of a stable high-density dipolar exciton fluid. *Phys. Rev. B* **74**, 045309 (2006).

[72] Gorbunov, A. V., Timofeev, V. B. & Demin, D. A. Electro-optical trap for dipolar excitons in a GaAs/AlAs schottky diode with a single quantum well. *Soviet Journal of Experimental and Theoretical Physics Letters* **94**, 800–805 (2012).

[73] Alloing, M., Lemaître, A., Galopin, E. & Dubin, F. Nonlinear dynamics and inner-ring photoluminescence pattern of indirect excitons. *Phys. Rev. B* **85**, 245106 (2012).

[74] Ivanov, A. L., Muljarov, E. A., Mouchliadis, L. & Zimmermann, R. Comment on "Photoluminescence ring formation in coupled quantum wells: Excitonic versus ambipolar diffusion". *Physical Review Letters* **104**, 179701 (2010).

[75] Laikhtman, B. & Rapaport, R. Correlations in a two-dimensional bose gas with long-range interaction. *EPL (Europhysics Letters)* **87**, 27010 (2009).

[76] Schindler, C. & Zimmermann, R. Analysis of the exciton-exciton interaction in semiconductor quantum wells. *Phys. Rev. B* **78**, 045313 (2008).

[77] Laikhtman, B. & Rapaport, R. Exciton correlations in coupled quantum wells and their luminescence blue shift. *Phys. Rev. B* **80**, 195313 (2009).

[78] Schinner, G. J. *et al.* Many-body correlations of electrostatically trapped dipolar excitons. *Phys. Rev. B* **87**, 205302 (2013).

[79] Pitaevskii, L. P. & Stringari, S. *Bose-einstein condensation* (Clarendon Press, Oxford, 2003).

[80] Pethick, C. J. & Smith, H. *Bose-Einstein Condensation in Dilute Gases* (Cambridge University Press, 2008).

[81] Blackwood, E., Snelling, M. J., Harley, R. T., Andrews, S. R. & Foxon, C. T. B. Exchange interaction of excitons in GaAs heterostructures. *Phys. Rev. B* **50**, 14246–14254 (1994).

[82] Efanov, A. V., Zhuravlev, K. S., Shamirzaev, T. S., Kellner, W. & Pascher, H. Exciton fine structure and spin dynamics in high purity AlGaAs layers. *Semiconductor Science Technology* **19**, 377 (2004).

[83] Combescot, M., Combescot, R., Alloing, M. & Dubin, F. Optical signatures of a fully dark exciton condensate. *EuroPhys. Letters* **105**, 47011 (2014).

[84] Nalitov, A. V., Vladimirova, M., Kavokin, A. V., Butov, L. V. & Gippius, N. A. Nonlinear optical probe of indirect excitons. *arXiv* 1311.0165 (2013).

[85] Butov, L. Exciton condensation in coupled quantum wells. *Solid State Communications* **127**, 89 – 98 (2003).

[86] Tersoff, J. Schottky barrier heights and the continuum of gap states. *Physical Review Letters* **52**, 465–468 (1984).

[87] Tersoff, J. Theory of semiconductor heterojunctions: The role of quantum dipoles. *Phys. Rev. B* **30**, 4874–4877 (1984).

[88] Lai, C.-W. E. *Spatially indirect excitons in coupled quantum wells.* Ph.D. thesis, University of California, Berkeley (2004).

[89] Butov, L. V. Condensation and pattern formation in cold exciton gases in coupled quantum wells. *Journal of Physics: Condensed Matter* **16**, R1577 (2004).

[90] Schinner, G. J. *Correlated behavior of electrostatically trapped dipolar excitons at low temperatures.* Ph.D. thesis, Ludwig-Maximilians-Universität München (2012).

[91] Vörös, Z. *Interaction of excitons in two-dimensional potential.* Ph.D. thesis, University of Pittsburgh (2008).

[92] Vörös, Z., Snoke, D. W., Pfeiffer, L. & West, K. Direct measurement of exciton-exciton interaction energy. *Physical Review Letters* **103**, 016403 (2009).

[93] Nag, B. *Electron Transport in Compound Semiconductors*, vol. 11 (Springer London, 1980).

[94] O'Donnell, K. P. & Chen, X. Temperature dependence of semiconductor band gaps. *Applied Physics Letters* **58**, 2924–2926 (1991).

[95] Semkat, D., Sobkowiak, S., Manzke, G. & Stolz, H. Comment on "Condensation of excitons in a trap". *Nano Letters* **12**, 5055–5057 (2012).

[96] Fogler, M. M., Yang, S., Hammack, A. T., Butov, L. V. & Gossard, A. C. Effect of spatial resolution on the estimates of the coherence length of excitons in quantum wells. *Phys. Rev. B* **78**, 035411 (2008).

[97] Zhang, B., Zerubia, J. & Olivo-Marin, J.-C. Gaussian approximations of fluorescence microscope point-spread function models. *Applied Optics* **46**, 1819–1829 (2007).

[98] Lagoudakis, K. *On the Physics of Exciton-Polariton Condensates*. Ph.D. thesis, Ecole Polytechnique Federale de Lausanne (2010).

[99] Roumpos, G. *et al.* Single vortex-antivortex pair in an exciton-polariton condensate. *Nature Physics* **7**, 129–133 (2011).

[100] Bloch, I., Hänsch, T. W. & Esslinger, T. Measurement of the spatial coherence of a trapped bose gas at the phase transition. *Nature* **403**, 166–170 (2000).

[101] Roland Combescot, private communication (2014).

[102] Mandel, L. & Wolf, E. *Optical coherence and quantum optics* (Cambridge University Press, 1995).

[103] Naraschewski, M. & Glauber, R. J. Spatial coherence and density correlations of trapped bose gases. *Phys. Rev. A* **59**, 4595–4607 (1999).

[104] Mouchliadis, L. *Transport and Coherence Properties of Indirect Excitons in Coupled Quantum Wells*. Ph.D. thesis, Cardiff University (2008).

[105] Kagan, Y., Kashurnikov, V. A., Krasavin, A. V., Prokof'ev, N. V. & Svistunov, B. V. Quasicondensation in a two-dimensional interacting bose gas. *Phys. Rev. B* **61**, 043608 (2000).

[106] Filinov, A., Prokof'Ev, N. V. & Bonitz, M. Berezinskii-Kosterlitz-Thouless transition in two-dimensional dipole systems. *Physical Review Letters* **105**, 070401 (2010).

[107] Denev, S. *et al.* Luminescence rings in quantum well structures. In *APS Meeting Abstracts*, 36006 (2004).

[108] Rapaport, R. *et al.* Charge separation of dense two-dimensional electron-hole gases: Mechanism for exciton ring pattern formation. *Physical Review Letters* **92**, 117405 (2004).

[109] Fluegel, B. *et al.* Exciton pattern generation in GaAs/Al$_x$Ga$_{1-x}$As multiple quantum wells. *Phys. Rev. B* **83**, 195320 (2011).

[110] Butov, L. V., Lai, C. W., Ivanov, A. L., Gossard, A. C. & Chemla, D. S. Towards bose-einstein condensation of excitons in potential traps. *Nature* **417**, 47–52 (2002).

[111] Mouchliadis, L. & Ivanov, A. L. Anti-trapping of indirect excitons by a current filament. *Journal of Physics Condensed Matter* **19**, C5215 (2007).

[112] Chernyuk, A. A. & Sugakov, V. I. Ordered dissipative structures in exciton systems in semiconductor quantum wells. *Phys. Rev. B* **74**, 085303 (2006).

[113] Paraskevov, A. V. Ring-shaped spatial pattern of exciton luminescence formed due to the hot carrier transport in a locally photoexcited electron-hole bilayer. *Soviet Journal of Experimental and Theoretical Physics* **114**, 1022–1036 (2012).

[114] Wilkes, J., Muljarov, E. A. & Ivanov, A. L. Drift-diffusion model of the fragmentation of the external ring structure in the photoluminescence pattern emitted by indirect excitons in coupled quantum wells. *Physical Review Letters* **109**, 187402 (2012).

[115] Andreev, S. V. Thermodynamic model of the macroscopically ordered exciton state. *Physical Review Letters* **110**, 146401 (2013).

[116] Andreev, S. V., Varlamov, A. A. & Kavokin, A. V. Scale invariance and universality in a cold gas of indirect excitons. *arXiv* 1307.3721 (2013).

[117] Butov, L. V. Cold exciton gases in coupled quantum well structures. *Journal of Physics: Condensed Matter* **19**, 295202 (2007).

[118] Chen, G., Rapaport, R., Simon, S. H., Pfeiffer, L. & West, K. Dynamics of the in-plane charge separation front in a two-dimensional electron-hole gas. *Phys. Rev. B* **71**, 041301 (2005).

[119] Alloing, M., Lemaître, A. & Dubin, F. Quantum signature blurred by disorder in indirect exciton gases. *EPL (Europhysics Letters)* **93**, 17007 (2011).

[120] Ivanov, A. L. *et al.* Origin of the inner ring in photoluminescence patterns of quantum well excitons. *EPL (Europhysics Letters)* **73**, 920–926 (2006).

[121] Hammack, A. T. *et al.* Kinetics of the inner ring in the exciton emission pattern in coupled GaAs quantum wells. *Phys. Rev. B* **80**, 155331 (2009).

[122] Kuznetsova, Y. Y. *et al.* Excitation energy dependence of the exciton inner ring. *Phys. Rev. B* **85**, 165452 (2012).

[123] Bar-Joseph, I. Trions in GaAs quantum wells. *Semiconductor Science Technology* **20**, 29 (2005).

[124] Combescot, M. *et al.* Many-body origin of the “trion line” in doped quantum wells. *Europhysics Letters* **71**, 431–437 (2005).

[125] Manassen, A., Cohen, E., Ron, A., Linder, E. & Pfeiffer, L. N. Exciton and trion spectral line shape in the presence of an electron gas in GaAs/AlAs quantum wells. *Phys. Rev. B* **54**, 10609–10613 (1996).

[126] Timofeev, V. B. *et al.* Charged excitonic complexes in GaAs/$Al_{0.35}Ga_{0.65}As$ p-i-n double quantum wells. *Phys. Rev. B* **60**, 8897–8901 (1999).

[127] Schinner, G. J. *et al.* Quantum hall signatures of dipolar mahan excitons. *Phys. Rev. B* **87**, 041303 (2013).

[128] Kowalik-Seidl, K. *et al.* Forming and confining of dipolar excitons by quantizing magnetic fields. *Phys. Rev. B* **83**, 081307 (2011).

[129] Stern, M., Garmider, V., Umansky, V. & Bar-Joseph, I. Mott transition of excitons in coupled quantum wells. *Physical Review Letters* **100**, 256402 (2008).

[130] Stern, M. *et al.* Photoluminescence ring formation in coupled quantum wells: Excitonic versus ambipolar diffusion. *Physical Review Letters* **101**, 257402 (2008).

[131] Butov, L. V., Shashkin, A. A., Dolgopolov, V. T., Campman, K. L. & Gossard, A. C. Magneto-optics of the spatially separated electron and hole layers in GaAs/$Al_xGa_{1-x}As$ coupled quantum wells. *Phys. Rev. B* **60**, 8753–8758 (1999).

[132] Denev, S., Simon, S. H. & Snoke, D. W. Luminescence ring formation in quantum wells : a model with coulomb interaction. *Solid State Communications* **134**, 59–62 (2005).

[133] Kowalik-Seidl, K. *et al.* Tunable photoemission from an excitonic antitrap. *Nano Letters* **12**, 326–330 (2012).

[134] High, A. A. *et al.* Spin currents in a coherent exciton gas. *Phys. Rev. Lett.* **110**, 246403 (2013).

[135] Kavokin, A. V. *et al.* Ballistic spin transport in exciton gases. *Phys. Rev. B* **88**, 195309 (2013).

[136] Peters, N., Altepeter, J., Jeffrey, E., Branning, D. & Kwiat, P. Precise creation, characterization, and manipulation of single optical qubits. *Quantum Information & Computation* **3**, 503–517 (2003).

[137] James, D. F. V., Kwiat, P. G., Munro, W. J. & White, A. G. Measurement of qubits. *Phys. Rev. B* **64**, 052312 (2001).

[138] Leonard, J. R. *et al.* Spin transport of excitons. *Nano Letters* **9**, 4204–4208 (2009).

[139] Kowalik-Seidl, K. *et al.* Long exciton spin relaxation in coupled quantum wells. *Applied Physics Letters* **97**, 011104 (2010).